Numerical Prediction of Free-Surface Flows Caused by Body/Fluid Interaction

David Irving Moffat Forehand

A thesis submitted in fulfilment of the requirements

for the degree of Doctor of Philosophy

to the

University of Edinburgh

1998

To My Sister Joannie.

Abstract

In this study numerical methods for free-surface flows are reviewed and their advantages and disadvantages over each other assessed. This results in the adoption of the Boundary-Integral Method (BIM) as the preferred method to model the flows of interest, namely free-surface flows in the vicinity of surface-piercing bodies. An improved BIM is then developed which takes features from various exiting BIMs and in some cases extends these features. Notable improvements include: the discretisation of the boundary, the treatment of corners in the boundary of the fluid domain and the control of free-surface instabilities. The results of this BIM are then compared with an analytical solution, results from another numerical method and results from an experiment. In all three cases very good agreement is found. The comparison with the analytical solution shows, for the first time, that a properly adapted BIM can accurately predict the fluid motion at the intersection between the free-surface and a body for an extreme free-surface flow caused by body/fluid interaction. In addition to this good comparison, hitherto unnoticed features of the analytical solution are also identified and presented. Finally, unlike in many experimental comparisons, in the one performed here the exact geometry of the wavetank and motion of the wavemaker are used as input for the present numerical wavetank.

Acknowledgements

I would firstly like to thank my supervisors: Professor Clive Greated, for his invaluable support and advice throughout; Dr. John Byatt-Smith, for his help with many mathematical points and Dr. David Skyner, for getting me through a difficult first year.

I would also like to thank the following academics from outside Edinburgh for their assistance during the course of this project: Dr. Martin Greenhow, Prof. Andy King and Prof. Howell Peregrine.

At Edinburgh I am very grateful to the following researchers who helped me: Michael Jakobsen, for performing the experiments which I compared my numerical method against; Akash Chopra, for the many useful discussions on numerical modelling and for joining me on a conference/holiday in California, and John Pullen, Tim Dewhirst & Alistair Young, for setting-up/maintaining the local Fluids Group Network.

I would also like to thank my friends at Edinburgh University who have made my time here very enjoyable. I would like to thank John Cosgrove, Tom Haydon, Alistair Arnott, Paul Stansell, Jon Entwistle, Vikram Pandya, Jim Buick, Dave Hann and all the rest of the old gang in the Fluids Group. Thanks also to the new gang in the Fluids Group (Susan's gang) for their friendship during my writing-up. Particular thanks must go to Narumon for her kindness, companionship and endless patience over the last year.

Outside the department my friends: Jenny & Sanj, Iain & Gavin, Barbara, Lesley *etc.*, I feel I owe them an apology for not visiting them enough; I thank them for still remembering me.

My greatest debt of gratitude goes to my family: Mum, Dad, Joan, Bob, John and Gran. I cannot thank them enough for all their support. Thanks also to my cousin Janet and her husband to be Martin for the times when they dragged me away from writing-up and showed me that there was life beyond my thesis!

This project was funded by the Engineering and Physical Sciences Research Council (EPSRC) and their support is greatly appreciated.

Table of Contents

List of Figures

List of Tables

Chapter 1

Introduction

In the late summer of 1995 what was planned to be the world's first commercial wave-powered electricity generator was launched into the River Clyde (see figure 1.1). The 20m high, 8000 ton Ocean Swell Powered Renewable Energy generator, or OSPREY, was then towed to Dounreay in the north of Scotland where it was to be anchored in 14 metres of water and then connected to Scottish Hydro-Electric's grid. Unfortunately, before the Osprey could be safely fixed to the seabed it sank in a storm.

The above example is just one of many which highlight the problem of the survival of surface-piercing marine structures in extreme seas. When engineers come to design such a structure they will try to design it so that it is just strong enough (plus some specified safety margin) to survive the most extreme wave it is likely to encounter[1]. If the engineer makes the structure too strong then it will be unnecessarily expensive and this may jeopardise the financial viability of the project. If on the other hand the engineer makes the structure too weak then the it might fail, as happened to the Osprey above. Unfortunately, knowing the size of the most extreme wave to hit a structure does not translate readily into the forces that that wave exerts on the structure. This is because the interaction between a

[1]An example of such a wave is "the fifty-year wave". This wave is so severe that it is only expected to appear once in a fifty year period.

Figure 1.1: A tug guides Osprey, with her massive air funnels, out of Clydebank for her sea trials (picture and caption courtesy of the Electronic Telegraph).

fluid with a free-surface and a surface-piercing body is a very complicated process.

There are three possible methods for analysing this process. Each method has its own advantages and disadvantages.

Firstly, there is the experimental approach. This involves taking measurements on a scale model in a wavetank. The advantage of this approach is that it completely models reality. However, this is done at a smaller scale and difficulties are experienced when trying to convert the results to the full scale problem. In addition, it can be expensive to set up the experimental facilities required and the process of obtaining measurements can be problematic.

Secondly, there is the analytical approach, whereby the full flow equations, or simplifications of them, are solved analytically. This is ideally the best technique as it produces closed-form solutions which can then be applied by engineers in the design and construction process. However, the full flow equations are highly

nonlinear and therefore extremely difficult to solve analytically in all but the simplest of cases. As will be seen in Chapter 4, solutions to simplified versions of these equations are possible but even these simplified equations cannot be solved easily for the flows of greatest interest, namely very steep waves.

The third approach, which is the method used in this study, is to solve the full flow equations, or simplifications of them, numerically. This method has a number of advantages over the experimental technique; principally it allows prediction of any property of the fluid at any point in the fluid domain at any time. In addition, it is generally a less expensive method. It should be noted however that the numerical approach is concerned with solving equations which are only approximations to reality. Furthermore, the discretisation inherent in the numerical approach may introduce numerical artifacts. Consequently, numerical methods cannot completely replace experiments.

1.1 Potential Flow and the Boundary-Integral Method

As mentioned above numerical solutions can be sought to simplifications of the full flow equations. One such simplification is to assume that the fluid motion is described by potential flow. In the next chapter it will be shown that potential flow adequately captures the essential physics involved in the flows of interest, namely free-surface flows in the vicinity of surface-piercing bodies.

One of the most successful numerical methods for modelling nonlinear free-surface potential flows is the Boundary-Integral Method (BIM). This is the method chosen for use in the present study. Since its inception two decades ago the Boundary-Integral Method has been highly developed and BIMs have been shown to be very accurate. Having said that, it is well known that BIMs can have prob-

lems at corners in the boundary of the fluid domain and especially at corners between the free-surface and surface-piercing bodies. Most of these problems are caused by the fact that the potential flow solution can be singular at such points. However, BIMs can still have problems at corners even if the exact mathematical solution is perfectly regular there.

In order to overcome these problems most BIMs are adapted at corners. However, very little work has been done assessing how well these adapted BIMs predict the flow near corners, especially when the flow is extreme and the corner in question is between the free-surface and a surface-piercing body.

This last sentence provides the main motivation for the first two aims of this study:

Aim 1. To develop a stable, accurate & efficient two-dimensional BIM.

Aim 2. To assess how well this BIM predicts the fluid motion at the intersection between a free-surface and a body for an extreme free-surface flow caused by body/fluid interaction.

Another area in which work needs to be carried out is in the area of experimental comparisons. In order to validate their BIMs some researchers have compared their numerical results against experimental measurements. The resultant studies are very notable and in general very good agreement was found, however there were discrepancies. Most of the researchers attributed these discrepancies to the fact that, in their studies, the experimental conditions were not matched by the numerical conditions. That is, the boundary conditions used by their BIM were not the same as those used in the experiment. This problem provides the motivation for the last two aims of the present study:

Aim 3. To construct a numerical wave flume (based on the present BIM) which

duplicates both the exact geometry of the physical wave flume and the exact motion of the physical wavemaker.

Aim 4. To assess how well the results from this numerical wave flume predict the results from the physical wave flume (this will be useful for aim 2).

Of the four aims, number 2 is the most important.

1.2 Thesis Outline

This section gives a chapter by chapter outline of the rest of this thesis.

Chapter 2 deals with the underlying mathematical theory and available numerical methods for modelling a fluid with a free-surface. At the start of the chapter the governing equation and boundary conditions for the potential flow of a fluid with a free-surface are presented. Following this the Boundary-Integral Method is introduced and BIMs are reviewed. Then other numerical methods for nonlinear free-surface flows are reviewed and their advantages and disadvantages when compared to BIMs are assessed. Finally in chapter 2 the reasons why the Boundary-Integral Method was chosen as the preferred numerical method for this study are discussed.

Chapter 3 describes in detail the development of the present two-dimensional BIM. The chapter shows how the present BIM takes features from various existing two-dimensional BIMs and in some cases extends these features. This chapter corresponds to aim 1 above.

In chapter 4 the results of the present BIM are compared against a recently published small-time analytical solution for an extreme potential flow at the intersection between a free-surface and a body. The author believes that this is the first time that this sort of comparison has been done. This chapter corresponds to aim 2 above.

In chapter 5 the results of the present BIM are compared against the results of another numerical method for nonlinear free-surface flows. This other method is the Volume of Fluid (VOF) method and the flow to which both methods are applied is that of a wave sloshing in a tank. The implications of this chapter are that at the end of this thesis the present BIM will have been compared against the three main investigative techniques used in science. That is, the results of the present BIM will have been compared against an analytical solution, the results of another numerical method and the results of an experiment.

In chapter 6 the results of the present BIM are compared against the results of an experiment. In the experiment deep-water waves are generated in a wave flume by a paddle wavemaker and then impacted against a vertical wall. The exact geometry of this flume and the motion of its wavemaker (measured in the experiment) are then used as the only input to the BIM. This chapter corresponds to aims 3 & 4 above. In addition, this chapter is very useful for aim 2 above.

Finally, chapter 7 summarises the findings of the previous chapters and then makes suggestions for further work.

Chapter 2

Theory & Numerical Methods

2.1 Potential Theory

Consider the motion of a homogeneous, incompressible Newtonian viscous fluid. This motion is governed by the Navier-Stokes equation

$$\frac{D\boldsymbol{u}}{Dt} = -\frac{1}{\rho}\nabla p + \boldsymbol{g} + \nu\nabla^2\boldsymbol{u} \tag{2.1}$$

and the continuity equation

$$\nabla.\boldsymbol{u} = 0, \tag{2.2}$$

where $\boldsymbol{u}$ is the fluid velocity, ρ is the density, p is the pressure, $\boldsymbol{g}$ is the acceleration due to gravity, ν is the kinematic viscosity and D/Dt denotes the time derivative following the motion of the fluid. Other names for D/Dt are "the material derivative" or "the Lagrangian derivative". In terms of Eulerian derivatives D/Dt is given by

$$\frac{D}{Dt} = \frac{\partial}{\partial t} + \boldsymbol{u}.\nabla$$

The Navier-Stokes equation is highly nonlinear and it is fortunate that it has simplifications which can still accurately model a wide variety of flows.

The first simplification is if the flow is inviscid, then the Navier-Stokes equation reduces to Euler's equation

$$\frac{D\boldsymbol{u}}{Dt} = -\frac{1}{\rho}\nabla p + \boldsymbol{g}, \tag{2.3}$$

which together with the continuity equation now govern the flow.

A further simplification is if the flow is also irrotational. In this case potential theory is applicable, that is there exists a scalar function ϕ such that

$$\boldsymbol{u} = \nabla\phi \tag{2.4}$$

and ϕ is called the *velocity potential.* Taking the divergence of equation (2.4) and using the continuity equation yields the governing equation for potential flow, namely Laplace's equation

$$\nabla^2\phi = 0. \tag{2.5}$$

Before going on to consider boundary conditions for the potential flow of a fluid with a free-surface it is important to establish whether or not any real fluid flows can be modelled using potential theory (see Svendsen & Jonsson [51]). For the flow of a real fluid to be regarded as potential flow there must be an absence of vorticity. Thus, the question arises as to where vorticity comes from in a real fluid and the answer is essentially from boundaries and it is contained mainly within boundary layers. In water wave motion of a reasonably short period (period $\lesssim$ 15 seconds), with which this study is primarily concerned, boundary layers separate regularly. These separated boundary layers then move out into the ambient fluid where they are dissipated by viscosity and therefore do not get a chance to build up. As a result, the flow remains irrotational except for a thin region along the boundaries. This leads to the conclusion that for this fluid motion the assumptions of potential theory will usually yield a remarkably good description of the flow, at least up until wave breaking.

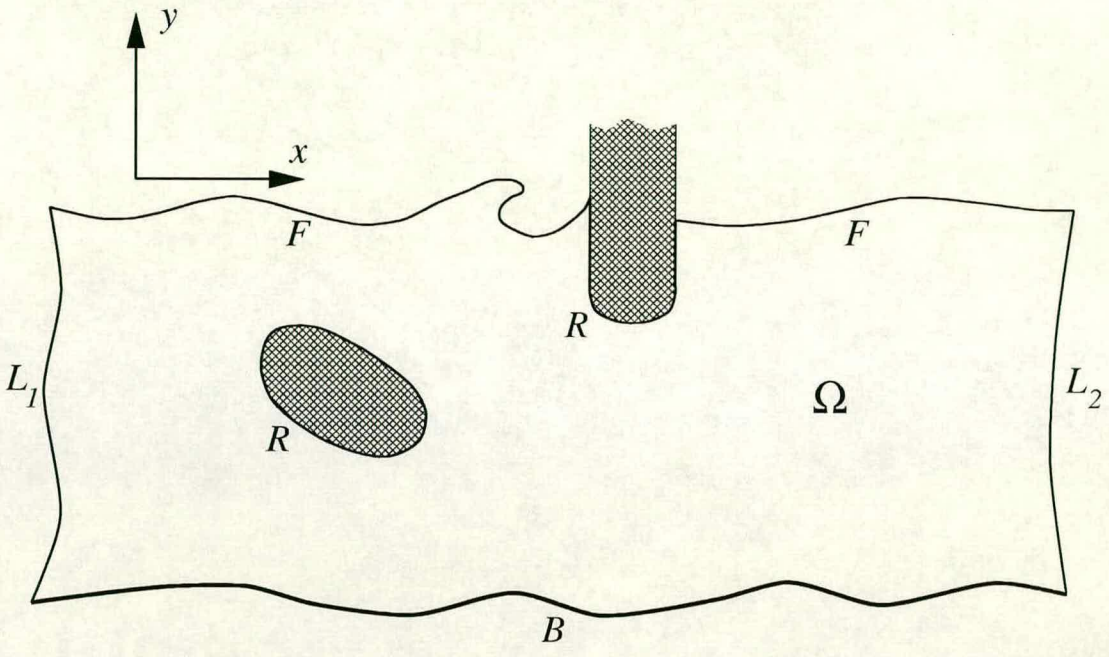

Figure 2.1: A typical two-dimensional fluid domain.

Having shown that the assumptions of potential theory seem reasonable for modelling some free-surface flows it is necessary to complete the mathematical model by stating the boundary conditions.

Shown in figure 2.1 is a typical two-dimensional fluid domain. The domain Ω is bounded by a free-surface F, a bottom B of varying depth and two lateral boundaries L_1 & L_2. In addition, rigid bodies, submerged or surface piercing, may also be present.

The first physical principle imposed on the free-surface states that a fluid particle once on the free-surface remains there. This gives rise to the *kinematic boundary condition* on the free-surface

$$\frac{D\boldsymbol{x}}{Dt} = \nabla\phi \quad \text{for} \quad \boldsymbol{x} \in F. \tag{2.6}$$

The second principle to be applied at the free-surface applies to the pressure p. Neglecting the effects of surface tension the pressure felt by a fluid particle on

the free-surface will just be the external applied pressure, say p_a. For hydrodynamic problems p_a will be a constant and equal to the atmospheric pressure. Substituting this into Bernoulli's equation for unsteady irrotational flow yields

$$\frac{\partial \phi}{\partial t} = -\frac{1}{2}\left(\left(\frac{\partial \phi}{\partial x}\right)^2 + \left(\frac{\partial \phi}{\partial y}\right)^2\right) - gy - \frac{p_a}{\rho} + c(t) \quad \text{for} \quad \boldsymbol{x} \in F, \tag{2.7}$$

where $c(t)$ is some function of time t and $g = |\boldsymbol{g}|$. Now adding a function of t alone to ϕ makes no difference to the flow velocity $\boldsymbol{u} = \nabla\phi$, and so, if p_a is a constant, the last two terms in equation (2.7) can be absorbed into ϕ_t to give

$$\frac{\partial \phi}{\partial t} = -\frac{1}{2}\left(\left(\frac{\partial \phi}{\partial x}\right)^2 + \left(\frac{\partial \phi}{\partial y}\right)^2\right) - gy \quad \text{for} \quad \boldsymbol{x} \in F. \tag{2.8}$$

This is called the *dynamic boundary condition* on the free-surface. Furthermore, using equation (2.8) together with the relationship

$$\frac{D\phi}{Dt} = \frac{\partial \phi}{\partial t} + \nabla\phi.\nabla\phi = \frac{\partial \phi}{\partial t} + \left(\left(\frac{\partial \phi}{\partial x}\right)^2 + \left(\frac{\partial \phi}{\partial y}\right)^2\right),$$

the *Lagrangian form* of the dynamic boundary condition can be obtained

$$\frac{D\phi}{Dt} = \frac{1}{2}\left(\left(\frac{\partial \phi}{\partial x}\right)^2 + \left(\frac{\partial \phi}{\partial y}\right)^2\right) - gy \quad \text{for} \quad \boldsymbol{x} \in F. \tag{2.9}$$

On the surface R of a rigid body the following boundary condition applies

$$\nabla\phi.\boldsymbol{n} \equiv \frac{\partial \phi}{\partial n} = \boldsymbol{U}.\boldsymbol{n} \quad \text{for} \quad \boldsymbol{x} \in R, \tag{2.10}$$

where $\boldsymbol{n}$ is the unit normal pointing out of the fluid domain at $\boldsymbol{x}$, n is the coordinate along $\boldsymbol{n}$ and $\boldsymbol{U}$ is the velocity of R at $\boldsymbol{x}$. Also, assuming a stationary and impermeable bottom B then equation (2.10) can be used with $\boldsymbol{U} = \boldsymbol{0}$ to obtain the boundary condition on B

$$\frac{\partial \phi}{\partial n} = 0 \quad \text{for} \quad \boldsymbol{x} \in B. \tag{2.11}$$

On the lateral boundaries L_1 & L_2 several different kinds of boundary conditions can be applied depending on the situation being modelled. Some of the common types of boundary conditions that can be used are:

- spatial periodicity
- wave generation
- reflection from a vertical or sloping wall
- wave radiation

Some of these will be described later in this chapter.

With the specification of initial conditions, for example the fluid being at rest at $t = 0$, the above mathematical model represents an *initial boundary value problem*. Several numerical methods can be used to solve this problem but one of the most successful of all such methods is the *Boundary-Integral Method* (BIM).

2.2 The Boundary-Integral Method

The Boundary-Integral Method was first proposed by Svendsen [50] as a means of modelling two-dimensional gravity waves on water. The method takes advantage of the fact that the motion of a fluid undergoing potential flow is completely determined by the fluid velocities around its boundary. Thus, only the motion of the boundary of the fluid domain needs to be considered and only the boundary itself needs to be discretised. This results in a substantial reduction in the number of unknowns and a subsequent reduction in computational effort.

2.2.1 Integral Representations of Laplace's Equation

In the Boundary-Integral Method an integral representation of Laplace's equation is used to reformulate the mathematical problem into a form which just involves the boundary of the fluid domain. Several integral representations are possible and two of the most commonly used ones are described in the following (see Otta *et al.* [40]).

Integral Representation Based on Green's Theorem

Consider the two-dimensional version of *Green's second identity* (Sternberg & Smith [49])

$$\iint_S (f\nabla^2 g - g\nabla^2 f)dS = \oint_C (fg_n - gf_n)ds, \tag{2.12}$$

where S is a region of the plane and C is the boundary of that region. The curve C must be continuous and smooth except for a finite number of corners. The subscript 'n' denotes the normal derivative to C in the outwards direction, away from S. Also, the functions f and g must be continuous, with continuous first derivatives and at least piecewise continuous second derivatives in the interior of the region S, while in the closed region $S + C$ only f, g, f_n and g_n must be continuous.

From equation (2.12) the following integral representation of Laplace's equation can be obtained (Otta *et al.* [40])

$$\theta(\boldsymbol{x}_0)\phi(\boldsymbol{x}_0) = \text{PV} \oint_C (\phi G_n(\boldsymbol{x}, \boldsymbol{x}_0) - \phi_n G(\boldsymbol{x}, \boldsymbol{x}_0))ds, \tag{2.13}$$

where C is the boundary of the fluid domain, $\boldsymbol{x}_0$ is a point on C and $\theta(\boldsymbol{x}_0)$ is the internal angle at $\boldsymbol{x}_0$ ($\theta = \pi$ at a smooth part of C). The function G is called the *free space Green's function in the plane* and is defined to be

$$G(\boldsymbol{x}, \boldsymbol{x}_0) = \ln r, \tag{2.14}$$

where $r = |\boldsymbol{x} - \boldsymbol{x}_0|$. The letters 'PV' in the equation (2.13) denote that the principal value of the integral is to be taken.

A major advantage of the integral representation of Laplace's equation based on Green's theorem is that it can be generalised to three dimensions. In three dimensions equation (2.12) becomes (Sternberg & Smith [49])

$$\iiint_V (f\nabla^2 g - g\nabla^2 f)dV = \iint_S (fg_n - gf_n)dS, \tag{2.15}$$

where V is a volume and the surface S is the boundary of that volume. The surface S must be smooth except for a finite number of edges. Also, a finite number of singular points are allowable on S; the vertex of a cone is an example of a singular point. The functions f and g must satisfy analogous conditions to those for the two-dimensional case.

From equation (2.15) the following integral representation of Laplace's equation in three dimensions can be obtained (Isaacson [32])

$$\alpha(\boldsymbol{x}_0)\phi(\boldsymbol{x}_0) = \mathrm{PV} \iint_S (\phi_n G(\boldsymbol{x}, \boldsymbol{x}_0) - \phi G_n(\boldsymbol{x}, \boldsymbol{x}_0)) dS, \tag{2.16}$$

where the surface S is the boundary of the fluid domain, $\boldsymbol{x}_0$ is a point on S and $\alpha(\boldsymbol{x}_0)$ is the interior solid angle at $\boldsymbol{x}_0$ ($\alpha = 2\pi$ at smooth parts of S). In three dimensions the free space Green's function becomes

$$G(\boldsymbol{x}, \boldsymbol{x}_0) = \frac{1}{r}, \tag{2.17}$$

where again $r = |\boldsymbol{x} - \boldsymbol{x}_0|$.

Integral Representation Based on Cauchy's Theorem

Suppose now that the flow is restricted to being two-dimensional. Using the fact that the fluid motion is also incompressible it is possible to define a new function called the *stream function* ψ, such that

$$u = \frac{\partial \psi}{\partial y}, \quad v = -\frac{\partial \psi}{\partial x}. \tag{2.18}$$

Using the relationship $\boldsymbol{u} = \nabla\phi$ then gives

$$\frac{\partial \phi}{\partial x} = \frac{\partial \psi}{\partial y}, \quad \frac{\partial \phi}{\partial y} = -\frac{\partial \psi}{\partial x}. \tag{2.19}$$

These two equations constitute the well known Cauchy-Riemann equations for the complex valued function

$$\beta \stackrel{\text{def}}{=} \phi + i\psi, \tag{2.20}$$

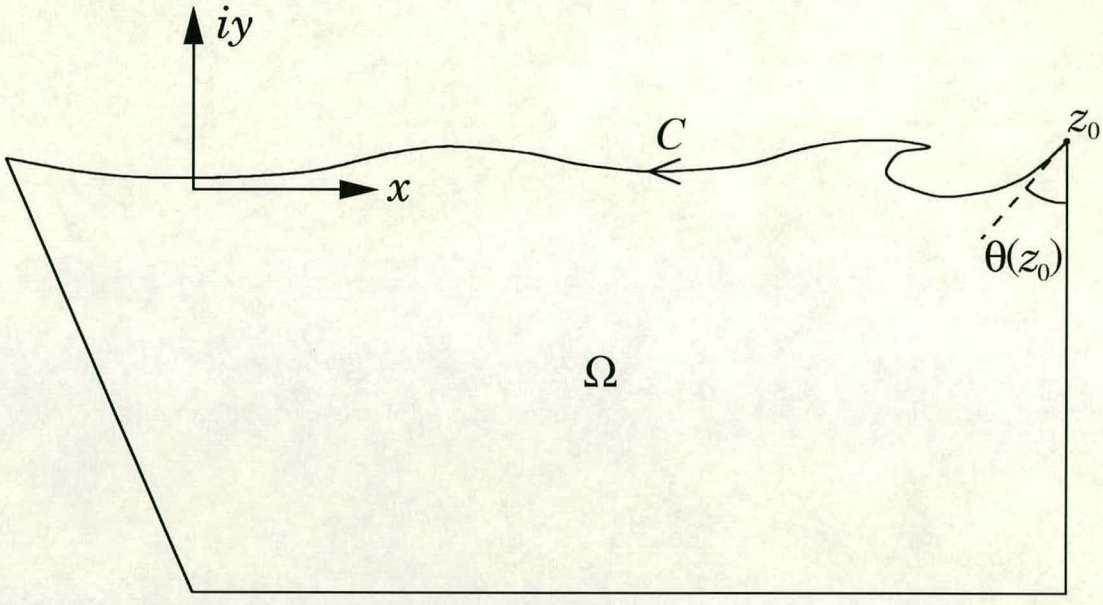

Figure 2.2: A typical two-dimensional fluid domain Ω.

where β is regarded as a function of the complex variable $z = x+iy$. This function $\beta(z)$ is called the *complex potential* and if the partial derivatives in equation (2.19) are continuous it is an analytic function (Priestley [44]).

Shown in figure 2.2 is a typical two-dimensional fluid domain Ω. Let C be the contour round the boundary of Ω and let z_0 be a point on C; in this case z_0 is shown at a corner but it can lie anywhere on C. The angle $\theta(z_0)$ is the internal angle at z_0.

Now consider the following principal value integral

$$I = \mathrm{PV} \oint_C \frac{\beta(z)}{z - z_0} dz. \tag{2.21}$$

In order to evaluate this integral a new domain Ω' is constructed (see figure 2.3), which is the same as Ω except that the partial disc of radius ε around z_0 is excluded. Let C' be the contour round the boundary of this new domain and let $c(\varepsilon)$ be the contour along the partial circumference around z_0, as shown in the magnified part of figure 2.3. Then it follows that

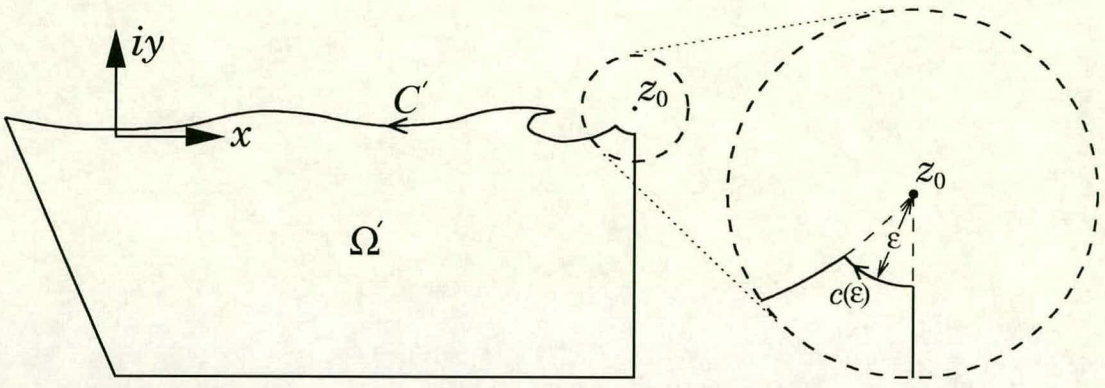

Figure 2.3: The new domain Ω'.

$$I = \lim_{\varepsilon \to 0} \left(\oint_{C'} \frac{\beta(z)}{z - z_0} dz - \int_{c(\varepsilon)} \frac{\beta(z)}{z - z_0} dz \right). \tag{2.22}$$

However the function $\beta(z)/(z-z_0)$ is an analytic function in Ω' and so by Cauchy's integral theorem (Priestley [44])

$$\oint_{C'} \frac{\beta(z)}{z - z_0} dz = 0. \tag{2.23}$$

Hence

$$I = -\lim_{\varepsilon \to 0} \int_{c(\varepsilon)} \frac{\beta(z)}{z - z_0} dz. \tag{2.24}$$

By using the fact that $\beta(z)$ is continuous and bounded in the partial disc around z_0 equation (2.24) becomes

$$I = -\beta(z_0) \left(\lim_{\varepsilon \to 0} \int_{c(\varepsilon)} \frac{dz}{z - z_0} \right) \tag{2.25}$$

but on $c(\varepsilon)$

$$z = z_0 + \varepsilon e^{-i\theta},$$

$$\therefore \quad dz = -i\varepsilon e^{-i\theta} d\theta.$$

Using these relations

$$\begin{aligned} I &= \beta(z_0) \left(\lim_{\varepsilon \to 0} \int_{c(\varepsilon)} i d\theta \right) \\ &= i\theta(z_0)\beta(z_0). \end{aligned} \tag{2.26}$$

Finally, using equations (2.21) & (2.26) an integral representation of Laplace's equation based on Cauchy's theorem can be obtained

$$i\theta(z_0)\beta(z_0) = \text{PV} \oint_C \frac{\beta(z)}{z - z_0} dz. \tag{2.27}$$

2.3 Review of Boundary-Integral Methods

The problem with the potential flow of a fluid with a free-surface, and free-surface flows in general, is that there is a free and moving boundary (the free-surface) on which there are nonlinear boundary conditions (see equations (2.6) & (2.9)). The position of this free and moving boundary is not known *a priori* and is in fact part of the problem. One of the main reasons why BIMs have been so successful is because they satisfy these nonlinear boundary conditions exactly, and they satisfy them on the free-surface. As a result BIMs are "fully-nonlinear" methods.

The basic computational procedure involved in all BIMs is very similar and consists of repeating the following two steps, with perhaps some slight variations:

1. Given the velocity potential ϕ on the free-surface (Dirichlet boundary condition) and its normal derivative ϕ_n on the rest of the boundary (Neumann boundary condition), Laplace's equation is solved to give ϕ_n (and hence the velocity $\boldsymbol{u} = \nabla\phi$) on the free-surface and ϕ on the rest of the boundary. This solution of Laplace's equation is obtained by solving a boundary-integral equation which is an integral representation of Laplace's equation, for example equation (2.13), (2.16) or (2.27).

2. The kinematic and dynamic boundary conditions (equations (2.6) & (2.9)) are integrated forward in time to give the location of the free-surface and the velocity potential on it at the next time-step.

In order to start the above process, initial conditions are required. At $t = 0$

the position of the free-surface and the velocity potential on it must be given. One approach is to start computations from an undulating free-surface corresponding to a specific wave, for example a solitary wave. However, in all but a few cases it is difficult to find the potential distribution on the free-surface for such a geometry. That is, only approximate theories are available to calculate this velocity potential. This is not a very satisfactory situation because it undermines the fully-nonlinear nature of the BIM being used. Alternatively, computations can be started from the still water condition ($\phi \equiv 0$ on a flat free-surface). In this case waves can be generated by either varying the pressure distribution on the free-surface or by specifying conditions on the lateral boundaries, for example a wavemaker or inflow conditions.

The first successful use of the Boundary-Integral Method to model surface gravity waves on water was by Longuet-Higgins & Cokelet [39] in 1976. In this study the motion of two-dimensional, space-periodic, deep-water waves was considered. The most notable feature of this work was that it demonstrated realistic overturning of the free-surface, which had not been done previously by any numerical method and is still well beyond the scope of any analytical technique to date.

The basic idea of Longuet-Higgins & Cokelet's method is as follows. Due to lateral periodicity it is possible just to consider one wavelength λ in the horizontal direction. Hence, the fluid domain becomes

$$0 \leq x \leq 2\pi; \quad -\infty < y \leq \eta, \tag{2.28}$$

where the spatial coordinates x and y have been normalised by $2\pi/\lambda$ and η is the normalised free-surface elevation. As described earlier, the velocity $\boldsymbol{u}$ on the free-surface is obtained by solving an integral representation of Laplace's equation; in this case the boundary-integral equation used is equation (2.13). However, the

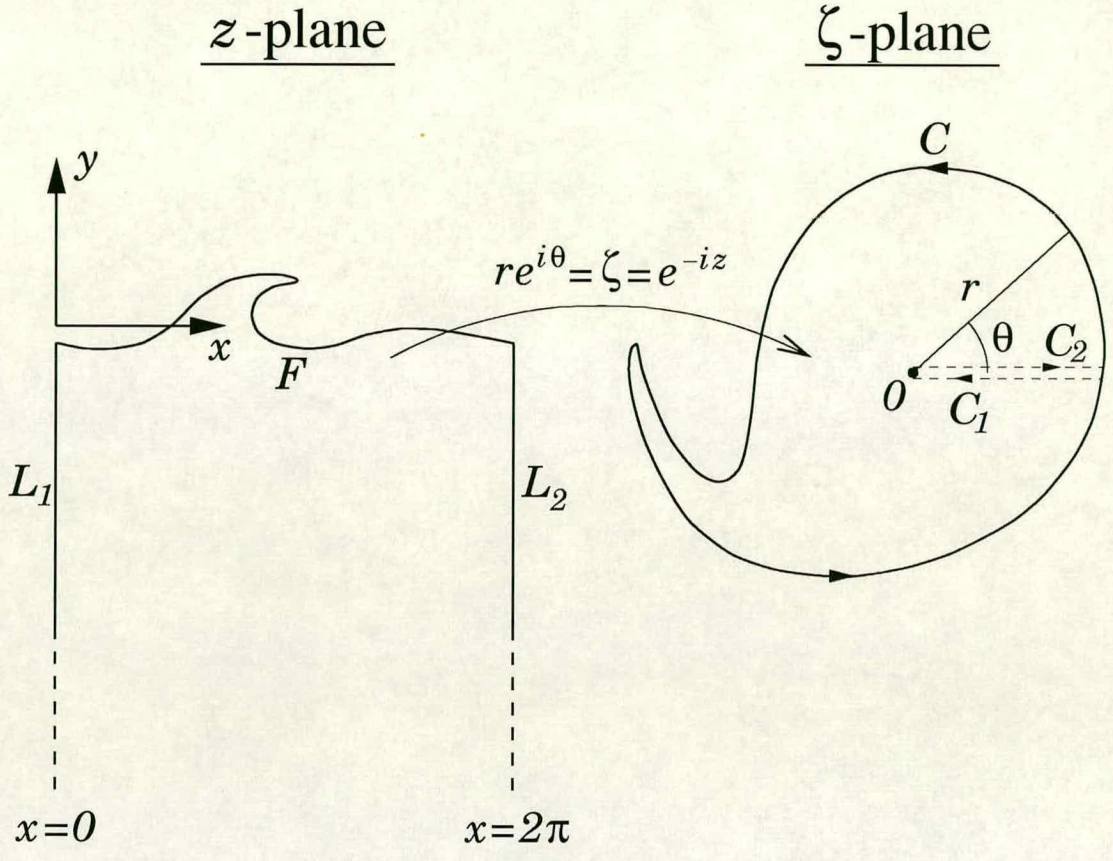

Figure 2.4: Conformal mapping from z-plane to ζ-plane.

fluid domain described by (2.28) is still unbounded in the y direction, and so its boundary is infinitely long. This problem is overcome by transforming to a simple finite domain (see figure 2.4) using the following conformal mapping

$$re^{i\theta} = \zeta = e^{-iz}, \tag{2.29}$$

where $z = x + iy$. With this transformation infinite depths are mapped to the origin, the lateral boundaries L_1 & L_2 are mapped to contours C_1 & C_2 respectively and the free-surface F is mapped to the contour C. The numerical solution is then performed over this new domain. Solution of equation (2.13) now becomes significantly easier because the integrals along the contours C_1 & C_2 cancel due to periodicity. Consequently, integration only needs to be performed along the

smooth contour C.

On the other hand, there is a problem with the integration along C. On the free-surface F, and therefore on the contour C, the velocity potential ϕ is prescribed and its normal derivative ϕ_n is unknown. When equation (2.13) is used to find ϕ_n the resulting integral equation is a Fredholm integral equation of the *first* kind. The problem is that this type of integral equation has inherent difficulties when it comes to solving it numerically. These numerical difficulties will be discussed later.

In order to model overturning flows Longuet-Higgins & Cokelet adopt a Lagrangian description of the free-surface rather than an Eulerian description, which would be invalid. In this description, the motion of the free-surface is obtained by following the time evolution of, say, N discrete fluid particles (nodes) on the free-surface. Most BIMs adopt this approach which was termed "mixed Eulerian-Lagrangian" by Longuet-Higgins & Cokelet. The term "Eulerian" refers to the fact that Laplace's equation is solved in the fluid domain at each time-step and the term "Lagrangian" refers to this Lagrangian description of the free-surface described above.

Having discretised the free-surface the integral equation (2.13) is also discretised and solved numerically, for ϕ_n, at each time-step. This numerical solution involves solving an $N \times N$ system of linear equations. Since (2.13) becomes a Fredholm integral equation of the first kind when it is used to find ϕ_n, this linear system is not diagonally dominant. This means that the linear system must be solved by a "slow" direct method (Gaussian elimination), rather than a "fast" iterative method (e.g. Gauss-Seidel). Direct methods have running times per time-step that increase like N^3, whereas iterative techniques have running times per time-step that only increase like N^2.

Once the normal velocity ϕ_n has been found along the free-surface F and the tangential velocity ϕ_s (s is arclength along F) has been obtained by numerical differentiation of ϕ along F, the velocity $\boldsymbol{u}$ on F can be calculated. Then, using this information together with the kinematic and dynamic boundary conditions (2.6) & (2.9), the position and velocity potential of the free-surface nodes can be integrated forward in time to the next time-step.

The procedure used to carry out the above time-stepping is a fourth order predictor-corrector method, known as the Adams-Bashforth-Moulton (ABM) method. However, since this method requires information from the previous three time-steps, a different scheme needs to be used to start computations from the initial conditions. The scheme used is a fourth order Runge-Kutta (RK) scheme, which uses no information from previous time-steps. This scheme is used to perform the first three time-steps.

Unfortunately, there are two serious disadvantages when this combined method for time-stepping is used.

Firstly, multiple solutions of Laplace's equation must be performed at each time-step. This is especially serious because the solution of Laplace's equation dominates the computational effort in a BIM. The ABM method requires two solutions of Laplace's equation at each time-step; one to "predict" and one to "correct". The RK method is even worse; requiring four solutions of Laplace's equation at each time-step.

Secondly, because the ABM method needs information from the three previous time-steps, it is very difficult to change the time-step Δt as computations progress. If Δt is changed it is usually necessary to go back a time-step and restart with three RK steps followed by ABM steps as before. This is very demanding in terms of computational effort.

Following Longuet-Higgins & Cokelet's work, Vinje & Brevig [55] & [56] developed a different BIM for modelling two-dimensional surface gravity waves on water. Their method has some major advantages over that of Longuet-Higgins & Cokelet's.

One advantage is that Vinje & Brevig work in the physical domain rather than in a conformally mapped domain. This allows easier inclusion of submerged and surface-piercing bodies as well as different types of lateral boundary conditions other than just periodic conditions. However, it does restrict the method to finite depths.

Another advantage of Vinje & Brevig's method concerns the type of integral equations used. In this method the solution of Laplace's equation at each time-step is obtained by solving the integral representation of Laplace's equation based on Cauchy's theorem (2.27). Since this integral equation is a complex equation it really represents two equations, namely its real and imaginary parts. Consider figure 2.5 which shows a typical fluid domain to which Vinje & Brevig's method can be applied. At each time-step ϕ is known and ϕ_n (or equivalently ψ) is unknown on the free-surface, and on the rest of the boundary ϕ is unknown and ϕ_n (or equivalently ψ) is known. Let C_ϕ be the part of the boundary C where ϕ is known and C_ψ be the part of C where ψ is known. Then, if the real or imaginary parts of equation (2.27) are taken when z_0 lies on C_ϕ or C_ψ respectively, the resulting integral equations are all Fredholm integral equations of the *second* kind. That is, for z_0 on C_ϕ

$$\theta(z_0)\psi(z_0) + \mathrm{Re}\left[\mathrm{PV}\oint_C \frac{\beta(z)}{z - z_0}dz\right] = 0 \tag{2.30}$$

and for z_0 on C_ψ

$$\theta(z_0)\phi(z_0) + \mathrm{Re}\left[\mathrm{PV}\oint_C \frac{i\beta(z)}{z - z_0}dz\right] = 0. \tag{2.31}$$

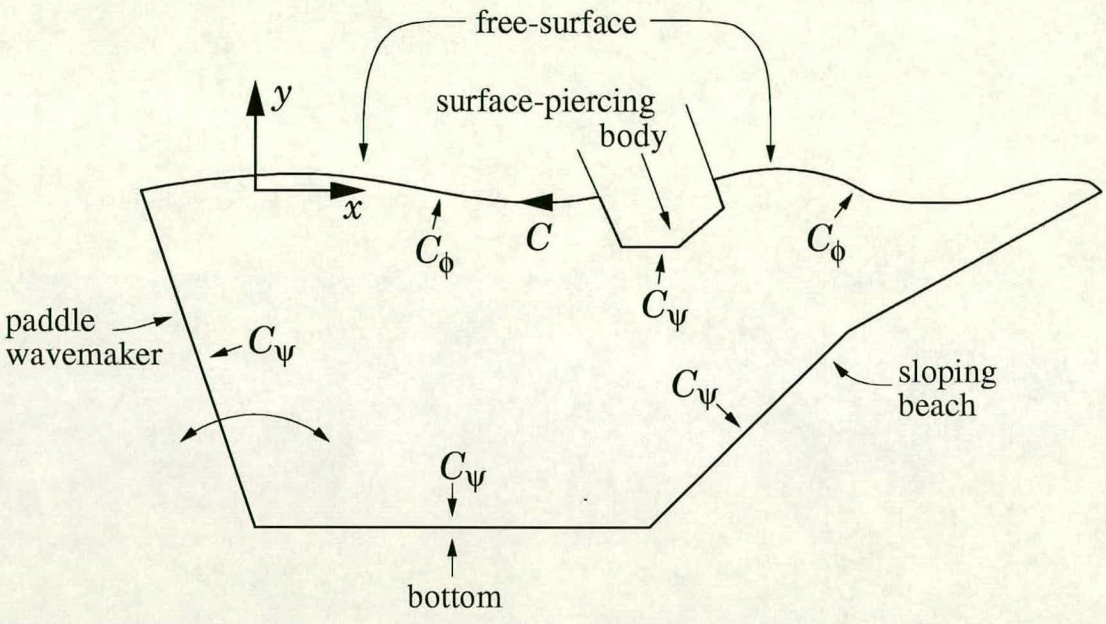

Figure 2.5: A typical fluid domain for Vinje & Brevig's method.

The advantage of having Fredholm integral equations of the second kind is that when these equations are discretised with a view to calculating a numerical solution the resultant linear system is diagonally dominant and therefore can be solved by "fast" iterative means.

A disadvantage of Vinje & Brevig's method is that, being based on complex theory, it is restricted to two-dimensional problems.

In their first paper [55] Vinje & Brevig model breaking waves on finite water depths. In this study computations are shown to continue successfully right up until the point where the breaking wave spout intersects the forward face of the wave. After this point the numerical scheme quickly breaks down. This is to be expected since no BIM can compute beyond free-surface merging due to the fluid domain no longer being simply connected.

In their second paper [56] Vinje & Brevig model two-dimensional ship motions in beam seas.

A somewhat different approach was used by Baker *et al.* [2] in 1982. In this approach an alternative integral representation of Laplace's equation to equations (2.13), (2.16) & (2.27) is used. This alternative integral representation is based on the fact that all potential flows may be constructed by means of a distribution of sources and dipoles round the boundary of the fluid domain (Kellogg [34, page 286]). Furthermore, if the dipoles are distributed along the free-surface (where the boundary condition is of Dirichlet type) and the sources are distributed along the solid boundaries (where the boundary condition is of Neumann type) then the resulting boundary integral equations are all Fredholm integral equations of the second kind.

The real benefit of this method of Baker *et al.* is that everything that has been said applies equally well in three dimensions as it does in two dimensions. Therefore, unlike methods which use the integral representation of Laplace's equation based on Cauchy's theorem (2.27), this method is not restricted to two dimensions. Also, unlike methods which use an integral representation of Laplace's equation based on Greens theorem (2.13) or (2.16), this method does not result in Fredholm integral equations of the first kind.

Unfortunately however, details of this method become very complicated if submerged or surface-piercing bodies are to be included.

The next significant advance in the development of BIMs was the work of Dold & Peregrine [15] in 1986. In this study an extremely efficient method was used to model the motion of two-dimensional, space-periodic, surface gravity waves on constant depths. In a similar way to Vinje & Brevig's method their formulation is based on an integral representation of Laplace's equation derived from Cauchy's theorem. However, instead of the complex potential β, the complex velocity $w \stackrel{\text{def}}{=} u - iv$ is used in equation (2.27). This is possible because, like β, w is an

analytic function of z, due to the fact that

$$w = u - iv = \frac{d\beta}{dz}. \tag{2.32}$$

Thus, the integral representation of Laplace's equation used by Dold & Peregrine is

$$i\theta(z_0)w(z_0) = \mathrm{PV} \oint_C \frac{w(z)}{z - z_0} dz. \tag{2.33}$$

The important feature which distinguishes Dold & Peregrine's method from all previous methods is the time-stepping procedure which they developed.

What Dold & Peregrine noticed was that, by taking the partial time derivative of equation (2.5), ϕ_t, like ϕ, satisfies Laplace's equation

$$\nabla^2 \phi_t = 0. \tag{2.34}$$

Indeed any order of partial time derivative of ϕ satisfies Laplace's equation

$$\nabla^2 \phi = \nabla^2 \phi_t = \nabla^2 \phi_{tt} = \cdots = 0. \tag{2.35}$$

Furthermore, they noticed that it was possible to solve each one of these Laplace's equations in turn to obtain successive Lagrangian time derivatives of the position of the free-surface and the velocity potential on it. The free-surface boundary condition for each Laplace's equation is obtained from the solution of the previous Laplace's equation.

That is, given the position of the free-surface F and the velocity potential ϕ on it, $\nabla^2 \phi = 0$ is solved to give $\boldsymbol{u} = D\boldsymbol{x}/Dt$, $D\phi/Dt$ and ϕ_t on F. Then, using ϕ_t on F, $\nabla^2 \phi_t = 0$ is solved to give $D^2\boldsymbol{x}/Dt^2$, $D^2\phi/Dt^2$ and ϕ_{tt} on F, and so on.

In principal any order of Lagrangian time derivative of the position of the free-surface and the velocity potential on it can be calculated by repeating the above process. However, in practice it is advantageous to only calculate a few such orders. This is because:

1. As the order increases it becomes increasingly more difficult to derive the formulae which, once the associated Laplace's equation has been solved, give the required Lagrangian time derivatives as well as the free-surface boundary condition for the next Laplace's equation.

2. As the order increases so does the order of Eulerian spatial derivatives that are contained in the above mentioned formulae. Numerical differentiation along the free-surface is used to evaluate these derivatives, and as their order increases so does the numerical error in calculating them.

Having obtained up to order m Lagrangian time derivatives Dold & Peregrine then use truncated Taylor series to time-step forward the position and velocity potential of the free-surface nodes. That is, if $\boldsymbol{x}_i$ is the position and ϕ_i is the velocity potential of the i^{th} free-surface node then

$$\boldsymbol{x}_i(t+\Delta t) = \boldsymbol{x}_i(t) + \Delta t \frac{D\boldsymbol{x}_i}{Dt}(t) + \cdots + \frac{(\Delta t)^m}{m!}\frac{D^m\boldsymbol{x}_i}{Dt^m}(t) \tag{2.36}$$

and

$$\phi_i(t+\Delta t) = \phi_i(t) + \Delta t \frac{D\phi_i}{Dt}(t) + \cdots + \frac{(\Delta t)^m}{m!}\frac{D^m\phi_i}{Dt^m}(t), \tag{2.37}$$

where the time-step is from time t to time $t+\Delta t$.

There are two distinct advantages of this time-stepping procedure. The first advantage is that the second and subsequent Laplace's equations in equation (2.35) can be solved in a fraction of the CPU time used to solve the first. This means that higher-order time-stepping can be achieved at very little extra computational cost. The second advantage is that, being an explicit method, the time-step Δt is free to be varied as computations progress. This is especially useful if the vigour of the fluid motion is continually changing with time.

In addition to this higher-order time-stepping procedure Dold & Peregrine also used a number of other techniques to try and make their method as efficient

as possible. The idea behind these techniques is to minimise the number of discretisation points (nodes) used to discretise equation (2.33), while still retaining a high level of accuracy. In so doing the size of the resultant linear system (which is iteratively solvable) is minimised and thus the overall number of required calculations is reduced. These techniques are described in the following.

Firstly, by reflecting the free-surface F in the flat bottom B ($y = -h$) and allowing the fluid to extend continuously down to this reflection of F the bottom boundary condition (2.11) is automatically satisfied. The fluid domain is now bounded above and below by F and its reflection, rather than F and B. Also, the complex velocity must now satisfy the following reflection condition

$$w(\overline{z} - 2ih) = \overline{w}(z), \tag{2.38}$$

where z is a point in this new fluid domain and the overbar denotes complex conjugate. The reason for doing this is because when equation (2.33) is applied to this new domain the integral along the reflection of F can be expressed in terms of an integral along F by using equation (2.38). As a result integration only needs to be performed along the free-surface F and the lateral periodic boundaries.

Secondly, assuming that the space dimensions have been suitably scaled so that the lateral period is exactly 2π, the physical domain is conformally mapped using the same mapping as that used by Longuet-Higgins & Cokelet (equation (2.29)). This is so that the integrals along the transformed lateral boundaries cancel due to periodicity. Consequently, by combining this technique with the previous technique, integration only needs to be performed along the closed smooth contour which is the conformally mapped free-surface and therefore only this transformed free-surface needs to be discretised.

Finally, by using high-order differencing formulae to discretise this transformed free-surface the number of required nodes for a given accuracy can be

further reduced.

In summary, Dold & Peregrine's time-stepping procedure together with all these other techniques combine to make their method very fast, accurate and efficient.

Since this seminal work of Dold & Peregrine there have been many applications and developments of their numerical scheme. Notable examples include the investigation of instabilities in solitary waves by Tanaka *et al.* [52]; the study of breaking-wave impacts on a vertical wall by Cooker & Peregrine [10] and the modelling of water wave motion over irregular beds by Cooker [9].

In the study by Tanaka *et al.* [52] the rather restrictive assumption of lateral periodicity in Dold & Peregrine's original method is replaced by allowing fluid domains of infinite length and constant depth. This is possible because Tanaka *et al.* model solitary waves and so a uniform flow condition is applicable in the far-field.

As regards the work of Cooker & Peregrine [10] the problem of a wave approaching a vertical wall is simulated by colliding two identical, but oppositely moving waves. In this way the need to have a rigid vertical wall as one of the lateral boundaries is overcome and the problem can be modelled directly using the method of Tanaka *et al.*.

Finally, the work of Cooker [9] further extends the method of Dold & Peregrine to include arbitrary bottom geometries. This is achieved by using the method of Tanaka *et al.* in conjunction with a conformal mapping technique. At each time-step the physical fluid domain is conformally mapped to a flat-bottomed domain. Then, as before, in this transformed domain symmetry is used so that discretisation points need only be used on the free-surface. Since the conformal mapping only contributes a relatively small amount of CPU time to each time-

step this method of Cooker's is much more efficient than methods which discretise the bottom B in addition to the free-surface F.

To conclude, all these numerical schemes continue the very efficient nature of Dold & Peregrine's original method. However, they are all limited in their applicability because they do not model more general types of lateral boundary conditions other than just periodicity or uniform flow.

Up to this point all the major BIMs, that were developed in the first ten years after Longuet-Higgins & Cokelet's initial paper, have been described. However, there are various other computational aspects of BIMs that are so important that they merit separate treatment.

2.3.1 Free-Surface Instabilities

A problem which seems to afflict all BIMs is the appearance of "saw-tooth" instabilities on the free-surface. These saw-tooth instabilities have a wavelength which is twice the node spacing and they tend to occur especially when the local wave steepness is high. Indeed, most numerical methods for nonlinear inviscid free-surface flows suffer from such instabilities (see page 41).

In Vinje & Brevig's method [55] & [56] no such unstable behaviour was mentioned, however it is believed that this method is also subject to saw-tooth instabilities on the free-surface because they were reported to have affected essentially the same method in the work of lin *et al.* [37] in 1984. Also, even the very accurate and efficient method of Dold & Peregrine experiences such high-wavenumber instabilities, albeit to a much lesser extent than those encountered in Longuet-Higgins & Cokelet's method.

Unfortunately, the precise cause of these instabilities is still unknown and will be, to some extent, dependent on the implementation of the particular BIM being studied. On the other hand, that these instabilities arise is to be expected

for simulating inviscid steep free-surface flows because the nonlinear interaction between wave components will eventually lead to energy accumulating in the highest resolvable wavenumber modes (see page 41 again).

In order to suppress these short-wave instabilities some sort of numerical filtering of the high-wavenumber modes is required. In the method of Longuet-Higgins & Cokelet this is achieved using a simple 5-point or 7-point smoothing formula. Similarly, in the method of Dold & Peregrine this is achieved by applying a higher order 15-point smoothing formula.

These free-surface instabilities affecting Dold & Peregrine's method were analysed by Dold [14] in 1992. In this analysis Dold found that there were three distinct types of instability. Furthermore, he showed that two of these instabilities could be eliminated by imposing suitable restrictions on the time-stepping procedure. However, he also showed that the third type of instability could only be removed by this numerical filtering of the high-wavenumber modes. Hence the use of the 15-point smoothing formula mentioned above.

As alluded to by Dold & Peregrine [15] and explicitly stated by Dommermuth & Yue [17], an important mechanism in the cause of these high-wavenumber instabilities affecting all the methods is the concentration of free-surface nodes in regions of high curvature. For a fixed time-step Δt, this concentration of nodes eventually leads to the violation of a local Courant type stability condition (see Dommermuth & Yue [17]) as the waves steepen. The errors in the calculated free-surface node velocities then increase, resulting in a rough free-surface profile and ultimately the break down of the numerical scheme.

As a result, in order to maintain stability, it is necessary to control the minimum node spacing. With this in mind Dommermuth & Yue [17] developed a regridding procedure for use in their BIM for modelling nonlinear axisymmetric

free-surface flows. This regridding procedure involves the rediscretisation of the free-surface at each time-step with equal-arclength spaced nodes. Essentially the same procedure was then used by Dommermuth *et al.* [18] in their comparison of the results of a BIM with those of an experiment. However, in this method regridding is not carried out at every time-step.

The idea of regridding is not a new one and was in fact originally used in the 1970s by Fink & Soh [19] in the context of simulating the motion of two-dimensional unsteady vortex sheets. Also, although regridding does act like a form of smoothing, by damping the high-wavenumber modes, it does actually have a couple of major advantages when compared to traditional smoothing techniques like those used by Longuet-Higgins & Cokelet and Dold & Peregrine.

Firstly, regridding has the capacity to alter the energy of the system by a lot less than smoothing (see Dommermuth & Yue [17]) .

Secondly, and perhaps more importantly, smoothing cannot be applied as easily as regridding near the intersection between the free-surface and a rigid body.

Having said this there is a problem with the two regridding procedures of Dommermuth *et al.* and Dommermuth & Yue. In both these schemes equal-arclength spaced nodes are used to regrid the free-surface, with the result that the desirable effect of free-surface nodes tending to gather in regions of large curvature, precisely where higher resolution is required (and conversely, the tendency of free-surface nodes to spread out in regions of small curvature, where low resolution is required) is lost.

This problem was overcome by Tsai & Yue [53] who developed an *adaptive* regridding procedure for use in their BIM for simulating the nonlinear interactions between a free-surface and a shed vortex shear layer in the inviscid wake of a

vertical surface-piercing plate. In this regridding procedure a larger density of nodes are placed in regions of higher curvature and a smaller density of nodes are placed in regions of lower curvature, subject to a minimum and maximum point spacing. In this way the stability of their numerical scheme is ensured, while at the same time its efficiency and accuracy is optimised.

2.3.2 Corner Problems

At each time-step in a Boundary-Integral Method Laplace's equation for ϕ (2.5) is solved subject to ϕ given on the free-surface (Dirichlet boundary condition) and ϕ_n given on the rest of the boundary (Neumann boundary condition). This type of problem is a "mixed" boundary value problem.

It is well known that at a corner of the fluid domain the solution of this problem might have a singularity (see Cointe [8]). Unfortunately, in the literature many researchers do not seem to define exactly what they mean by a singularity. In this study, for two-dimensional problems, a singularity will be defined to be a point where the complex potential $\beta(z)$ is non-analytic[1] (or, possibly, where a partial time derivative of $\beta(z)$ is non-analytic).

The existence of a singularity at a corner of the fluid domain will cause major problems for a BIM and large errors will result if it is not treated properly. Since a BIM is a time-marching scheme these errors will not remain confined near the corner in question but will propagate out into the whole domain with the result that the accuracy and stability of the numerical scheme can be seriously affected.

Having said this, in many cases the solution of (2.5) will be perfectly regular at a corner of the fluid domain. However, numerical difficulties can still be encountered at such a corner and BIMs must also be specially adapted here to take

[1]Technically, the complex potential β is really a function of z *and* t, and therefore a singularity in β corresponds to a position and time where either β is not analytic in z or β is not analytic in t, or both.

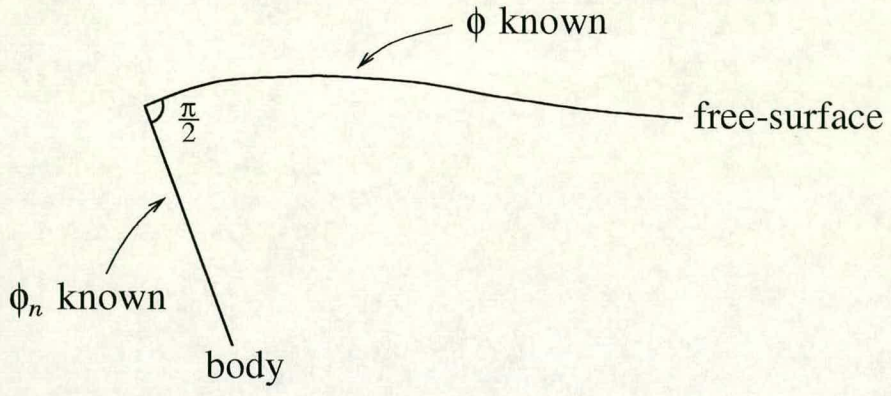

Figure 2.6: Free-surface intersecting body at right angles.

account of this. In this case the errors that arise are due to numerical artifacts rather than any problem with the underlying mathematical model.

Corners between Dirichlet & Neumann Sides

This is the most important case and it requires the most detailed analysis. A representative example of this type of corner is the intersection between the free-surface and a rigid body, for example a wavemaker.

Consider the situation that, at some time t, the free-surface intersects the body at right angles, as shown in figure 2.6. Then if the gradient of ϕ along the free-surface at the corner does not match ϕ_n on the body at the corner there will be a $z\log z$ type singularity in $\beta(z)$ (or if the gradient of ϕ_t along the free-surface at the corner does not match ϕ_{tn} on the body at the corner there will be a $z\log z$ type singularity in $\beta_t(z)$).

In this study it is postulated that the chances of getting a singularity when the intersection angle is not a right angle are much less than if, under similar circumstances (for example the same body motion), the intersection angle had been a right angle. Also, if a singularity did occur it would be a weaker singularity. In Appendix A the problem of an impulsively started plate moving into an initially

undisturbed strip of water is examined analytically. In this examination it is found that if the plate is vertical then $\beta(z)$ is singular at the intersection point at $t = 0$ (intersection angle $\frac{\pi}{2}$), whereas if the plate is sloping then $\beta(z)$ is *analytic* at the intersection point at $t = 0$ (intersection angle not $\frac{\pi}{2}$).

In order to try and overcome the difficulties encountered by BIMs at an intersection between the free-surface and a body, several numerical techniques have been used.

As has already been suggested, the reason for this possible singular behaviour at such corners is due to the confluence of two different boundary conditions (see figure 2.6). In Vinje & Brevig's method [56] only the body boundary condition is applied at this type of intersection point, with no regard to the dynamic boundary condition on the free-surface. That is, only the stream function ψ is prescribed here (equivalent to prescribing the velocity normal to the body ϕ_n). The velocity potential ϕ is treated as an unknown and obtained by solving the integral equation (2.27). Once this integral equation has been solved and time-stepping has taken place the new position of the intersection point is obtained via extrapolation.

Unfortunately, this method does not work well. In the study by Greenhow *et al.* [24] on the capsize of Salter's Duck this method was used. However, in the computations it was found that, in order to produce acceptable results, it was necessary to use information from experimental observations to fix the locations of the intersection points.

Following on from this Lin *et al.* [37], in 1984, developed an adaption of Vinje & Brevig's method where both boundary conditions are satisfied at the intersection point. Consequently, both ϕ and ψ are prescribed here and there are no unknowns at this corner point. If, for example, there were 2 such corner points

this would mean that the final linear system would be an $(N-2)\times(N-2)$ system rather than an $N\times N$ system, where N is the total number of nodes. The nodes at the intersection points are then treated as free-surface nodes for the purposes of time-stepping.

This method does work significantly better than Vinje & Brevig's original approach; see the study by Greenhow [22] on the wedge entry problem (relevant to ship slamming). In addition, this method can also be generalised to more than two dimensions, for example the study by Dommermuth & Yue [17] on nonlinear axisymmetric free-surface flows.

Further improvements to the treatment of these intersection points can be found in the work by Otta *et al.* [40]. The BIM developed in their study is based on an earlier BIM developed by Grilli *et al.* [25] and Grilli & Svendsen [27]. All these methods use the integral representation of Laplace's equation based on Green's theorem (2.13) rather than the integral representation used by Vinje & Brevig, namely the integral representation of Laplace's equation based on Cauchy's theorem (2.27). Unfortunately, there is a problem at corners in the fluid domain if equation (2.13) is used instead of equation (2.27). The problem is that the role of the stream function ψ is now taken over by ϕ_n and ϕ_n is discontinuous at corners. Grilli *et al.* overcome this problem by using "double-nodes" at corners. That is, at each corner two nodes are used; these nodes are coincident but one node is regarded as belonging to one side of the corner and the other node is regarded as belonging to the other side of the corner. When using double-nodes care must be taken to ensure that ϕ is equal at the two nodes (continuity of ϕ) otherwise the final linear system might be ill-conditioned or even singular.

There are in fact three important techniques described in Otta *et al.* [40] which advance the treatment of corners. The first two techniques apply to corners

in general but the last technique is specific to corners between the free-surface and a body.

The first of these techniques deals with how equation (2.13) is integrated near corners. In order to discretise this equation the integral on the right hand side is expressed as a sum of the integrals over small segments C_i's which comprise the boundary C. Each C_i will start at a node and will end on another node (not necessarily adjacent to the first node). Also, no C_i can cross a corner. Once the boundary has been split up in this way the geometry of each segment and the variation of the flow quantities ϕ and ϕ_n in each segment are approximated using Lagrange polynomials based on discrete nodal values. Then the integrals are integrated numerically. When performing integration along a particular C_i the integrand will be singular if $\boldsymbol{x}_0 \in C_i$. If this is the case great care is taken to perform the numerical integration along C_i accurately. If however $\boldsymbol{x}_0 \notin C_i$ then the integrand will be regular and integration along C_i can normally be done perfectly accurately using *Gaussian quadrature* with a reasonable number of integration points (normally taken to be 10). What Grilli *et al.* and Grilli & Svendsen noticed was that even if $\boldsymbol{x}_0 \notin C_i$, so that the integrand is technically regular, the integrand can be "quasi-singular" if $\boldsymbol{x}_0$ is close to C_i. This is because if $\boldsymbol{x}_0$ is close to C_i then $G(\boldsymbol{x}, \boldsymbol{x}_0)$ and $G_n(\boldsymbol{x}, \boldsymbol{x}_0)$ will vary very rapidly as $\boldsymbol{x}$ moves along C_i. The associated integral will then not be integrated accurately using standard Gaussian quadrature unless an excessive number of integration points are used. This situation of $\boldsymbol{x}_0$ being close to, but not belonging to, C_i will occur most often at the corners of the fluid domain, with $\boldsymbol{x}_0$ lying on one side of the corner and C_i lying on the other. As a result, if nothing is done about these quasi-singular integrals, large errors will occur at corners even if the exact mathematical solution is regular there. In order to overcome this problem Grilli

& Svendsen developed an "adaptive integration" procedure which can reduce integration errors to almost arbitrarily small levels, even for domains with sharp corners. Unfortunately, this procedure is computational expensive and must be limited to a few predefined integrals associated with certain $(\boldsymbol{x}_0, C_i)$ pairs. With this disadvantage in mind Grilli & Subramanya [26] developed a new adaptive integration procedure which is much more computational efficient and accurate, and therefore does not require the predefining mentioned above.

The second technique described by Otta *et al.* relates to how the flow quantities ϕ and ϕ_n are approximated in each segment C_i. Otta *et al.* show that not only $G(\boldsymbol{x}, \boldsymbol{x}_0)$ and $G_n(\boldsymbol{x}, \boldsymbol{x}_0)$ can vary rapidly at corners for certain $\boldsymbol{x}_0$ but ϕ and ϕ_n can also vary rapidly here (see page 39). Consequently, they show that the Lagrange polynomials used to approximate ϕ and ϕ_n in each C_i must be of a sufficiently high order to correctly model the flow. Therefore, they conclude that high-order "boundary elements" are needed to accurately simulate flow in domains with corners.

The final technique is concerned with the uniqueness of the component of velocity of the fluid particle at the intersection between the free-surface and a body in a direction normal to that body. For example, consider the intersection between the free-surface and a paddle wavemaker as shown in figure 2.7. The choice of a paddle wavemaker is not essential for the analysis and a piston wavemaker would also suffice. In the figure nodes i & $i+1$ are "double-nodes". Node i is consider to belong to the free-surface and node $i+1$ is considered to belong to the wavemaker. The position and velocity potential of the free-surface nodes are determined through numerical updating (see equations (2.6) & (2.9)), whereas the position and the normal derivative of the velocity potential of the wavemaker nodes are specified exactly, due to the predetermined motion of the wavemaker.

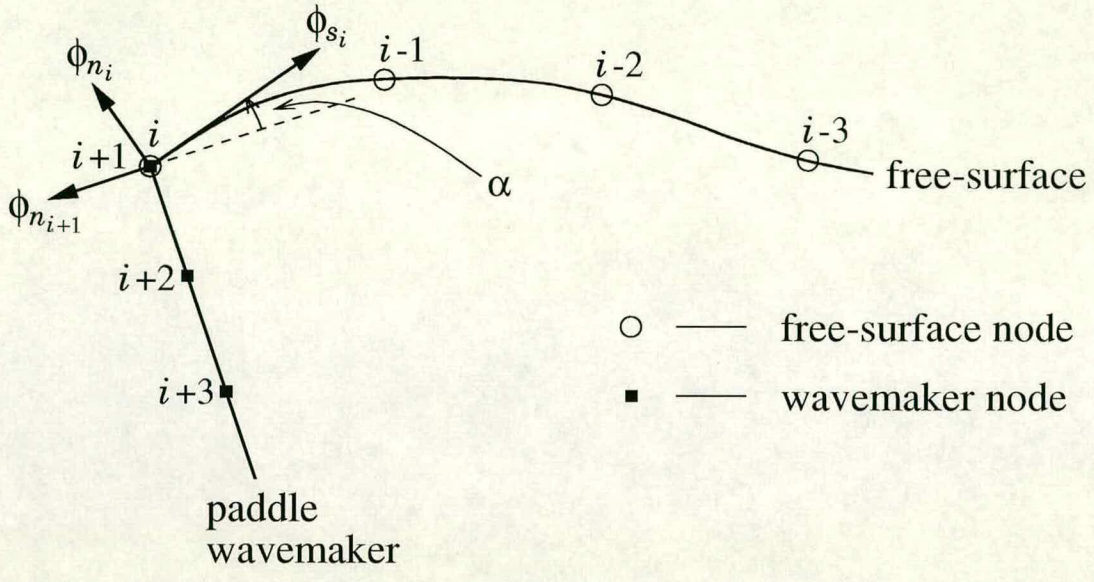

Figure 2.7: The intersection between a free-surface and a paddle wavemaker.

From a kinematic point of view the free-surface node i is free to move tangentially along the wavemaker but its velocity normal to the wavemaker must be that of the wavemaker itself. However, after time-stepping, due to numerical inaccuracies, the updated position of node i will not lie on the new position of the wavemaker, as it should. This problem is overcome by simply projecting node i back onto the wavemaker.

Furthermore, Since Otta *et al.* only consider non-singular flows the above kinematic condition implies that

$$(\phi_s \cos\alpha - \phi_n \sin\alpha)_i = -\phi_{n_{i+1}}. \tag{2.39}$$

As well as numerical inaccuracies causing errors in the updated positions of the free-surface nodes there will also be updating errors in the velocity potential of these nodes. Consequently, at node i, there will be a small deviation in the tangential derivative of ϕ along the free-surface ϕ_{s_i}. In addition, there will be an error in the normal derivative ϕ_{n_i}. This normal derivative is obtained by solving

the integral equation and the error in it comes from the errors in the position and velocity potential of the free-surface nodes as well as the errors which come from solving the integral equation itself. As a result equation (2.39) will not be satisfied. This situation may lead to unacceptable numerical behaviour which some researchers, in the past, might have incorrectly attributed to the existence of a singularity in the exact mathematical solution. Otta *et al.* overcome this problem by forcing equation (2.39), or more correctly its discretised version, to hold. The way equation (2.39) is discretised is as follows. The tangential derivative ϕ_{s_i} is approximated by numerically differentiating ϕ along the free-surface using a Lagrange polynomial based on, say, m discrete nodal values of ϕ along the free-surface, *i.e.* $\phi_{i-m+1}, \ldots, \phi_i$. Normally $\phi_{i-m+1}, \ldots, \phi_i$ would be considered as known from the usual free-surface updating procedure; however Otta *et al.* consider ϕ_i as an unknown. The value of ϕ_i $(= \phi_{i+1})$ as well as the values of $\ldots, \phi_{n_{i-1}}, \phi_{n_i}, \phi_{i+2}, \phi_{i+3}, \ldots$ are then obtained by solving the normal linear system with one of the rows replaced by the discretised version of equation (2.39). Otta *et al.* call this procedure "BC-correction". The "BC-correction" procedure is only used for small $|\alpha|$ because Otta *et al.* found that if the procedure was used for values of $|\alpha|$ close to $\pi/2$ then errors would be introduced.

Corners between Dirichlet & Dirichlet Sides

A representative example of this type of corner is the intersection between two rigid stationary walls, intersecting with angle α, as shown in figure 2.8.

The complex potential for the flow confined between these two walls is

$$\beta(z) = Az^n, \tag{2.40}$$

where $A \in \mathbb{R}$ and $n = \pi/\alpha$ (see Batchelor [4]).

Now consider the unsteady flow in a general fluid domain where there are two

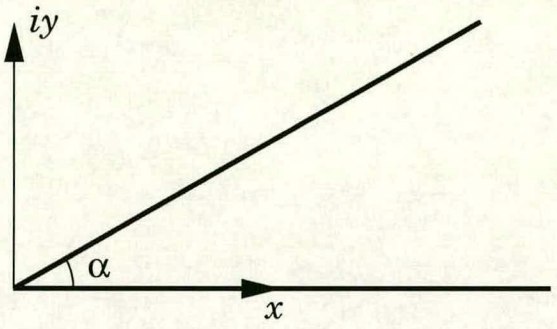

Figure 2.8: Two infinitely long, straight, rigid, stationary walls intersecting with angle α.

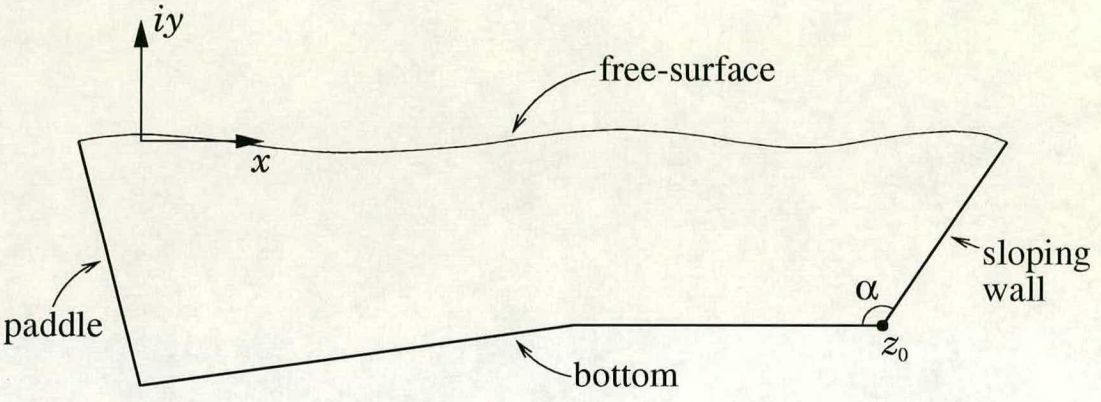

Figure 2.9: General fluid domain with two rigid, stationary walls intersecting with angle α.

rigid, stationary walls intersecting with angle α at z_0, as shown in figure 2.9. Then from equation (2.40) the complex potential for this flow at z_0 behaves locally like

$$A(z - z_0)^n + B, \tag{2.41}$$

where $A, B \in \mathbb{C}$ are functions of t only and again $n = \pi/\alpha$.

From equation (2.41) it can be seen that the complex potential $\beta(z)$ can vary rapidly at z_0 depending on α. Hence the conclusion of Otta *et al.* [40] that higher order boundary elements should be used to approximate the flow quantities (see page 36). Furthermore, if $\alpha > \pi$ then the fluid velocity will be undefined at z_0.

2.4 Other Numerical Methods for Free-Surface Flows

According to Tsai & Yue [54] numerical methods for nonlinear free-surface flows, which treat the free-surface explicitly as a discontinuity, fall into two main groups: *boundary-discretisation* methods and *volume-discretisation* methods. As to which one of these two methods is applicable in a certain situation depends on which underlying theory for fluid flow is being used. To be more specific if the underlying theory results in a governing field equation which is linear then a boundary-discretisation method can be used. If on the other hand the governing field equation turns out to be nonlinear then a volume-discretisation method must be used.

2.4.1 Boundary-Discretisation Methods

If the flow is potential then the governing field equation is Laplace's equation

$$\nabla^2 \phi = 0, \tag{2.42}$$

which is linear and so boundary-discretisation methods can be used. The BIMs met in sections 2.2 & 2.3 are examples of such boundary-discretisation methods.

For viscous flows it is also possible to use boundary-discretisation methods but only when the Reynolds number is sufficiently small. This is because for low Reynolds number flow the Navier-Stokes equation can be linearised by dropping the nonlinear convective term. See Pozrikidis [42] for a description of such methods.

High-Order Spectral Methods

An alternative boundary-discretisation method to BIMs for modelling inviscid, incompressible and irrotational free-surface flows is the *High-Order Spectral* (HOS)

method developed independently by Dommermuth & Yue [16] and by West *et al.* [58]. This method robustly, accurately and efficiently models gravity waves whose nonlinearities are not necessarily small. A good review of HOS methods is given in Tsai & Yue [54].

In the HOS method a large number N (typically $N \sim 10^3$) of free Fourier wave modes are allowed to evolve in time subject to their own evolution equations. These evolution equations come from the nonlinear free-surface boundary conditions, which are treated in a pseudo-spectral manner. In reality each one of these Fourier wave modes will interact in a nonlinear way with all the others. In the HOS method these nonlinear interactions are accounted for up to a specified order M in wave steepness. The computational effort involved in the HOS method increases only linearly with M and N, and convergence with M and N is exponentially fast for waves of up to approximately 80% of Stokes limiting steepness ($ka \sim 0.35$), beyond which convergence is poorer and eventually fails.

As with BIMs, the computational procedure involved in HOS methods consists of repeating the following two steps:

1. Given the surface elevation $\eta(\boldsymbol{x}, t)$ and the velocity potential $\phi(\boldsymbol{x}, \eta, t)$ on that surface at some instant of time t, Laplace's equation is solved to give the velocity potential ϕ inside the fluid domain.

2. The kinematic and dynamic boundary conditions are then used to time step forwards the free-surface η and the velocity potential ϕ on it to a time $t+\Delta t$.

Another similarity with BIMs is that HOS methods also tend to suffer from high-wavenumber instabilities. In the HOS method, due to the finite truncation in the number (N) of wave modes, energy is not conserved. When the free-surface becomes too steep there is a rapid growth in the energy of the highest wavenumber modes and a subsequent loss of smoothness and breakdown of the solution. As

with BIMs these instabilities can be effectively controlled by applying smoothing. In fact smoothing can be used to enable computations to be continued beyond wave breaking and, although the breaking event itself is not correctly modelled, the solution after breaking maintains reasonable agreement with experimental observations (Dommermuth & Yue [16]). This makes the HOS method suitable for studying the long-term evolution of wavetrains. Another merit that the HOS method possesses is that it readily extends from two to three dimensions.

Thus, to recap, the linear efficiency and exponential accuracy of the HOS technique makes it a powerful method for studying nonlinear wave-wave interactions and long-time evolutions of wavetrains in two and three dimensions.

On the other hand, although the HOS method has been extended to include submerged bodies (Liu *et al.* [38]), it has not yet been extended to include surface-piercing bodies, with which this study is primarily concerned. Also the HOS method assumes a single-valued continuous free-surface and so cannot model overturning. Moreover it can't even model very steep phenomenon. Therefore, since very steep and overturning free-surfaces can occur in the vicinity of a surface-piercing body, HOS methods are not considered further in this work.

2.4.2 Volume-Discretisation Methods

For general viscous flows it is not possible to linearise the Navier-Stokes equation and so volume-discretisation methods must be used. Of course, discretising the whole volume of the fluid domain, rather than just discretising the boundary, has the disadvantage of resulting in many more unknowns and thus increased computational effort. Typically, in two dimensions if there are N discretisation points on the boundary there will be $O(N^2)$ discretisation points throughout the whole domain.

Tsai & Yue [54] classify these volume-discretisation methods, according to

the spatial discretisation used, into *boundary-fitted* methods and *Eulerian grid* methods.

Boundary-Fitted Methods

In boundary-fitted methods the physical fluid domain is mapped on to a simpler computational domain in which the transformed equations are discretised and solved. The complexity of this mapping depends on how complicated the shape of the physical fluid domain is. Also the more complicated the mapping the more complicated the transformed field equations and boundary conditions become.

Like BIMs these methods tend to be high-order methods. However, they are also similar to BIMs in that they cannot cope with interface merging. As a result, for flows that are essentially irrotational these methods have no advantage over BIMs. They only have the disadvantage of increased computational effort for a similar accuracy, being volume-discretisation methods. Thus, for these situations BIMs are much more efficient.

Eulerian Grid Methods

In these methods a fixed grid is used which covers the whole region of interest, even parts where there is initially no fluid. Then, at each time step the governing field equations are solved on this grid and the location of the free-surface within this grid is time stepped forwards.

These methods tend to be very stable and reasonably straightforward to implement but their most notable feature is their ability to cope with interface merging. On the other hand Eulerian grid methods tend to be low order and therefore inefficient when high resolution is required. This is especially true when differentiating along the free-surface for quantities like free-surface slope or curvature *etc.*.

One of the first Eulerian grid methods was the *Marker and Cell* (MAC) method developed by Harlow & Welch [28].

Volume of Fluid Methods A more recent type of Eulerian grid method which has been undergoing much development lately is the *Volume of Fluid* (VOF) method. Originally devised by Debar [13] it was then further developed by a number of researchers including Hirt & Nichols [29] (who coined the name "Volume of Fluid"). A recent review of VOF methods is given by Kothe & Rider [36].

In the VOF method a function f is defined which takes the value 1 at points in the fluid and 0 at points outside the fluid. This function f is then averaged within each cell of the fixed Eulerian grid to give a new function F. This new function F is naturally the fraction of fluid within each cell and is therefore called the *fluid volume fraction.*

At the start of a simulation F is initialised using the initial conditions. Exact free-surface location information is then discarded in favour of F and the simulation proceeds by advecting this function in time using the solution of a standard convection equation. A defining feature of the VOF technique is that this advection is done by a geometrical procedure rather than a high-order algebraic scheme. This results in minimal numerical diffusion and in so doing prevents the smearing out of discontinuities such as the free-surface.

Suppose the simulation is at some time-step and there is a given distribution of F. In order to advect F to the next time-step volume fluxes need to be calculated and in order to do this the location of the free-surface is required. Unfortunately, a given distribution of F does not guarantee a unique free-surface geometry. Instead the free-surface geometry is inferred from the local fluid volume fraction data and assumptions of the particular VOF method being used. These assumptions are: the assumed shape of the free-surface within a cell and the

method by which free-surface normals are to be calculated.

The simplest assumed free-surface shape is referred to as "piecewise constant". This implies that within each cell the free-surface is assumed to be a line (or a plane in three dimensions) aligned with one of the logical mesh coordinates. A slightly better approximation is when the assumed free-surface shape is what is called "piecewise constant stair-stepped". In this case, within each cell the free-surface is again forced to align with the mesh coordinates but is additionally allowed to "stair-step". However, following the work of Youngs [60], the most accurate VOF methods to date assume a free-surface shape which is piecewise linear.

Figures 2.10, 2.11 & 2.12 are schematics showing the reconstruction of a free-surface (continuous line) from F data using the three different assumed free-surface shapes. The numbers denote the cell fluid volume fractions.

As for the method by which free-surface normals are calculated, this is either one-dimensional, using one-dimensional volume fraction differences, or multi-dimensional, using a 9 point (27 point in three dimensions) stencil applied to the volume fractions.

Once the assumed shape of the free-surface within each cell has been decided on and a method to find the free-surface normals has been chosen it is then possible to calculate the volume fluxes given a solution to the velocity field.

Finally, using these volume fluxes, F can be advected to the next time step. In a similar way to calculating the free-surface normals, this is either done in a one-dimensional or multi-dimensional manner. One-dimensional means F is advected in one coordinate direction at a time (operator split). Multi-dimensional means F is advected in all coordinate directions simultaneously.

One area in which VOF methods show great potential is in simulating the

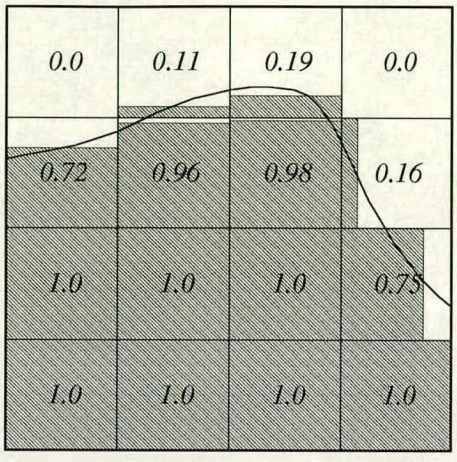

Figure 2.10: Piecewise constant reconstruction

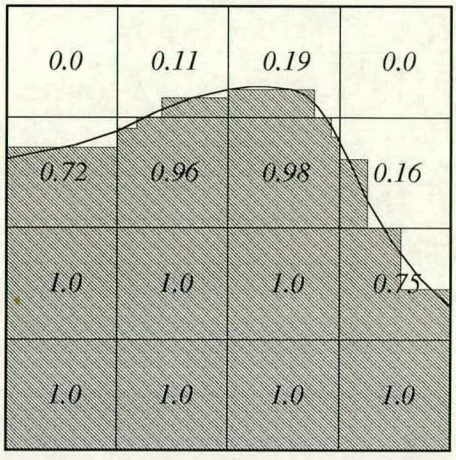

Figure 2.11: Piecewise constant stair-stepped reconstruction

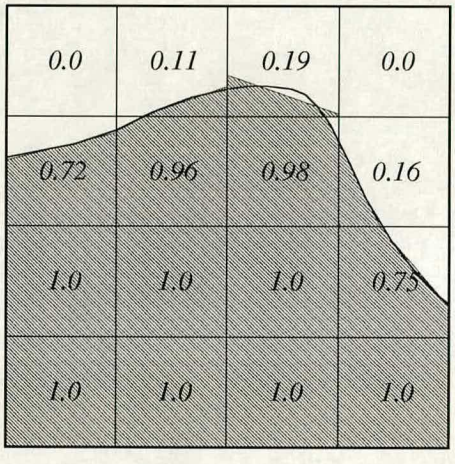

Figure 2.12: Piecewise linear reconstruction

interaction between a fluid with a free-surface and a surface-piercing body. This is particularly because of the ability of Eulerian grid methods to cope with interface merging. To this end Chopra & Greated [7] developed a way of modelling an air pocket within a VOF code with a view to simulating the air entrapped by a plunging breaker when it hits a wall.

In summary, VOF methods, and Eulerian grid methods in general, can be used to model nonlinear viscous free-surface flows and their greatest advantage is

their ability to model large surface distortions like fluid/fluid impacts. However, there are many reasons why, in this study, a BIM has been chosen, instead of a VOF method, to model the flows of interest, namely free-surface flows in the vicinity of a surface-piercing body.

Firstly, as discussed in section 2.1, water wave motion can be effectively modelled using the simplified theoretical framework of potential flow. This assertion is further reinforced by the experimental work of Skyner [47]. In his study the experimental technique of PIV was used to obtain instantaneous full-field velocity measurements of a plunging breaker. Plots were then made of isovelocity contours of u and v and these were found to be almost precisely orthogonal to each other everywhere, even right up into the plunging tip. This shows that plunging breaker wave motion remains essentially irrotational throughout the whole breaking process up to the point of re-entry of the plunging jet.

For the case of a surface-piercing body being present, consider the representative example of a wave impacting on a rigid wall. In this situation the compressibility of the flow can be ignored because the impact velocity will be much smaller than the speed of sound in the fluid. Also viscosity and surface tension effects can be neglected since inertial forces are dominant during the impact process (Cooker & Peregrine [11]). Thus again potential theory is applicable.

Another reason why a BIM has been chosen, as opposed to a VOF method, is because of the advantages that BIMs have over VOF methods. In general BIMs tend to be higher order in their description of the free-surface than VOF methods; Young's VOF method [60] is formally first-order accurate. Also VOF methods can only approximately satisfy the free-surface boundary conditions, partly due to this low-order accuracy discussed above. On the other hand BIMs satisfy the fully nonlinear free-surface boundary conditions exactly. Yet another

advantage of BIMs is that they only need to discretise the boundary and not the whole domain like VOF methods and so BIMs typically require a significantly less computational effort.

Finally, it is very well known that the potential flow solution at the intersection between a free-surface and a body may exhibit a weak singularity. As a result, any BIM being used to attempt to model such a flow must be specially adapted to account for this possibly non-analytic behaviour. However, for these adapted BIM codes very little work has been done on assessing how well they approximate either experimental results or analytical solutions in the vicinity of these intersection points. The fact that there has been very little in the way of comparisons with analytical solutions is because not many analytical solutions exist to date! Thus, one of the main aims of this study is to try to address this lack of knowledge and understanding by comparing the results from an adapted BIM with those from a recently published analytical solution as well as with the results from experiments.

Chapter 3

Development of the Present Boundary-Integral Method

This chapter describes in detail the present Boundary-Integral Method. Along with the description of each feature of the code is a discussion of the motivation behind its development.

3.1 Two-Dimensional Flow & Surface-Piercing Bodies

In this study only two-dimensional free-surface flows will be studied, with particular emphasis on two-dimensional free-surface flows in the vicinity of surface-piercing bodies. For the latter situation the author feels that much work still needs to be done to assess how well BIMs predict such flows, especially very close to the intersection between the free-surface and the body (see section 2.3.2). In addition, the author also feels that there is little point in looking at fully three-dimensional flows (not just axisymmetric flows) with surface-piercing bodies until the above two-dimensional case has been satisfactorily resolved.

3.2 The Basis of the Present Boundary-Integral Method

The basis of the present boundary-integral method is Vinje & Brevig's method (see [55] & [56]). The main reasons for choosing this method are: (a) its proven stability [17], (b) its proven accuracy [18] and (c) the number of major papers that are based on developments of this approach [37], [18], [53] & [61]. Tsai & Yue, in their paper on the nonlinear interactions between a free-surface and a shed vortex shear layer in the inviscid wake of a vertical surface-piercing plate [53], summed up the position well:

> We are especially encouraged by the promising results of Vinje & Brevig (1981) for simulation of nonlinear free-surface motions.

Further reasons for choosing Vinje & Brevig's method will be given later.

3.3 Non-Dimensionalisation of the Problem

From now on in this dissertation, unless otherwise stated, the following non-dimensionalisation will be used. The units of mass, length and time are chosen so that the fluid density $\rho \equiv 1$, the gravitational acceleration $g \equiv 1$ and a representative water depth $h \equiv 1$. Therefore, the following transformation equations apply

$$\boldsymbol{x} = \frac{\boldsymbol{x}^*}{h}, \quad t = t^* \sqrt{\frac{g}{h}}, \quad \boldsymbol{u} = \frac{\boldsymbol{u}^*}{\sqrt{gh}}, \quad p = \frac{p^*}{\rho g h}, \tag{3.1}$$

where $\boldsymbol{x}^*$, t^*, $\boldsymbol{u}^*$ & p^* are respectively the dimensional position, time, velocity and pressure, and $\boldsymbol{x}$, t, $\boldsymbol{u}$ & p are their non-dimensional equivalents.

3.4 Basic Method

To restate the problem that was briefly described in Chapter 2. The fluid is assumed to be homogeneous, incompressible and irrotational and the flow is assumed to be two-dimensional. Thus the fluid motion is completely determined by the complex potential

$$\beta = \phi + i\psi.$$

Since β is an analytic function of $z = x + iy$ the following principal value form of Cauchy's integral theorem holds

$$i\theta(z_0)\beta(z_0) = \text{PV} \oint_C \frac{\beta(z)}{z - z_0} dz, \tag{3.2}$$

where z_0 is a point on the boundary C of the fluid domain and $\theta(z_0)$ is the internal angle at z_0. In this study the boundary C is assumed to consist of a free-surface and various rigid boundaries which are either stationary (for example the bottom), free to move (for example a ship) or constrainted to move in some prescribed manner (for example a wavemaker). The above equation is the integral representation of Laplace's equation based on Cauchy's theorem (2.27).

At each time-step ϕ is known and ψ is unknown on the free-surface. The velocity potential ϕ is known on the free-surface from either the initial conditions, in the case of the first time-step, or from integrating the dynamic boundary condition (2.9) from the previous time-step.

In addition, at each time-step ψ is known and ϕ is unknown on the rest of the boundary. The stream function ψ is known on the rest of the boundary from the kinematic body boundary condition. For a moving body this kinematic boundary condition is (see [56])

$$\psi(x, y; t) = U(y - Y) - V(x - X) - \frac{1}{2}\dot{\theta}r^2 + \Psi(t), \tag{3.3}$$

where (X, Y) and (U, V) are respectively the position and velocity of the centre of gravity or axis of rotation of the body. Also, $\dot{\theta}$ is the angular velocity of the body in the anti-clockwise sense, $r = \sqrt{(x-X)^2 + (y-Y)^2}$ and $\Psi(t)$ is an arbitrary time-dependent constant. For a stationary body equation (3.3) reduces to

$$\psi(x, y; t) = \Psi(t) \tag{3.4}$$

and usually this time-dependent constant can be chosen to be zero.

As a result, at each point on the boundary C either the real or imaginary part of β is known and the other part is unknown. The only exception to this rule is at intersection points between the free-surface and a body, where essentially both parts of β are known due to the confluence of two different boundary conditions.

Let C_ϕ be the part of the boundary on which ϕ is known and C_ψ be the part of the boundary on which ψ is known, as in figure 2.5. Then taking the real part of equation (3.2) for z_0 on C_ϕ yields

$$\theta(z_0)\psi(z_0) + \mathrm{Re}\left[\mathrm{PV}\oint_C \frac{\beta(z)}{z - z_0} dz\right] = 0 \tag{3.5}$$

and taking the imaginary part of equation (3.2) for z_0 on C_ψ yields

$$\theta(z_0)\phi(z_0) + \mathrm{Re}\left[\mathrm{PV}\oint_C \frac{i\beta(z)}{z - z_0} dz\right] = 0. \tag{3.6}$$

These two equations form a Fredholm integral equation of the second kind from which β can be found on C.

Once β has been found on C it can be differentiated on the free-surface to obtain the velocities of fluid particles on the free-surface. That is, the complex conjugate of the complex velocity $u + iv$ of a fluid particle is given by

$$w \overset{\text{def}}{=} u - iv = \frac{d\beta}{dz}. \tag{3.7}$$

This can then be substituted into the kinematic condition on the free-surface

$$\frac{Dz}{Dt} = u + iv = \overline{w} \tag{3.8}$$

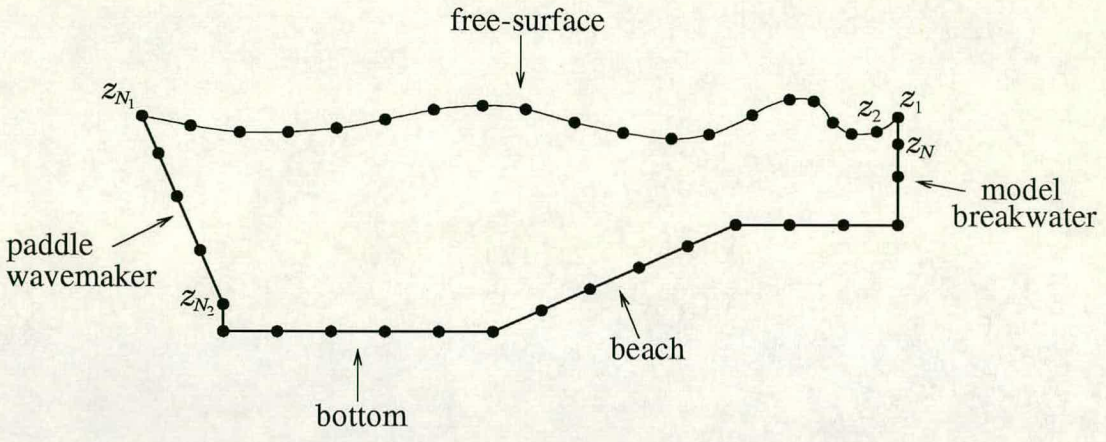

Figure 3.1: Discretisation of a numerical wavetank.

and the Lagrangian form of the dynamic boundary condition on the free-surface (non-dimensional form)

$$\frac{D\phi}{Dt} = \frac{1}{2}\left(u^2 + v^2\right) - y = \frac{1}{2}w\overline{w} - y. \tag{3.9}$$

Finally, in order to update the position of and velocity potential on the free-surface the above two equations are integrated forward in time to the next time-step. As well as this, the rigid boundaries are also updated so that the whole process can be started again.

3.5 Numerical Solution

The numerical solution starts with the discretisation of the boundary. This involves placing, say, N discretisation points (nodes) round the whole boundary. Figure 3.1 gives an example of the discretisation of a numerical wavetank. In this study no conformal mapping or method of images technique is used to reduce the amount of boundary that needs to be discretised. This decision was taken because of the conceptual simplicity and flexibility of working in the physical domain. However, these two benefits must be weighed up against the disadvantage that discretising the whole boundary is not very computationally efficient.

Once the N nodes $(z_1, \ldots, z_N)$ have been placed on the boundary the contour C can be split up into N subcontours, with each subcontour running between adjacent nodes. Let $C_{j,j+1}$ be the subcontour running between node j and node $j+1$. The integral on the right hand side of (3.2) can now be expressed as a sum of integrals over the $C_{j,j+1}$'s

$$\left.\begin{aligned} i\theta(z_k)\beta(z_k) &= \mathrm{PV}\oint_C \frac{\beta(z)}{z-z_k}dz \\ &= \mathrm{PV}\left(\sum_{j=1}^{N}\left(\int_{C_{j,j+1}} \frac{\beta(z)}{z-z_k}dz\right)\right) \end{aligned}\right\} \quad \text{for } k = 1, \ldots, N. \qquad (3.10)$$

In order to proceed further it would normally be necessary to approximate the variation of $\beta(z)$ and the geometry of C in each $C_{j,j+1}$ in terms of discrete nodal values and then use some numerical integration technique to evaluate the above integrals. However, in Vinje & Brevig's method there is no need to obtain an approximation to the geometry of C in each $C_{j,j+1}$ and there is no need to use a numerical integration technique. In their method they assume that β varies linearly between nodes and under this assumption the integrals over the subcontours in equation (3.10) can be integrated analytically. Furthermore, the value of these integrals is independent of the path taken between nodes.

There appears to be some confusion in the literature about this last point, with many researchers claiming that Vinje & Brevig's method assumes a linear variation of the *geometry* between nodes. In fact a properly implemented BIM based on Vinje & Brevig's method assumes nothing about the geometry between nodes.

These advantages of Vinje & Brevig's method are another reason why it was chosen as a basis for the present BIM. However, although the BIM developed in this study is based on Vinje & Brevig's method it contains many adaptions.

Firstly, the present BIM goes beyond Vinje & Brevig's method by assuming

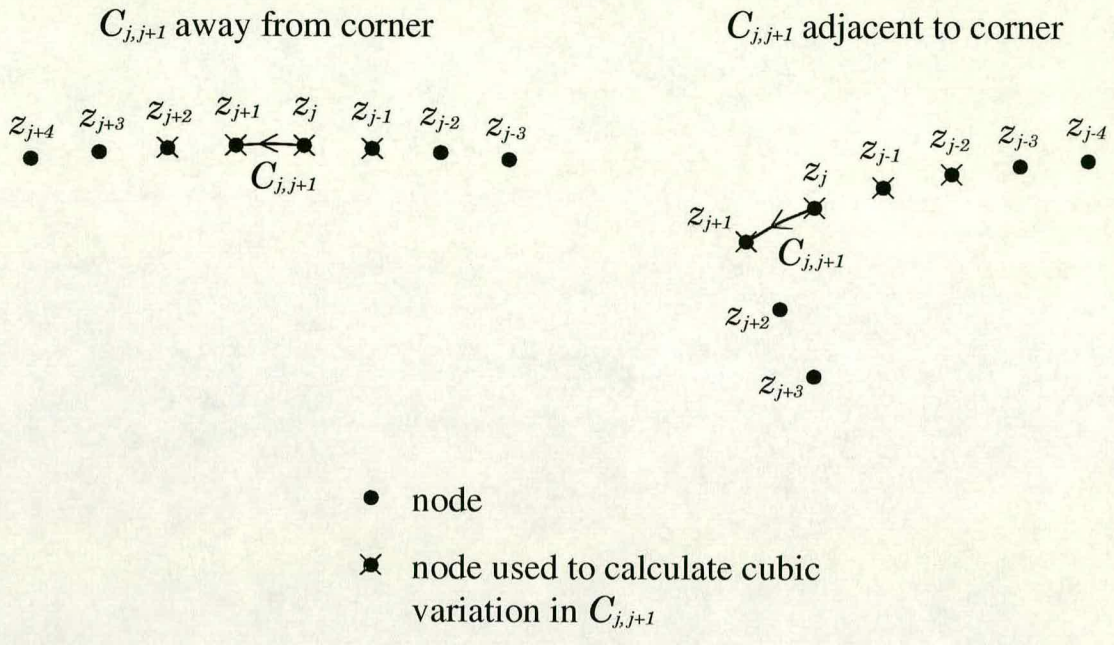

Figure 3.2: Nodes used to calculate the cubic variation of $\beta(z)$ in subcontour $C_{j,j+1}$.

that $\beta(z)$ varies cubically between nodes. In order to calculate this cubic variation of $\beta(z)$ in each $C_{j,j+1}$ the position and β value of four discrete nodes are required. Normally the four nodes used would be z_{j-1}, z_j, z_{j+1} & z_{j+2}; that is the four nodes that have $C_{j,j+1}$ at their centre. However, if $C_{j,j+1}$ is adjacent to a corner then the first four nodes on the same side of the corner as $C_{j,j+1}$ would be used instead (see figure 3.2).

The reason for this different treatment near corners is because of the possibly very rapid, or even singular, behaviour of $\beta(z)$ at corners (see subsection 2.3.2). Consequently, to assume that β varies cubically across a corner could result in large errors.

Having decided on this method for calculating the cubic approximation to $\beta(z)$ in each $C_{j,j+1}$ the full discretisation of equation (3.10) is as follows.

Let β_k be the approximation to $\beta(z_k)$, then the discretised version of equa-

tion (3.10) is

$$i\theta(z_k)\beta_k = \sum_{j=1}^{N} \Gamma_{k,j}\beta_j \quad \text{for } k = 1, \ldots, N. \tag{3.11}$$

where $\Gamma_{k,j}$ is the influence function of node z_j. Appendix B shows how these influence functions are calculated. Great care is required in making sure that they are correct. This care is especially needed when dealing with *branch cuts* of complex logarithms. Also, in appendix B it is shown that the angle $\theta(z_k)$ does not need to be calculated. Indeed, no angle ever needs to be calculated except implicitly through the imaginary part of complex logarithms. In fact, in appendix B the $\Gamma_{k,j}$ are redefined so that the left hand side of equation (3.11) is cancelled, and as a result equation (3.11) becomes

$$\sum_{j=1}^{N} \Gamma_{k,j}\beta_j = 0 \quad \text{for } k = 1, \ldots, N. \tag{3.12}$$

The next step is to obtain a system of linear equations for the unknown part of β at each z_k from the above equation. In order to do this it is firstly necessary to decide on a method to treat corners at the intersection between the free-surface and a surface-piercing body. At this stage, in this study, the corner treatment method of Lin *et al.* [37] will be used (see page 33). Further improvements to the treatment of such corners will be given later.

In the method of Lin *et al.* both the dynamic boundary condition on the free-surface (3.9) and the kinematic boundary condition on the body (3.3) are satisfied at these corners. Consequently, both ϕ and ψ are prescribed here and no part of β is unknown here. If z_l is the node at such a corner then the equation corresponding to $k = l$ in (3.12) is dropped and the resultant system of linear equations is constructed from the remaining equations in (3.12).

Let the resultant system of linear equations be written in matrix form

$$A\boldsymbol{x} = \boldsymbol{b}. \tag{3.13}$$

In all situations the coefficient matrix A will be diagonally dominant due to the fact that equations (3.5) & (3.6) form a Fredholm integral equation of the *second* kind.

Appendix C shows how the matrix A and the right hand side vector $\boldsymbol{b}$ are constructed for the discretised numerical wavetank in figure 3.1.

Having constructed the matrix equation (3.13) the next stage is to solve it. In this study the method chosen to do this is a rather slow direct solver (Gaussian elimination) as opposed to a faster iterative solver. The reasons for making this apparently strange decision will be discussed later.

Once equation (3.13) has been solved, so that β is now known at every node round the boundary, it is then possible to differentiate β along the free-surface. In order to do this a five-point numerical differentiation scheme is used which is the same numerical scheme as that used by She *et al.* in their two-dimensional numerical wavetank [46]. In this scheme the five points normally used are the five nodes whose central node is the node where the derivative is required. However, if this node is at a corner, or immediately adjacent to a corner, then the five points used are the first five nodes on the free-surface at that corner.

As with the cubic approximation to $\beta(z)$ between nodes this different treatment at corners is because of the possibly very rapid, or even singular, behaviour of $\beta(z)$ at these corners (see section 2.3.2).

Appendix D gives a more detailed description of the five point numerical differentiation scheme. This numerical differentiation scheme represents another example of how the present BIM goes beyond Vinje & Brevig's BIM because their method only uses a lower order three-point scheme, which is not specially adapted at corners.

Finally, having obtained the complex velocity $\overline{w}$ of each of the free-surface

nodes it is then possible to time-step forwards the position and velocity potential of these nodes using equations (3.8) & (3.9).

In the following subsections the time-stepping procedure (used to perform the above), as well as other specialised features of the present BIM will be discussed.

3.5.1 The Time-Stepping Procedure

In this study the explicit time-stepping procedure of Dold & Peregrine [15] is used (see page 24). However, unlike in Dold & Peregrine's method, where three successive Laplace's equations are solved at each time-step ($\nabla^2\phi = 0$, $\nabla^2\phi_t = 0$ & $\nabla^2\phi_{tt} = 0$), here only the first two of these Laplace's equations are solved at each time-step ($\nabla^2\phi = 0$ & $\nabla^2\phi_t = 0$). Thus the present time-stepping procedure is second-order explicit.

The main reason for not extending the time-stepping procedure used here to higher order is given by the second item in the enumerated list on page 25. Further weight is added to this reason by the type of numerical differentiation scheme used in this study (see Appendix D). It is well known that errors in a numerical differentiation scheme are minimised if the point where the derivative is required is the central point out of the points being used by the scheme. However, for the present numerical differentiation scheme, if the point where the derivative is required lies near a corner it will not be the central point of its associated scheme. Therefore, numerical errors can be quite large if the present numerical differentiation scheme is used to find *high-order* derivatives near corners.

The details of the present time-stepping procedure are as follows.

The function $\beta_t(z)$, like $\beta(z)$, is an analytic function of z. Consequently it can also be used in equation (3.2), giving

$$i\theta(z_k)\beta_t(z_k) = \mathrm{PV}\oint_C \frac{\beta_t(z)}{z - z_k}dz \quad \text{for} \quad k = 1, \ldots, N. \tag{3.14}$$

At each time-step, after the first integral equation (3.10) has been solved to find $\beta(z)$ round the whole boundary and $\beta(z)$ has been differentiated on the free-surface to obtain the velocity on the free-surface, it is then possible to find ϕ_t on the free-surface from the Eulerian form of the dynamic boundary condition on the free-surface

$$\frac{\partial \phi}{\partial t} = -\frac{1}{2} w\overline{w} - y. \tag{3.15}$$

In addition, ψ_t can be found on the rest of the boundary from the following equation (see [56])

$$\begin{aligned} \psi_t(x,y;t) = (y-Y)a_X - (x-X)a_Y - \frac{1}{2}\ddot{\theta}r^2 + Uv - Vu \\ + ((U-u)(x-X) + (V-v)(y-Y))\dot{\theta}, \end{aligned} \tag{3.16}$$

where (X,Y), (U,V) and (a_X, a_Y) are respectively the position, velocity and acceleration of the centre of gravity or axis of rotation of the body. Also, $\dot{\theta}$ & $\ddot{\theta}$ are the angular velocity & angular acceleration of the body in the anti-clockwise sense, $r = \sqrt{(x-X)^2 + (y-Y)^2}$ and (u,v) is the fluid velocity at (x,y).

The next step is to discretise equation (3.14). Again, cubics are used to approximate the variation of $\beta_t(z)$ between nodes in exactly the same way as was done for $\beta(z)$. This results in the following discretised version of equation (3.14)

$$\sum_{j=1}^{N} \Gamma_{k,j}(\beta_t)_j = 0 \quad \text{for } k = 1, \ldots, N, \tag{3.17}$$

where the influence functions $\Gamma_{k,j}$ are the same as in equation (3.12) and $(\beta_t)_j$ is an approximation to $\beta_t(z_j)$. If the method of Lin *et al.* [37] is used at corners between the free-surface and a body, so that ϕ_t and ψ_t are both considered prescribed here, then the above equation leads to a matrix equation for the unknown part of β_t at each z_k which has the same coefficient matrix as equation (3.13) but a different right hand side vector.

This matrix equation is then solved using Gaussian elimination to obtain $\beta_t(z)$ all round the boundary. Again, the reason for using Gaussian elimination as opposed to an iterative method will be discussed later.

Once $\beta_t(z)$ has been found round the boundary it is numerically differentiated on the free-surface to obtain $w_t(z)$ on the free-surface. This is possible because

$$\frac{\partial w}{\partial t} = \frac{\partial}{\partial t}\left(\frac{d\beta}{dz}\right) = \frac{d}{dz}\left(\frac{\partial \beta}{\partial t}\right).$$

The above numerical differentiation is performed using the same five-point numerical differentiation scheme as that described in Appendix D. Furthermore, this numerical differentiation scheme is also used to find $\frac{dw}{dz}(z)$ on the free-surface from $w(z)$ on the free-surface.

At this point there is now sufficient information to calculate the acceleration of each one of the free-surface nodes. This acceleration is given by the formula

$$a_x - ia_y = \frac{Dw}{Dt} = \frac{\partial w}{\partial t} + \overline{w}\frac{dw}{dz}, \tag{3.18}$$

where a_x & a_y are respectively the horizontal & vertical components of acceleration (in this case the subscripts x & y do not mean partial differentiation w.r.t. x & y respectively).

Unfortunately, the above "acceleration equation" is not the same as the one given by Vinje & Brevig (see [55], [56] & [57]). In their equation they take the complex conjugate of $\frac{dw}{dz}$ rather than the complex conjugate of w. Appendix E shows why equation (3.18) is the correct version of the acceleration equation to take.

The final quantity that needs to be calculated is the second material time derivative of the velocity potential ϕ on the free-surface. This is achieved by

taking the material time derivative of equation (3.9) as follows

$$\begin{aligned}\frac{D^2\phi}{Dt^2} &= \frac{1}{2}\left(\overline{w}\,\frac{Dw}{Dt} + w\frac{D\overline{w}}{Dt}\right) - v \\ &= \mathrm{Re}\left(\overline{w}\,\frac{Dw}{Dt}\right) - v. \end{aligned} \tag{3.19}$$

With this information it is then possible to use second-order truncated Taylor series to time-step forward the position and velocity potential of the free-surface nodes. That is, if z_i is the complex position and ϕ_i is the velocity potential of the i^{th} free-surface node then

$$z_i(t+\Delta t) = z_i(t) + \Delta t\,\overline{w}_i(t) + \frac{(\Delta t)^2}{2}\,\overline{\frac{Dw_i}{Dt}}(t) \tag{3.20}$$

and

$$\phi_i(t+\Delta t) = \phi_i(t) + \Delta t\frac{D\phi_i}{Dt}(t) + \frac{(\Delta t)^2}{2}\frac{D^2\phi_i}{Dt^2}(t), \tag{3.21}$$

where the time-step is from time t to time $t+\Delta t$.

The Matrix Equation Solver

As was stated earlier LU decomposition (Gaussian elimination) is used in this study to solve both the matrix equation for the unknown part of $\beta(z)$ at each z_k, as well as the matrix equation for the unknown part of $\beta_t(z)$ at each z_k. There are several reasons why this direct method was chosen as opposed to an iterative method. These reasons come from the review paper by Greenhow [23].

Firstly, the computation time is dominated by the time taken to set up the coefficient matrix A and so the time taken to solve these matrix equations is not too important.

Secondly, the matrix equation for the unknown part of $\beta_t(z)$ at each z_k has the same coefficient matrix A as the matrix equation for the unknown part of $\beta(z)$ at each z_k. Therefore, if LU decomposition is used to solve the latter matrix

equation (which is solved first) then the former matrix equation can be solved with little extra computational effort.

Finally, for an iterative scheme an excellent initial guess is given by the solution at the previous time-step. However, this is not the case when a body is present and it also becomes awkward to apply when regridding is being used or when the number of nodes is changing with time, or both (see subsection 3.5.3).

Having said all this, there is a problem with the large rounding errors that are associated with standard LU decomposition. This problem is easily overcome by simply adding partial pivoting and iterative refinement to the basic Gaussian elimination technique.

The Time-Stepping of the Rigid Boundaries

On rigid boundaries which move, nodes are time-stepped forwards to lie on the new position of their respective boundaries. Also, in this study, if the length of a rigid boundary between corners changes, for example the bottom of a wavetank with a piston wavemaker or a vertical wall reflecting a wave, then the relative node spacing on that side is kept constant so that the number of nodes on that side is constant.

There is a problem with nodes that lie at the intersection between the free-surface and a body. The problem is that the position of these nodes is updated according to equation (3.20) but that this updated position probably will not lie on the new position of the body. This problem and other free-surface/body intersection problems will be discussed in the following subsection.

3.5.2 Free-Surface/Body Intersection Points

This subsection describes how free-surface/body intersection points are treated in the present Boundary-Integral Method.

Suppose for example that the wavetank with the paddle wavemaker in figure 3.1 is being modelled. Furthermore, suppose that time-stepping has just taken place from a time t to a time $t + \Delta t$, so that the next logical step is to solve Laplace's equation for ϕ (2.5) in the fluid domain at time $t + \Delta t$. However, before this can be done there are several procedures that need to be carried out on the nodes which lie at the free-surface/body intersection points. Consider for example the node z_{N_1} which lies at the intersection between the free-surface and the paddle wavemaker (other types of free-surface/body intersection points are treated in a very similar way).

Firstly, as mentioned at the end of the last subsection, after time-stepping this node will not in general lie on the new position of the wavemaker. This problem is overcome by using exactly the same method as that used by Otta *et al.* [40] (see page 37). That is, z_{N_1} is simply projected perpendicularly back onto the paddle. Note, this projection would be unnecessary if the smoothing & regridding procedure (described in the next subsection) had been used after the time-step from t to $t + \Delta t$.

The second procedure that needs to be applied to the node z_{N_1} relates to the possibility that $\beta(z)$, or $\beta_t(z)$, or both, are singular at this intersection point (see subsection 2.3.2). If the exact mathematical solution does have a singularity here then this procedure smoothes it out. If, on the other hand, the exact mathematical solution is perfectly regular here then this procedure ensures that numerical inaccuracies do not suggest the existence of a singularity.

Consider first $\beta(z)$. If $\beta(z)$ is analytic at z_{N_1} then the following two Cauchy-Riemann equations are satisfied at z_{N_1}

$$\phi_x = \psi_y \tag{3.22}$$

$$\& \qquad \phi_y = -\psi_x. \tag{3.23}$$

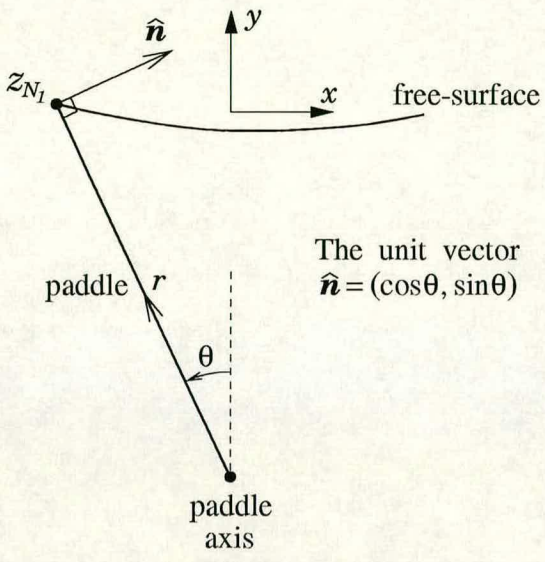

Figure 3.3: The coordinate r along the paddle and the coordinate n normal to the paddle.

These two equations are equivalent to the following two equations

$$\phi_n = \psi_r \tag{3.24}$$

$$\& \qquad \phi_r = -\psi_n, \tag{3.25}$$

where r is the radial coordinate measured from the paddle axis up the paddle and n is the coordinate normal to the paddle measured in the sense of decreasing θ (see figure 3.3).

Now, from equation (3.3), the stream function on the paddle is given by

$$\psi = -\frac{1}{2} r^2 \dot{\theta} \tag{3.26}$$

and therefore equation (3.24) becomes

$$\begin{aligned} & \phi_n = -r\dot{\theta} \\ \Leftrightarrow \quad & \hat{\boldsymbol{n}}.\nabla\phi = -r\dot{\theta} \\ \Leftrightarrow \quad & \phi_x \cos\theta + \phi_y \sin\theta = -r\dot{\theta} \\ \Leftrightarrow \quad & \mathrm{Re}\left(\frac{d\beta}{dz}\right)\cos\theta - \mathrm{Im}\left(\frac{d\beta}{dz}\right)\sin\theta = -r\dot{\theta}. \end{aligned} \tag{3.27}$$

To Recap, if $\beta(z)$ is analytic at z_{N_1} then this last equation must be satisfied there. Consequently, in the present BIM, equation (3.27), or more correctly its discretised version, is forced to hold. The way equation (3.27) is discretised is as follows.

From Appendix D the derivative $d\beta/dz$ at z_{N_1} is approximated by the following five-point numerical differentiation scheme

$$\frac{d\beta}{dz}(z_{N_1}) \approx c_1\beta_{N_1-4} + c_2\beta_{N_1-3} + c_3\beta_{N_1-2} + c_4\beta_{N_1-1} + c_5\beta_{N_1}, \tag{3.28}$$

where $c_1, \ldots, c_5$ are known coefficients depending only on $z_{N_1-4}, \ldots, z_{N_1}$. Furthermore, each $c_j\beta_k$ term in equation (3.28) can be split into its real and imaginary parts as follows

$$\begin{aligned} c_j\beta_k &= \big(\mathrm{Re}(c_j) + i\mathrm{Im}(c_j)\big)(\phi_k + i\psi_k) \\ &= \mathrm{Re}(c_j)\phi_k - \mathrm{Im}(c_j)\psi_k + i\big(\mathrm{Re}(c_j)\psi_k + \mathrm{Im}(c_j)\phi_k\big). \end{aligned} \tag{3.29}$$

Therefore, by using equations (3.28) & (3.29) together, the discretised version of equation (3.27) is

$$\begin{aligned} &\Big(\mathrm{Re}(c_1)\phi_{N_1-4} - \mathrm{Im}(c_1)\psi_{N_1-4} + \mathrm{Re}(c_2)\phi_{N_1-3} - \mathrm{Im}(c_2)\psi_{N_1-3} \\ &\quad + \cdots + \mathrm{Re}(c_5)\phi_{N_1} - \mathrm{Im}(c_5)\psi_{N_1}\Big)\cos\theta \\ -&\Big(\mathrm{Re}(c_1)\psi_{N_1-4} + \mathrm{Im}(c_1)\phi_{N_1-4} + \mathrm{Re}(c_2)\psi_{N_1-3} + \mathrm{Im}(c_2)\phi_{N_1-3} \\ &\quad + \cdots + \mathrm{Re}(c_5)\psi_{N_1} + \mathrm{Im}(c_5)\phi_{N_1}\Big)\sin\theta \\ &\qquad\qquad = -r\dot{\theta}. \end{aligned} \tag{3.30}$$

Now, if the corner treatment method of Lin *et al.* [37] is used (see page 33), then prior to the solution of Laplace's equation at time $t + \Delta t$ the unknowns in equation (3.30) are ψ_{N_1-4}, ψ_{N_1-3}, ψ_{N_1-2} & ψ_{N_1-1} and the knowns are ϕ_{N_1-4}, ϕ_{N_1-3}, ϕ_{N_1-2}, ϕ_{N_1-1}, ϕ_{N_1} & ψ_{N_1}. However, when compared to all the equations in the linear system $A\boldsymbol{x} = \boldsymbol{b}$ (see page 56), equation (3.30) represents an extra

equation that needs to be satisfied and as a result an extra unknown is required. In the present BIM this extra unknown is ϕ_{N_1} and its value is altered so that equation (3.30) is satisfied. That is, equation (3.30) now becomes row N_1 of the above linear system, in place of the row dropped by Lin *et al.*'s method (see page 56). With this in mind equation (3.30) is rewritten with the unknowns on the LHS and the knowns on the RHS as follows

$$\begin{aligned}
&-\Big(\mathrm{Im}(c_1)\cos\theta+\mathrm{Re}(c_1)\sin\theta\Big)\psi_{N_1-4}-\Big(\mathrm{Im}(c_2)\cos\theta+\mathrm{Re}(c_2)\sin\theta\Big)\psi_{N_1-3}\\
&-\Big(\mathrm{Im}(c_3)\cos\theta+\mathrm{Re}(c_3)\sin\theta\Big)\psi_{N_1-2}-\Big(\mathrm{Im}(c_4)\cos\theta+\mathrm{Re}(c_4)\sin\theta\Big)\psi_{N_1-1}\\
&+\Big(\mathrm{Re}(c_5)\cos\theta-\mathrm{Im}(c_5)\sin\theta\Big)\phi_{N_1}\\
&=-\Big(\mathrm{Re}(c_1)\cos\theta-\mathrm{Im}(c_1)\sin\theta\Big)\phi_{N_1-4}-\Big(\mathrm{Re}(c_2)\cos\theta-\mathrm{Im}(c_2)\sin\theta\Big)\phi_{N_1-3}\\
&\quad-\Big(\mathrm{Re}(c_3)\cos\theta-\mathrm{Im}(c_3)\sin\theta\Big)\phi_{N_1-2}-\Big(\mathrm{Re}(c_4)\cos\theta-\mathrm{Im}(c_4)\sin\theta\Big)\phi_{N_1-1}\\
&\quad+\Big(\mathrm{Im}(c_5)\cos\theta+\mathrm{Re}(c_5)\sin\theta\Big)\psi_{N_1}-r\dot{\theta}.
\end{aligned}\tag{3.31}$$

Bearing in mind that this above procedure only applies to corners between a body and the free-surface it is called, for brevity, "corner-correction". Furthermore, this "corner-correction" procedure is very similar to the "BC-correction" procedure of Otta *et al.* [40] (see page 38), and in fact equations (3.27) & (2.39) are equivalent.

Having said all this, the "corner-correction" procedure is not always used. As explained on page 57 the coefficient matrix A of the linear system $A\boldsymbol{x}=\boldsymbol{b}$ is diagonally dominant. Consequently, "corner-correction" is only used if, when equation (3.31) is added to this linear system, the new coefficient matrix A is still diagonally dominant. This is a similar condition to the condition that the "BC-correction" procedure of Otta *et al.* is only used for small $|\alpha|$ (see page 38). If "corner-correction" is not used then the present BIM just simply reverts back to using Lin *et al.*'s corner treatment method instead.

As alluded to earlier this "corner-correction" procedure also applies to the function $\beta_t(z)$. Fortunately, the details of how it applies to $\beta_t(z)$ are very similar to the details of how it applies to $\beta(z)$, and so an in-depth description of "corner-correction" for $\beta_t(z)$ is unnecessary. However, having said that, the calculation of one of the terms in one of the equations in the analysis for $\beta_t(z)$ does not follow directly from the analysis for $\beta(z)$. The equation in question is

$$\phi_{tn} = \psi_{tr} \tag{3.32}$$

and the term is the ψ_{tr} term. This equation is equivalent to equation (3.24) in the analysis for $\beta(z)$, and its RHS is calculated as follows.

From equation (3.16) the partial time derivative of the stream function on the paddle is given by

$$\psi_t = -\frac{1}{2}r^2\ddot{\theta} + r\dot{\theta}(u\sin\theta - v\cos\theta), \tag{3.33}$$

where (u, v) is the fluid velocity. Thus

$$\begin{aligned}
\psi_{tr} &= -r\ddot{\theta} + \dot{\theta}\big(u\sin\theta - v\cos\theta + r(u_r\sin\theta - v_r\cos\theta)\big) \\
&= -r\ddot{\theta} + \dot{\theta}\Big(u\sin\theta - v\cos\theta + r\big((u_y\cos\theta - u_x\sin\theta)\sin\theta \\
&\qquad\qquad + (v_x\sin\theta - v_y\cos\theta)\cos\theta\big)\Big) \\
&= -r\ddot{\theta} + \dot{\theta}\Big(u\sin\theta - v\cos\theta + r\big((v_x\cos\theta - u_x\sin\theta)\sin\theta \\
&\qquad\qquad + (v_x\sin\theta + u_x\cos\theta)\cos\theta\big)\Big),
\end{aligned} \tag{3.34}$$

where the following three facts have been used:

1. From figure 3.3

$$\frac{\partial}{\partial r} = \frac{\partial x}{\partial r}\frac{\partial}{\partial x} + \frac{\partial y}{\partial r}\frac{\partial}{\partial y} = -\sin\theta\frac{\partial}{\partial x} + \cos\theta\frac{\partial}{\partial y}.$$

2. Since the flow is irrotational

$$u_y = v_x.$$

3. Since the flow is incompressible

$$v_y = -u_x.$$

As a result it can be seen that ψ_{tr} is completely prescribed because the linear system to find $\beta_t(z)$ round the whole boundary is solved *after* the linear system to find $\beta(z)$ round the whole boundary. Therefore, the quantities u, v, u_x & v_x in equation (3.34) are known from repeated numerical differentiation of $\beta(z)$ (see Appendix D), together with the equations

$$u - iv = w = \frac{d\beta}{dz}$$

$$\& \qquad u_x - iv_x = \frac{dw}{dz} = \frac{d^2\beta}{dz^2}.$$

Final Remarks about Free-Surface/Body Intersection Points

In summary, this subsection described two procedures which apply to the free-surface/body intersection points.

In the first procedure the nodes which lie at these intersection points are projected back on to their respective bodies after time-stepping.

In the second procedure, called "corner-correction", the complex potential $\beta(z)$ and its partial time derivative $\beta_t(z)$ are forced to be analytic at these intersection points. This is achieved by correcting the values of ϕ and ϕ_t at these points so that the Cauchy-Riemann equations for $\beta(z)$ and $\beta_t(z)$ respectively are not violated here.

3.5.3 Smoothing & Regridding

As mentioned in subsection 2.3.1 some sort of numerical filtering of the high-wavenumber modes is necessary in order to remove free-surface instabilities. In this study the smoothing & regridding procedure of Tsai & Yue [53] (which was

also briefly described in section 2.3.1) is adopted. The author feels that of all the methods developed so far, to control free-surface instabilities, this one is the most promising. This is because of its variable smoothing and adaptive regridding.

However, there is a problem, in Tsai & Yue's paper very few details of their procedure are given. As a result the procedure used here had to be developed virtually from scratch. During this development several features of the present problem were exploited in order to try and make the present smoothing & regridding algorithm as efficient as possible.

A desirable effect of time-stepping is that free-surface nodes tend to gather together in regions of high curvature, where the free-surface and velocity potential on it are varying rapidly. In addition, free-surface nodes also tend to spread out in regions of low curvature, where the free-surface and the velocity potential on it are varying slowly. This gives better resolution of these quantities in precisely the regions where they need to be resolved well and does not waste resolution in regions where they do not need to be resolved well. Unfortunately however, if the node spacing becomes too small then a local Courant type stability condition is violated and the free-surface becomes unstable (see page 29).

What Tsai & Yue's smoothing & regridding procedure does is to firstly smooth the free-surface to some user-defined degree. Then the free-surface nodes are redistributed along this smoothed free-surface so that more nodes are placed in regions of high curvature and less nodes are placed in regions of low curvature, subject to a minimum point spacing $h_{\min}$ (to preserve stability) and a maximum point spacing $h_{\max}$ (to ensure a minimum *a priori* accuracy).

The details of the smoothing & regridding procedure developed here from the method of Tsai & Yue are as follows.

Smoothing & regridding is performed after time-stepping, usually every few

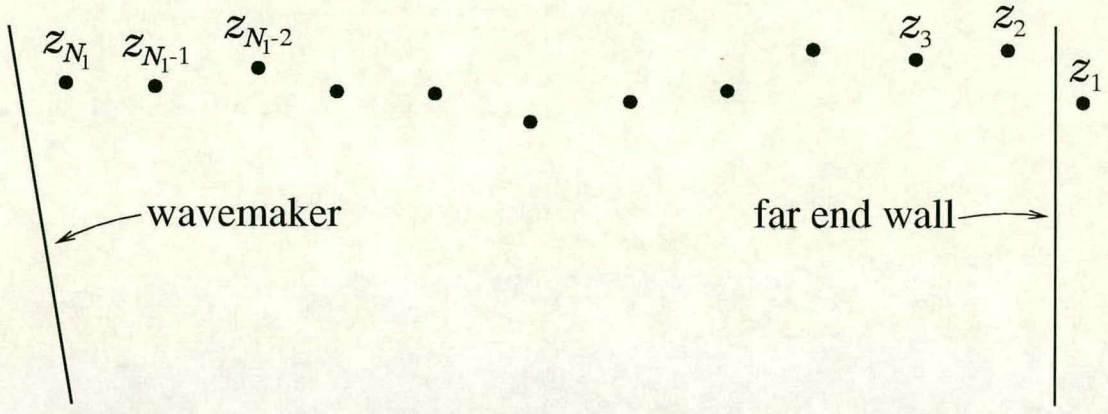

Figure 3.4: N_1 free-surface nodes after time-stepping.

time-steps. Suppose for example that a wavetank with a paddle wavemaker is being modelled, and N_1 free-surface nodes have just been time-stepped forwards ready for smoothing & regridding, as shown in figure 3.4. Due to numerical inaccuracies node z_1 will not lie exactly on the far end wall and node z_{N_1} will not lie exactly on the wavemaker. In figure 3.4 these errors are greatly exaggerated for clarity.

The first step of smoothing & regridding is the smoothing procedure.

The Smoothing Procedure

The free-surface and the velocity potential on it are smoothed using cubic smoothing splines (see de Boor [12]), which are not calculated in the least squares sense as claimed by Tsai & Yue.

Unfortunately, normal description of these cubic splines in terms of Cartesian coordinates is not valid because of the possibility that the free-surface may become multi-valued due to overturning. However, a parameter which does have monotonic behaviour along the free-surface is the arclength s, or equivalently a parameter τ which equals the node index at each node. That is, if τ takes the

value τ_i at node i then

$$\tau_i = i \quad \text{for} \quad i = 1, \ldots, N_1. \tag{3.35}$$

It is now possible to calculate these smooth curves. They are obtained by minimising, for a given $\lambda \in (0,1)$, the functional

$$F(S) = \lambda \sum_{i=1}^{N_1} \big(f_i - S(\tau_i)\big)^2 + (1-\lambda) \int_{\tau_1}^{\tau_{N_1}} \big(S''(\tau)\big)^2 d\tau, \tag{3.36}$$

over all functions $S(\tau)$ with two derivatives.

It turns out that the function $S(\tau)$ which does minimise equation (3.36) is indeed a cubic spline with simple knots at $\tau_2, \ldots, \tau_{N_1-1}$ and satisfying the "natural" end conditions

$$S''(\tau_1) = S''(\tau_{N_1}) = 0. \tag{3.37}$$

The data values $f_1, \ldots, f_{N_1}$ in equation (3.36) can either take the values of $x_1, \ldots, x_{N_1}$ or $y_1, \ldots, y_{N_1}$ or $\phi_1, \ldots, \phi_{N_1}$. That is, $f_1, \ldots, f_{N_1}$ can either take the values of the x coordinates, the y coordinates or the velocity potentials of the free-surface nodes. This results in three cubic smoothing splines $S_x(\tau)$, $S_y(\tau)$ & $S_\phi(\tau)$ for the x coordinate, y coordinate and velocity potential on the free-surface, respectively.

The parameter λ in equation (3.36) is the smoothing parameter and it measures the compromise between smoothing (λ closer to 0) and interpolating the data (λ closer to 1). In the work by de Boor this smoothing parameter is called p. Furthermore, the smoothing parameter λ used by Tsai & Yue is defined differently from the one used here.

Details of how these cubic smoothing splines are calculated can be found in Appendix F. The algorithm described in this appendix is made very efficient by exploiting the implications of equation (3.35) as well as the fact that matrices

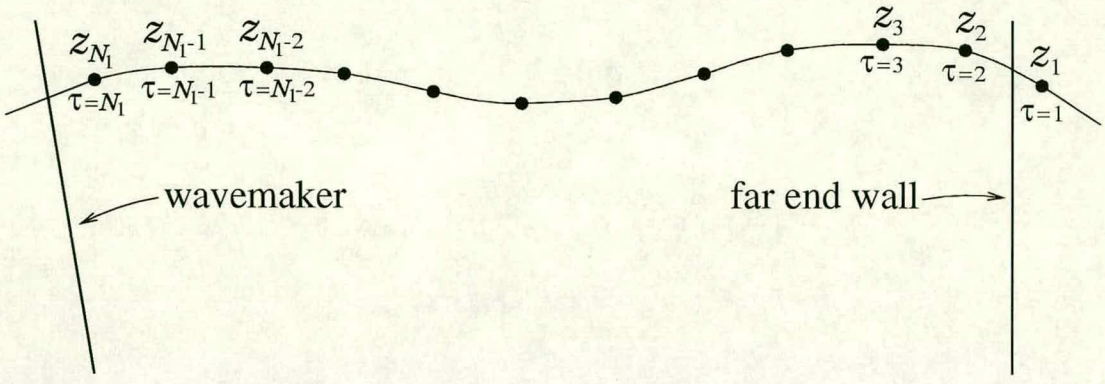

Figure 3.5: The smoothed free-surface with N_1 new free-surface nodes.

used in this algorithm have a similar structure from one smoothing & regridding to the next.

Once the free-surface has been smoothed there is a new set of N_1 free-surface nodes $(z_1, \ldots, z_{N_1})$ which lie on this smoothed free-surface (see figure 3.5).

Again, z_1 will not lie exactly on the far end wall and z_{N_1} will not lie exactly on the wavemaker. For z_{N_1} this problem is overcome by simply moving it along the smoothed free-surface until it meets the wavemaker[1], as shown in figure 3.6. In order to achieve this Newton-Raphson iteration is applied to the equation

$$d_{N_1}(\tau) = 0,$$

with a view to finding the root $\tau = \tau_{\text{wavemaker}}$. A similar method is then used to move z_1 along the smoothed free-surface to the intersection with the far end wall, where $\tau = \tau_{\text{end}}$.

To sum up, the free-surface has now been smoothed and there are N_1 nodes $(z_1, \ldots, z_{N_1})$ lying on it, with z_1 at the intersection with the far end wall and z_{N_1} at the intersection with the wavemaker. Therefore, the free-surface is now ready for regridding.

[1]**Extrapolation**: Note that, in this study, the cubic smoothing splines are assumed to be linear outside the range $1 \leq \tau \leq N_1$. An alternative would have been to extend the cubics that are defined between $\tau = 1$ & $\tau = 2$ and between $\tau = N_1 - 1$ & $\tau = N_1$.

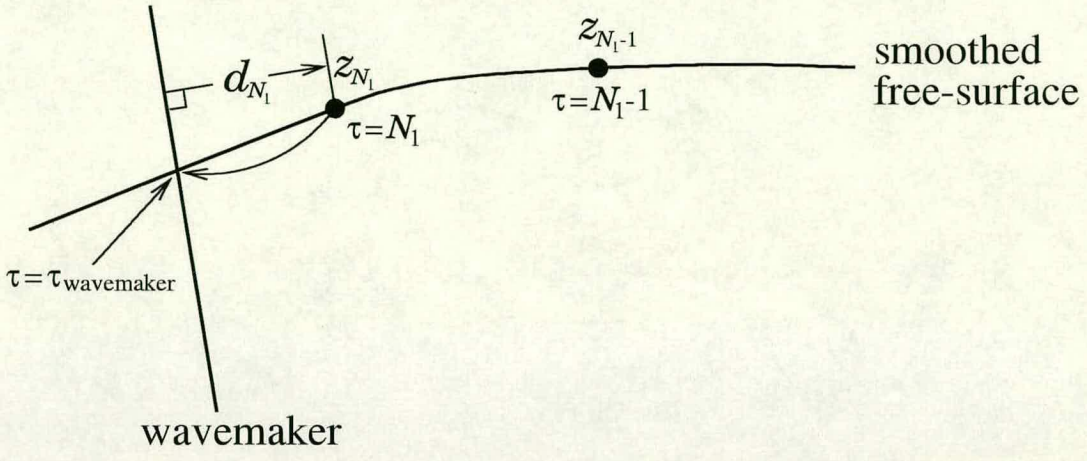

Figure 3.6: Moving the node z_{N_1} along the smoothed free-surface to the intersection with the wavemaker.

The Adaptive Regridding Procedure

Briefly the adaptive regridding procedure can be described as follows. Firstly, the unsigned curvature of the free-surface is found and integrated right along the free-surface. The result is then divided up into equal increments and the regridded nodes (mesh points) placed in such a way that the integral of the unsigned curvature between them is equal to this increment. Thus in regions of high curvature there will be a high density of nodes and in regions of low curvature there will be a low density of nodes. The algorithm used to do this is the *inverse interpolation method* (see Hyman & Naughton [31]), which works by trying to *equidistribute* the unsigned curvature between adjacent nodes along the free-surface. However, there is a problem; the algorithm has to be slightly modified because of the need to impose constraints $h_{\min}$ & $h_{\max}$ on the size of the node spacing.

In the details of this algorithm given below it can be seen that only low order numerical schemes are used, for example the trapezoidal rule for numerical integration and linear interpolation for approximating functions between data

points. This is because:

1. There is no point using higher order schemes to equidistribute the curvature well if this equidistribution is then destroyed by imposing constraints on the node spacing.

2. The curvature of the free-surface is only an indicator of how rapidly varying the velocity potential is on the free-surface and so equidistributing it will not result in the most optimal mesh. In fact the most optimal mesh is virtually unobtainable and it is not the purpose of the wider scheme.

3. Higher order schemes are computationally expensive and would slow down the algorithm.

Consequently, this algorithm will result in a suboptimal mesh. However, this mesh will be less likely to cause instabilities when compared to the mesh that has not been regridded. Furthermore, this mesh will significantly improve the accuracy and efficiency of the numerical scheme as a whole when compared to an equally spaced mesh with the same number of mesh points.

The details of the regridding algorithm are as follows.

Let s be the arclength along the free-surface measured from z_1 on the far end wall, where $s = s_1 = 0$. Also, let $\kappa(s)$ be the unsigned curvature of the free-surface at arclength s. That is

$$\kappa(s) = \kappa(\tau) = \left| \frac{x'(\tau)y''(\tau) - x''(\tau)y'(\tau)}{\left((x'(\tau))^2 + (y'(\tau))^2\right)^{\frac{3}{2}}} \right|, \tag{3.38}$$

where τ is the value of the node index parameter at arclength s. This unsigned curvature $\kappa(s)$ is then integrated along the free-surface to form

$$I(s) = \int_{s_1=0}^{s} \kappa(t)dt, \tag{3.39}$$

where t is a dummy variable of integration representing the arclength.

At a node z_i the arclength s can be approximated by s_i, the length of the piecewise linear curve from z_1 to z_i, which is made up of the line segments connecting adjacent z_j's. Thus

$$s_i = h_1 + \ldots + h_{i-1},$$

where $h_j = |z_{j+1} - z_j|$.

Using the above approximation, together with the trapezoidal rule, I at z_i can be approximated by

$$\begin{aligned} I_i &= \sum_{j=1}^{i-1} \frac{(\kappa_{j+1} + \kappa_j)}{2}(s_{j+1} - s_j) \\ &= \sum_{j=1}^{i-1} \frac{(\kappa_{j+1} + \kappa_j)}{2} h_j, \end{aligned} \tag{3.40}$$

where κ_j is the unsigned curvature at node z_j. In addition, between nodes I is approximated by linear interpolation. Therefore, I is approximated by

$$I_i + \frac{(\kappa_{i+1} + \kappa_i)}{2}(s - s_i) \quad \text{for} \quad s_i \leq s < s_{i+1}, \tag{3.41}$$

where s now measures the arclength along the piecewise linear curve.

Now suppose $N_{1_{\text{desired}}}$ is the desired number of nodes on the regridded free-surface, then the incremental increase in I between the regridded nodes is

$$I_{\text{step}} = I_{N_1}/(N_{1_{\text{desired}}} - 1). \tag{3.42}$$

Finally then regridding can be carried out by inverse interpolation of $I(s)$. That is, for $k = 1, \ldots, N_{1_{\text{desired}}}$

$$I(\tilde{s}_k) = (k-1)I_{\text{step}} \tag{3.43}$$

or

$$\begin{gathered} \tilde{s}_k = I^{-1}\big((k-1)I_{\text{step}}\big) = s_i + \frac{2\big((k-1)I_{\text{step}} - I_i\big)}{\kappa_{i+1} + \kappa_i} \\ \text{where} \quad I_i \leq (k-1)I_{\text{step}} < I_{i+1}. \end{gathered} \tag{3.44}$$

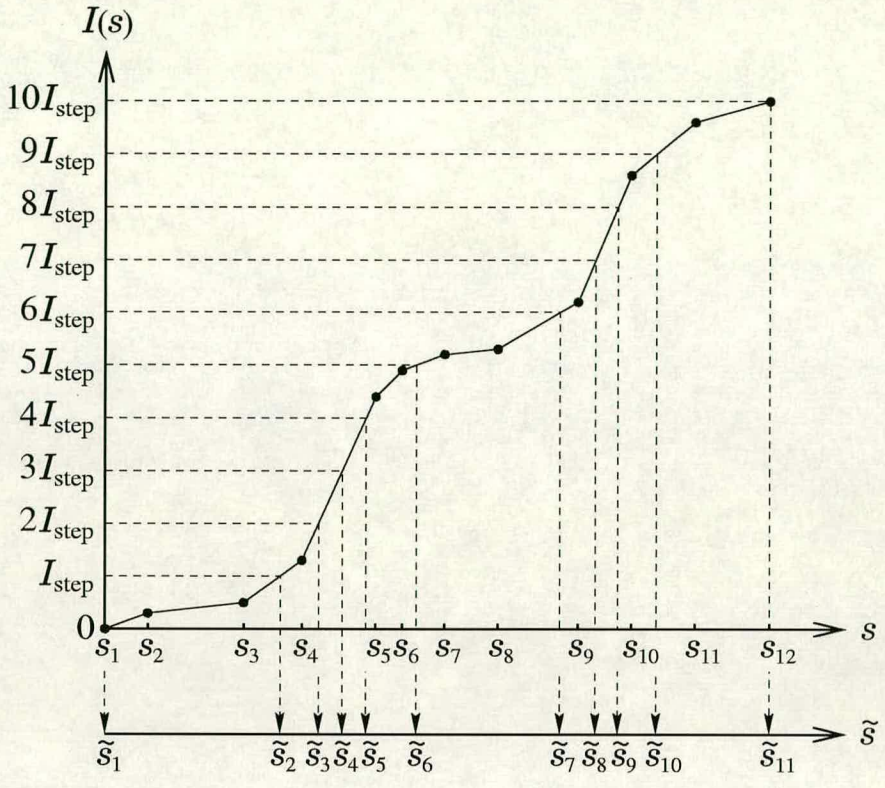

Figure 3.7: Inverse interpolation of $I(s)$ to generate an equidistributing mesh $\{\tilde{s}_k\}$ with $N_1 = 12$ & $N_{1_{\text{desired}}} = 11$.

In the above equations the tilde ~ indicates regridded mesh values. This procedure is also illustrated graphically in figure 3.7.

Once each $\tilde{s}_k$ has been found a corresponding $\tilde{\tau}_k$ can be calculated via linear interpolation

$$\tilde{\tau}_k = \tau_i + \frac{(\tilde{s}_k - s_i)}{h_i}(\tau_{i+1} - \tau_i) \quad \text{for} \quad s_i \leq \tilde{s}_k < s_{i+1}, \tag{3.45}$$

where τ_i is the value of the parameter τ at node z_i. In general, as shown before, $\tau_i = i$, except $\tau_1 = \tau_{\text{end}}$ and $\tau_{N_1} = \tau_{\text{wavemaker}}$. Since the smoothed free-surface and the velocity potential on it are both known explicitly as functions of τ it is then possible to obtain the regridded node $\tilde{z}_k$ and its velocity potential $\widetilde{\phi}_k$.

As mentioned earlier the above algorithm has to be adapted because of the need to impose constraints $h_{\min}$ & $h_{\max}$ on the node spacing. This adapted

algorithm is described in Appendix G. One consequence of these alterations is that in general the actual number of nodes on the regridded free-surface $\widetilde{N}_1$ will not equal the desired number of nodes on the regridded free-surface $N_{1_{\text{desired}}}$.

3.5.4 Dynamic Time-Stepping

In this subsection the Dynamic Time-Stepping procedure developed for use in the present Boundary-Integral Method is described.

As mentioned on page 25 an advantage of explicit time-stepping is that the time-step Δt is free to be varied from one time-step to another. In fact, because of the second-order explicit time-stepping used here (see subsection 3.5.1 and more particularly equation (3.20)), there is an additional advantage. This advantage is that for each free-surface node and each coordinate direction the time-step required to move a certain distance in that direction can be easily calculated. With this in mind the details of the present dynamic time-stepping procedure are as follows.

Firstly, before a simulation can be started the user must select values for various quantities. These quantities are as follows:

1. The output times at which results (for example the free-surface profile) are required.

2. The maximum time-step $(\Delta t)_{\text{max}}$.

3. The maximum distance, say L, that a free-surface node can move in either coordinate direction at each time-step.

Next, suppose that the simulation has reached a time t and the velocity and acceleration of the free-surface nodes have just been calculated, so that everything is ready for time-stepping. Then, for each free-surface node and each coordinate

direction the time-step necessary to move a distance L in that direction is calculated. Appendix H gives details of how this is done. Once all of these time-steps have been calculated their minimum is found and stored in $(\Delta t)_{\text{dynamic}}$. Finally, the actual time-step used is the minimum of this time-step, the maximum time-step $(\Delta t)_{\text{max}}$ and the time to the next outputting, say $(\Delta t)_{\text{output}}$. That is

$$\Delta t = \min\{\, (\Delta t)_{\text{dynamic}}, (\Delta t)_{\text{max}}, (\Delta t)_{\text{output}} \,\}. \tag{3.46}$$

As a result of this no free-surface node will move more[2] than a distance L in either of the coordinate directions in a time-step. Consequently, if the fluid motion is gentle then the time-step will be large and if the fluid motion is vigorous then the time-step will be small.

In conclusion, note that just as the adaptive regridding of the previous subsection corresponds to a spatial rediscretisation of the present problem so the dynamic time-stepping of this subsection corresponds to a temporal rediscretisation of the present problem.

3.5.5 Volume & Energy Conservation

In addition to testing the accuracy of the present Boundary-Integral Method against analytical solutions or experimental results it is also necessary to check volume and energy conservation. In this study great care is taken to ensure that these checks are done very accurately by using high-order numerical differentiation and numerical integration routines. Unfortunately, this strive for accuracy does come at the expense of the time taken to do these checks. However, having said that, the volume and energy checks still run in a reasonable time and do not add significantly to the length of a time-step.

[2]Note that if $\Delta t = (\Delta t)_{\text{dynamic}}$ in equation (3.46) then at least one of the free-surface nodes will move *exactly* a distance L in one of the coordinate directions in that time-step.

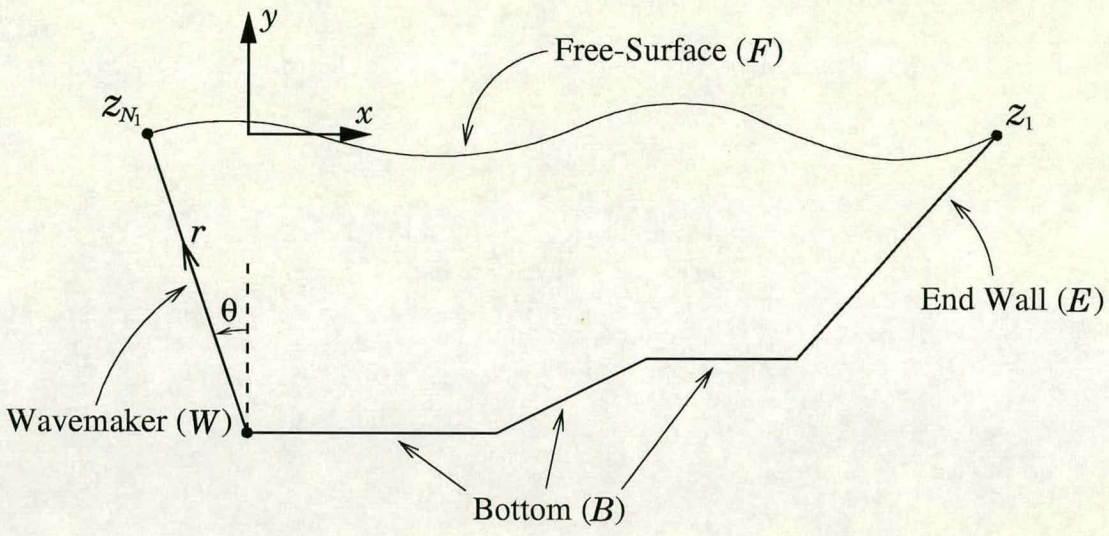

Figure 3.8: A Wavetank with a paddle wavemaker.

As an example of how the volume and energy checks are applied consider the wavetank with the paddle wavemaker shown in figure 3.8. In this study the wavemaker (W) and the end wall (E) are considered to be straight lines while the bottom (B) is considered to consist of straight lines.

Volume Conservation

The volume[3] of a region is given by the following formula

$$\text{Volume} = \frac{1}{2}\oint_C x\,dy - y\,dx, \tag{3.47}$$

where C is the boundary of the region and integration is in the anticlockwise sense round the region. The fact that the above integral does give the volume of the region can be verified by simply applying Green's theorem in the plane.

In order to evaluate the above integral for the wavetank in figure 3.8 first consider the integration along the free-surface. In that case

$$\frac{1}{2}\int_F x\,dy - y\,dx = \frac{1}{2}\int_1^{N_1}\left(x\frac{dy}{d\tau} - y\frac{dx}{d\tau}\right)d\tau, \tag{3.48}$$

[3]In fact this is volume per unit tank width, *i.e.* area.

where τ is a parameter parameterising the free-surface and taking the value of the node index at each node. The integral on the RHS of equation (3.48) can then be approximated by performing the following two steps.

Step 1 Fit end-derivative cubic splines to the data

$$(\tau_i, x_i) \quad \text{for} \quad i = 1, \ldots, N_1$$

$$i.e. \quad (i, x_i) \quad \text{for} \quad i = 1, \ldots, N_1$$

and to the data

$$(\tau_i, y_i) \quad \text{for} \quad i = 1, \ldots, N_1$$

$$i.e. \quad (i, y_i) \quad \text{for} \quad i = 1, \ldots, N_1,$$

and differentiate these cubic splines in order to obtain approximations to $dx/d\tau$ and $dy/d\tau$.

Step 2 Fit an end-derivative cubic spline to the integrand of the integral on the RHS of equation (3.48) and integrate this cubic spline to obtain an approximation to the integral.

In both steps 1 & 2 the end-derivatives are calculated by using a five-point numerical differentiation scheme similar to that in appendix D, although now the dependent & independent variables are real instead of complex.

The next step is to integrate the integrand of the integral on the RHS of equation (3.47) along the straight lines which comprise the rest of the boundary. This can be done *exactly* and the solution is shown in the following.

Consider integrating the integrand along a line L from a point[4] (x_1, y_1) to a point (x_2, y_2) then

$$\frac{1}{2}\int_L x\,dy - y\,dx = \frac{1}{2}(x_1 y_2 - y_1 x_2). \tag{3.49}$$

[4]Here the indices 1 & 2 of the points do not refer to the nodes 1 & 2.

With this above result there is now sufficient information to calculate the volume of the fluid domain.

Energy Conservation

Energy conservation in the wavetank in figure 3.8 can be summed up in the equation:

$$-\int_W pr\dot{\theta}\, ds = \frac{1}{2}\frac{d}{dt}\left[\int_{W\cup F} \phi\, d\psi + \int_{W\cup F\cup E} y^2 n_y\, ds\right], \tag{3.50}$$

where p is the total pressure

$$p = -\left(\frac{\partial\phi}{\partial t} + \frac{1}{2}w\overline{w} + y\right) \tag{3.51}$$

and n_y is the component of the unit outward-pointing normal in the vertical direction. Also, the direction of integration in the first integral in the square brackets on the RHS of equation (3.50) is in the anticlockwise sense round the fluid domain.

In equation (3.50) the LHS represents the power input per unit tank width by the wavemaker, whereas the first and second terms on the RHS represent respectively the rate of change of the kinetic energy of the fluid per unit tank width and the rate of change of the potential energy of the fluid per unit tank width.

Note that equation (3.50) is equivalent to the following equation, which is equation (4.2) in [18] and is for a wavetank with a piston wavemaker, a flat bottom and a vertical end wall:

$$\int_B pU\, ds = \frac{1}{2}\frac{d}{dt}\left[\int_{B\cup F} \phi\, d\psi + \int_F y^2 n_y\, ds\right] + \frac{1}{2}U. \tag{3.52}$$

In this equation U is the velocity of the wavemaker B. Notice that Dommermuth *et al.* [18] call their wavemaker B instead of the W used here.

In order to test for energy conservation both sides of equation (3.50) must be evaluated. Consider first the LHS.

The integral on the LHS of equation (3.50) simplifies as follows

$$-\int_W pr\dot{\theta}\, ds = -\dot{\theta}\int_0^l pr\, dr, \tag{3.53}$$

where l is the wetted length of the paddle. After this simplification the above integral can be integrated in exactly the same way that the integral along the free-surface for the volume (see "**Step 2**" on page 80) was integrated. That is, an end-derivative cubic spline is fitted to the integrand of the integral on the RHS of equation (3.53) and integrated.

Next, consider the first integral inside the square brackets on the RHS of equation (3.50) and for the moment just consider the integration along the wavemaker. This integral simplifies as follows

$$\int_W \phi\, d\psi = \int_l^0 \phi\frac{d\psi}{dr}\, dr = -\dot{\theta}\int_l^0 \phi r\, dr = \dot{\theta}\int_0^l \phi r\, dr, \tag{3.54}$$

where the fact that $\psi = -\frac{1}{2}\dot{\theta}r^2$ on the paddle (see equation (3.26)) has been used. Once again this last integral is integrated by fitting an end-derivative cubic spline to the integrand and integrating this.

Now consider the integration along the free-surface on the RHS of equation (3.50). That is, consider

$$\begin{aligned}
&\int_F \phi\, d\psi + \int_F y^2 n_y\, ds \\
&= \int_F \phi\, d\psi - \int_F y^2\, dx \\
&= \int_1^{N_1} \left(\phi\frac{d\psi}{d\tau} - y^2\frac{dx}{d\tau}\right) d\tau.
\end{aligned} \tag{3.55}$$

As before the parameter τ in the above equation parameterises the free-surface and takes the value of the node index at each node. Also, as before differentiated

end-derivative cubic splines are used to find $d\psi/d\tau$ & $dx/d\tau$ and an integrated end-derivative cubic spline is used to evaluate the integral.

The last term in the square brackets on the RHS of equation (3.50) that needs to be evaluated is the term:

$$\int_{W\cup E} y^2 n_y \, ds = -\int_{W\cup E} y^2 \, dx, \tag{3.56}$$

where the integration in the integral on the RHS of the above equation is in the anticlockwise sense. This integral can be integrated exactly, as shown in the following.

Since the wavemaker and the end wall are straight lines consider integration along a line L from a point (x_1, y_1) to a point (x_2, y_2). That is, consider

$$-\int_L y^2 \, dx.$$

For the wavemaker (x_1, y_1) is where it meets the free-surface and (x_2, y_2) is the pivot. For the end wall (x_1, y_1) is where it meets the bottom and (x_2, y_2) is where it meets the free-surface.

Now, on L

$$y = mx + c \quad \text{where} \quad m = \frac{y_2 - y_1}{x_2 - x_1}.$$

Therefore

$$\begin{aligned} -\int_L y^2 \, dx &= -\int_{x_1}^{x_2} (mx + c)^2 dx \\ &= -\frac{1}{3m}\left((mx_2 + c)^3 - (mx_1 + c)^3\right) \\ &= -\frac{1}{3m}({y_2}^3 - {y_1}^3) \\ &= -\frac{(x_2 - x_1)}{3(y_2 - y_1)}({y_2}^3 - {y_1}^3) \\ &= \frac{1}{3}(x_1 - x_2)({y_1}^2 + y_1 y_2 + {y_2}^2). \end{aligned} \tag{3.57}$$

Finally, the time derivative on the RHS of equation (3.50) is obtained by yet again first fitting an end-derivative cubic spline to the data (this time the terms contained within the square brackets) and then differentiating this cubic spline.

On completion of this differentiation with respect to time both sides of equation (3.50) are now fully evaluated. Therefore, all that remains to be done is to compare the results to see how well the present BIM conserves energy.

3.6 Summary of Chapter 3

This chapter described in detail the development of the present two-dimensional Boundary-Integral Method.

The BIM of Vinje & Brevig [55] & [56] was chosen as the basis for the present BIM. The reasons for choosing Vinje & Brevig's method were: (a) its proven stability, (b) its proven accuracy and (c) the number of major paper which are based on developments of it. In addition, in Vinje & Brevig's method there is no need to approximate the geometry of the boundary between nodes (a point misunderstood by some researchers) and in Vinje & Brevig's method the integrals can be integrated analytically rather than numerically.

Although the present BIM is based on Vinje & Brevig's method it contains many adaptions.

Firstly, the present BIM goes beyond Vinje & Brevig's method by assuming that the complex potential $\beta(z)$ varies cubically between nodes, instead of just linearly. The way this cubic approximation is calculated depends on whether the interval of interest is adjacent to a corner or not. This extension of Vinje & Brevig's method was performed rigorously and it was found that:

1. Great care is required when choosing the right branch cut for complex logarithms. This point also applies to the case when $\beta(z)$ varies linearly

between nodes but it was not mentioned by any of the researchers using that method.

2. There is no need to calculate internal angles at the boundary nodes. That is, there is no need to calculate $\theta(z_k)$ for $k = 1, \ldots, N$ (see equation (3.10)).

Another way in which the present BIM goes beyond Vinje & Brevig's method relates to the type of numerical differentiation scheme used. The present BIM uses a five-point numerical differentiation scheme which is specially adapted at corners in the boundary of the fluid domain. This scheme was originally devised by She *et al.* [46]. In contrast, Vinje & Brevig only use a three-point numerical differentiation scheme in their method.

The present BIM also uses the explicit, truncated Taylor series method of Dold & Peregrine [15] for time-stepping. For this study a second-order truncated Taylor series is used.

A method to smooth out possible weak singularities in $\beta(z)$ or $\beta_t(z)$ at free-surface/body intersection point was developed. This method works by forcing the Cauchy-Riemann equations for $\beta(z)$ and $\beta_t(z)$ to hold at such points. It was named the "corner-correction" method and it is similar to the "BC-correction" method of Otta *et al.* [40].

In order to suppress free-surface instabilities, a smoothing & regridding procedure was developed. This procedure is based on the smoothing & regridding procedure of Tsai & Yue [53]. The smoothing procedure uses cubic smoothing splines to smooth the free-surface and the regridding procedure uses an inverse interpolation method to place more nodes in regions of high curvature and less nodes in regions of low curvature subject to a minimum and maximum node spacing. These two procedures were developed rigorously. Also, features of the present problem were exploited in order to make the present smoothing procedure

as efficient as possible.

Finally, the last major procedure described in chapter 3 was the new dynamic time-stepping procedure. This procedure exploits the relatively simple nature of the present time-stepping procedure in order to ensure that no free-surface node moves more than a specified distance in one time-step.

Chapter 4

Results Part 1: The Uniformly Accelerating Plate Problem

In this chapter the results of the present BIM are compared against an "exact"[1] analytical solution for a potential[2] flow at the intersection between a free-surface and a body. In fact the author believes that this is the first time that this sort of comparison has be done.

In 1984 Lin *et al.* [37] compared the results of a BIM against a small-time analytical solution (see Peregrine [41]) for the impulsively started vertical plate problem of Appendix A. Unfortunately, although very good agreement was found away from the plate, no comparison could be carried out near the plate/free-surface intersection point because the small-time analytical solution was not valid there.

In 1987 Greenhow [22] compared the results of a BIM against analytical solutions for wedge entry/exit problems. However, in this case none of the analytical solutions were exact because each one of them involved some sort of simplification, for example zero gravity. Consequently, no quantitative comparison could be carried out between the numerically predicted flow and the analytically predicted

[1]Having said that, the analytical solution is only valid for small-time.

[2]The fact that the analytical solution is for *potential flow* means that like is being compared with like.

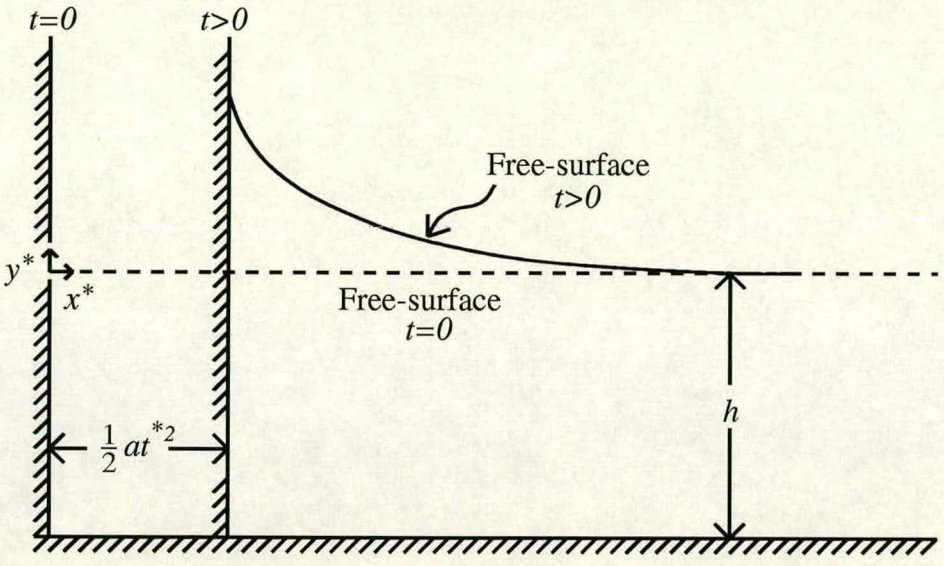

Figure 4.1: Sketch of the flow caused by a vertical plate accelerating uniformly from rest with acceleration $a > 0$.

flow near the wedge/free-surface intersection points.

The flow at the intersection between a free-surface and a body is well known to cause problems for a BIM (see subsection 2.3.2). Moreover, the free-surface/body corner flow studied here is an extreme example, which exhibits singular behaviour and therefore tests the present BIM to the full.

4.1 Statement of the Problem

The problem is to find the flow of a semi-infinite strip of inviscid, incompressible fluid of finite depth h which is disturbed from its equilibrium under gravity by a vertical plate uniformly accelerating from rest so as to try and compress the fluid. Experimentally it is observed that a jet is formed which rises rapidly up the vertical plate (see Yang & Chwang [59]).

The above situation is illustrated schematically in figure 4.1. Note that the superscript * in the figure denotes dimensional time and space coordinates. Also in figure 4.1 it can be seen that a Cartesian coordinate system (x^*, y^*) is chosen

with its origin at the rest position of the plate and its x^*-axis pointing along the undisturbed free-surface.

4.1.1 Non-Dimensionalisation of the Problem

The problem is non-dimensionalised by using the same non-dimensionalisation as that described in section 3.3 (see the transformation equations (3.1)).

With this non-dimensionalisation the position of the plate at time t is given by

$$x = \sigma t^2, \tag{4.1}$$

where the parameter $\sigma = a/2g$ is half of the ratio of the plate acceleration to the gravitational acceleration.

4.2 The Small-Time Analytical Solution

A small-time analytical solution to the above problem was obtained by King & Needham [35] in 1994. The details of how they obtained this solution are described briefly in the following.

As a starting point for their analysis King & Needham use Euler's equation plus the continuity condition and the relevant boundary conditions. From there they seek a small-time solution by posing a standard expansion in time t. However, terms in this expansion become singular as the free-surface/plate intersection point is approached, revealing this to be the outer expansion. From equation (2.7d) in [35] and the sentence below equation (2.12), also in [35], the outer solution for the free-surface elevation is

$$\eta(x,t) = \frac{2\sigma t^2}{\pi} \ln\left(\coth\frac{\pi(x-\sigma t^2)}{4}\right) + O(t^3). \tag{4.2}$$

King & Needham then rescale the variables near the intersection point to obtain an inner expansion and asymptotically match these two solutions to obtain a uniformly valid small-time solution. By using equations (2.19*d*), (2.22*c*), (A1*d*), (A11) & (A14*b*) from [35] the free-surface elevation in the inner region is given by

$$\eta(x_{\text{inner}}, t) = -\frac{4\sigma}{\pi} t^2 \ln t - t^2 \left(\frac{2\sigma}{\pi} (\ln x_{\text{inner}} + \lambda) + \eta^* \right) + o(t^2), \tag{4.3}$$

where $\lambda = \ln(-\ln t) - \ln(4/\pi)$ (note this is different from the smoothing parameter λ of subsection 3.5.3) and x_{inner} is an inner variable defined as follows

$$x_{\text{inner}} = -\frac{(x - \sigma t^2)}{t^2 \ln t}. \tag{4.4}$$

From the above equation it can be seen that the width of the inner region is $O(-t^2 \ln t)$ (note that t is small and therefore $\ln t$ is negative).

The only term that now remains to be defined in equation (4.3) is η^*. This term can be obtained by using equation (A26) from [35] together with the sentence below equation (A31), also in [35], and it turns out that η^* is the following contour integral

$$\eta^* = \frac{\sigma \Gamma\left(\frac{3}{2}\right)}{2\pi i} \int_{c-i\infty}^{c+i\infty} \frac{(2\sigma/\pi x_{\text{inner}})^p \, dp}{p(1+p) \sin\left(\frac{1}{2}\pi p\right) \Gamma\left(p + \frac{3}{2}\right)} \quad (0 < c < 2). \tag{4.5}$$

For small x_{inner} the leading order behaviour of the above contour integral can be calculated. This is achieved by firstly constructing a "return" contour, which together with the above contour of integration forms a closed rectangular contour (see figure 4 in [35]). Then Cauchy's Residue Theorem is applied to the poles inside this closed contour in order to evaluate η^*. The result of all this is that

the free-surface elevation for small x_{inner} and small t is

$$\eta(x_{\text{inner}},t) = -\frac{4\sigma}{\pi}t^2\ln t - \frac{2\sigma t^2}{\pi}\left\{\lambda + \ln\left(\frac{2\sigma}{\pi}\right) - 1 - \frac{\Gamma'\left(\frac{3}{2}\right)}{\Gamma\left(\frac{3}{2}\right)} + \frac{\pi^2 x_{\text{inner}}}{8\sigma} + o(x_{\text{inner}})\right\} + o(t^2). \tag{4.6}$$

There are a couple of important conclusions to be drawn from equation (4.6):

1. The free-surface leaves the plate in a linear manner and the slope of the free-surface at the plate is

$$\eta_x = \frac{\pi}{4\ln t}. \tag{4.7}$$

   This above equation was obtained by using equation (4.4) in addition to equation (4.6).

2. The height of the free-surface at the plate is

$$\eta = -\frac{4\sigma}{\pi}t^2\ln t - \frac{2\sigma t^2}{\pi}\left\{\ln(-\ln t) - \ln\left(\frac{4}{\pi}\right) + \ln\left(\frac{2\sigma}{\pi}\right) - 1 - \frac{\Gamma'\left(\frac{3}{2}\right)}{\Gamma\left(\frac{3}{2}\right)}\right\} + o(t^2). \tag{4.8}$$

4.2.1 Plotting the Analytical Free-Surface Profile in the Inner Region

In this subsection original material is presented which relates to how the analytical free-surface elevation in the inner region is evaluated.

In order to obtain the analytical free-surface elevation at a point within the inner region (see equation (4.3)) it is first necessary to find η^* for that point via equation (4.5). Unfortunately however, it is not a trivial task to evaluate the contour integral on the RHS of equation (4.5).

As pointed out by King & Needham the contour integral on the RHS of equation (4.5) can be evaluated by firstly adding a semicircular "return" contour ($p = Re^{i\theta}$ such that $-\frac{1}{2}\pi < \theta < \frac{1}{2}\pi$) in $\mathrm{Re}(p) > 0$ and noting that the integrand decays on this semicircle as $R \to \infty$. Then Cauchy's Residue Theorem is applied to the poles inside the resultant closed contour to give

$$\eta^* = -\frac{2\sigma\Gamma\left(\frac{3}{2}\right)}{\pi} \sum_{n=1}^{\infty} \frac{(-1)^n (2\sigma/\pi x_{\text{inner}})^{2n}}{2n(2n+1)\Gamma\left(2n+\frac{3}{2}\right)}. \tag{4.9}$$

As also pointed out by King & Needham, although the above series diverges for $x_{\text{inner}} = 0$, it is absolutely convergent for all $x_{\text{inner}} \neq 0$ and is in fact asymptotic for large x_{inner}. Consequently, η^* can be evaluated accurately for both moderate and large x_{inner} by summing the first few terms in series (4.9). However, for small x_{inner} terms in the series first rapidly increase and then rapidly decrease with the result that large rounding errors occur no matter how many terms in (4.9) are summed.

It turns out that a much more robust method of calculating η^*, which works for all $x_{\text{inner}} \neq 0$, is to integrate the integral on the RHS of equation (4.5) directly by numerical means. This is possible because although the interval of integration is infinite the integrand decays very rapidly away from the real axis. An extremely good approximation to η^* can then be obtained by integrating from $c-iY$ (instead of $c-i\infty$) to $c+iY$ (instead of $c+i\infty$) for some sufficiently large $Y > 0$. Moreover, a bound on the absolute value of the error in approximating η^* by this truncated integral can be found (see Appendix I) and this bound is

$$\frac{\sigma}{\sqrt{2}\pi} \frac{(2\sigma/\pi x_{\text{inner}})^c e^{c+\frac{1}{2}}}{(c+2)Y^{c+2}}. \tag{4.10}$$

In this study Y is chosen to be 20 and c is chosen to be $\frac{3}{2}$ (from equation (4.5) it can be seen that c can lie anywhere between 0 and 2).

The results of using this method to calculate η^* are shown in figures 4.2 & 4.3. Figure 4.2 shows the analytical free-surface profile in the inner region for $\sigma = \frac{1}{4}$

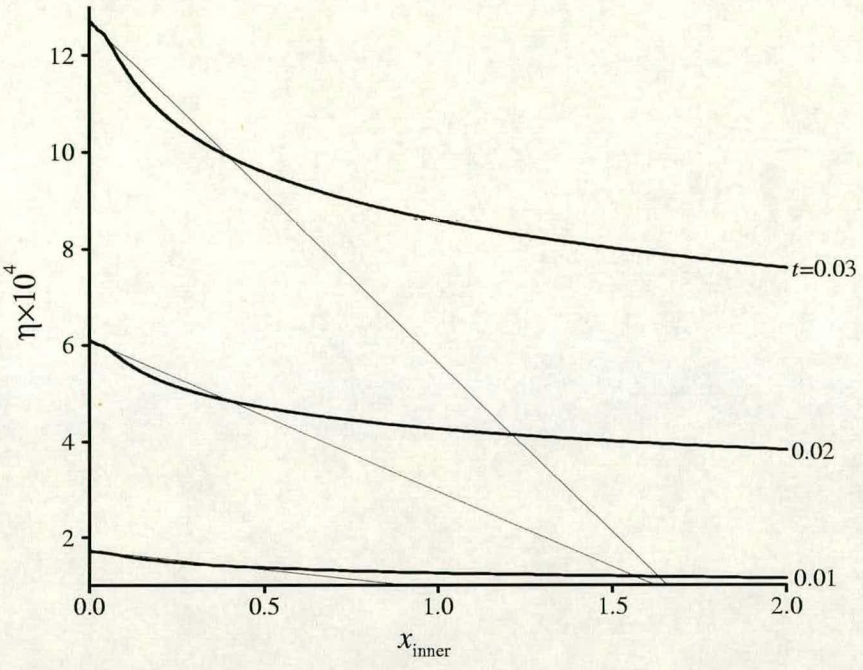

Figure 4.2: The analytical free-surface elevation in the inner region for $\sigma = \frac{1}{4}$ and $t = 0.01,\ 0.02$ & 0.03.

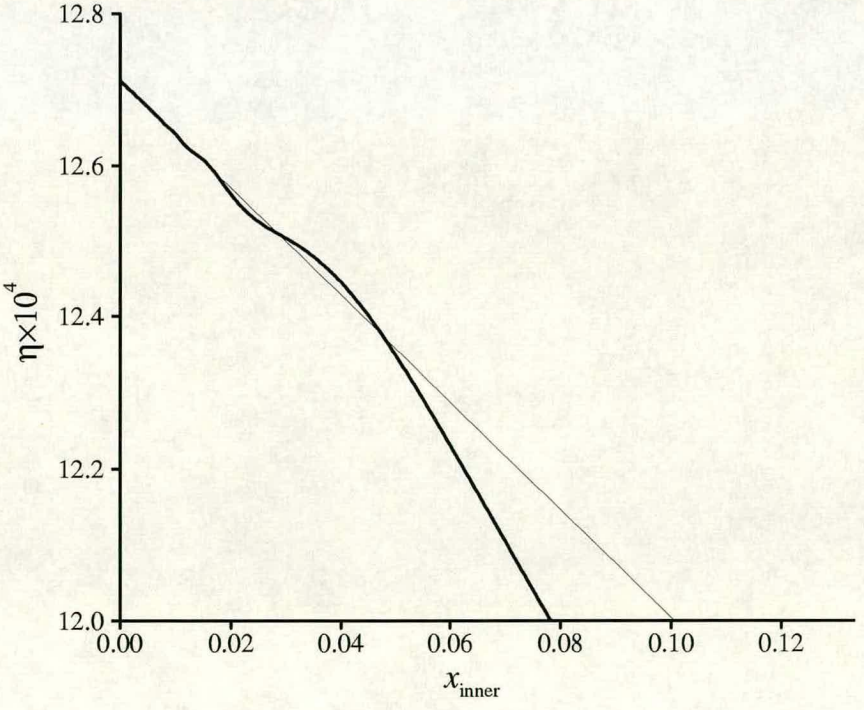

Figure 4.3: The analytical free-surface elevation near the plate in the inner region for $\sigma = \frac{1}{4}$ and $t = 0.03$.

(corresponding to a plate acceleration of $\frac{1}{2}g$) and for three different times. Notice that x_{inner} is always equal to zero at the accelerating plate (see equations (4.4) & (4.1)). This figure is exactly the same as figure 2 in King & Needham's paper [35]. However, in figure 2 of King & Needham's paper there is no "kink" in the free-surface near the plate; King & Needham's free-surfaces approach the plate "smoothly". Greater confidence that these "kinks" are correct is obtained in the following two different ways:

1. Also shown in figure 4.2 are the tangents to the free-surface at the plate for the three different times. These tangents are shown as the fainter lines in the figure and they are computed by using equation (4.7) together with equation (4.8). As can be seen, these tangents support the existence of the "kinks".

2. As can be seen from equation (4.3), a bound on the absolute value of the error in the free-surface elevation in the inner region due to the "truncated integral" method of calculating η^* is t^2 times the bound (4.10). Therefore, since here $Y = 20$, $c = \frac{3}{2}$ & $\sigma = \frac{1}{4}$ a bound on the absolute value of the error in the free-surface elevation in the inner region due to this method of calculating η^* is

$$\left.\frac{\sigma}{\sqrt{2\pi}}\frac{(2\sigma/\pi x_{\text{inner}})^c e^{c+\frac{1}{2}}}{(c+2)Y^{c+2}}t^2\right|_{Y=20,\ c=\frac{3}{2}\ \&\ \sigma=\frac{1}{4}} \approx 2.10825\times 10^{-7}\frac{t^2}{(x_{\text{inner}})^{\frac{3}{2}}} \tag{4.11}$$

and of the three different times this bound is maximum at $t = 0.03$, when it has the value

$$\frac{1.89742\times 10^{-10}}{(x_{\text{inner}})^{\frac{3}{2}}}. \tag{4.12}$$

Figure 4.3 shows a closeup of the "kink" in figure 4.2 for $t = 0.03$. This figure reveals that the "kink" is actually an oscillation which decays in both amplitude

and wavelength as the free-surface/plate intersection point is approached. The figure also shows that the analytical free-surface does leave the plate in a linear manner, as predicted by King & Needham, and that the tangent to the analytical free-surface (the fainter line) again supports the existence of the "kink".

In summary, in this subsection a robust method for evaluating the analytical free-surface elevation in the inner region is presented and used. The results of this method reveal a hitherto unnoticed feature of the analytical solution. This feature is very important because it is very close to the main point of interest, namely the free-surface/plate intersection point.

4.3 The Numerical Solution

As pointed out by King & Needham the flow being studied is irrotational. Consequently, a numerical solution can be sought by applying the present BIM. The way this BIM is applied is described in the following.

The main aim of most of this chapter is to compare the numerical solution from the BIM with the small-time analytical solution. With this in mind, two values of the parameter σ are chosen. These two values are $\sigma = \frac{1}{4}$ and $\sigma = 1$, corresponding to a plate acceleration of $\frac{1}{2}g$ and $2g$ respectively (note that one plate acceleration is less than g while the other is greater than g). Also, for the comparison with the small-time analytical solution the computational domain is truncated by placing a stationary vertical wall at a moderate distance from the rest position of the plate. This is possible because of the fact that the comparison is only for *small-time* and so disturbances will not travel very far from the plate. In this study the vertical wall is placed at $x = 5$.

Taking into account the above information the computational fluid domain is shown in figure 4.4. The way this domain is discretised is described in the

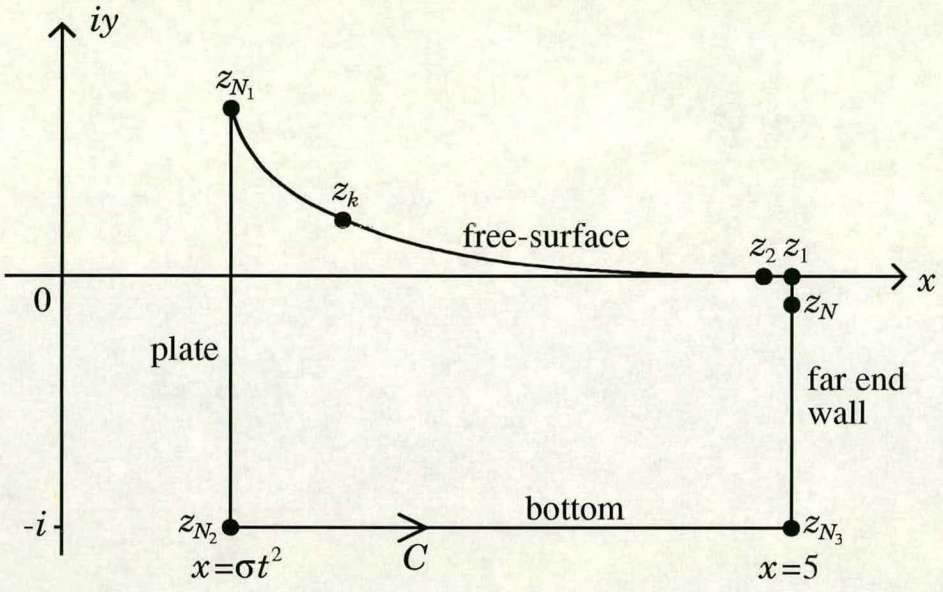

Figure 4.4: The computational domain for some time $t > 0$.

following.

Along the bottom 51 equally-spaced nodes are placed and along the far end wall 11 equally-spaced nodes are placed (these numbers include the end nodes). The initial node spacing on either side of the free-surface/plate intersection point is set to the same value, say Δx. Usually Δx is chosen to be quite small in order to give good resolution in this part of the computational fluid domain. The initial node spacing on the free-surface and the plate then gradually increases (by a common ratio each time) away from this intersection point. The number of nodes on the free-surface and hence the common ratio on the free-surface is determined by requiring that the initial node spacing at the other end of the free-surface is as near as possible to a prescribed value, here taken to be 0.3 for $\sigma = \frac{1}{4}$ and 0.15 for $\sigma = 1$. Similarly, the number of nodes on the plate and hence the common ratio on the plate is determined by requiring that the initial node spacing at the bottom of the plate is as near as possible to another prescribed value, here taken to be 0.1 for $\sigma = \frac{1}{4}$ and 0.05 for $\sigma = 1$.

Now consider the temporal discretisation of the problem. In this chapter only fixed time-steps (Δt's) are used. That is, the dynamic time-stepping procedure of subsection 3.5.4 is not used.

For each σ three values of Δt and three values of Δx are chosen, and using these values five runs are performed.

For $\sigma = \frac{1}{4}$ the values of Δt are $\Delta t = 0.00025$, $\Delta t = 0.0005$ & $\Delta t = 0.001$ and the values of Δx are $\Delta x = 0.0001$, $\Delta x = 0.0002$ & $\Delta x = 0.0004$. Also, the runs performed using these values of Δt and Δx are:

- Run 1: ($\sigma = \frac{1}{4}$, $\Delta t = 0.00025$ & $\Delta x = 0.0002$).
- Run 2: ($\sigma = \frac{1}{4}$, $\Delta t = 0.0005$ & $\Delta x = 0.0001$).
- Run 3: ($\sigma = \frac{1}{4}$, $\Delta t = 0.0005$ & $\Delta x = 0.0002$).
- Run 4: ($\sigma = \frac{1}{4}$, $\Delta t = 0.0005$ & $\Delta x = 0.0004$).
- Run 5: ($\sigma = \frac{1}{4}$, $\Delta t = 0.001$ & $\Delta x = 0.0002$).

For $\sigma = 1$ the values of Δt are $\Delta t = 0.0025$, $\Delta t = 0.005$ & $\Delta t = 0.01$ and the values of Δx are $\Delta x = 0.005$, $\Delta x = 0.01$ & $\Delta x = 0.02$. Also, the runs performed using these values of Δt and Δx are:

- Run 6: ($\sigma = 1$, $\Delta t = 0.0025$ & $\Delta x = 0.01$).
- Run 7: ($\sigma = 1$, $\Delta t = 0.005$ & $\Delta x = 0.005$).
- Run 8: ($\sigma = 1$, $\Delta t = 0.005$ & $\Delta x = 0.01$).
- Run 9: ($\sigma = 1$, $\Delta t = 0.005$ & $\Delta x = 0.02$).
- Run 10: ($\sigma = 1$, $\Delta t = 0.01$ & $\Delta x = 0.01$).

σ	$\frac{1}{4}$			1		
Δx	0.0001	0.0002	0.0004	0.005	0.01	0.02
Number of nodes on the free-surface	131	120	109	117	97	78
Number of nodes on the plate	68	61	55	52	41	31

Table 4.1: The number of nodes on the free-surface and the plate for the various Δx's.

For the above values of Δx the number of nodes on the free-surface and the number of nodes on the plate are shown in table 4.1. Again, the end nodes are included in these numbers.

To begin with, runs 1 to 10 are performed without using either the "corner-correction" procedure of subsection 3.5.2 or the smoothing & regridding procedure of subsection 3.5.3. Figure 4.5 shows the free-surface profile after one time-step for run 8. As can be seen from the figure, instabilities start to occur immediately and because of these instabilities the run breaks down within a few time-steps. In fact, all the other runs behave in a very similar way and so their results are not shown here.

Fortunately, this above behaviour can be explained as follows. By a similar analysis to that in Appendix A, for this accelerating plate problem the complex potential at $t = 0$ is

$$\beta(z) \equiv 0 \tag{4.13}$$

and the partial time derivative of the complex potential at $t = 0$ is (*cf.* equation (A.3))

$$\beta_t(z) = \frac{4\sigma i}{\pi} z \log z + \text{analytic part.} \tag{4.14}$$

Therefore, at $t = 0$ the complex potential $\beta(z)$ is analytic everywhere in the fluid domain but its partial time derivative $\beta_t(z)$ has a singularity at the free-

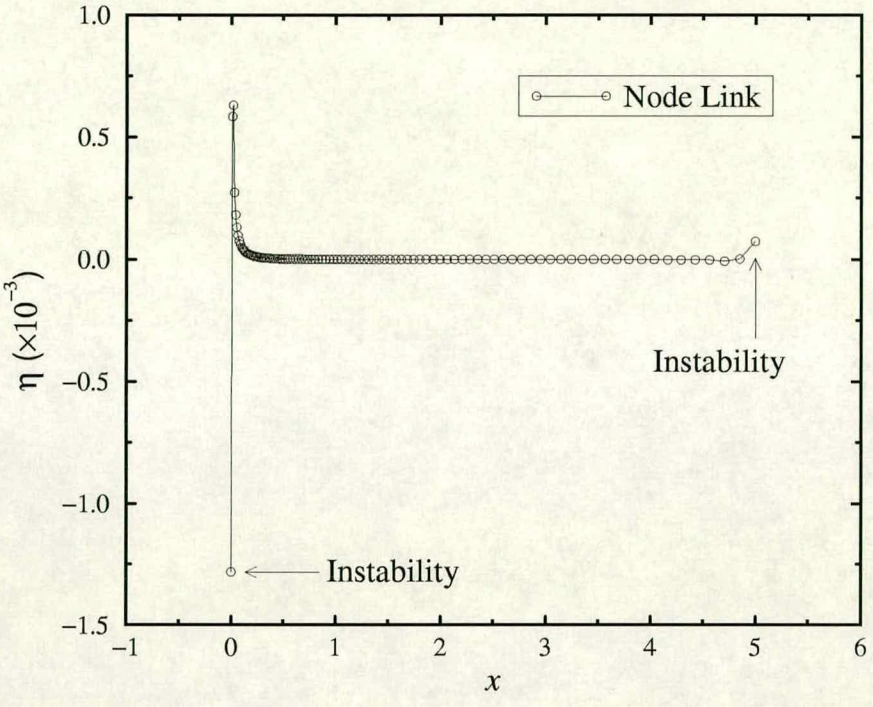

Figure 4.5: The numerical free-surface profile after one time-step for $\sigma = 1$, $\Delta t = 0.005$, $\Delta x = 0.01$ and without "corner-correction".

surface/plate intersection point ($z = 0$). The reason for this singularity is because the Cauchy-Riemann equations for $\beta_t(z)$ at $t = 0$ are violated at $z = 0$.

Now, from equation (4.13) the velocity $w = d\beta/dz$ is zero in the entire fluid domain at $t = 0$. Therefore, from equation (3.18) the acceleration in the fluid domain at $t = 0$ is given by

$$a_x - ia_y = \frac{\partial w}{\partial t} \left(= \frac{d}{dz} \left(\frac{\partial \beta}{\partial t} \right) \right), \tag{4.15}$$

where a_x & a_y are respectively the horizontal & vertical components of acceleration. By using equation (4.14) the above formula for the acceleration in the fluid domain at $t = 0$ becomes

$$a_x - ia_y = \frac{4\sigma i}{\pi} \log z + \text{analytic part}, \tag{4.16}$$

where the analytic part here is, up to a constant, the z-derivative of the analytic

part in equation (4.14). Finally, in polar notation (4.16) becomes

$$a_x - ia_y = \frac{4\sigma i}{\pi}(\log r + i\theta) + \text{analytic part}, \tag{4.17}$$

so that

$$a_y = -\frac{4\sigma}{\pi}\log r - \text{Im(analytic part)}. \tag{4.18}$$

By definition the analytic part is necessarily bounded and so its imaginary part is also bounded. As a result, a_y is dominated by the $\log r$ term as $r \to 0$ and hence the upward acceleration at $t = 0$ of the fluid particle at $z = 0$ is unbounded. This result can also be obtained from the small-time analytical solution by differentiating the analytical height of the free-surface at the plate (equation (4.8)) twice w.r.t. t and then taking the limit as $t \to 0$.

There is now sufficient information to explain why the instabilities shown in figure 4.5 occurred. From subsection 3.5.1 it can be seen that the present BIM not only solves for $\beta(z)$ round the fluid domain at each time-step but it also solves for $\beta_t(z)$ round the fluid domain at each time-step. This is so that the acceleration as well as the velocity of the free-surface nodes can be found, which in turn allows second-order explicit time-stepping to be used. However, it is now known that $\beta_t(z)$ is singular at $t = 0$ and $z = 0$, and the present BIM cannot model singular behaviour. As mentioned in section 3.5 the present BIM uses cubics to approximate the behaviour of $\beta(z)$ and $\beta_t(z)$ between nodes and cubics are analytic functions. Furthermore, the present BIM then tries to calculate the acceleration of the free-surface node at the free-surface/plate intersection point at $t = 0$ and there is no possibility of it calculating the correct value, which is unbounded. Hence the instabilities seen in figure 4.5.

To conclude, far from being a disaster the instabilities shown in figure 4.5 in fact show, to some extent, that the present BIM is doing what it should do.

From now on in this study the "corner-correction" procedure of subsection 3.5.2 will be used, provided that the criterion about the associated row not upsetting the diagonal dominance of the coefficient matrix A is satisfied (see page 66). This procedure ensures that the Cauchy-Riemann equations for $\beta(z)$ and $\beta_t(z)$ are not violated at the free-surface/body intersection points. That is, it ensures that $\beta(z)$ and $\beta_t(z)$ are analytic at these points by smoothing out any possible singularities there. Consequently, this procedure results in a slightly different problem being solved when compared to the exact mathematical problem. However, it will be shown in the following that this procedure not only stabilises the numerical scheme but also does not affect good agreement between the numerical solution and the exact mathematical solution.

Runs 1 to 10 are now performed again but this time with "corner-correction". The results of these new runs are shown in the following.

4.3.1 The Outer Region

Figure 4.6 shows both numerical and analytical free-surface profiles at three different times and at the scale of the outer region for run 3. The x-axis in figure 4.6 starts as $x = -0.2$ in order to provide clarity at $x = 0.0$. As can be seen from the figure there is very good agreement between the numerical solution and the outer analytical solution. This good agreement goes all the way to the end of the computational fluid domain at $x = 5$, however this part of the computational domain is not shown because the main area of interest is the outer region *near* the plate. Note, the numerical free-surface profiles for runs 1, 2, 4 & 5 are not shown in figure 4.6 because they are virtually indistinguishable from those of run 3.

Similarly, figure 4.7 shows both numerical and analytical free-surface profiles at three different times and at the scale of the outer region for run 8. Again, it can be seen that there is very good agreement between the numerical solution

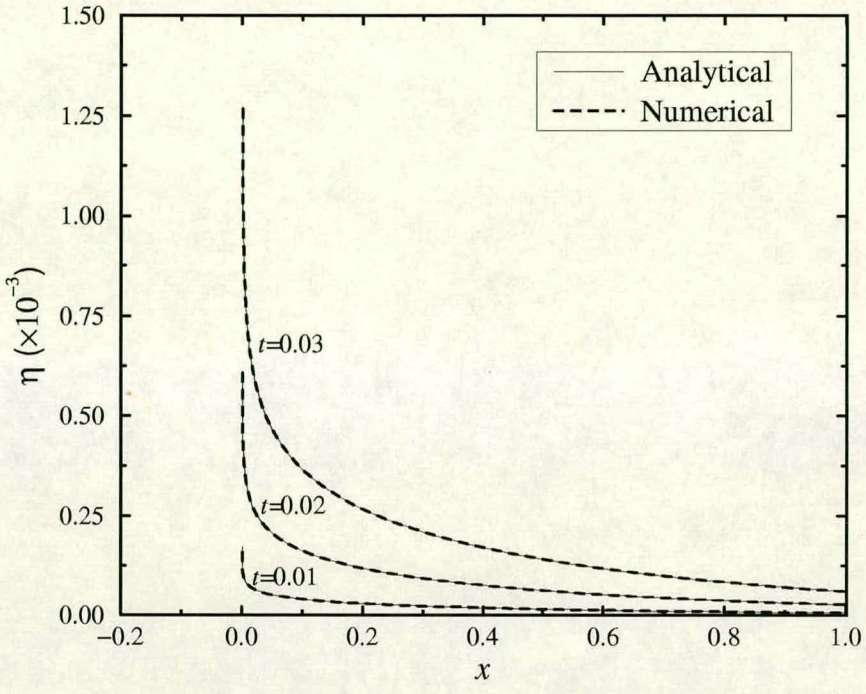

Figure 4.6: Numerical and analytical free-surface profiles for $\sigma = \frac{1}{4}$ and $t = 0.01$, 0.02 & 0.03. The numerical results are for the case $\Delta t = 0.0005$ & $\Delta x = 0.0002$.

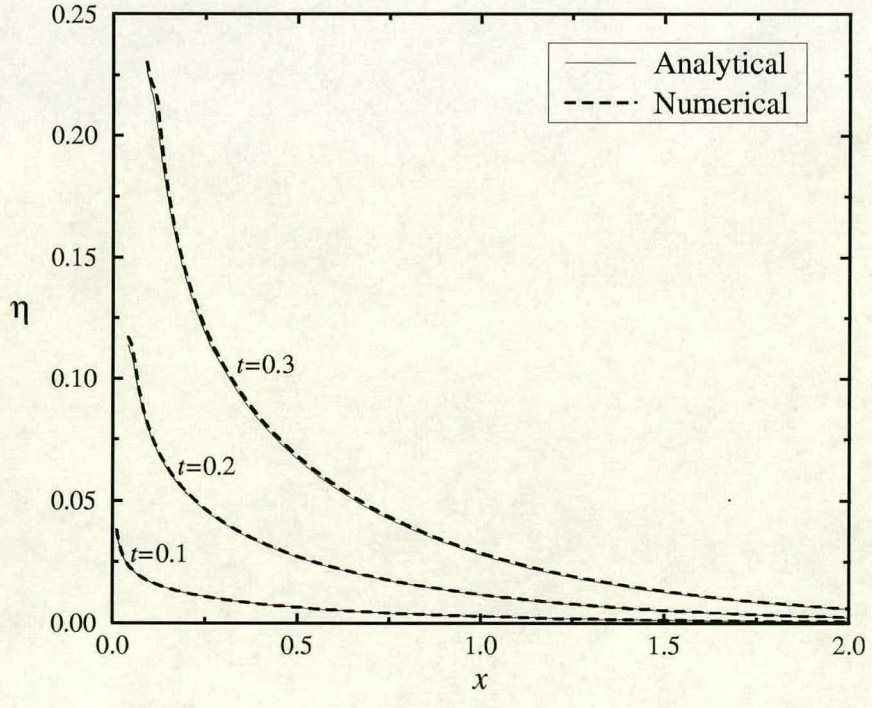

Figure 4.7: Numerical and analytical free-surface profiles for $\sigma = 1$ and $t = 0.1$, 0.2 & 0.3. The numerical results are for the case $\Delta t = 0.005$ & $\Delta x = 0.01$.

t	0.01	0.02	0.03	0.1	0.2	0.3
$-t^2 \ln t$	0.461×10^{-3}	1.565×10^{-3}	3.156×10^{-3}	0.0230	0.0644	0.1084

Table 4.2: The value of $-t^2 \ln t$ for $t = 0.01,\ 0.02,\ 0.03,\ 0.1,\ 0.2$ & 0.3.

and the outer analytical solution. Also, the results of runs 6, 7, 9 & 10 are not shown in figure 4.7 because they are indistinguishable from those of run 8.

4.3.2 The Inner Region

Now consider looking at the numerical free-surface profiles near the plate to see how well the present BIM can predict the inner solution. Figures 4.8 & 4.9 are exactly the same as figures 4.6 & 4.7 respectively, except that figures 4.8 & 4.9 look closer at the free-surface/plate intersection points. In addition, on the numerical free-surface profiles in figures 4.8 & 4.9 the free-surface nodes are shown and these are indicated by circles.

As mentioned in section 4.2 the width of the inner region (measured from the plate) is $O(-t^2 \ln t)$. The value of $-t^2 \ln t$ for each of the six times in figures 4.8 & 4.9 is given in table 4.2.

As can be seen from figure 4.8, the numerical free-surface profiles agree very well with the analytical inner solution except near the "kink". The reason for this poor agreement in the vicinity of the "kink" is because the node spacing is too large to resolve the "kink". A similar conclusion can be reached for the numerical free-surface profile for $t = 0.1$ in figure 4.9. However, for $t = 0.2$ and $t = 0.3$ in figure 4.9 several free-surface nodes now lie within the "kink" region and hence the the qualitatively good description of the "kink" by these numerical free-surface profiles.

From figure 4.3 it was concluded that the "kink" in the inner analytical solution was actually a complicated oscillation, and so to resolve it well a very

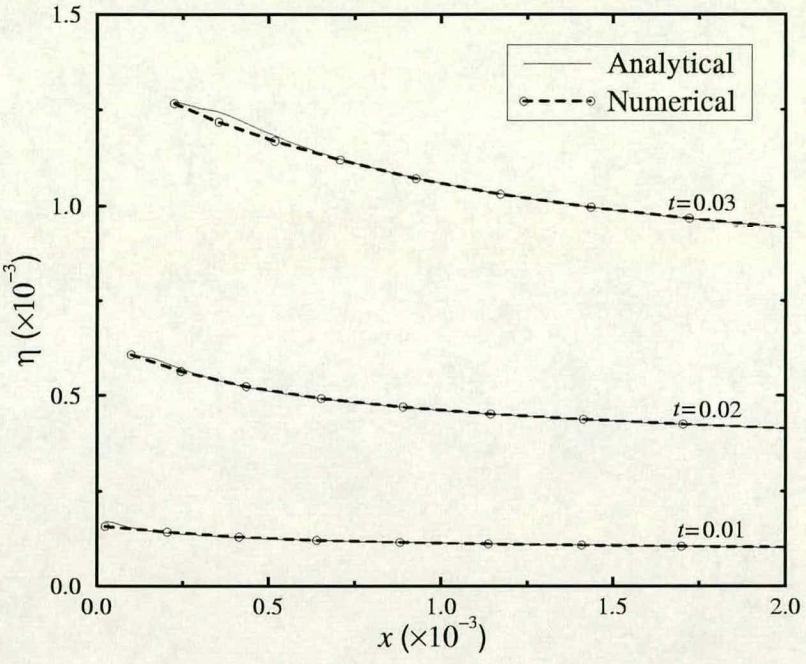

Figure 4.8: Numerical and analytical free-surface profiles near the plate for $\sigma = \frac{1}{4}$ and $t = 0.01,\ 0.02\ \&\ 0.03$. The numerical results are for the case $\Delta t = 0.0005\ \&\ \Delta x = 0.0002$.

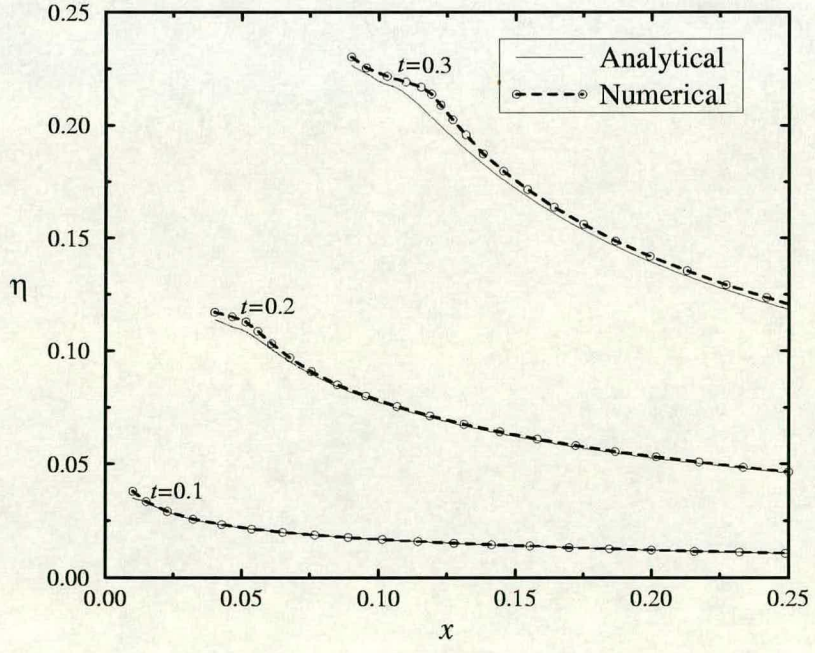

Figure 4.9: Numerical and analytical free-surface profiles near the plate for $\sigma = 1$ and $t = 0.1,\ 0.2\ \&\ 0.3$. The numerical results are for the case $\Delta t = 0.005$ $\&\ \Delta x = 0.01$.

small node spacing would be required. However, experience from many test runs shows that if the node spacing is reduced then to maintain stability the time-step should also be reduced and the time-step should be reduced by a much larger factor than the node spacing. This node spacing dependent restriction on the time-step indicates that a local Courant type stability condition applies to the present BIM (see pages 29 & 69). Later on in this chapter quantitative evidence will be presented to show that such a stability condition does apply.

Figure 4.9 also highlights another problem. Initially the width of the inner region is zero and then it subsequently increases with time. As a result a node spacing which resolves the inner solution satisfactorily at one time will be completely inappropriate for resolving the inner solution at another time.

Fortunately, this above problem does not seem to have major implications for the numerical solution as a whole. That is, the present BIM appears to accurately predict the outer solution no matter how well it resolves the inner solution. Furthermore, it also appears to accurately predict the height of the free-surface at the plate no matter what the node spacing is (within reason). Graphs comparing the numerical height of the free-surface at the plate as a function of time against the analytical height of the free-surface at the plate as a function of time are shown in the next subsection.

Once again, only the numerical free-surface profiles from run 3 and not from runs 1, 2, 4 & 5 are shown in figure 4.8. Also, only the numerical free-surface profiles from run 8 and not from runs 6, 7, 9 & 10 are shown in figure 4.9. This is because these other numerical free-surface profiles are virtually indistinguishable from the ones in figures 4.8 & 4.9 respectively, except near the "kink".

Figure 4.10 shows a closeup of the "kink" for the case when $\sigma = \frac{1}{4}$ and $t = 0.03$, and figure 4.11 shows a closeup of the "kink" for the case when $\sigma = 1$

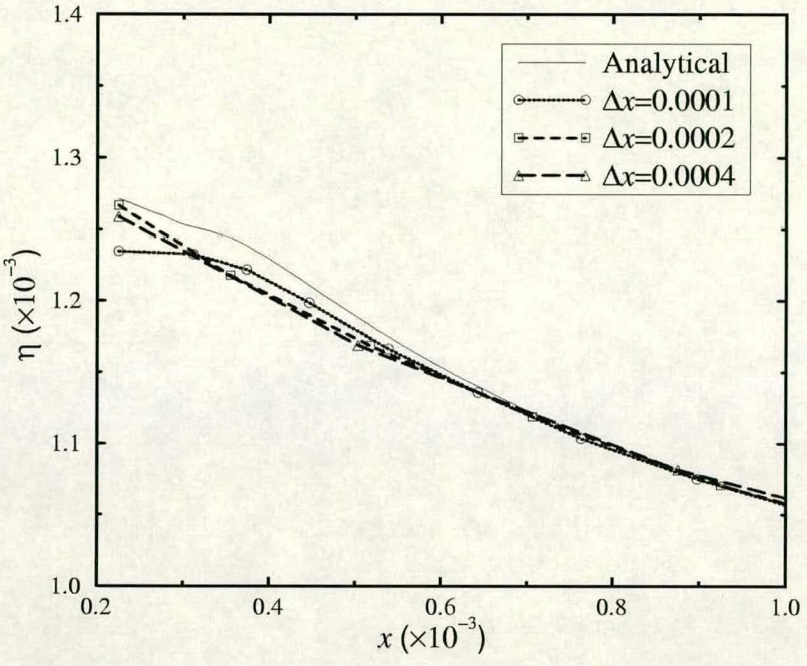

Figure 4.10: Numerical and analytical free-surface profiles very near the plate for $\sigma = \frac{1}{4}$ and $t = 0.03$. All the numerical results correspond to a time-step $\Delta t = 0.0005$.

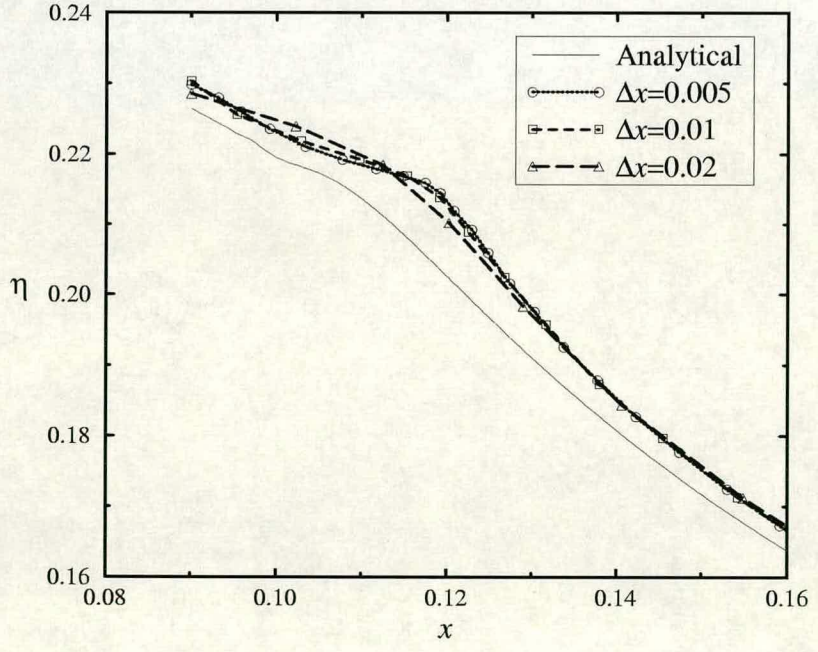

Figure 4.11: Numerical and analytical free-surface profiles very near the plate for $\sigma = 1$ and $t = 0.3$. All the numerical results correspond to a time-step $\Delta t = 0.005$.

and $t = 0.3$. In figure 4.10 the analytical free-surface profile is shown together with numerical free-surface profiles from runs 2, 3 & 4. The numerical free-surface profiles from runs 1 & 5 are not shown in figure 4.10 because they are virtually indistinguishable from the numerical free-surface profile from run 3. Note that runs 1 & 5 have the same Δx as run 3 but they have different Δt's to run 3. Similarly, in figure 4.11 the analytical free-surface profile is shown together with numerical free-surface profiles from runs 7, 8 & 9. The numerical free-surface profiles from runs 6 & 10 are not shown in figure 4.11 because they are virtually indistinguishable from the numerical free-surface profile from run 8. Note that runs 6 & 10 have the same Δx as run 8 but they have different Δt's to run 8.

Figures 4.10 & 4.11 confirm that the numerical free-surface profiles only give a (qualitatively) good description of the "kink" if the node spacing is small enough.

Finally, in this subsection, figure 4.2, which corresponds to figure 2 in King & Needham's paper [35], is redrawn (see figure 4.12) but this time numerical free-surface profiles from run 3 are also included. Note that the large change in node spacing between the numerical free-surface profiles in figure 4.12 is mainly due to the scaling from x to x_{inner} (see equation (4.4)). Once again, figure 4.12 shows that there is very good agreement between the numerical free-surface profiles and the analytical free-surface profiles in the inner region, except near the "kink". Furthermore, figure 4.12 also shows that the reason for this poor agreement in the vicinity of the "kink" (for all three times) is due to the node spacing being too large to resolve the "kink" (for all three times).

4.3.3 The Height of the Free-Surface at the Plate

Now consider the height of the free-surface at the plate. Figure 4.13 shows a comparison between the numerical height of the free-surface at the plate as a function of time t and the analytical height of the free-surface at the plate as a

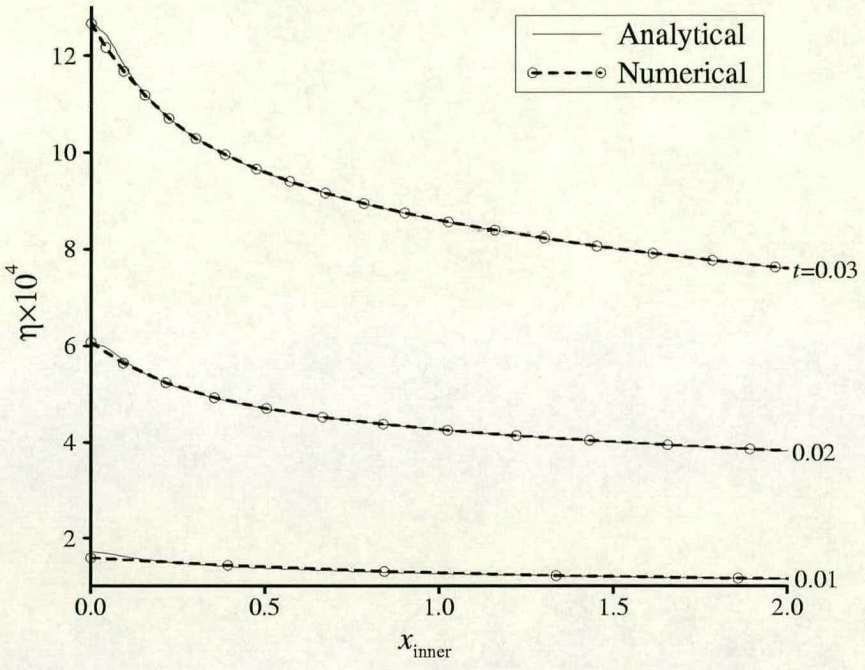

Figure 4.12: Numerical and analytical free-surface profiles in the inner region for $\sigma = \frac{1}{4}$ and $t = 0.01,\ 0.02\ \&\ 0.03$. The numerical results are for the case $\Delta t = 0.0005\ \&\ \Delta x = 0.0002$.

function of t for $\sigma = \frac{1}{4}$. The numerical height comes from run 3 and the analytical height comes from equation (4.8). Numerical results from runs 1, 2, 4 & 5 are not shown in figure 4.13 because they are virtually indistinguishable from those of run 3. Similarly, figure 4.14 shows a comparison between the numerical height of the free-surface at the plate as a function of t and the analytical height of the free-surface at the plate as a function of t for $\sigma = 1$. In this case the numerical height comes from run 8. Numerical results from runs 6, 7, 9 & 10 are not shown in figure 4.14 because they are virtually indistinguishable from those of run 8.

As can be seen from figures 4.13 & 4.14 there is very good agreement between the numerical height of the free-surface at the plate as a function of t and the analytical height of the free-surface at the plate as a function of t. This is despite the fact that the "corner-correction" procedure of subsection 3.5.2 smoothes

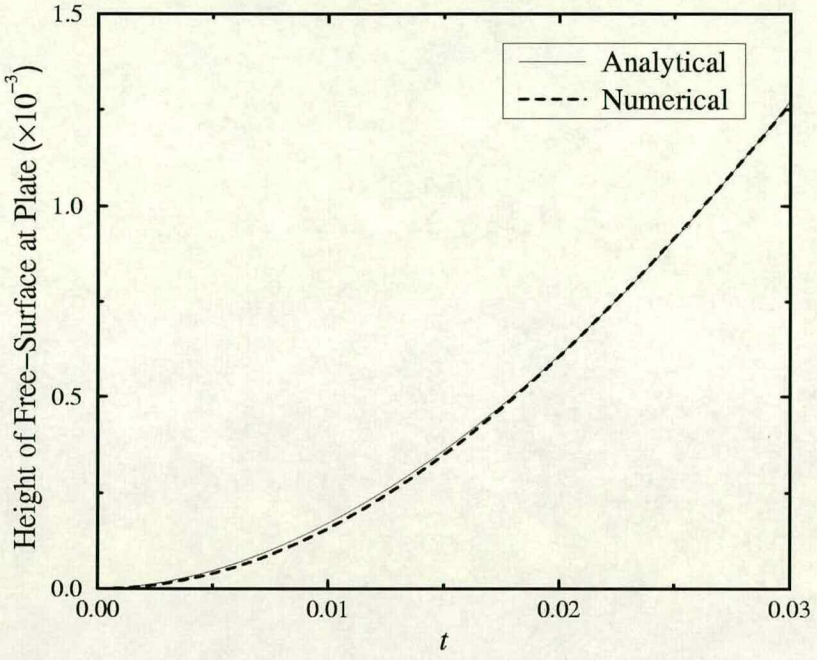

Figure 4.13: Numerical and analytical heights of the free-surface at the plate against time t for $\sigma = \frac{1}{4}$. The numerical height corresponds to the case $\Delta t = 0.0005$ & $\Delta x = 0.0002$.

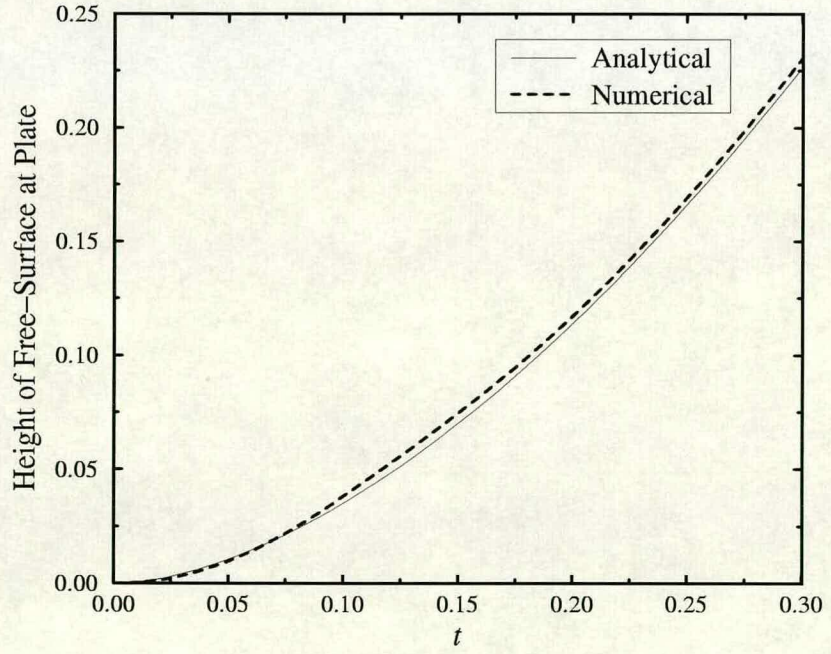

Figure 4.14: Numerical and analytical heights of the free-surface at the plate against time t for $\sigma = 1$. The numerical height corresponds to the case $\Delta t = 0.005$ & $\Delta x = 0.01$.

out the initial singularity in $\beta_t(z)$ at the free-surface/plate intersection point, so that the present BIM actually solves a slightly different problem to the exact mathematical problem.

4.3.4 The Velocity Potential and its Partial Time Derivative at the Jet Tip

A very important test of the present BIM is to see how well it predicts the velocity potential and the partial time derivative of the velocity potential at free-surface/body intersection points. As mentioned in subsection 3.5.2 if $\beta(z)$ (or $\beta_t(z)$) is singular at such a point then the "corner-correction" procedure alters the value of ϕ (or ϕ_t) there, from its exact mathematical value, in order to smooth out the singularity. If on the other hand $\beta(z)$ (or $\beta_t(z)$) is analytic at such a point then the "corner-correction" procedure should help to ensure that the predicted value of ϕ (or ϕ_t) there is very close to its exact mathematical value. The free-surface/plate intersection point in the present accelerating plate problem provides an excellent candidate on which to carry out the above analysis, especially since it is known that $\beta_t(z)$ is singular there at $t = 0$.

In order to perform the above analysis on the free-surface/plate intersection point it is first necessary to find the analytical values of ϕ and ϕ_t there from the small-time analytical solution. These values are obtained by using the dynamic boundary condition on the free-surface (see equations (2.8) & (2.9)) as follows.

The Lagrangian form of the dynamic boundary condition on the free-surface is

$$\frac{D\phi}{Dt} = \frac{1}{2}\left(u^2 + v^2\right) - y. \tag{4.19}$$

For the free-surface/plate intersection point the value of y in the above equation is obtained from equation (4.8) and the values of u & v in the above equation are

found by differentiating equations (4.1) & (4.8) respectively w.r.t. t. Then, using the fact that ϕ is zero at this point at $t = 0$ (initial condition), equation (4.19) is numerically integrated in time to obtain the analytical velocity potential at the free-surface/plate intersection point as a function of t.

The Eulerian form of the dynamic boundary condition on the free-surface is

$$\frac{\partial \phi}{\partial t} = -\frac{1}{2}\left(u^2 + v^2\right) - y. \tag{4.20}$$

Once again, for the free-surface/plate intersection point the value of y in the above equation is obtained from equation (4.8) and the values of u & v in the above equation are found by differentiating equations (4.1) & (4.8) respectively w.r.t. t. Equation (4.20) then gives the analytical partial time derivative of the velocity potential at the free-surface/plate intersection point as a function of t.

Figure 4.15 shows a comparison between the numerically predicted velocity potential at the free-surface/plate intersection point as a function of t and the analytically predicted velocity potential at the free-surface/plate intersection point as a function of t, for $\sigma = 1$. The numerical curve comes from run 8. As can be seen from the figure there is good agreement between the two curves, especially for $t < 0.075$ and $t > 0.2$.

Figure 4.16 shows a comparison between the numerically predicted partial time derivative of the velocity potential at the free-surface/plate intersection point as a function of t and the analytically predicted partial time derivative of the velocity potential at the free-surface/plate intersection point as a function of t, for $\sigma = 1$. As before, the numerical results come from run 8. Also, the quantity k is a parameter which alters the criterion for deciding when to use the "corner-correction" procedure. How k affects this criterion will be discussed later but for the moment just consider the case $k = 1$. This value of k leaves the basic criterion (described on page 66) unaltered.

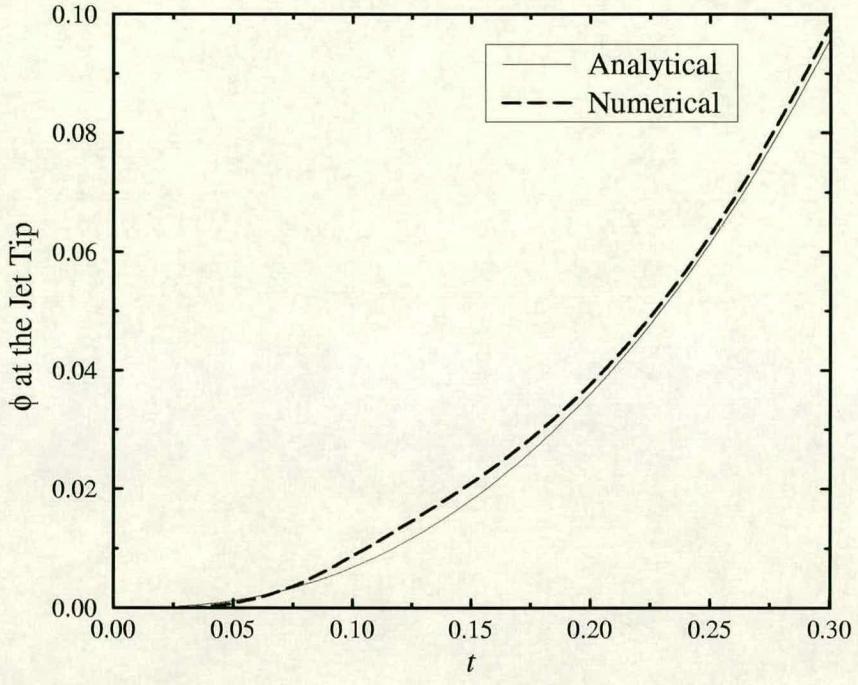

Figure 4.15: ϕ at the free-surface/plate intersection point against time t, for $\sigma = 1$. The numerical curve is for the case $\Delta t = 0.005$ & $\Delta x = 0.01$.

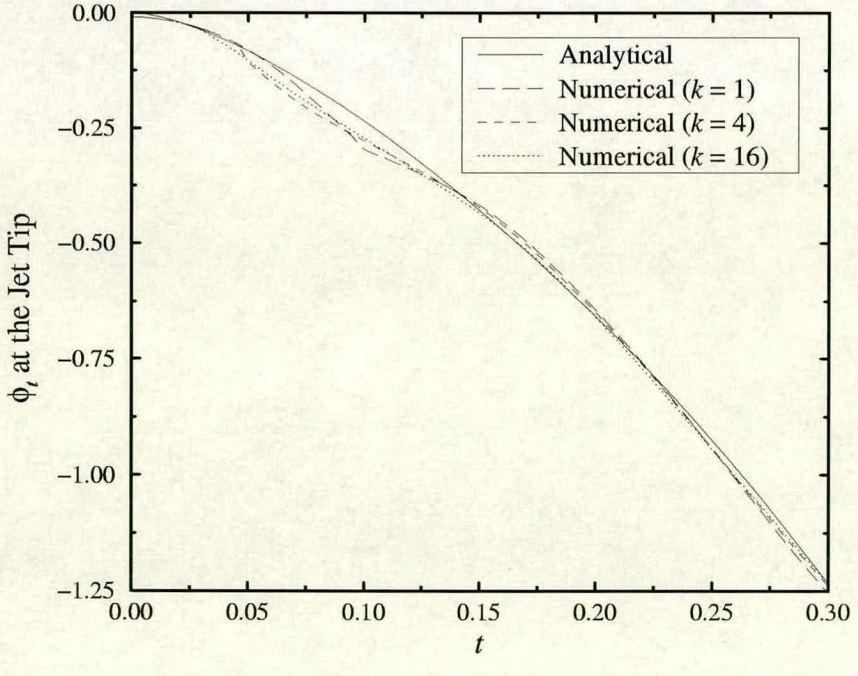

Figure 4.16: ϕ_t at the free-surface/plate intersection point against time t, for $\sigma = 1$. The numerical results are for the case $\Delta t = 0.005$ & $\Delta x = 0.01$. Also, k is a parameter related to the "corner-correction" procedure.

From Figure 4.16 it can be seen that there is good agreement between the numerically predicted ϕ_t and the analytically predicted ϕ_t, except near $t = 0.1$. It can also be seen that at $t = 0.1$ there is a sharp change in the gradient of the numerically predicted ϕ_t curve. This is because the "corner-correction" procedure is "switched off" at that time. Another look at the numerically predicted ϕ_t curve shows that it begins to diverge from the analytical curve around $t = 0.05$. This suggests that even better results might be obtained if the "corner-correction" procedure was "switched off" earlier.

As mentioned in subsection 3.5.2 the "corner-correction" procedure is only used if the associated discretised equation (equation (3.31)) does not destroy the diagonal dominance of the coefficient matrix A when it is placed in row N_1 of the linear system (3.13). That is, the "corner-correction" procedure is only used if

$$|\mathrm{Re}(c_5)\cos\theta - \mathrm{Im}(c_5)\sin\theta| > \sum_{i=1}^{4} |\mathrm{Im}(c_i)\cos\theta + \mathrm{Re}(c_i)\sin\theta|. \tag{4.21}$$

The above inequality is for the case of a paddle wavemaker making an angle θ with the vertical direction. However, in the present case the wavemaker is a vertical plate. Hence, for the present case $\theta = 0$ in inequality (4.21) and the criterion for the use of the "corner-correction" procedure becomes

$$|\mathrm{Re}(c_5)| > \sum_{i=1}^{4} |\mathrm{Im}(c_i)|. \tag{4.22}$$

This criterion can be tightened by multiplying the RHS of the above inequality by a constant $k > 1$. Consequently, this produces the new criterion

$$|\mathrm{Re}(c_5)| > k \sum_{i=1}^{4} |\mathrm{Im}(c_i)|. \tag{4.23}$$

This new criterion ensures that the "corner-correction" procedure is used less often than if criterion (4.22) had been used instead.

In figure 4.15 the numerically predicted ϕ curves for the cases $k = 4$ & $k = 16$ are not shown because they are virtually indistinguishable from the numerically

predicted ϕ curve[3] already shown. In figure 4.16 the numerically predicted ϕ_t curves for the cases $k = 4$ & $k = 16$ are shown because they are sufficiently different from the numerically predicted ϕ_t curve for the case $k = 1$. For the case $k = 4$ the "corner-correction" procedure is "switched off" at $t = 0.045$ and for the case $k = 16$ it is "switched off" at $t = 0.025$. As can be seen from figure 4.16 there is a slight reduction in the maximum absolute error[4] in ϕ_t with increasing k. However, it was decided that this improvement was not significant enough to merit changing the criterion for using the "corner-correction" procedure. Hence, for the rest of this study k is kept at a value of 1.

Finally, in figure 4.16 note that the numerically predicted value[5] of ϕ_t at $t = 0$ is slightly negative, whereas its exact mathematical value is zero. This small negative value is the value that the "corner-correction" procedure changes ϕ_t to in order to smooth out the $z\log z$ type singularity in $\beta_t(z)$ at the free-surface/plate intersection point at $t = 0$ (see equation (4.14)).

4.3.5 Mid-Term Solutions & Free-Surface Instabilities

Now consider results of the present BIM for the accelerating plate problem and for times which go beyond the time when the small-time analytical solution ceases to be valid. According to King & Needham [35] the small-time analytical solution is valid provided

$$t \ll \min\{O(1), O(e^{-1/\sigma})\}. \tag{4.24}$$

Figure 4.17 shows numerical free-surface profiles for runs 3 & 4 and for times which include and go beyond the times when the small-time analytical solution

[3]This numerically predicted ϕ curve corresponds to the case $k = 1$.

[4]The error in ϕ_t is taken to be the difference between the numerically predicted value and the analytically predicted value.

[5]All three numerically predicted ϕ_t curves in figure 4.16 are the same up until $t = 0.025$ when the "corner-correction" procedure is "switched off" for the case $k = 16$.

is valid. For run 3 these times are $t = 0.05, 0.075, 0.1, \ldots, 0.375$ and for run 4 they are $t = 0.05, 0.075, 0.1, \ldots, 0.425$. Figure 4.17 clearly shows how the "kink", initially seen in the inner solution of the small-time analytical solution, grows with time. The figure also shows that the numerical free-surface profiles for the two different Δx's agree very well right up until the last free-surface profile shown for run 3 at $t = 0.375$. Unfortunately, due to the growth of free-surface instabilities, computations for run 3 break down shortly after this time. Very close examination of the last free-surface profile shown for run 3 reveals these free-surface instabilities near the plate but they are too small to be seen in figure 4.17. Computations for run 4 last slightly longer; run 4 breaks down shortly after the last free-surface profile shown in the figure. Again, there are free-surface instabilities near the plate on this last free-surface profile but again they are too small to be seen properly. The numerical free-surface profiles for runs 1, 2 & 5 are not shown in figure 4.17. However, these free-surface profiles agree very well with those of runs 3 & 4 and the only differences between the various runs are the times to breakdown.

Similarly, figure 4.18 shows numerical free-surface profiles for runs 8 & 9 and for times which include and go beyond the times when the small-time analytical solution is valid. For run 8 these times are $t = 0.05, 0.1, 0.15, \ldots, 0.55$ and for run 9 they are $t = 0.05, 0.1, 0.15, \ldots, 0.75$. Once again, the free-surface profiles for the two different Δx's agree very well right up until one run (run 8) becomes unstable. Furthermore, the numerical free-surface profiles for runs 6, 7 & 10 are not shown in figure 4.18 but these profiles are almost indistinguishable from those of runs 8 & 9 and the only differences between the various runs are the times to breakdown. The main difference between figure 4.18 and figure 4.17 is that the free-surface instabilities are much more evident in figure 4.18.

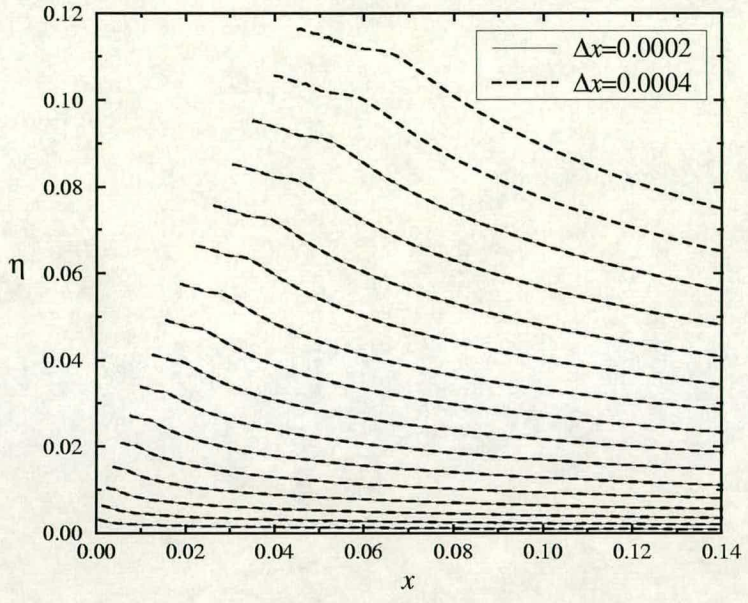

Figure 4.17: Numerical free-surface profiles from two different runs for $\sigma = \frac{1}{4}$. For both runs the time-step used was $\Delta t = 0.0005$. For $\Delta x = 0.0002$ the free-surface profiles are for the times $t = 0.05, 0.075, 0.1, \ldots, 0.375$ and for $\Delta x = 0.0004$ they are for the times $t = 0.05, 0.075, 0.1, \ldots, 0.425$.

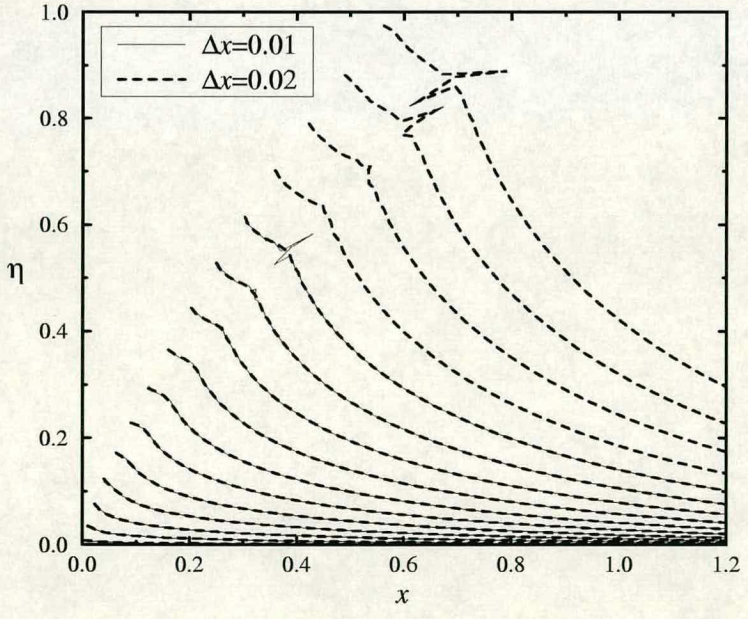

Figure 4.18: Numerical free-surface profiles from two different runs for $\sigma = 1$. For both runs the time-step used was $\Delta t = 0.005$. For $\Delta x = 0.01$ the free-surface profiles are for the times $t = 0.05, 0.1, 0.15, \ldots, 0.55$ and for $\Delta x = 0.02$ they are for the times $t = 0.05, 0.1, 0.15, \ldots, 0.75$.

The fact that runs 1 to 10 all break down is to be expected. This is because for this accelerating plate problem a lot of energy is being fed into the system and the rate at which this energy is being fed in is increasing with time.

Figures 4.19 and 4.20 show closeups of the free-surface instabilities affecting run 3 in figure 4.17 and run 8 in figure 4.18, respectively. In these figures the free-surface nodes are shown and they are indicated by circles. By close examination of figures 4.19 & 4.20 it can be seen that free-surface instabilities seem to emanate from regions where the nodes are tightly packed. This observation is consistent with the stability of the present BIM being determined by a local Courant type condition. A local Courant type stability condition is a condition which requires that the time-step must be less than a certain value which depends[6] on the local node spacing. If somewhere on the free-surface this condition is violated then free-surface instabilities will occur there.

Further evidence that the stability of the present BIM is determined by a local Courant type condition can be obtained from table 4.3. This table shows both the number of time-steps to breakdown and the time to breakdown for each of the 10 runs. From the table it can be seen that for a fixed Δt the time to breakdown increases as Δx increases (see runs 2, 3 & 4 and runs 7, 8 & 9). Also, for a fixed Δx the time to breakdown decreases as Δt increases (see runs 3 & 5 and runs 8 & 10). These two observations support the assertion that a local Courant type condition applies. Two observations which seem to go against this assertion come from comparing run 1 with run 3 and run 6 with run 8. In both cases Δx is the same for the two runs but the time to breakdown for the run with larger Δt is actually slightly larger, rather than smaller, than the time to breakdown for the

[6]Precisely what the relationship is between this value and the local node spacing depends on the particular numerical scheme being studied, however the relationship must be such that if the local node spacing reduces then so must this value.

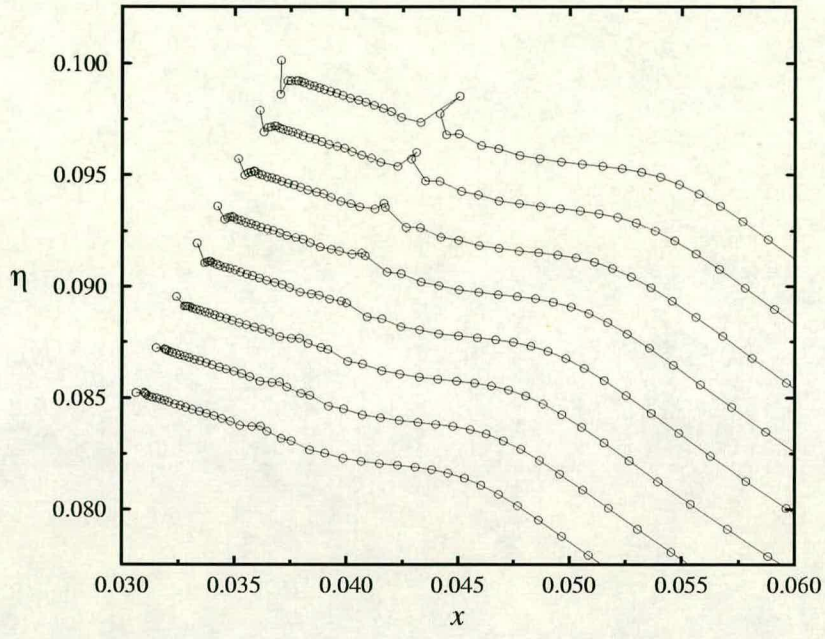

Figure 4.19: The growth of two free-surface instabilities for the case $\sigma = \frac{1}{4}$, $\Delta t = 0.0005$ & $\Delta x = 0.0002$. The numerical free-surface profiles are for the times $t = 0.35, 0.355, 0.36, \ldots, 0.385$.

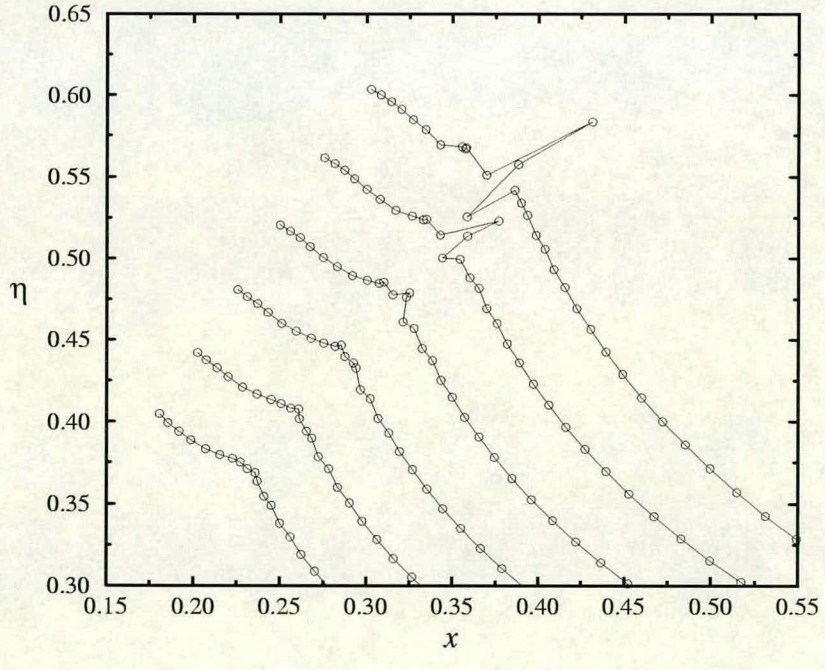

Figure 4.20: The growth of a free-surface instability for the case $\sigma = 1$, $\Delta t = 0.005$ & $\Delta x = 0.01$. The numerical free-surface profiles are for the times $t = 0.425, 0.45, 0.475, \ldots, 0.55$.

σ	Run	Δt	Δx	Number of time-steps to breakdown	Time to breakdown
$\frac{1}{4}$	1	0.00025	0.0002	1411	0.35275
	2	0.0005	0.0001	305	0.1525
	3	0.0005	0.0002	774	0.387
	4	0.0005	0.0004	873	0.4365
	5	0.001	0.0002	260	0.26
1	6	0.0025	0.01	224	0.56
	7	0.005	0.005	104	0.52
	8	0.005	0.01	114	0.57
	9	0.005	0.02	160	0.8
	10	0.01	0.01	53	0.53

Table 4.3: The number of time-steps to breakdown and the time to breakdown for each of the 10 runs.

run with the smaller Δt. This apparent contradiction could possibly be explained by the fact that although runs 1 & 6 breakdown before runs 3 & 8 respectively, runs 1 & 6 perform substantially more time-steps than runs 3 & 8 respectively. Furthermore, since each time-step will introduce a very small error the number of time-steps performed will be a factor in influencing when a run breaks down.

4.3.6 Volume & Energy Conservation

In addition to comparing the results of the present BIM for the accelerating plate problem with the small-time analytical solution it is also necessary to check volume & energy conservation (see subsection 3.5.5).

Figures 4.21 & 4.22 show the relative error in the volume against time t for the 10 different runs. As mentioned on page 95 the computational domain is truncated by a vertical end wall at $x = 5$. Therefore, since the undisturbed depth of the strip of water is 1, the volume should be 5. Consequently, the relative error in the volume is given by

$$\text{relative error in volume} = \frac{\text{volume} - 5}{5}.$$

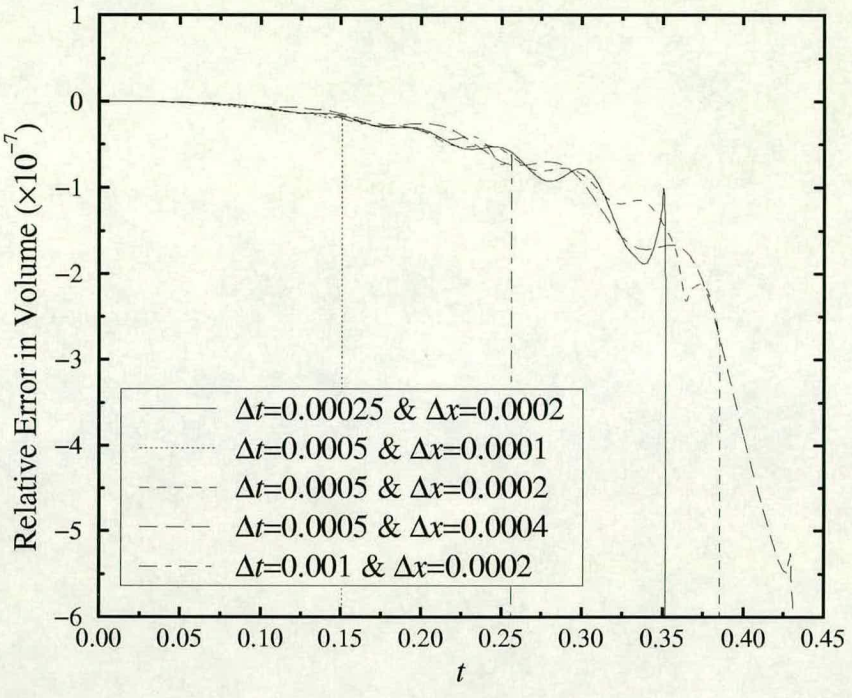

Figure 4.21: The relative error in the volume against time t for $\sigma = \frac{1}{4}$. The results come from runs 1, 2, 3, 4 & 5.

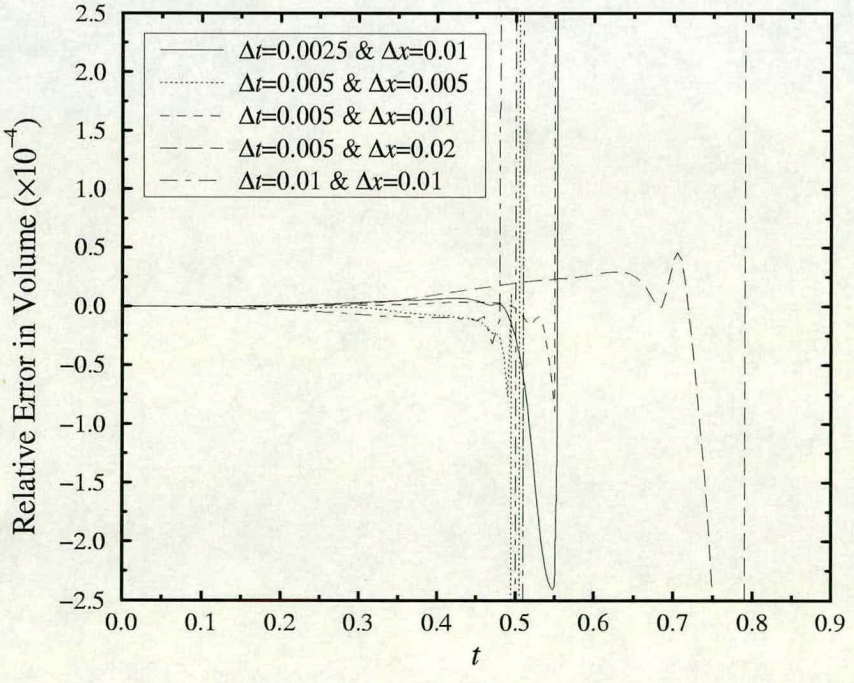

Figure 4.22: The relative error in the volume against time t for $\sigma = 1$. The results come from runs 6, 7, 8, 9 & 10.

As can be seen from figures 4.21 & 4.22 volume is conserved very well for each run right up until that run starts to break down.

Figures 4.23 & 4.24 show the power supplied by the plate and the rate of change of the energy of the fluid against time t for run 4 & run 9 respectively. As can be seen from these figures, energy is conserved very well for both runs right up until breakdown. In fact, for run 4 in figure 4.23 the rate of change of the energy of the fluid is indistinguishable from the power supplied by the plate. The results from runs 1, 2, 3 & 5 are not shown in figure 4.23 and the results from runs 6, 7, 8 & 10 are not shown in figure 4.24 because these results are virtually identical to those already displayed, except that the times to breakdown are different.

A much better way to see how well the present BIM conserves energy for this accelerating plate problem is to look at the difference between the rate of change of the energy of the fluid and the power supplied by the plate. Figures 4.25 & 4.26 show the rate of change of the energy of the fluid minus the power supplied by the plate against time t for the 10 different runs. Once again, these figures show that energy is conserved very well for each run right up until that run starts to break down.

4.3.7 Long-Term Solutions with Smoothing & Regridding

In this subsection results are presented for the case when the smoothing & regridding procedure of subsection 3.5.3 is added to the present BIM. This smoothing & regridding procedure is introduced to try and suppress free-surface instabilities like those seen in figures 4.18 to 4.20. The parameters which govern this procedure are: the smoothing parameter $\lambda \in (0,1)$ (λ closer to 0 means more smoothing and λ closer to 1 means better interpolating), the desired number of nodes on a regridded free-surface $N_{1_{\text{desired}}}$, the maximum and minimum node spacings $h_{\max}$ and $h_{\min}$, and the number of time-steps between each smoothing

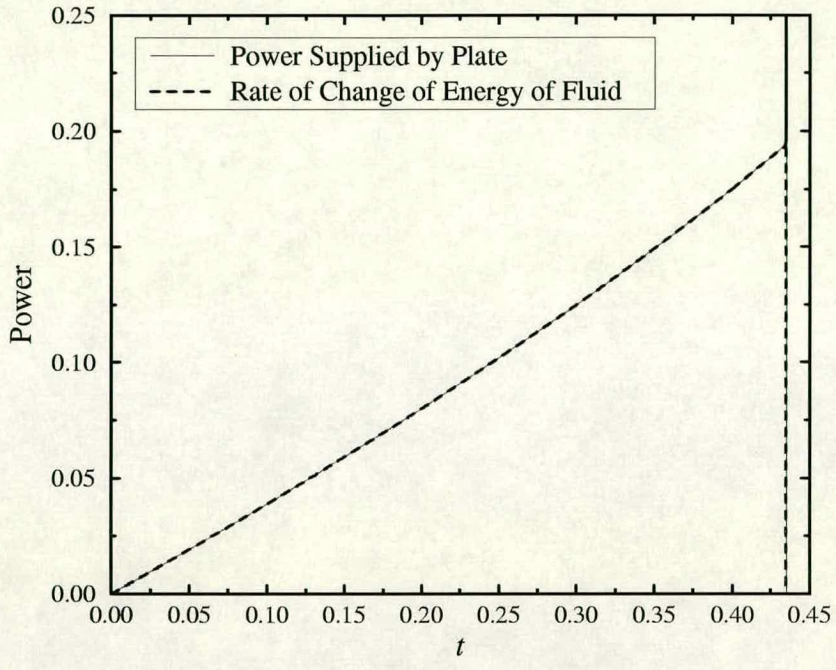

Figure 4.23: The power supplied by the plate and the rate of change of the energy of the fluid against time t for $\sigma = \frac{1}{4}$, $\Delta t = 0.0005$ & $\Delta x = 0.0004$.

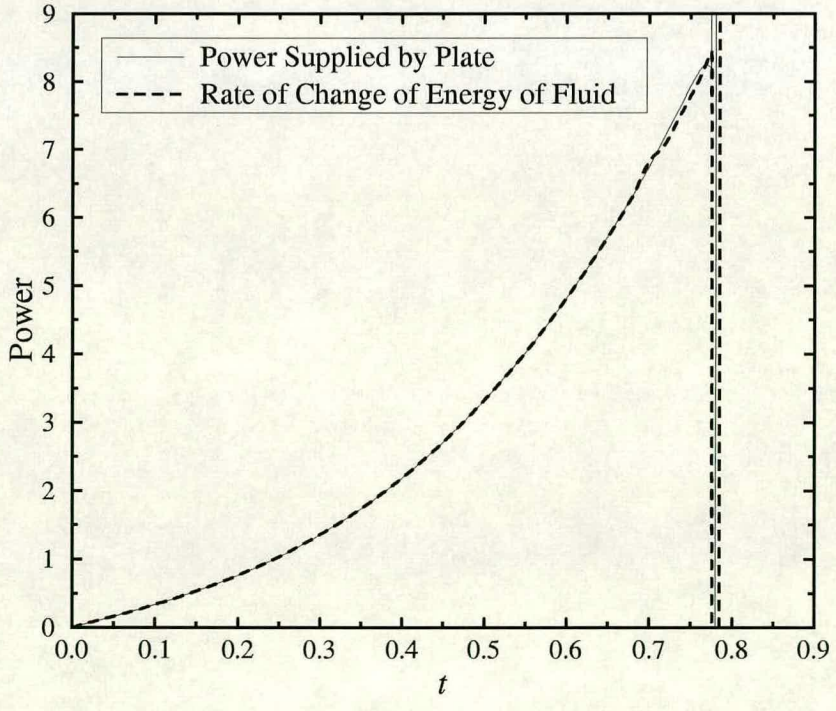

Figure 4.24: The power supplied by the plate and the rate of change of the energy of the fluid against time t for $\sigma = 1$, $\Delta t = 0.005$ & $\Delta x = 0.02$.

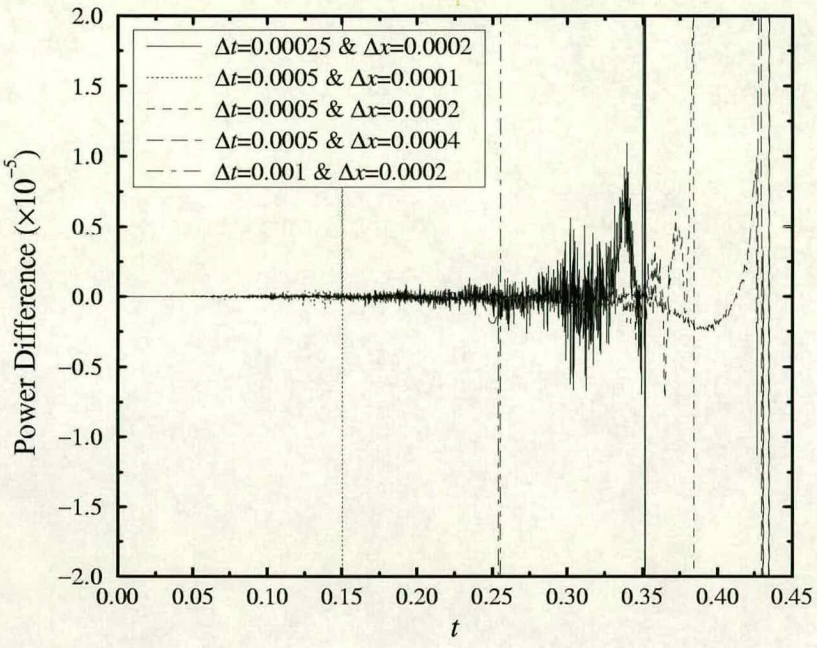

Figure 4.25: The rate of change of the energy of the fluid minus the power supplied by the plate against time t for $\sigma = \frac{1}{4}$. The results come from runs 1, 2, 3, 4 & 5.

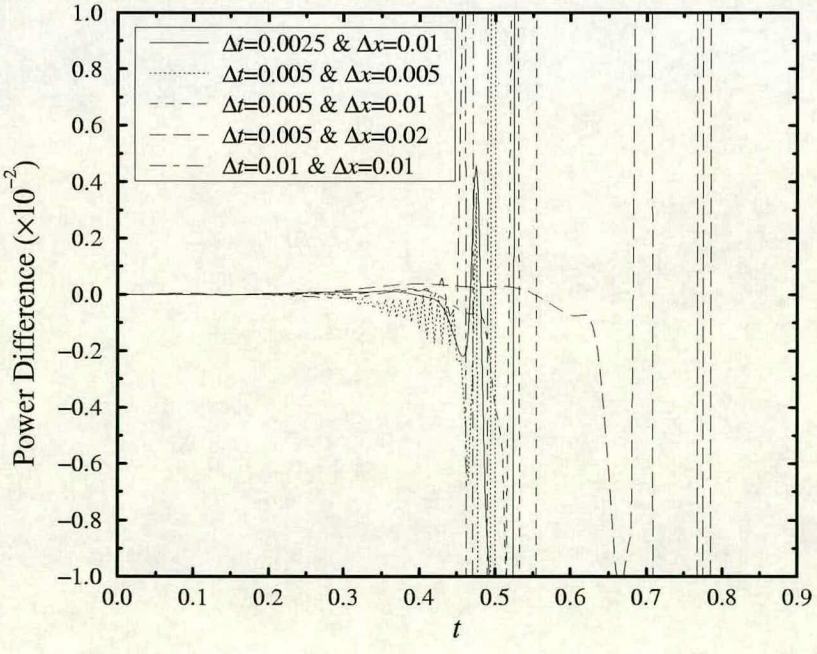

Figure 4.26: The rate of change of the energy of the fluid minus the power supplied by the plate against time t for $\sigma = 1$. The results come from runs 6, 7, 8, 9 & 10.

& regridding. During test runs it was found that setting $h_{\max}$ to equal $5h_{\min}$ was a good policy. This policy has the advantage of reducing the relatively large number (5) of degrees of freedom associated with using the smoothing & regridding procedure by 1. Also, in this subsection only the case $\sigma = 1$ is considered.

The first step is to rerun one of the runs shown in figure 4.18 but this time with smoothing & regridding. The case to be rerun is run 9. In order that a meaningful comparison can be carried out between the case with smoothing & regridding and the case without, the parameters which control the smoothing & regridding procedure must be chosen with care. Firstly, $h_{\min}$ must equal Δx, and for run 9 the value of Δx was 0.02. Secondly, $N_{1_{\text{desired}}}$ should equal 78, which was the number of nodes on the free-surface for run 9 (see table 4.1). This then leaves two free parameters to control the smoothing & regridding procedure. The smoothing parameter λ is set to 0.9999999 and the number of time-steps between each smoothing & regridding is set to 10.

Figure 4.27 is a redrawing of figure 4.18 but this time only with the numerical free-surface profiles from run 9 and the corresponding numerical free-surface profiles from the run with smoothing & regridding. The figure shows how successful the smoothing & regridding procedure is at suppressing free-surface instabilities. The figure also shows that during the time that the run without smoothing & regridding is stable the run with smoothing & regridding agrees very well with it. This indicates that careful use of the smoothing & regridding procedure can not only stabilise the present BIM but also not adversely affect its accuracy. In fact, the run with smoothing & regridding, shown in figure 4.27, lasts over twice as long[7] as the run without (run 9). The run with smoothing & regridding breaks

[7]Even with smoothing & regridding the present BIM will eventually break down when it is applied to the accelerating plate problem because a lot of energy is being fed into the system and the rate at which this energy is being fed in is increasing with time.

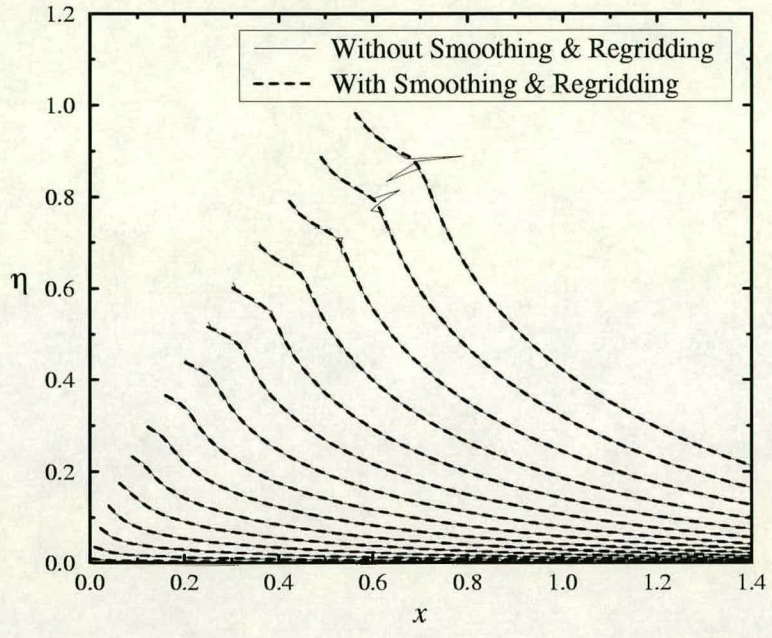

Figure 4.27: Numerical free-surface profiles for the run without smoothing & regridding (run 9) and the run with smoothing & regridding, for $\sigma = 1$. The free-surface profiles are for the times $t = 0.05, 0.1, 0.15, \ldots, 0.75$.

down at time-step 386 (time $t = 1.93$) and from table 4.3 the run without breaks down at time-step 160 (time $t = 0.8$).

Figure 4.28 is the same as figure 4.27 except that it also shows numerical free-surface profiles for later times for the run with smoothing & regridding. From the figure notice how much longer the run with smoothing & regridding remains stable when compared to the run without smoothing & regridding. Also notice that at the vertical reflecting wall at the far end of the computational domain ($x = 5$) the free-surface elevation is beginning to rise. This means that for the larger times shown in figure 4.28 ($t \gtrsim 1$) the problem of a vertical plate accelerating into a *semi-infinite* strip of water is no longer being properly modelled. Consequently, for runs which last longer than $t \approx 1$ the far end wall must be placed further away from the rest position of the plate.

In the rest of this subsection the far end wall is placed at $x = 40$ so that very

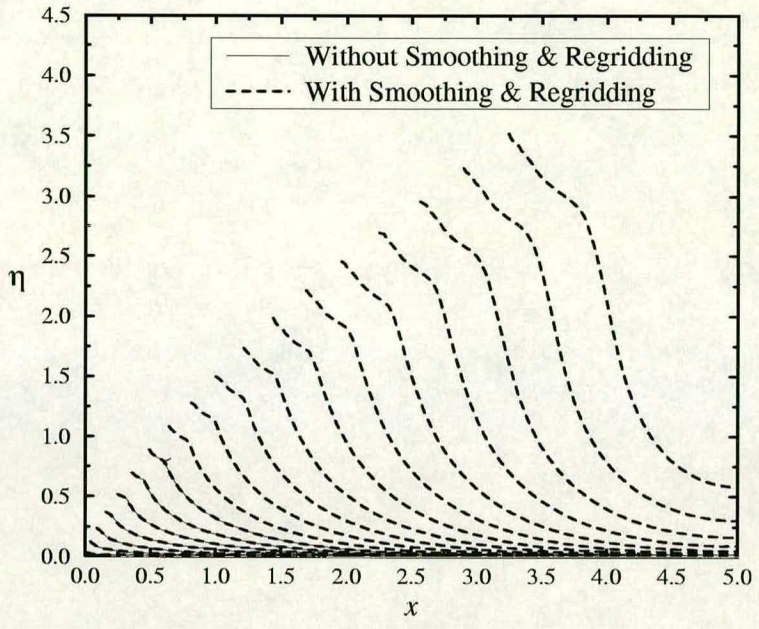

Figure 4.28: Numerical free-surface profiles for the run without smoothing & regridding (run 9) and the run with smoothing & regridding, for $\sigma = 1$. For run 9 the free-surface profiles are for the times $t = 0.1, 0.2, 0.3, \ldots, 0.7$ and for the run with smoothing & regridding they are for the times $t = 0.1, 0.2, 0.3, \ldots, 1.8$.

long-term simulations can be run. For these simulations the values of Δt & Δx, as well as the number of nodes on the plate, the bottom and the far end wall are all kept the same as they were for run 9. In addition, the parameter $N_{1_{\text{desired}}}$ is taken to be the nearest integer to

$$\frac{\text{length of tank}}{\text{average of } h_{\min} \text{ and } h_{\max}} + 1 = \frac{40}{\frac{1}{2}(h_{\min} + h_{\max})} + 1 = \frac{40}{3h_{\min}} + 1$$

and the number of time-steps between each smoothing & regridding is taken to be 10. This then leaves two free parameters to fully determine a simulation, namely the smoothing parameter λ and the minimum node spacing $h_{\min}$.

Figure 4.29 shows numerical free-surface profiles for the three simulations which lasted the longest out of those tried.

1. The simulation with $\lambda = 0.99999$ & $h_{\min} = 0.04$ broke down at time-step 896 (time $t = 4.48$).

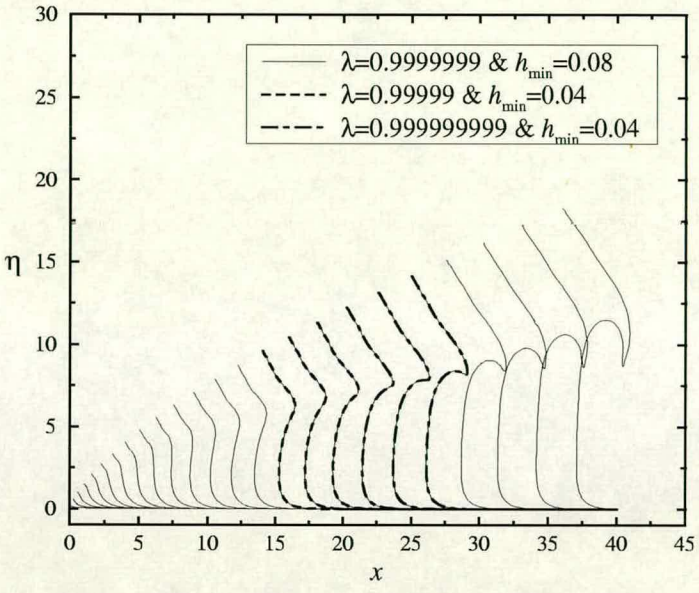

Figure 4.29: The overturning of the free-surface for $\sigma = 1$. For the case $\lambda = 0.9999999$ & $h_{\min} = 0.08$ the free-surface profiles are for the times $t = 0.25, 0.5, 0.75, \ldots, 6$, for the case $\lambda = 0.99999$ & $h_{\min} = 0.04$ they are for the times $t = 3.75$, 4 & 4.25 and for the case $\lambda = 0.999999999$ & $h_{\min} = 0.04$ they are for the times $t = 4.5$, 4.75 & 5.

2. The simulation with $\lambda = 0.999999999$ & $h_{\min} = 0.04$ broke down at time-step 1030 (time $t = 5.15$).

3. The simulation with $\lambda = 0.9999999$ & $h_{\min} = 0.08$ did not break down but continued to the end of the run at time-step 1200 (time $t = 6$).

As can be seen from figure 4.29 the free-surface eventually starts to overturn. Figure 4.29 also shows that there can be great confidence in the accuracy of the numerical free-surface profiles displayed. This is because of the very good agreement between the free-surface profiles from the three different simulations shown in the figure.

Even more confidence that the free-surface profiles shown in figure 4.29 are correct comes from looking at volume and energy conservation.

Figure 4.30 shows the relative error in the volume against time t for the longest

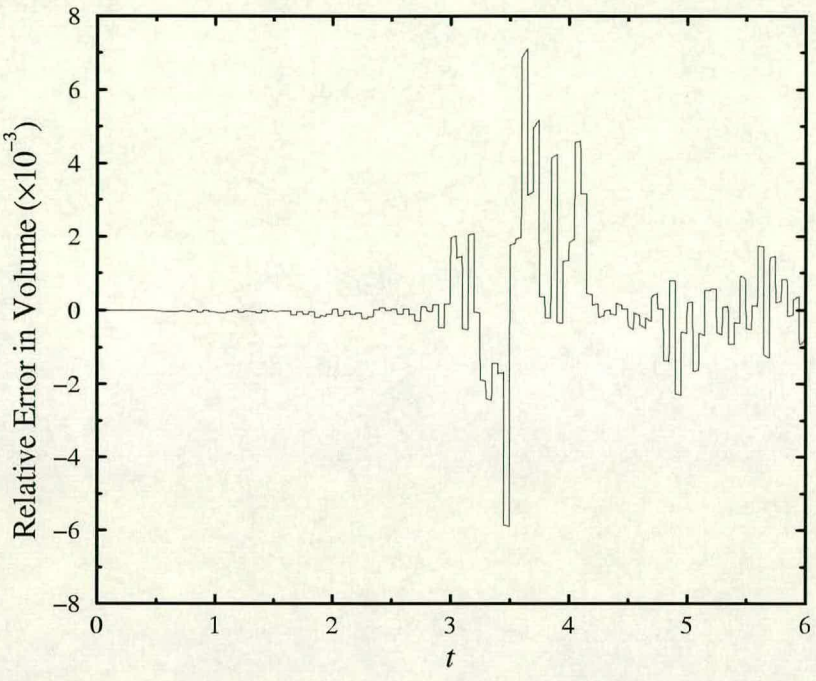

Figure 4.30: The relative error in the volume for the run with $\lambda = 0.9999999$ & $h_{\text{min}} = 0.08$.

running simulation in figure 4.29 ($\lambda = 0.9999999$ & $h_{\text{min}} = 0.08$). As can be seen, volume is conserved very well for this simulation; the maximum absolute relative error in the volume is less than 0.75%. In the figure the regular discontinuous jumps in the relative error are due to the fact that the free-surface is being smoothed & regridded at these times.

Figure 4.31 shows the energy supplied by the plate and the energy of the fluid against time t for the simulation with $\lambda = 0.9999999$ & $h_{\text{min}} = 0.08$. As can be seen from this figure energy is conserved very well for this simulation.

Finally, to give an example of what the results shown in figure 4.29 might mean in reality consider the following situation. Suppose there is a very long waveflume which is 0.5m wide and which has very high walls. Suppose also that this waveflume has a very powerful, very high piston wavemaker and that it is filled to an undisturbed depth h of 1m. Then if x and η in figure 4.29 are measured

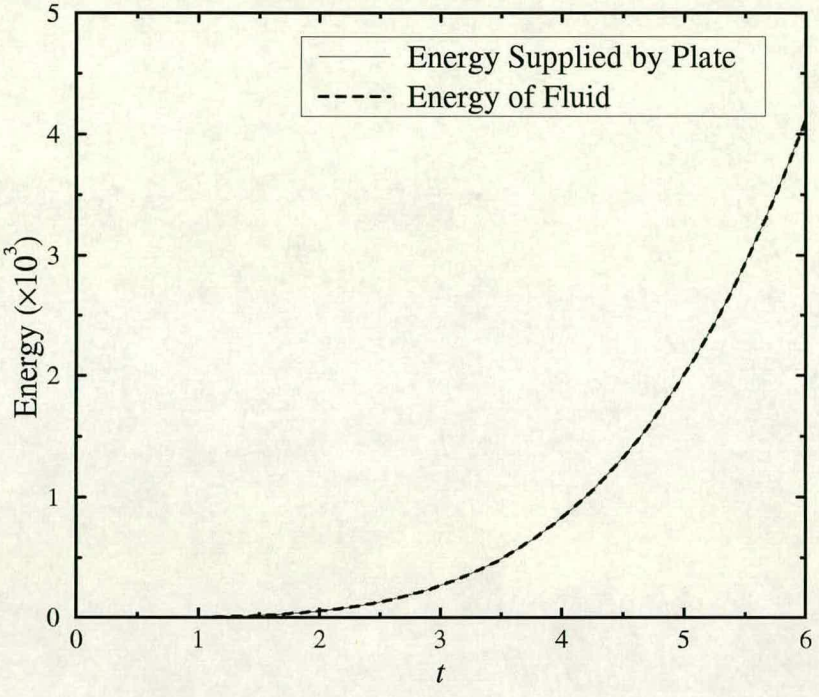

Figure 4.31: The energy supplied by the plate and the energy of the fluid for the run with $\lambda = 0.9999999$ & $h_{\min} = 0.08$.

in metres the free-surface profiles shown in the figure are the free-surface profiles for the case when the above piston wavemaker is accelerated from rest at $2g$ into the undisturbed fluid. In that case the last free-surface profile shown in the figure corresponds to a time $t = 1.916$s. At this time the wavemaker has travelled 36m from its rest position and it is travelling at 37.59ms^{-1} (or 84.08mph). Also, at this time the height of the free-surface at the wavemaker is 18.28m and the power being supplied by the wavemaker to the fluid[8] is 41.72MW.

4.4 Summary of Chapter 4

In this chapter the results of the present BIM were compared against a small-time analytical solution for an extreme potential flow at the intersection between

[8]The dimensional power per unit tank width being supplied by the wavemaker is obtained from the non-dimensional power per unit tank width being supplied by the wavemaker by multiplying it by $\rho g^{\frac{3}{2}} h^{\frac{5}{2}}$.

a free-surface and a body. This is the flow caused by a vertical plate uniformly accelerating from rest into an initially undisturbed semi-infinite strip of inviscid, incompressible fluid of finite depth h. The author believes that this is the first time that such a comparison has been made.

In addition to the above comparison a previously unnoticed feature of the analytical solution was identified and presented in this chapter. This feature is the "kink" near the plate in the inner analytical solution. Since this feature is so close to the main point of interest, namely the free-surface/plate intersection point, it is very important.

After this "kink" in the inner analytical solution was examined the present BIM was then applied to the above accelerating plate problem.

Initially, the "corner-correction" procedure of subsection 3.5.2 was not used and it was found that the numerical scheme broke down almost immediately. The reason for this breakdown was shown to be the $z\log z$ type singularity in $\beta_t(z)$ at the free-surface/plate intersection point at $t = 0$. Following this it was decided that the "corner-correction" procedure should be used for the rest of this study.

Although the "corner-correction" procedure smoothes out singularities in $\beta(z)$ and $\beta_t(z)$ at free-surface/body intersection points, and in so doing slightly alters the mathematical problem being solved, it was found that there was very good agreement between the numerical results and the small-time analytical solution for the accelerating plate problem. The BIM managed to predict very well the outer solution, the inner solution, the height of the free-surface at the plate and the velocity potential (& its partial time derivative) at the free-surface/plate intersection point. In addition, if the node spacing was small enough, the BIM managed to qualitatively predict the "kink" in the inner analytical solution. How-

ever, the BIM was not able to fully resolve the "kink"[9] because a very small node spacing would require an extremely small time-step in order not to violate a local Courant type stability condition.

Next, the results of the present BIM for the accelerating plate problem and for times after the time when the small-time analytical solution ceases to be valid were examined. These results appear to be very good: both volume and energy are conserved very well. However, the numerical scheme eventually broke down due to free-surface instabilities.

Finally, the present BIM, with the smoothing & regridding procedure of subsection 3.5.3, was applied to the accelerating plate problem. It was found that careful use of the smoothing & regridding procedure successfully suppressed free-surface instabilities, enabling very long-term runs to be performed. A very long-term run was carried out for the case of the plate accelerating at $2g$ and it was found that the free-surface began to overturn.

[9]The "kink" (which is actually a complicated oscillation) is really a very small feature, even on the scale of the inner region it is small, and so resolving the "kink" with the BIM is very difficult.

Chapter 5

Results Part 2: The Sloshing Wave Problem

In this chapter the results of the present BIM are compared against the results of another numerical method. This other numerical method is a Volume of Fluid (VOF) method which was developed by A. Chopra at the University of Edinburgh [7] (VOF methods are described in subsection 2.4.2). The defining features of this particular VOF method are:

1. The assumed free-surface shape is "piecewise constant stair-stepped".

2. The free-surface normals are calculated using a multi-dimensional technique.

3. The cell fluid volume fraction function F is advected at each time-step using a multi-dimensional technique.

The problem which these two numerical methods are applied to is of a wave sloshing in a tank. This problem was original proposed by Det Norske Veritas[1] as a test problem in a comparative study of modelling techniques for nonlinear free-surface flows [45]. The details of the problem are as follows.

[1] An independent Norwegian foundation who produced a report as part of a Norwegian Joint Industry Project.

The length of the tank is 160m and its depth is 70m. Also, at $t = 0$ the fluid is at rest and the free-surface elevation is given by

$$\eta(x,0) = \alpha \left[1 - \left(\frac{x}{\beta} \right)^2 \right] e^{-\left(\frac{x}{\gamma}\right)^2}, \tag{5.1}$$

where $\alpha = 12\text{m}$, $\beta = 53\text{m}$ and $\gamma = 76\text{m}$.

Figures 5.1 to 5.6 show the computed free-surface profiles from the two methods at two second intervals. Both methods used a fixed time-step $\Delta t = 0.05\text{s}$. For the VOF method the computational domain was discretised into $1\text{m} \times 1\text{m}$ cells. For the BIM the free-surface was discretised by 100 nodes[2]; each end wall was discretised by 35 equally-spaced nodes and the bottom was discretised by 50 equally-spaced nodes. Also, for the BIM the "corner-correction" procedure of subsection 3.5.2 was used but the smoothing & regridding procedure of subsection 3.5.3 was not.

As can be seen from figures 5.1 to 5.6 the free-surface profiles for the two different methods agree very well. However, small discrepancies do begin to appear as time progresses. These discrepancies are thought to be due to the higher order nature of the BIM making its results more accurate. For example, the BIM uses second-order explicit time-stepping whereas the VOF method only uses first-order explicit time-stepping (Euler's method).

[2]Initially, these nodes were equally spaced in the horizontal direction.

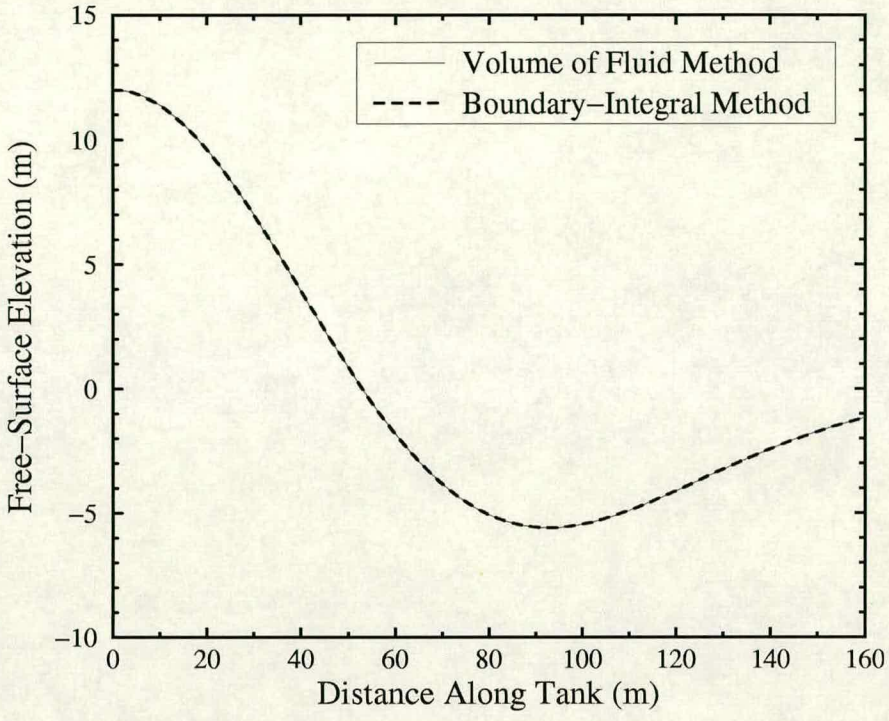

Figure 5.1: VOF and BIM free-surface profiles at $t = 0$s.

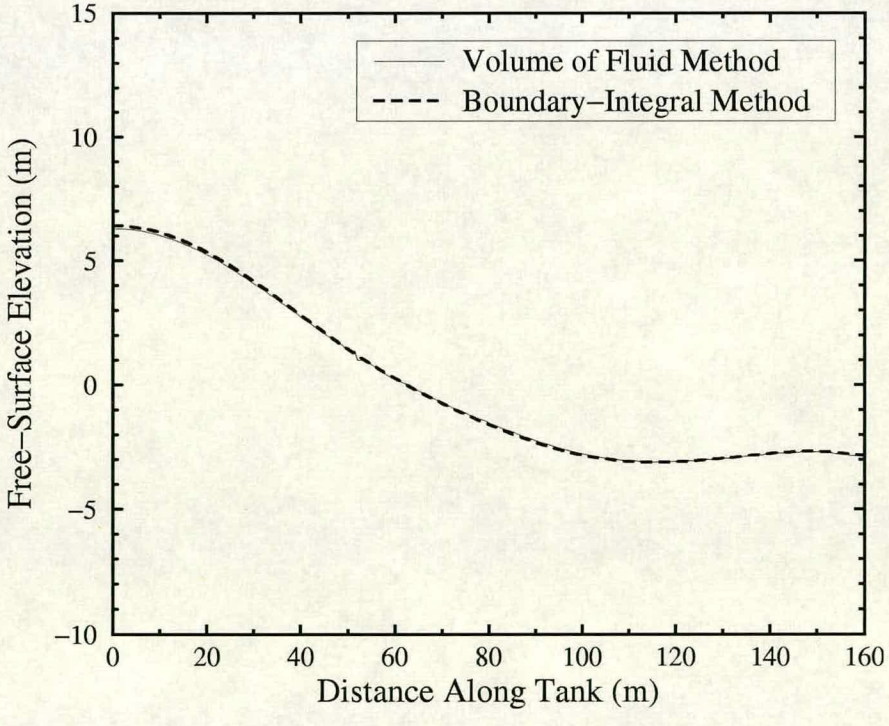

Figure 5.2: VOF and BIM free-surface profiles at $t = 2$s.

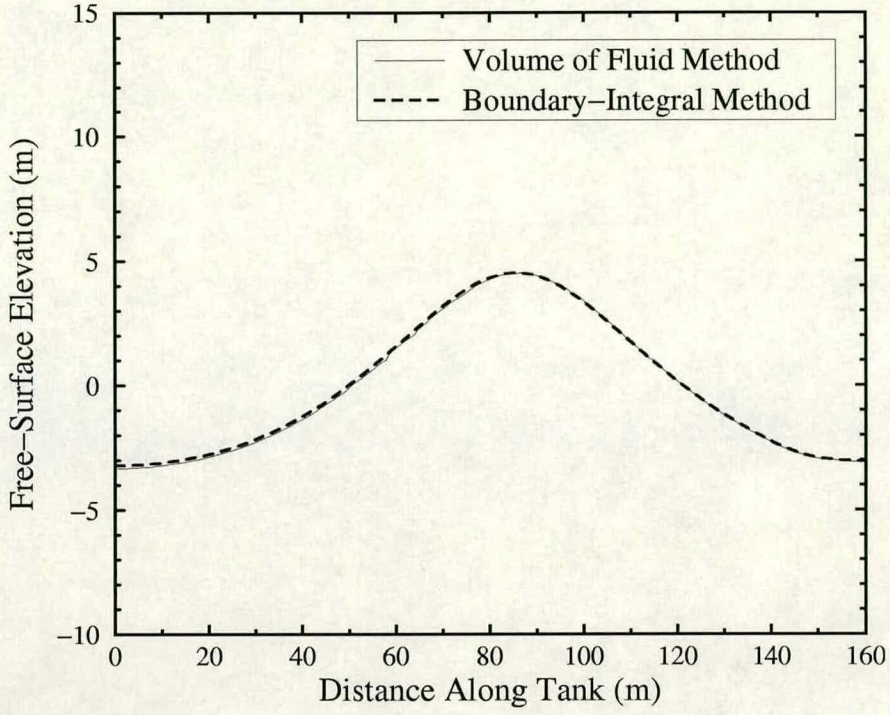

Figure 5.3: VOF and BIM free-surface profiles at $t = 4$s.

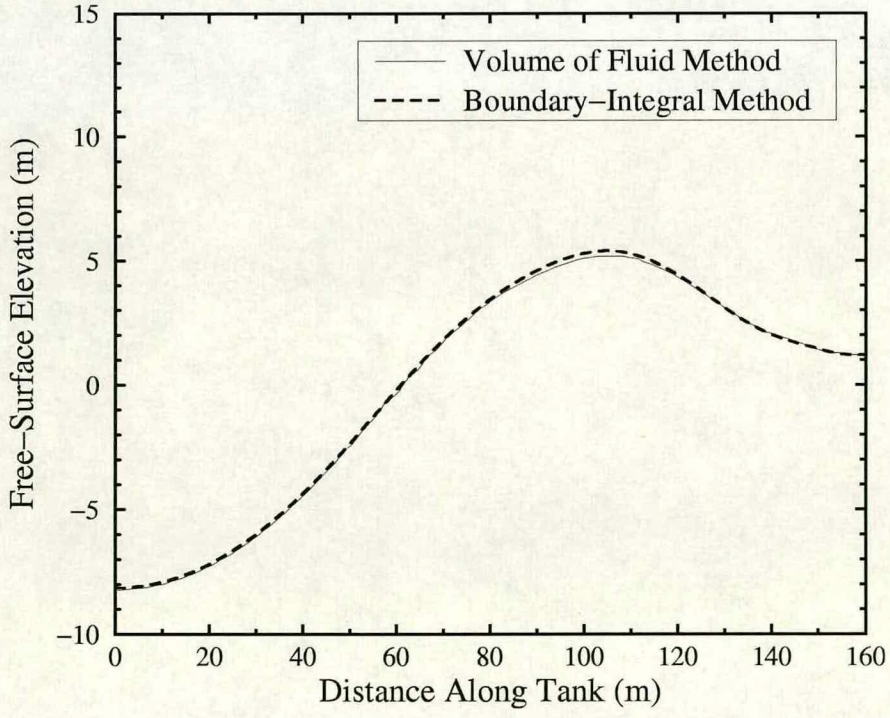

Figure 5.4: VOF and BIM free-surface profiles at $t = 6$s.

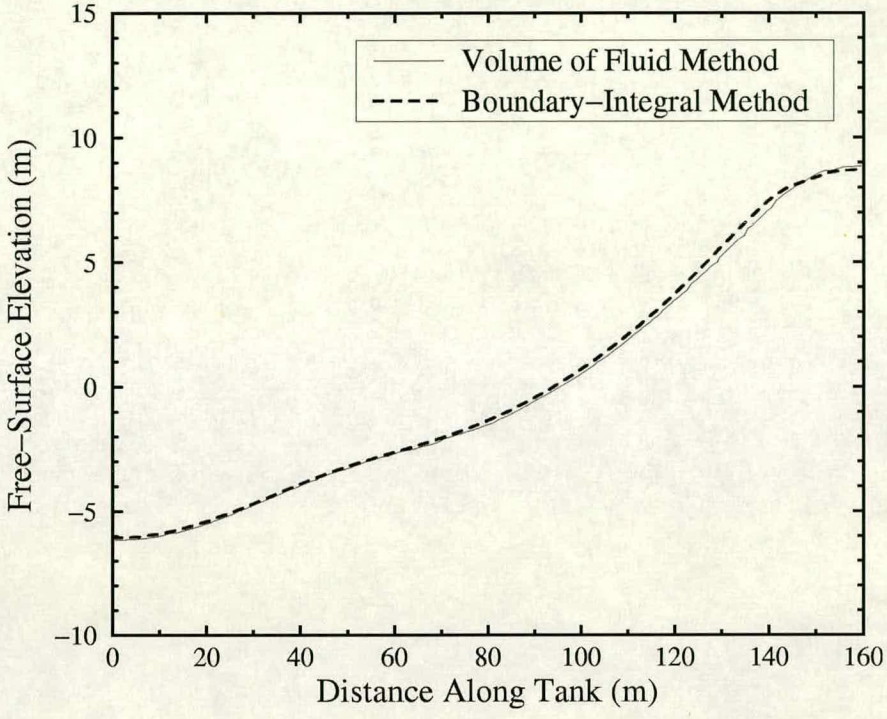

Figure 5.5: VOF and BIM free-surface profiles at $t = 8$s.

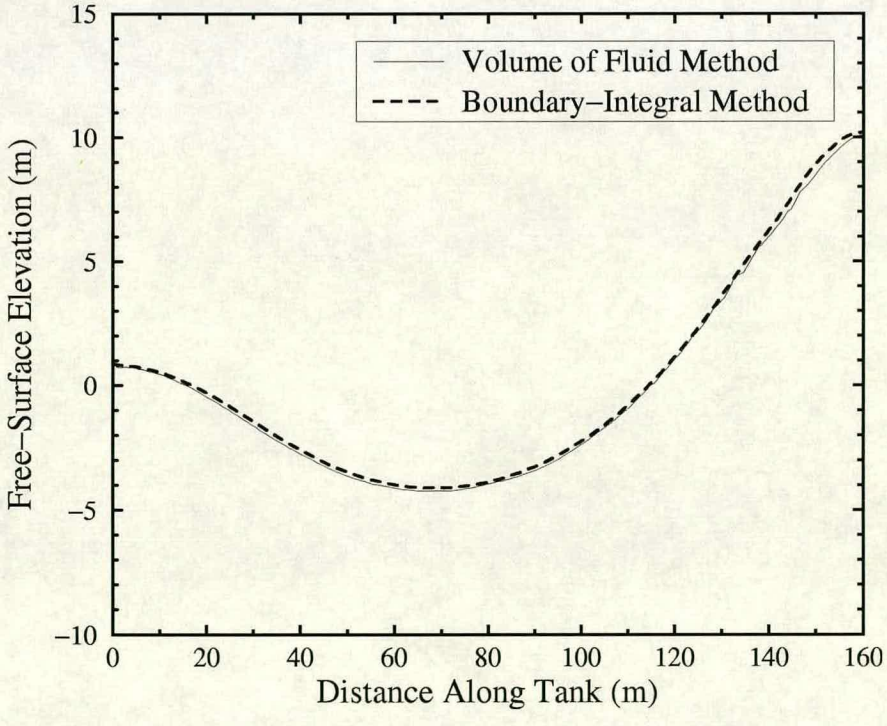

Figure 5.6: VOF and BIM free-surface profiles at $t = 10$s.

Chapter 6

Results Part 3: Wave Impacts against a Vertical Wall

In this chapter the results of the present BIM are compared against the results of an experiment. In the experiment deep-water waves are generated in a wave flume by a paddle wavemaker. These waves are then allowed to travel down the wave flume and impact against a rigid vertical wall located at the opposite end of the flume to the wavemaker. The exact geometry of the flume and the motion of the paddle (measured in the experiment) are then used as the only input to the BIM.

There have not been many studies which compare numerical results against experimental results for deep-water breaking waves. This is probably because of the difficulty in controlling such waves (as mentioned by Chan & Melville [5]) and the difficulty in arranging similar experimental and numerical conditions (as mentioned by Skyner [48]). However, the few studies which do exist are very notable.

In 1988 Dommermuth *et al.* [18] compared the results of their BIM against the results of an experiment. In the experiment a single deep-water plunging breaker was produced in a wave flume by a programmed piston-type wavemaker. During the experiment the motion of the wavemaker was recorded so that it

could be reproduced by an identical piston wavemaker in the numerical wave flume. Very good agreement was found between measured and predicted free-surface elevations and between measured and predicted point velocities at various locations down the flume. However, the exact geometry of the numerical and experimental wave flumes was not the same and this was used to explain any discrepancies between the results. That is, the numerical wave flume modelled a physical wave flume which was 12m long and had a vertical reflecting wall at the far end, whereas the experimental wave flume was 25m long and had an absorbing beach at the far end. In addition to this difference, there was no comparison between the numerically predicted behaviour of the flow and the actual behaviour of the flow near a surface-piercing body (with which the present study is primarily concerned). For example, the nearest wavegauge to the wavemaker was 1.9m from its rest position.

Another limitation which can be levied against the work of Dommermuth *et al.* [18] is that none of the velocity measurements were made near where the wave broke. This problem was overcome by Skyner [48] in his comparison between numerics and experiments. In this study Skyner generated a numerical deep-water plunging breaker using the BIM[1] of Dold & Peregrine [15] (see page 23). He then tried to duplicate this breaker in a physical wave flume by using an iterative technique which matched the measured free-surface elevation time-series at a position upstream of the breaking point to the numerically predicted free-surface elevation time-series at the same position. Once this had been done, and a small shift in time and space[2] had been applied to the numerical results, Skyner found that there was very good agreement between the measured and

[1]This BIM uses periodic boundary conditions on the lateral boundaries.

[2]Dommermuth *et al.* [18] also found it necessary to apply a small shift in time and space to their numerical results.

numerically predicted free-surface profiles as the wave broke. He also found that there was very good agreement between the measured instantaneous velocity fields[3] and the predicted instantaneous velocity fields as the wave broke, even right up into the plunging spout. However, there were discrepancies between the numerical results and the experimental results, for example the shift mentioned above. Consequently, Skyner says in his conclusions:

> It is suggested that use of a numerical wave tank, configured to be as similar as possible to the experimental facility, might reduce the number of differences between the predictions and measurements in any future work.

The author finds this quote particularly encouraging for the present study.

A very recent study which in some respects goes beyond the work presented in this chapter is that of Zhang *et al.* [61]. In this study Zhang *et al.* develop a numerical model for simulating the impact of a plunging wave on a vertical wall. Before the impact of the plunger Zhang *et al.* use a BIM, similar to the one used by Dommermuth *et al.* [18], to track the evolution of the wave. Then, during the initial stages of impact, they approximate the plunging tip by a liquid wedge which is hitting the wall at an oblique angle. This approximation of the plunging tip allows the use of a similarity solution which is then matched to the BIM solution away from the wall. Finally, the BIM is continued after impact so that the effect of the air cushion trapped between the plunger and the wall can be investigated.

Having developed and tested their numerical method Zhang *et al.* go on to compare it to an experiment of Chan & Melville [5]. In this experiment a deep-water wave which plunges against a vertical wall is generated by a programmed

[3]These measured instantaneous velocity fields were obtained using the experimental technique of Particle Image Velocimetry (PIV).

piston-type wavemaker in a wave flume. Zhang *et al.* then duplicate exactly the geometry of this wave flume and the motion of its wavemaker in their numerical model. After taking into account the effect of spray and air leakage in the trapped air pocket, the effect of elasticity of the vertical wall and the effect of the size and the spacing of the pressure transducers in the experiment, Zhang *et al.* find that there is very good agreement between the measured and predicted maximum impact pressure and its rise time[4] (These are the two quantities which Zhang *et al.* are most interested in). In addition, Zhang *et al.* also find that there is very good agreement between measured free-surface profiles[5] of the impact event and the corresponding numerically predicted free-surface profiles. However, Chan & Melville state in their paper [5] that these measured free-surface profiles are only supposed to provide a qualitative description of the impact process. Consequently, the author believes that for deep-water waves impacting against a vertical wall there is still much to be gained from a quantitative comparison of full-length numerically predicted and measured free-surface elevation time-series for the point at the intersection between the free-surface and the wall. Furthermore, assessing how well the present BIM predicts the motion of such a free-surface/body intersection point is the main aim of the present study.

Note that in this chapter the values of all the quantities mentioned are dimensional.

6.1 The Experiments

Figure 6.1 shows the experimental setup that was used for the present study. The length of the wave flume was 6.383m and the undisturbed water depth was 0.75m.

[4]The time from the instant of the initial impact to the instant when the maximum impact pressure is reached.

[5]These measured free-surface profiles were obtained from a high-speed film (*ca.* 1100 frames per second) of Chan & Melville's experiment.

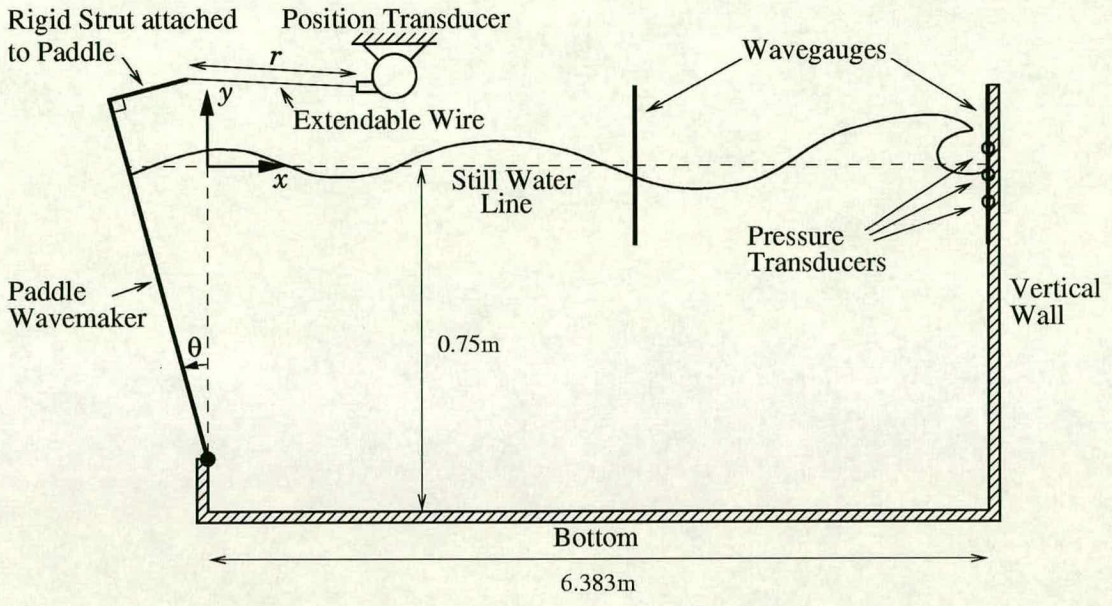

Figure 6.1: The wave flume used for the experiments.

At one end of the wave flume there was a paddle wavemaker and at the other end there was a vertical wall. The paddle wavemaker had two functions: it not only generated outgoing waves but it also absorbed incoming reflections through a force feedback mechanism. This meant that the experiments could proceed without the waves being contaminated by re-reflections from the paddle. Two wavegauges were used in the experiments: one was placed roughly half way down the flume (2.579m from the wall) and the other was on the vertical wall. Also, on the vertical wall were three pressure transducers (placed at 0.681m, 0.731m and 0.781m up the wall respectively) so that wave impact pressures could be recorded. Finally, a position transducer was attached to the paddle so that wavemaker angle (θ) time-series could be recorded during the experiments and used as input to the numerical simulations.

In each of the experiments performed a steep or breaking wave was impacted against the vertical wall through the focusing action of the paddle. That is, for each experiment the wavemaker was programmed to generate a wavepacket which

consisted of a range of equally-spaced frequency components whose phases were automatically chosen to give constructive interference near the wall. In all, six experiments were performed and these were called "gentle" wave, "moderate" wave, "severe" wave, "vertical" wave, "air 1" wave and "air 2" wave. The names of the waves indicate the increasing severity of breaking. For each of the waves a table containing the frequency, amplitude and phase of each component in the corresponding wavepacket can be found in Appendix C of A. Chopra's Ph.D. Thesis [6].

6.2 The Wavemaker Angle

As mentioned in the previous section, the position transducer was used to obtain wavemaker angle time-series for each of the six waves. The position transducer was in fact a very accurate potentiometer whose output voltage V was linearly related to the extension r of the wire connecting it to the paddle. Consequently, after calibration, r could be obtained from V. Then, after measuring some fixed distances and using some simple trigonometry, θ could be obtained from r.

Figure 6.2 shows the wavemaker angle time-series obtained from the position transducer for the "air 2" wave case. Unfortunately, as can be seen from the figure, there is some noise in this time-series. This noise caused a problem because not only $\theta(t)$ but also $\dot{\theta}(t)$ and $\ddot{\theta}(t)$ were required to do the numerical simulations (see equations (3.3) & (3.16)). As a result, some sort of smoothing of the wavemaker angle time-series was necessary. The method of smoothing that was used was the same as that used to smooth the free-surface in the smoothing & regridding procedure (see subsection 3.5.3 & appendix F), namely cubic smoothing splines.

Figure 6.3 shows a closeup of one of the "peaks" in figure 6.2. Also shown in figure 6.3 are three smoothed wavemaker angle time-series for the "air 2"

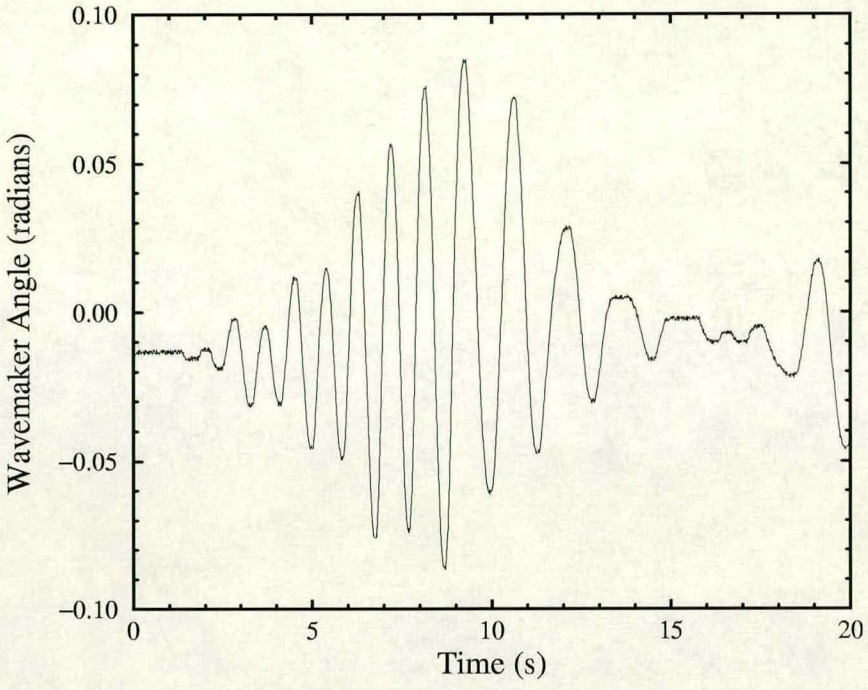

Figure 6.2: The unsmoothed wavemaker angle time-series for the "air 2" wave case.

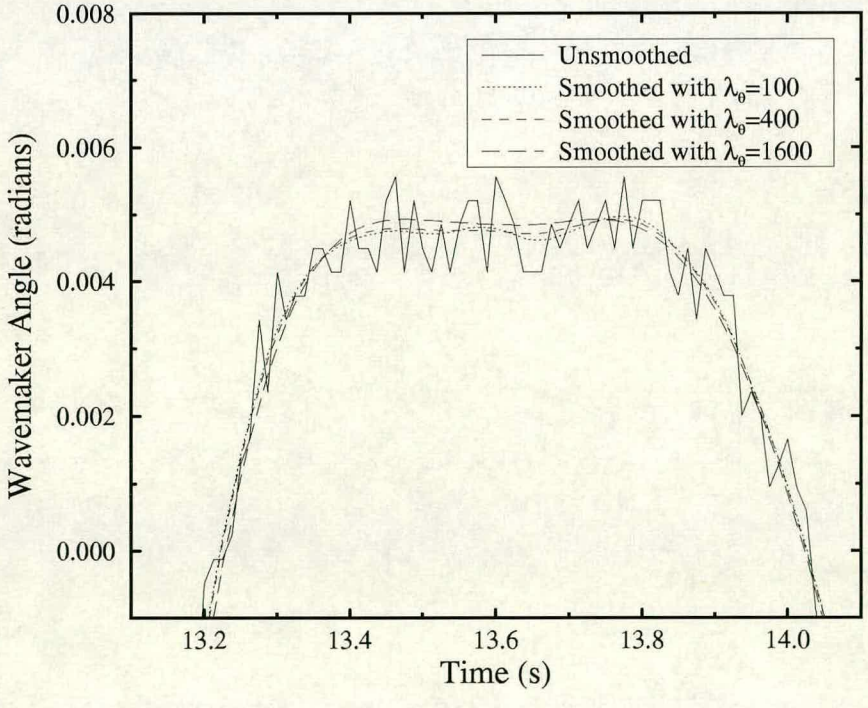

Figure 6.3: A closeup of the unsmoothed and some smoothed wavemaker angle time-series for the "air 2" wave case.

wave case. These three smoothed wavemaker angle time-series correspond to smoothing parameter values of $\lambda_\theta = 100$, $\lambda_\theta = 400$ and $\lambda_\theta = 1600$ respectively. Notice that this smoothing parameter λ_θ is different to the smoothing parameter λ in equation (3.36) but that the two are related through the equation

$$\lambda_\theta = \frac{1-\lambda}{\lambda}. \tag{6.1}$$

The reason why the three smoothed wavemaker angle time-series are not shown in figure 6.2 is because, at the scale used in that figure, they are virtually indistinguishable from the unsmoothed wavemaker angle time-series.

The method of choosing which value of λ_θ to use for a simulation was just to examine various smoothed wavemaker angle time-series against the unsmoothed wavemaker angle time-series and to take the most reasonable smoothed one. In this study the value of λ_θ chosen was always 400.

6.3 The Simulations

As mentioned before, the exact geometry of the wave flume and the motion of the paddle were duplicated exactly in the numerical simulations. Furthermore, the simulations also used the "corner-correction" procedure of subsection 3.5.2, the smoothing & regridding procedure of subsection 3.5.3 and the dynamic time-stepping procedure of subsection 3.5.4.

In order to reduce the number of free parameters involved in the discretisation of the problem, the following method (which seemed sensible) was used to pick the number of nodes on the various sides.

Firstly, the minimum and maximum node spacing on a regridded free-surface $h_{\min}$ and $h_{\max}$ (both measured in metres) were chosen. Then their average was

calculated and stored in a new variable called h_{mid}. That is

$$h_{\text{mid}} \stackrel{\text{def}}{=} \frac{h_{\text{min}} + h_{\text{max}}}{2}. \tag{6.2}$$

Following this the initial number of nodes on the free-surface and the desired number of nodes on a regridded free-surface $N_{1_{\text{desired}}}$ were chosen to be the nearest integer to

$$\frac{\text{length of wave flume}}{h_{\text{mid}}} + 1 = \frac{6.383\text{m}}{h_{\text{mid}}} + 1. \tag{6.3}$$

Also, the number of nodes on the paddle was chosen to be the nearest integer to

$$\frac{\text{undisturbed depth of paddle pivot}}{h_{\text{mid}}} + 1 = \frac{0.681\text{m}}{h_{\text{mid}}} + 1. \tag{6.4}$$

The number of nodes on the bottom was chosen to be the nearest integer to

$$\frac{\text{length of wave flume}}{h_{\text{max}}} + 1 = \frac{6.383\text{m}}{h_{\text{max}}} + 1. \tag{6.5}$$

Finally, the number of nodes on the vertical wall was chosen to be the nearest integer to

$$\frac{\text{undisturbed water depth}}{h_{\text{mid}}} + 1 = \frac{0.75\text{m}}{h_{\text{mid}}} + 1. \tag{6.6}$$

On either side of the free-surface/paddle intersection point the initial node spacing was set to h_{min}. The initial node spacing on the free-surface and the paddle then gradually increased (by a common ratio each time) away from this intersection point. Similarly, on the vertical wall the initial node spacing was set to h_{min} at the intersection with the free-surface and then it gradually increased (by a common ratio each time) away from this point.

In all, 9 runs were performed: 2 each for the first 3 waves and 1 each for the last 3 waves. For all of these runs the smoothing parameter λ was set to a value of 0.99999999 (corresponding to a very small amount of smoothing) and the maximum time-step $(\Delta t)_{\text{max}}$ was set to a value of 0.005s. Table 6.1 shows the values of the other parameters used for the 9 runs.

Run number	1	2	3	4	5	6	7	8	9
Wave	"Gentle"		"Moderate"		"Severe"		"Vertical"	"Air 1"	"Air 2"
Maximum distance moved by a free-surface node in one time-step	0.002m	0.0015m	0.0015m	0.00075m	0.001m	0.001m	0.002m	0.002m	0.0015m
Number of time-steps between each smoothing & regridding	1	1	1	1	1	1	3	3	4
Minimum node spacing on a regridded free-surface h_{min}	0.03m	0.02m	0.03m	0.02m	0.03m	0.02m	0.03m	0.03m	0.03m
Maximum node spacing on a regridded free-surface h_{max}	0.09m	0.08m	0.09m	0.08m	0.09m	0.08m	0.09m	0.09m	0.09m
Desired number of nodes on the free-surface	107	129	107	129	107	129	107	107	107
Number of nodes on the paddle	12	15	12	15	12	15	12	12	12
Number of nodes on the bottom	72	81	72	81	72	81	72	72	72
Number of nodes on the vertical wall	14	16	14	16	14	16	14	14	14

Table 6.1: Parameter values for the 9 runs.

6.3.1 "Gentle" Wave

For this wave the wavepacket was set to focus[6] 0.983m in front of the wall. Also, the amplitude was kept small to prevent breaking from taking place. This resulted in a wave which simply hit the wall with a large sloshing motion. The wavegauge and pressure transducer records are shown in figures 6.4 to 6.8. These figures and the following figures are printed at the end of the chapter so as not to break up the text.

Before going on to discuss how the numerical results compare with the experimental results it must be pointed out that there is a slight drift in the experimentally measured pressure at the three pressure transducers. This is especially evident in figure 6.8 where the measured "zero" pressure at the end of the run is actually slightly positive. The reason for this slight drift in the measured pressure is because of heat transfer effects on the transducer diaphragms caused by the impinging wave. With hindsight this problem could have been overcome by recessing the transducer faces relative to the wall surface, and then filling the recesses with silicon grease which acts as a pressure transmission medium and a thermal insulator for the transducer diaphragms. This was the method used by Chan & Melville in their experiments (see [5]).

As can be seen from figures 6.4 to 6.8, there is excellent agreement between the numerical results and the experimental results. In figure 6.5 the maximum height of the free-surface at the wall is predicted very well. In figures 6.6 & 6.7 the maximum (impact) pressures at the bottom & middle pressure transducer respectively are also predicted very well. However, the predicted maximum (impact) pressure at the top pressure transducer is slightly in error (see figure 6.8).

[6]This focus position is for the case when there is no vertical wall and it was calculated using linear theory. Consequently, the actual (nonlinear) focus in the presence of the wall is at a slightly different position.

In general the finer resolution run (run 2) is better than the coarser resolution run (run 1): run 2 tends to predict the local maxima and minima better than run 1.

In 1997 Chopra simulated the same set of experiments using the VOF method which he developed (see [6]). Unfortunately, the agreement between his numerical results and the experimental results was not as good as it is here. The reason for this poor agreement was that the numerical scheme could not successfully absorb incoming reflections at the paddle. In the VOF method it is very difficult to model a moving body like a paddle. Consequently, some sort of non-reflective (to model the absorbing nature of the paddle wavemaker) input boundary was required, and such a boundary is extremely difficult to devise. To date no satisfactory non-reflective boundary has been developed.

With this above discussion in mind it is unfortunate that the VOF method developed by Chopra was not used to simulate the same experiment of Chan & Melville [5] that Zhang *et al.* [61] simulated (see page 139). In that experiment the wavemaker was a non-absorbing wavemaker: the waves typically took 30 minutes to settle down between runs, whereas in the experiments performed for the present study the waves settled down after about 2 minutes. As a result there would be no need to have a non-reflective input boundary to simulate the experiment of Chan & Melville.

It is especially unfortunate that the above VOF method was not used to simulate the experiment of Chan & Melville because, unlike the present BIM, the VOF method can go beyond breaking and this particular VOF method was designed to model trapped air dynamics. However, the parallel machine that the VOF code was implemented on no longer exists and the code was specific to that machine.

Finally, returning to the comparison between the present BIM and the present set of experiments, the results show that the paddle wavemaker is as good an absorbing wavemaker in the numerical wave flume as it is in the physical wave flume.

6.3.2 "Moderate" Wave

For this wave the frequency spectrum and focus point were kept the same as those used for "gentle" wave, however the amplitude of each frequency component was increased. This resulted in a wave which was steeper at impact but was still unbroken. The wavegauge and pressure transducer records are shown in figures 6.9 to 6.13.

Unfortunately, for this wave and for all the following waves the jet which rose up the wall after impact went beyond the upper measuring limit (approximately 0.22m above the still water line) of the wavegauge on the wall. This can be seen in figure 6.10 where the highest maxima in the measured free-surface elevation at the wall is truncated with a "flat top" at this limit.

In addition, in some of the above cases this jet also overtopped the wall resulting in lose of fluid from the flume and splashing as the jet fell back down. Both of these last points will adversely affect the agreement between the numerical results and the experimental results after impact.

Despite these problems there is still very good agreement between the numerical results and the experimental results for "moderate" wave (see figures 6.9 to 6.13).

6.3.3 "Severe" Wave

This wave also used the same frequency spectrum and focus point as the previous two waves, however the amplitude of each frequency component was increased

even further. This resulted in a wave which was steeper than "moderate" wave at impact but again it was still unbroken. The wavegauge and pressure transducer records for this wave are shown in figures 6.14 to 6.18. Once more the figures show very good agreement between the numerical and experimental results.

6.3.4 "Vertical" Wave

This wave used a different frequency spectrum and focus point to the previous three waves. This time, instead of the focus point being set in front of the wall, it was set behind the wall. The reason for doing this was because during tests in the physical wave flume it was found that reflections from the wall caused breaking to occur long before the wavepacket had focused. The resulting plunging breaker turned out to be a very good one and it was decided to use it for the final three waves.

For "vertical" wave the focus point was set such that the plunger just failed to develop before the wall, giving a vertical face. The wavegauge and pressure transducer records for this wave are shown in figures 6.19 to 6.23.

As can be seen from the figures, computations broke down at about 14.9 seconds. The reason for this breakdown was because the jet which rose up the wall after impact became very thin and no longer properly resolved by the numerical scheme. Despite this the numerical results on the whole agree very well with the experimental results. However, in the few seconds before impact the predicted free-surface elevation at the wall and the predicted pressures at the bottom two pressure transducers are slightly at variance. In addition, the predicted impact pressure at the top pressure transducer is also slightly in error[7].

[7]Note that the rise time (the time taken for the pressure to rise from the "trough" in the pressure time-series before the impact to the impact pressure) for the top pressure transducer is quite short: the pressure was only sampled three times during this rise time. Consequently, the actual impact pressure at this pressure transducer might have been somewhat higher than the measured impact pressure here. This means that the error in the predicted impact pressure

6.3.5 "Air 1" Wave

This wave used the same frequency spectrum and the same amplitude of each frequency component as "vertical" wave. However, the focus point was slightly adjusted so that overturning would just begin to occur when the wave hit the wall. This resulted in a small air pocket being trapped between the wave face and the wall at impact. The wavegauge and pressure transducer records for this wave are shown in figures 6.24 to 6.28.

According to Chan & Melville [5] this kind of impact results in the highest impact pressures and the shortest rise times of all the impacts. Furthermore, they also showed that high frequency pressure oscillations occur just after the pressure maximum and they attributed these pressure oscillations to oscillations of the air pocket. Finally, they showed that these above three factors (the high impact pressures, their short rise times and the frequency of the pressure oscillations) vary significantly between repeats of the same experiment for this type of impact.

The high impact pressures are confirmed by the experimentally measured pressure at the top pressure transducer (see figure 6.28). Although not shown in this figure the pressure "spike" in the measured pressure goes up to approximately 4200 Pa.

As can be seen from figures 6.24 to 6.28, computations broke down at about 14.4 seconds. From figure 6.24 it can be seen that the numerically predicted free-surface elevation at the flume wavegauge agrees very well with the experimentally measured free-surface elevation right up until breakdown. Also, except for the last few seconds before impact, the numerical results agree well with the experimental results for the wall wavegauge (see figure 6.25). However, it is surprising that the numerical scheme can predict the jet which rises up the wall after impact. This is

is probably even worse.

surprising because, unlike the BIM of Zhang *et al.* [61], the present BIM cannot model the air pocket entrapped between the wall and the plunger. The present BIM should therefore break down before this jet starts to rise up the wall. The reason why the BIM does not break down will be explained in subsection 6.3.7 when some numerically predicted free-surface profiles are examined.

Despite the above problem the impact pressures at the two lower pressure transducer are predicted quite well (see figures 6.26 & 6.27). These two wall locations are away from the region of trapped air and the region where the plunger impacts and so the impact pressures here are lower and do not vary significantly between runs of the same experiment.

On the other hand, the impact pressure at the top pressure transducer is not predicted very well (see figure 6.28). Due to the size of the measured impact pressure ($\approx 4200\,\text{Pa}$) it is clear that this wall location is in the region of trapped air or the region where the plunger impacts. Consequently, the impact pressure here is not very repeatable from one run of the same experiment to the next. However, even taking this variability of the impact pressure into account the numerically predicted impact pressure is far too low[8]. Once again the reason for why this happened will be explained in subsection 6.3.7 when some numerically predicted free-surface profiles are examined.

6.3.6 "Air 2" Wave

Like "air 1" wave this wave used the same frequency spectrum and the same amplitude of each frequency component as "vertical" wave. However, the focus point was slightly adjusted again so that this time a larger air pocket was trapped

[8]As for "vertical" wave the pressure rise time for this wave at the top pressure transducer is quite short: the pressure was only sampled three times during this rise time. Consequently, the actual impact pressure at this pressure transducer might have been somewhat higher than the measured impact pressure here. This means that again the error in the predicted impact pressure is probably even worse.

between the plunger and the wall at impact. The wavegauge and pressure transducer records for this wave are shown in figures 6.29 to 6.33.

As can be seen from the figures, computations broke down at about 14.5 seconds. Once again the numerical results agree very well with the experimental results for the flume wavegauge right up until breakdown (see figure 6.29). Also, as for "air 1" wave, the numerical scheme manages to predict the jet which rises up the wall after impact even though it should break down before this jet is formed (see figure 6.30). Finally, although the impact pressure at the middle pressure transducer is predicted very well (see figure 6.32) the impact pressures at the bottom and top pressure transducers are not predicted well (see figures 6.31 and 6.33). The reason for this disagreement between the predicted and measured impact pressures, as well as the reason why the numerical scheme manages to predict the jet which rises up the wall after impact will be given in the next subsection.

6.3.7 Free-Surface Profiles

In this subsection some numerically predicted free-surface profiles are examined.

Figure 6.34 shows waves being generated by the paddle wavemaker for the experiment "air 2" wave. In the figure seven numerically predicted free-surface profiles (from run 9) together with the corresponding positions of the paddle and the position of the bottom are displayed.

Figure 6.35 shows "air 2" wave impacting against the vertical wall. In this figure nine numerically predicted free-surface profiles (from run 9) together with the position of the wall and the position of the bottom are displayed.

From figure 6.35 it can be seen that although the numerically predicted wave does steepen before impact it does not overturn and entrap an air pocket at impact as it should. A possible reason for why overturning does not occur is that the

minimum node spacing on a regridded free-surface $h_{\min}$ is too large. For run 9, $h_{\min}$ was 0.03m and the number of time-steps between each smoothing & regridding was 4. For most of the run this minimum node spacing was sufficiently small to resolve the free-surface, however at the end of the run it was too large to resolve the plunging breaker and so this could account for why overturning was suppressed. The fact that breaking does not occur explains why the BIM was able to predict the jet which rose up the wall after impact for "air 2" wave. It also explains the differences between the numerically predicted impact pressures and the measured impact pressures for the same wave. However, if the BIM had correctly predicted overturning there would have been no numerically predicted impact pressures at all because unlike the numerical scheme of Zhang *et al.* [61] the present scheme cannot model the plunger hitting the wall.

This above steepening problem also affected the impacts in the simulations of all the other experiments: from "air 1" wave all the way down to "gentle" wave. However, it affected each of the above waves in turn to a lesser degree because going from "air 1" wave down to "gentle" wave the waves get less steep at impact.

In an attempt to overcome this problem $h_{\min}$ was reduced. However, it was found that the present BIM suffered from slight stability problems over such long runs (the total number of time-steps in one run was usually around 10000) and these stability problems became worse as $h_{\min}$ was reduced. This meant that for small $h_{\min}$ it was very difficult to find values for the other 5 controlling parameters[9] in order to give a stable run.

There are three possible causes for why the present BIM appears to be slightly less stable than, for example, the BIM of Zhang *et al.*.

[9]The 6 parameters which determine a run are: $h_{\min}$, $h_{\max}$, λ, the number of time-steps between each smoothing & regridding, $(\Delta t)_{\max}$ and the maximum distance moved by a free-surface node in one time-step.

Firstly, the present BIM uses an explicit second-order Taylor series scheme for time-stepping and in general explicit schemes are known to be more unstable than implicit scheme. Having said that, the BIM of Dold & Peregrine [15] uses a similar explicit scheme for time-stepping and their code is very stable. Furthermore, the BIM of Zhang *et al.* uses a fourth-order Runge-Kutta scheme for time-stepping and Runge-Kutta schemes are also explicit.

The second and most likely cause of the stability problems affecting the present BIM is its higher order discretisation of the boundary and its use of a higher order numerical differentiation scheme when compared to the BIM of Zhang *et al.*. Although these higher order schemes will usually allow the boundary to be discretised by less nodes for the same accuracy they may also result in problems, especially at corners. In the present BIM the complex potential $\beta(z)$ is assumed to vary cubically between nodes, whereas in the BIM of Zhang *et al.* it is assumed to vary linearly between nodes. Also, in the present BIM a five-point numerical differentiation scheme is used, whereas in the BIM of Zhang *et al.* a three-point numerical differentiation scheme is used. The unfortunate situation is that at corners these higher order schemes need to be modified in order to use only nodal values from one side of the corner (see pages 55 & 57) and it is these modified numerical schemes which tend to be slightly less accurate and may introduce errors which eventually result in instabilities.

Finally, the smoothing & regridding procedure itself might contribute to these stability problems. This is despite the fact that it is designed to suppress free-surface instabilities. In the short-term it certainly does stabilise the numerical scheme. However, it is unclear how this procedure will affect long-term stability because it actually slightly alters the mathematical problem begin solved.

6.3.8 Volume & Energy Conservation

In this subsection two graphs are examined: the first graph shows an example of volume conservation in the numerical wave flume and the second graph shows an example of energy conservation in the numerical wave flume.

Figure 6.36 shows the relative error in the volume against time for the simulation of "air 2" wave (run 9). As can be seen from the figure, volume is conserved very well for the whole length of the run. However, in the last few seconds before breakdown the error starts to increase because $h_{\min}$ is too large to resolve the overturning of the free-surface (see subsection 6.3.7).

Figure 6.37 shows the power supplied by the paddle and the rate of change of the energy of the fluid against time for the simulation of "air 2" wave (run 9). As can be seen from this figure, energy is conserved well for most of the run except for the last few seconds. Again, this disagreement in the last few seconds before breakdown is caused by $h_{\min}$ being too large to resolve the overturning of the free-surface (see subsection 6.3.7).

6.4 Summary of Chapter 6

In this chapter the results of the present BIM were compared against those of an experiment. In the experiment deep-water waves were generated in a wave flume by a paddle wavemaker and then impacted against a vertical wall. The geometry of the flume and the motion of the wavemaker were then duplicated exactly in the numerical wavetank.

In all, six different types of deep-water waves were impacted against the vertical wall; from steep unbroken waves which simply sloshed violently against the wall to waves which broke against the wall entrapping air pockets.

For these waves, full-length[10] numerically predicted wavegauge records were compared against full-length measured wavegauge records for two wavegauges: one located approximately half way down the flume and the other located on the vertical wall. Also, full-length numerically predicted pressure transducer records were compared against full-length measured pressure transducer records for three pressure transducers on the wall. For this study the main interest was in the wall wavegauge records. In general the numerical results agreed very well with the results from the experiments.

However, for some of the runs agreement was not so good during the last few seconds before impact. This problem might have been caused by the fact that the minimum node spacing on a regridded free-surface $h_{\min}$ was too large to properly resolve the steepening and overturning of the free-surface. Attempts were made to reduce $h_{\min}$ but it was found that the present BIM had slight stability problems over such long runs, especially for small $h_{\min}$. It was proposed that the most likely cause of these stability problems was the *modified* higher order discretisation of the boundary at corners and the *modified* high-order numerical differentiation scheme at corners.

Incidentally, the author believes that this chapter represents the first time that the motion of an *absorbing* wavemaker has been duplicated in a numerical wave flume. Consequently, because of the generally good agreement between the numerical results and the results from the experiments, it can be concluded that the wavemaker in the numerical wave flume is as good an absorbing wavemaker as the wavemaker in the physical wave flume.

[10]That is, for the whole length of the run.

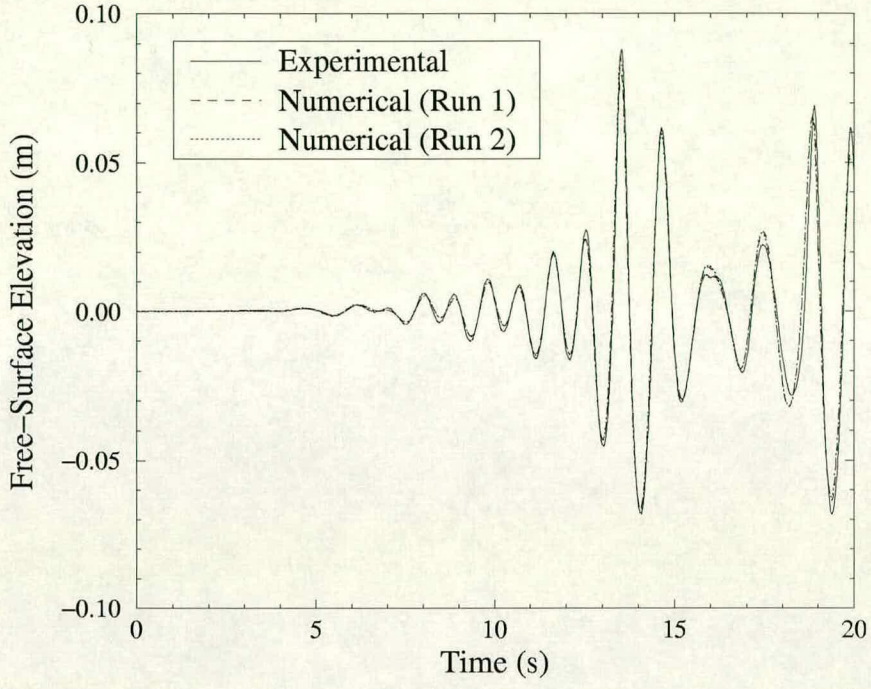

Figure 6.4: Flume wavegauge records for "gentle" wave. The flume wavegauge is located 2.579m from the vertical wall.

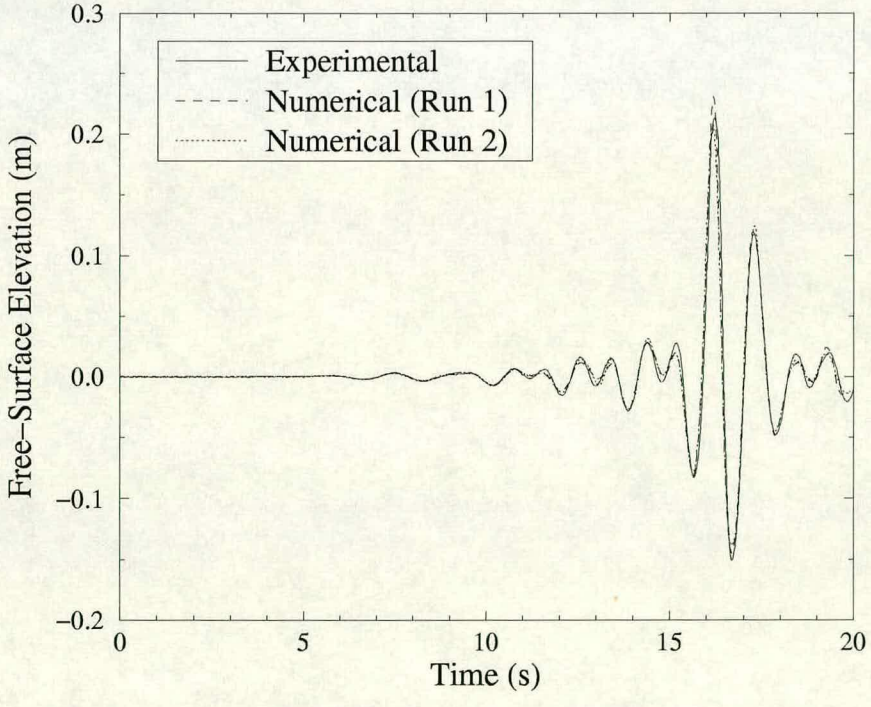

Figure 6.5: Wall wavegauge records for "gentle" wave. The wall wavegauge is located on the vertical wall.

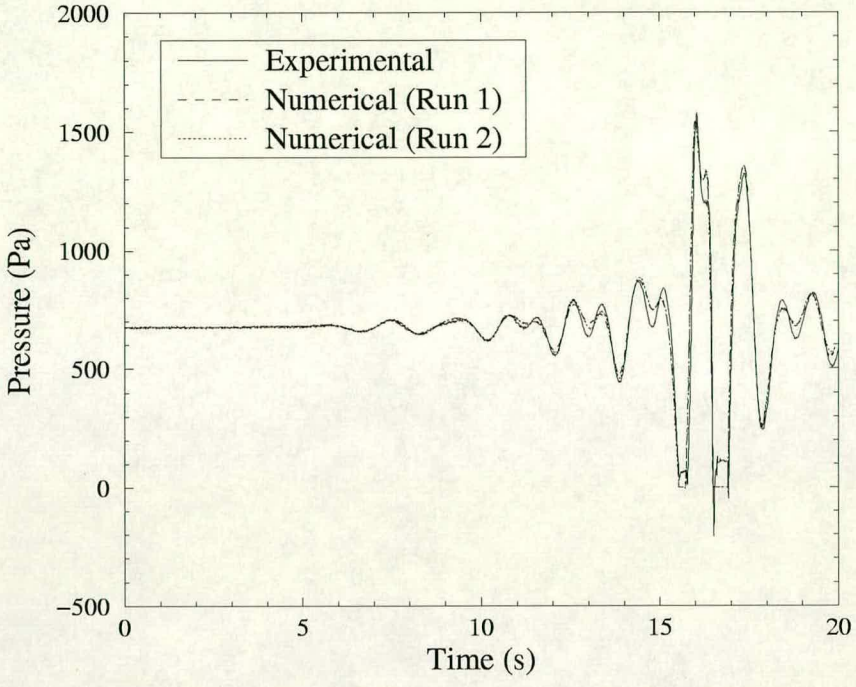

Figure 6.6: Bottom pressure transducer records for "gentle" wave. The bottom pressure transducer is located 0.681m up the vertical wall.

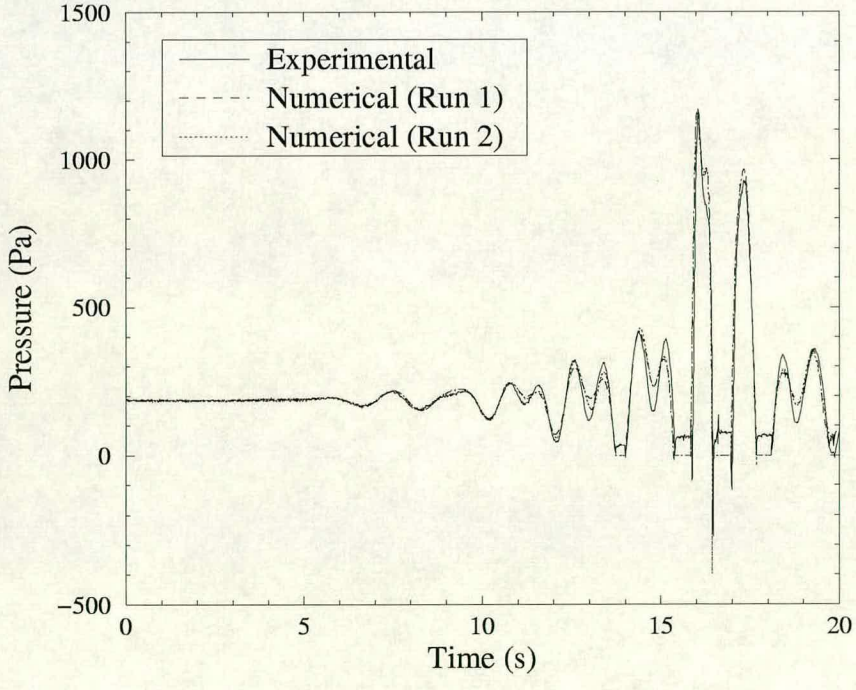

Figure 6.7: Middle pressure transducer records for "gentle" wave. The middle pressure transducer is located 0.731m up the vertical wall.

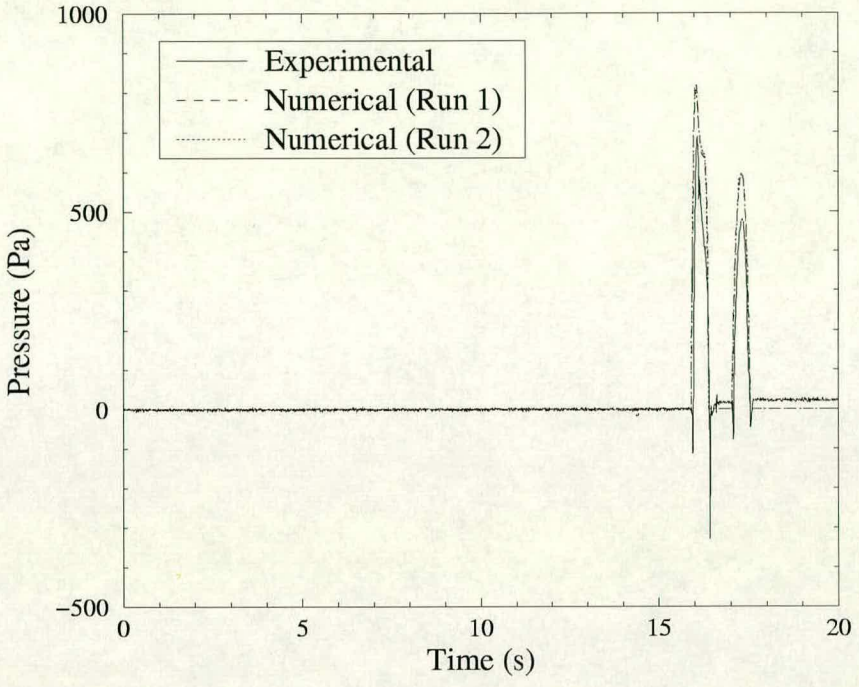

Figure 6.8: Top pressure transducer records for "gentle" wave. The top pressure transducer is located 0.781m up the vertical wall.

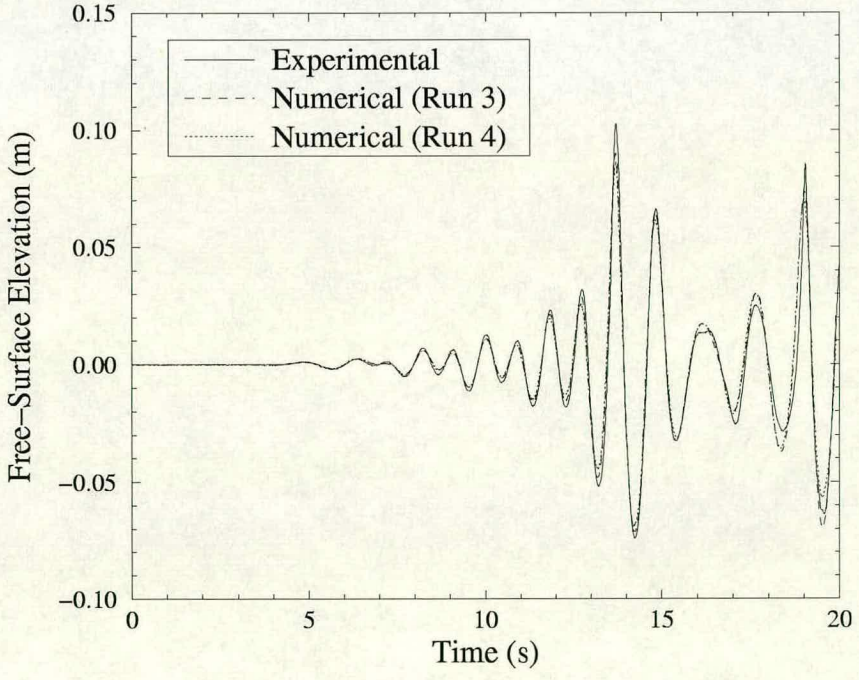

Figure 6.9: Flume wavegauge records for "moderate" wave. The flume wavegauge is located 2.579m from the vertical wall.

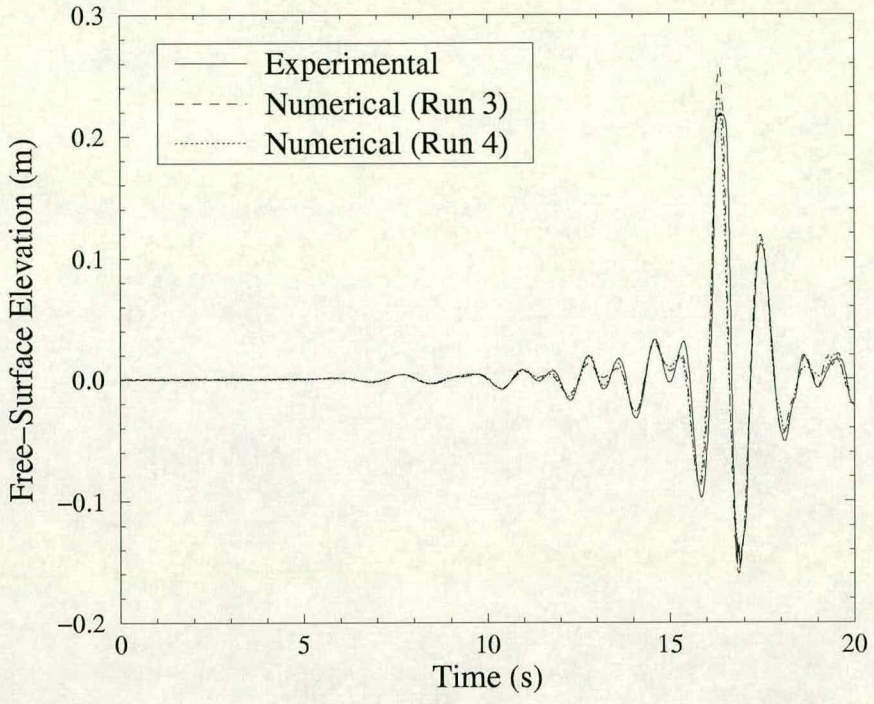

Figure 6.10: Wall wavegauge records for "moderate" wave. The wall wavegauge is located on the vertical wall.

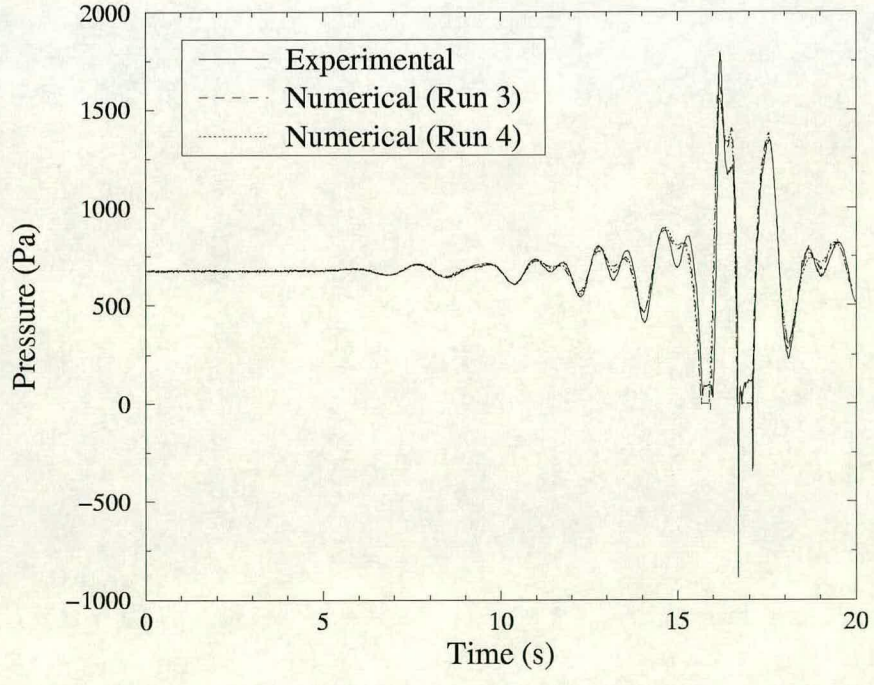

Figure 6.11: Bottom pressure transducer records for "moderate" wave. The bottom pressure transducer is located 0.681m up the vertical wall.

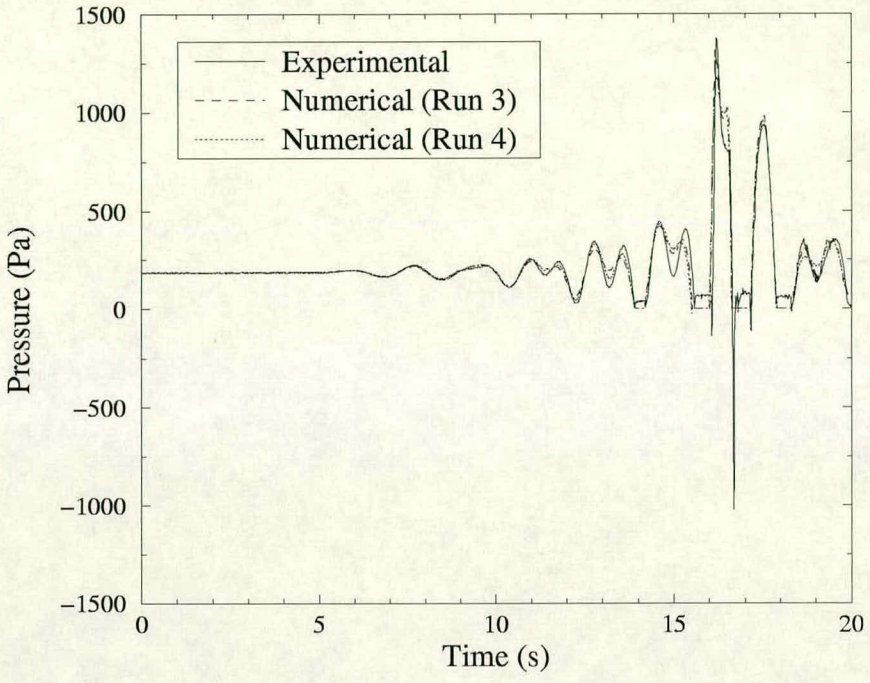

Figure 6.12: Middle pressure transducer records for "moderate" wave. The middle pressure transducer is located 0.731m up the vertical wall.

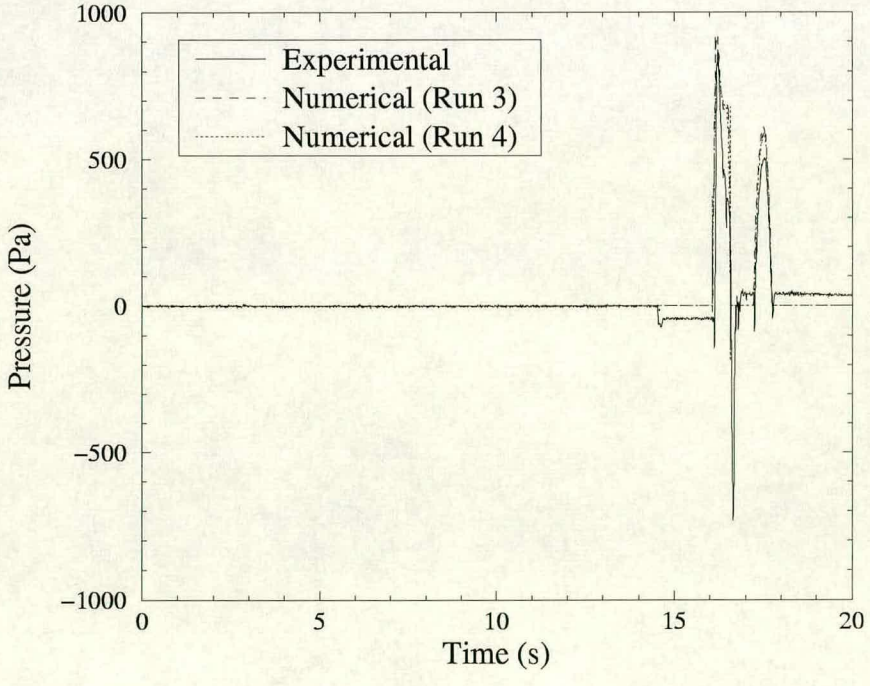

Figure 6.13: Top pressure transducer records for "moderate" wave. The top pressure transducer is located 0.781m up the vertical wall.

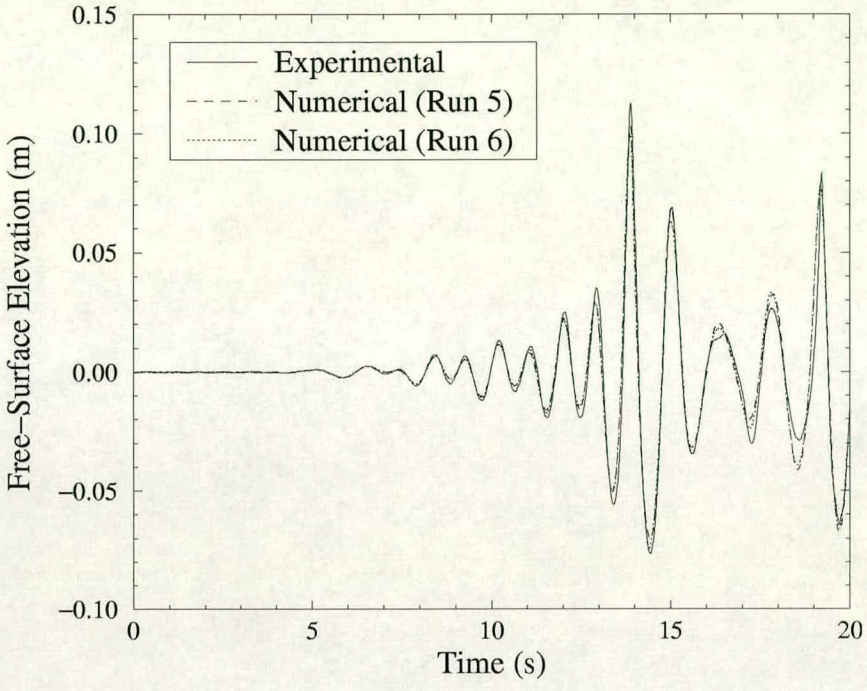

Figure 6.14: Flume wavegauge records for "severe" wave. The flume wavegauge is located 2.579m from the vertical wall.

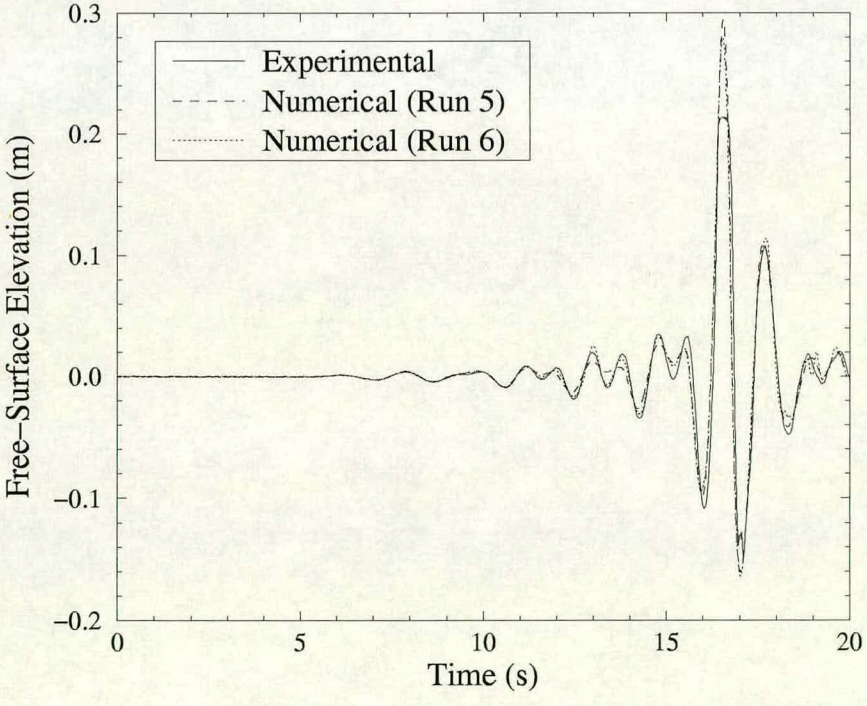

Figure 6.15: Wall wavegauge records for "severe" wave. The wall wavegauge is located on the vertical wall.

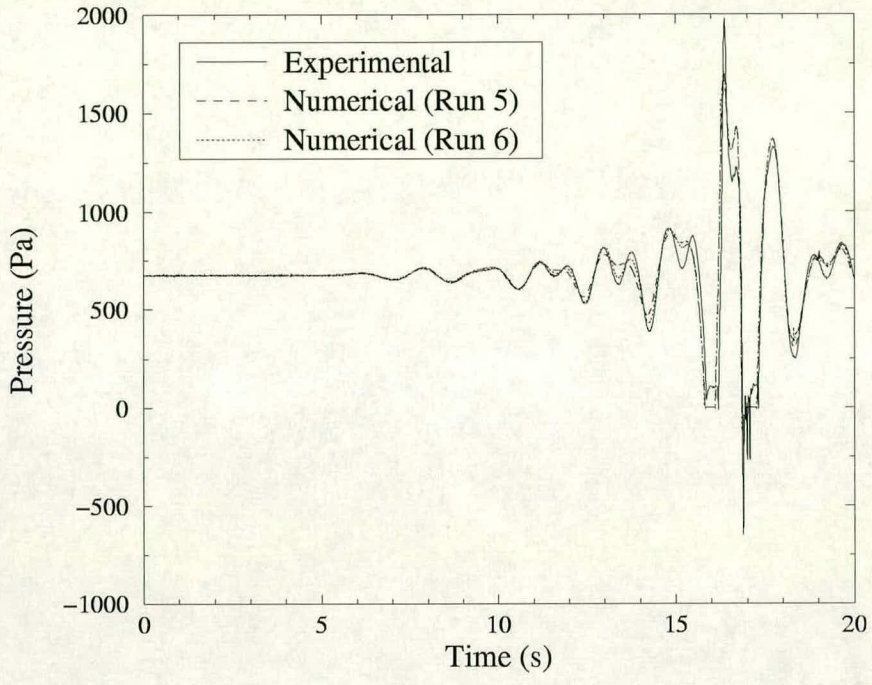

Figure 6.16: Bottom pressure transducer records for "severe" wave. The bottom pressure transducer is located 0.681m up the vertical wall.

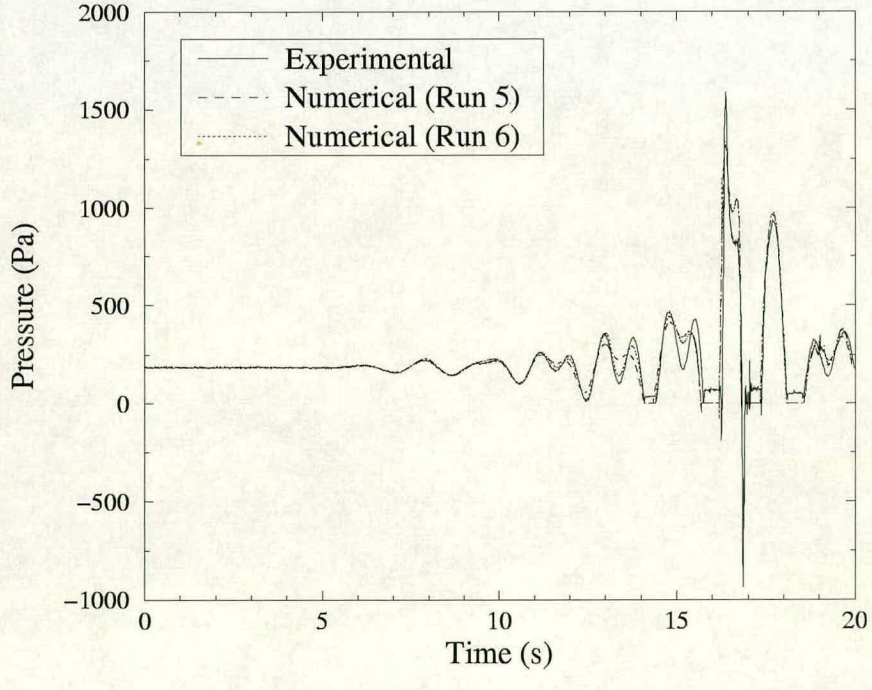

Figure 6.17: Middle pressure transducer records for "severe" wave. The middle pressure transducer is located 0.731m up the vertical wall.

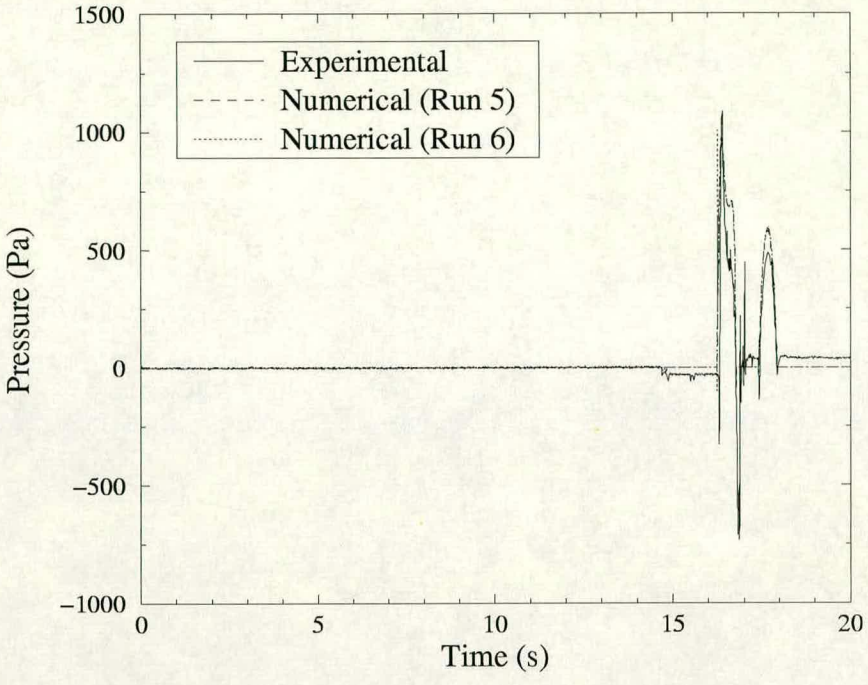

Figure 6.18: Top pressure transducer records for "severe" wave. The top pressure transducer is located 0.781m up the vertical wall.

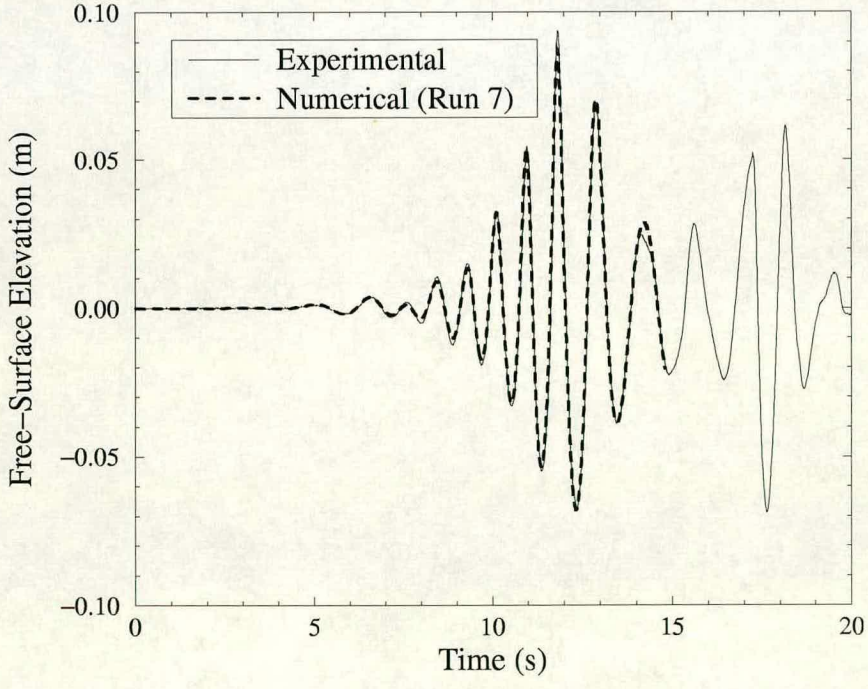

Figure 6.19: Flume wavegauge records for "vertical" wave. The flume wavegauge is located 2.579m from the vertical wall.

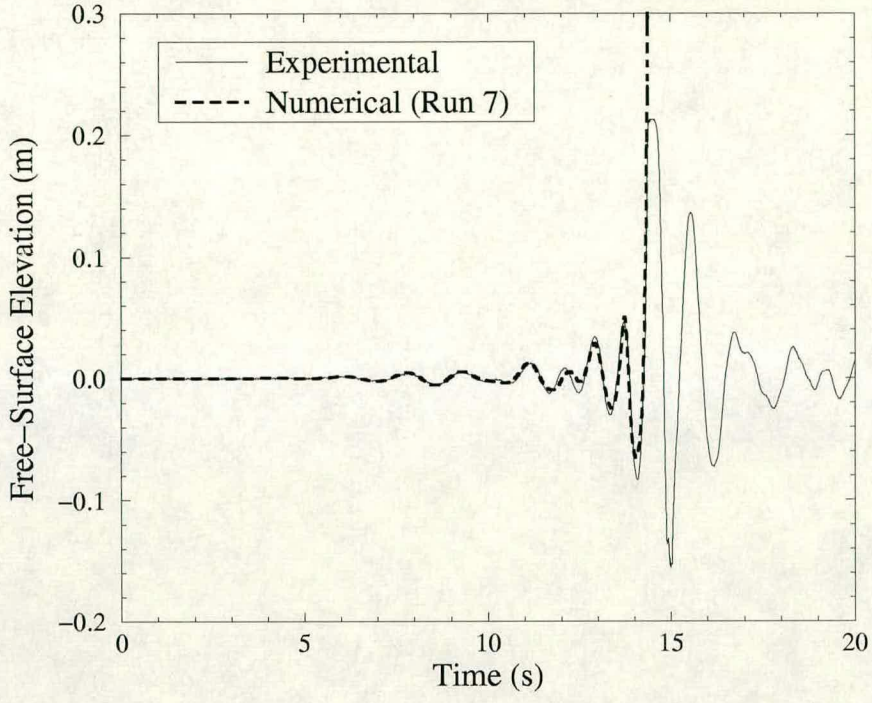

Figure 6.20: Wall wavegauge records for "vertical" wave. The wall wavegauge is located on the vertical wall.

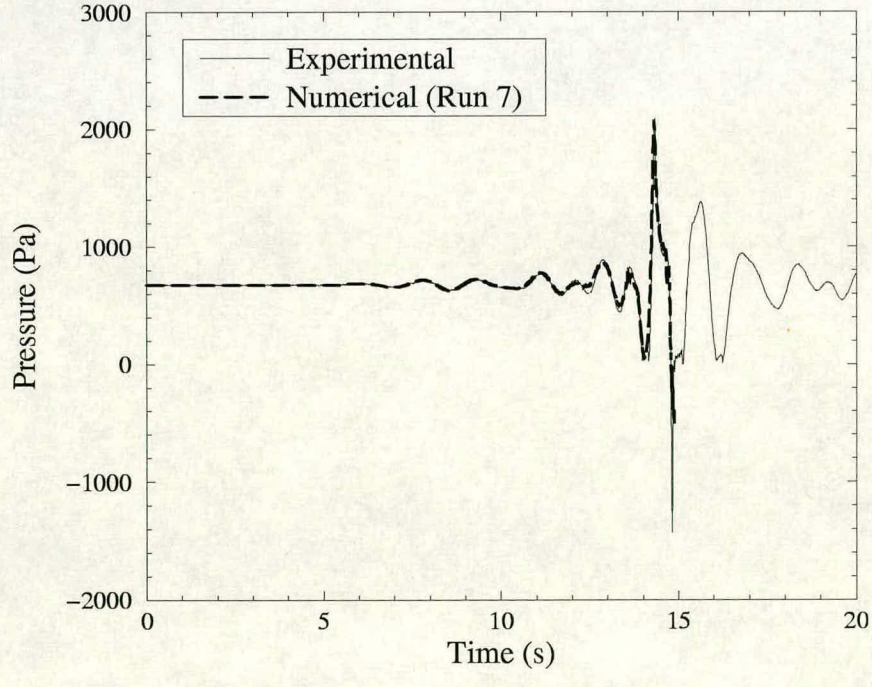

Figure 6.21: Bottom pressure transducer records for "vertical" wave. The bottom pressure transducer is located 0.681m up the vertical wall.

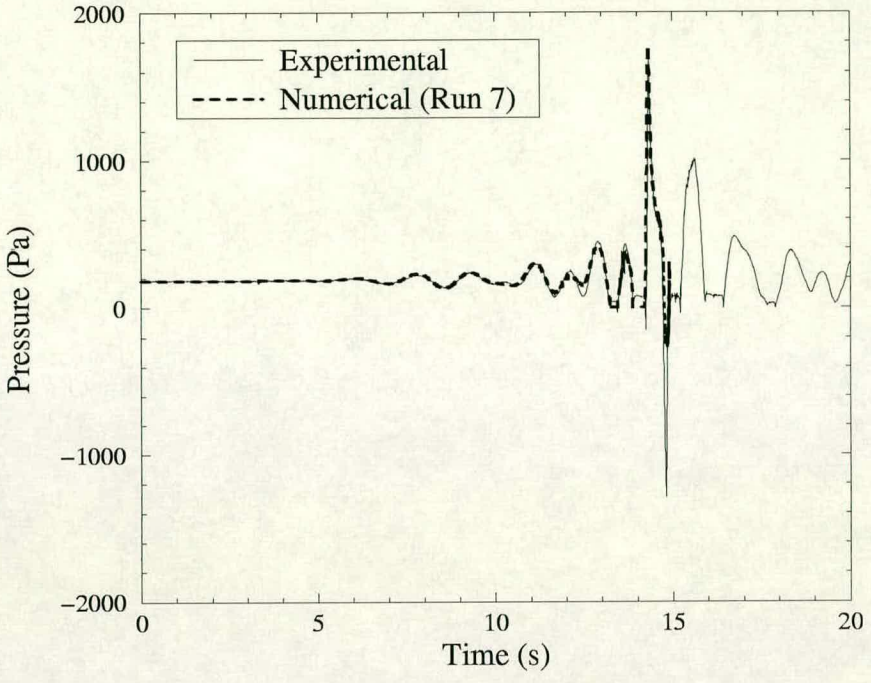

Figure 6.22: Middle pressure transducer records for "vertical" wave. The middle pressure transducer is located 0.731m up the vertical wall.

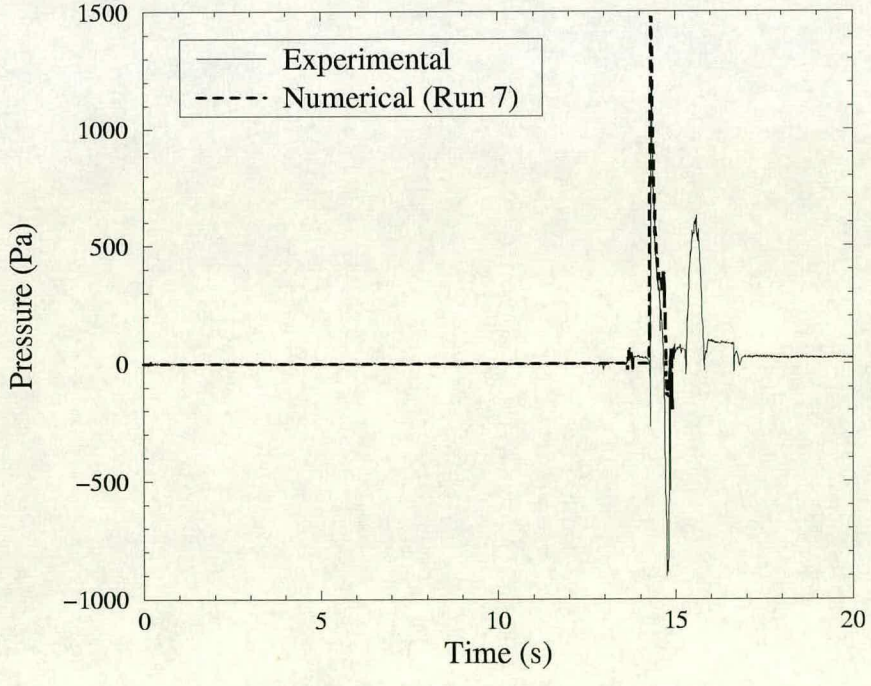

Figure 6.23: Top pressure transducer records for "vertical" wave. The top pressure transducer is located 0.781m up the vertical wall.

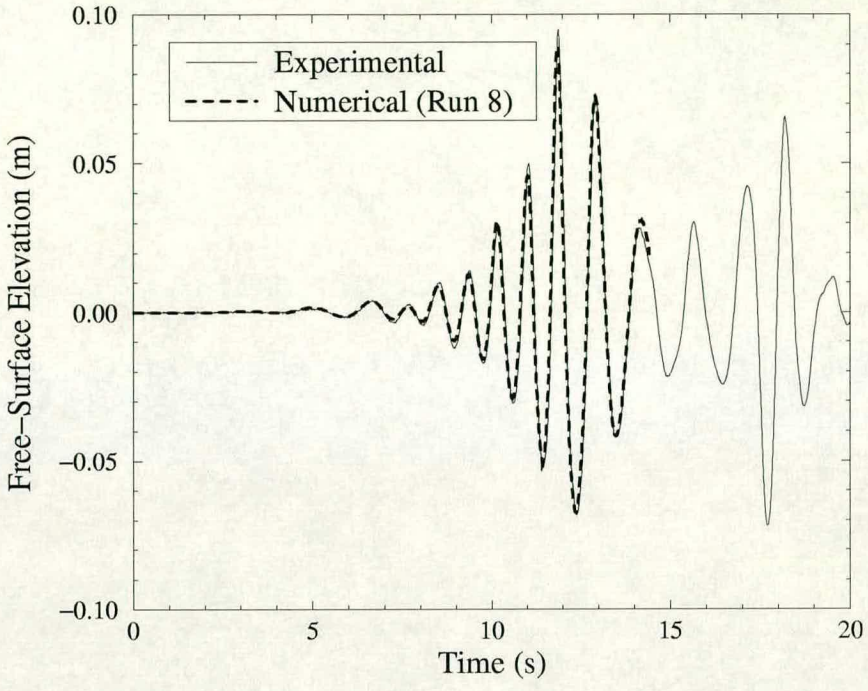

Figure 6.24: Flume wavegauge records for "air 1" wave. The flume wavegauge is located 2.579m from the vertical wall.

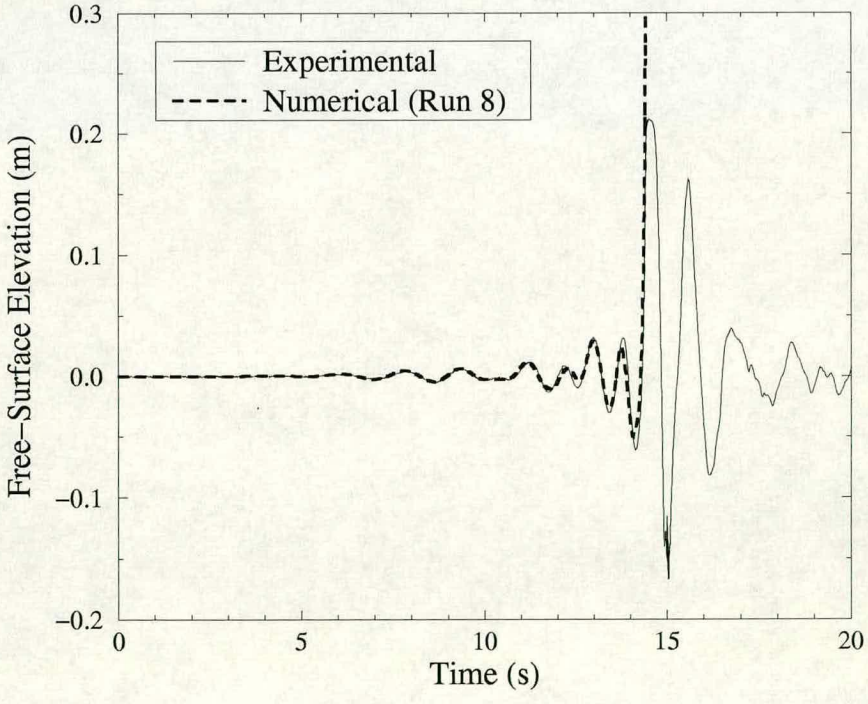

Figure 6.25: Wall wavegauge records for "air 1" wave. The wall wavegauge is located on the vertical wall.

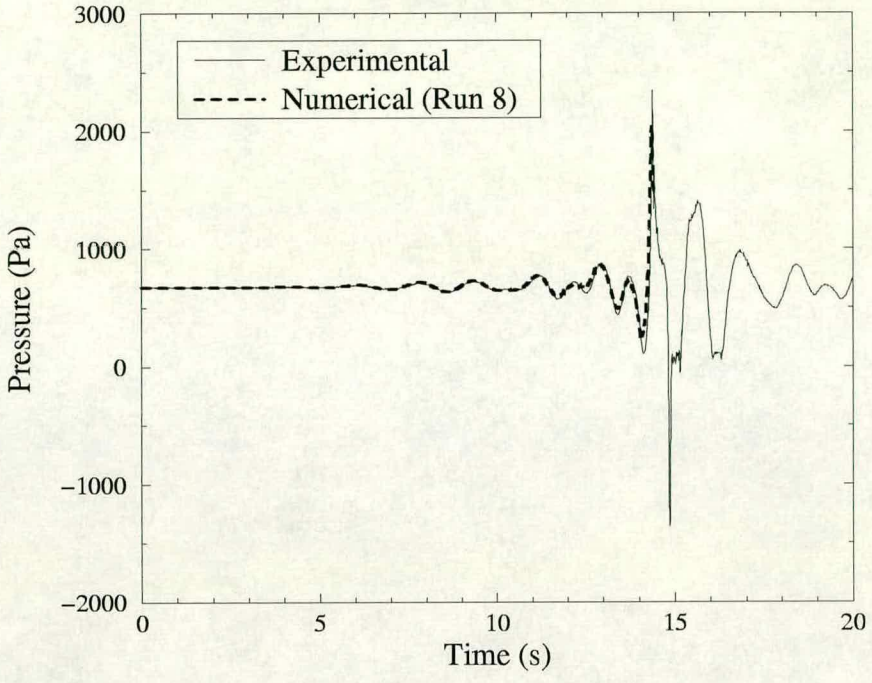

Figure 6.26: Bottom pressure transducer records for "air 1" wave. The bottom pressure transducer is located 0.681m up the vertical wall.

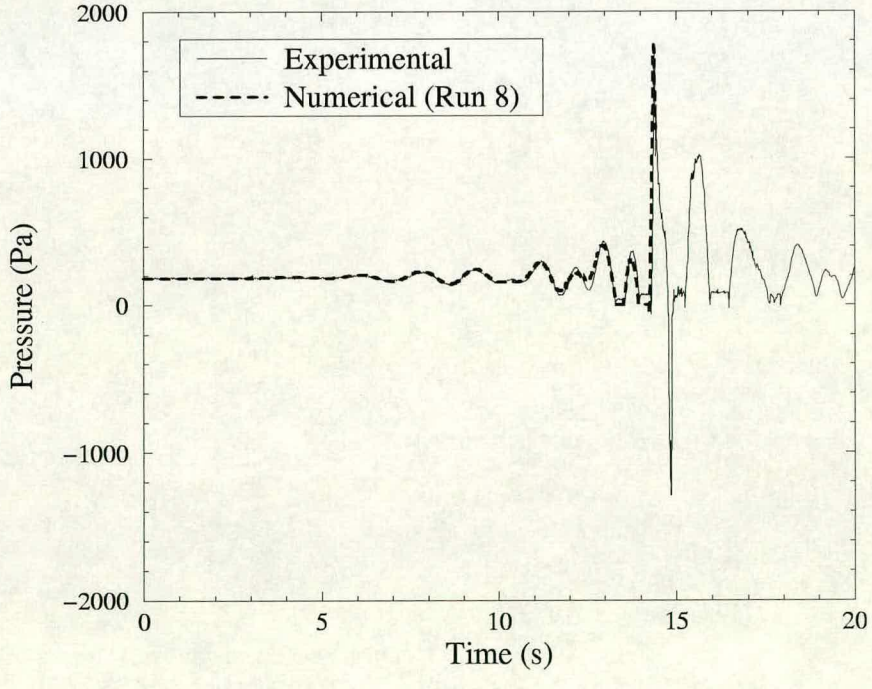

Figure 6.27: Middle pressure transducer records for "air 1" wave. The middle pressure transducer is located 0.731m up the vertical wall.

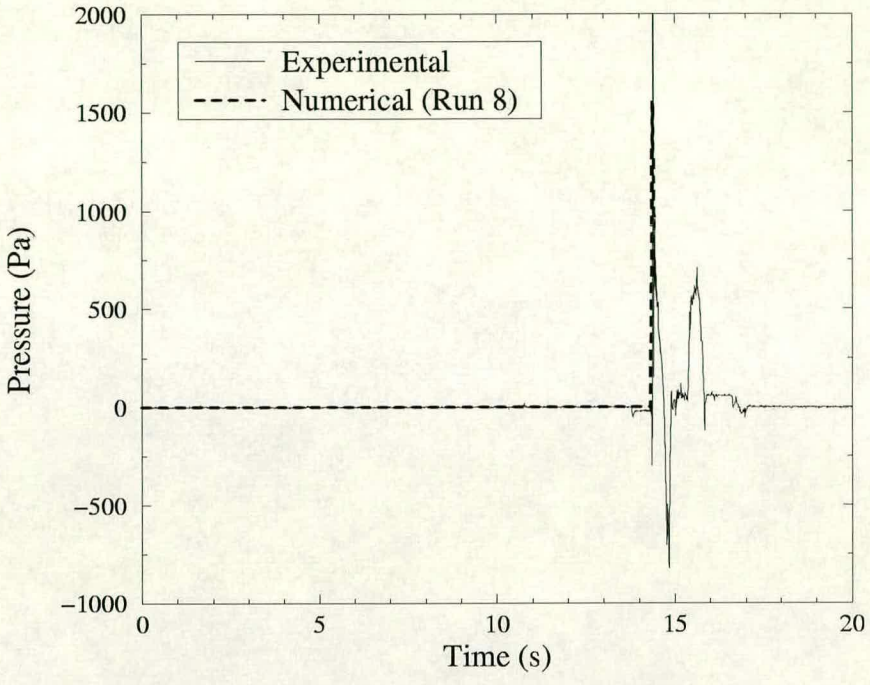

Figure 6.28: Top pressure transducer records for "air 1" wave. The top pressure transducer is located 0.781m up the vertical wall.

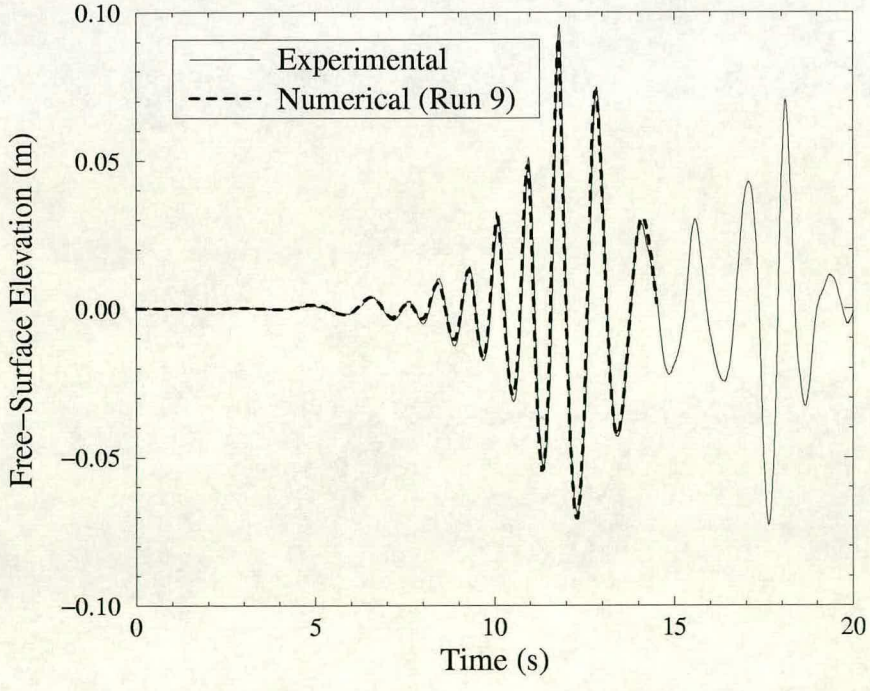

Figure 6.29: Flume wavegauge records for "air 2" wave. The flume wavegauge is located 2.579m from the vertical wall.

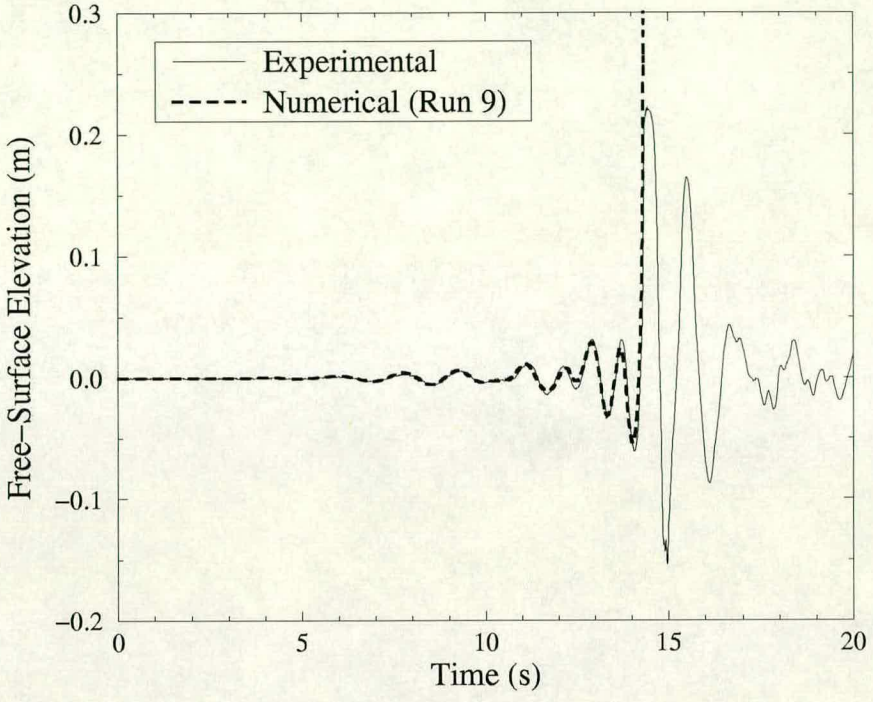

Figure 6.30: Wall wavegauge records for "air 2" wave. The wall wavegauge is located on the vertical wall.

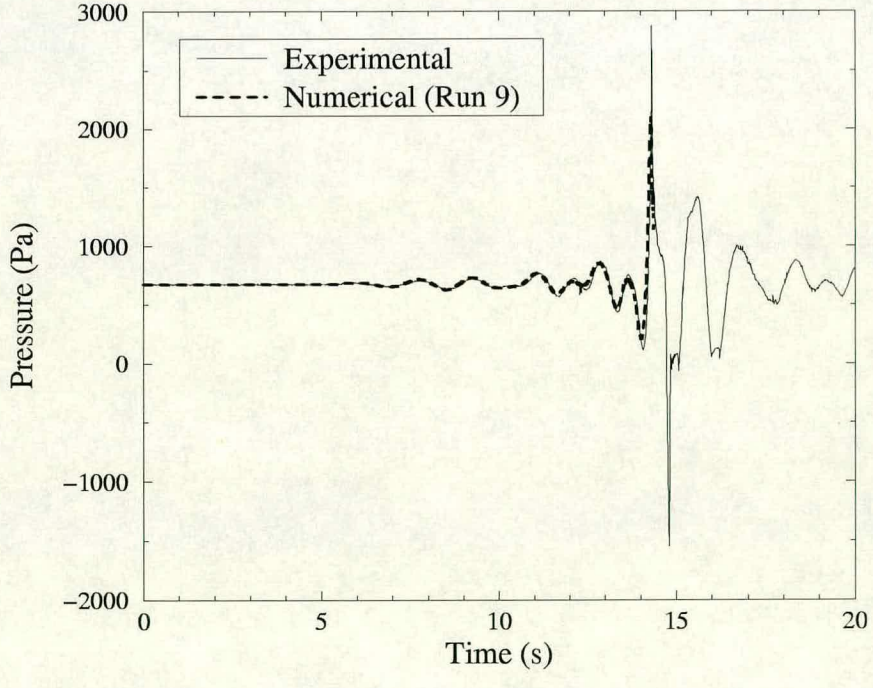

Figure 6.31: Bottom pressure transducer records for "air 2" wave. The bottom pressure transducer is located 0.681m up the vertical wall.

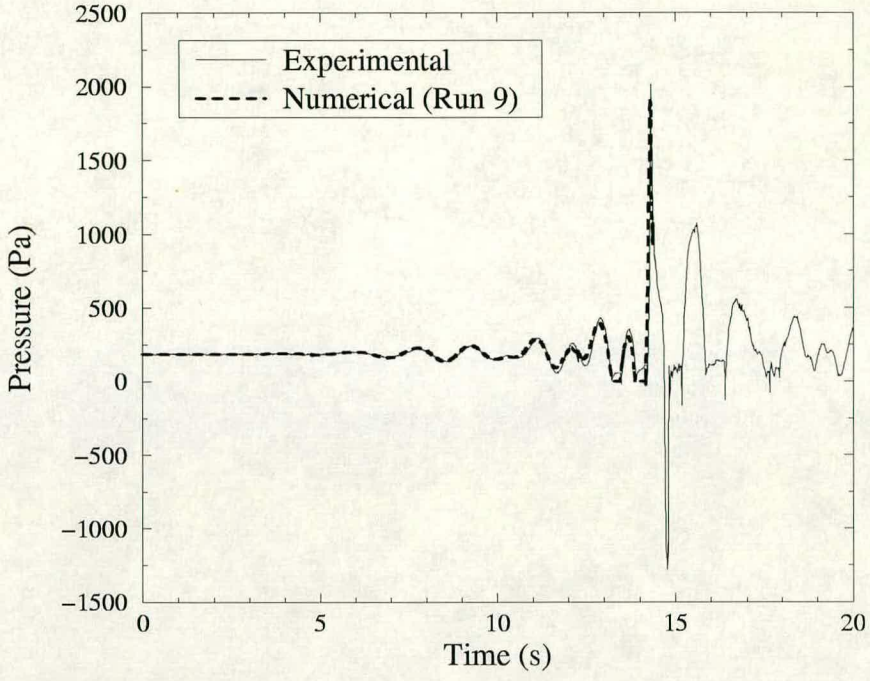

Figure 6.32: Middle pressure transducer records for "air 2" wave. The middle pressure transducer is located 0.731m up the vertical wall.

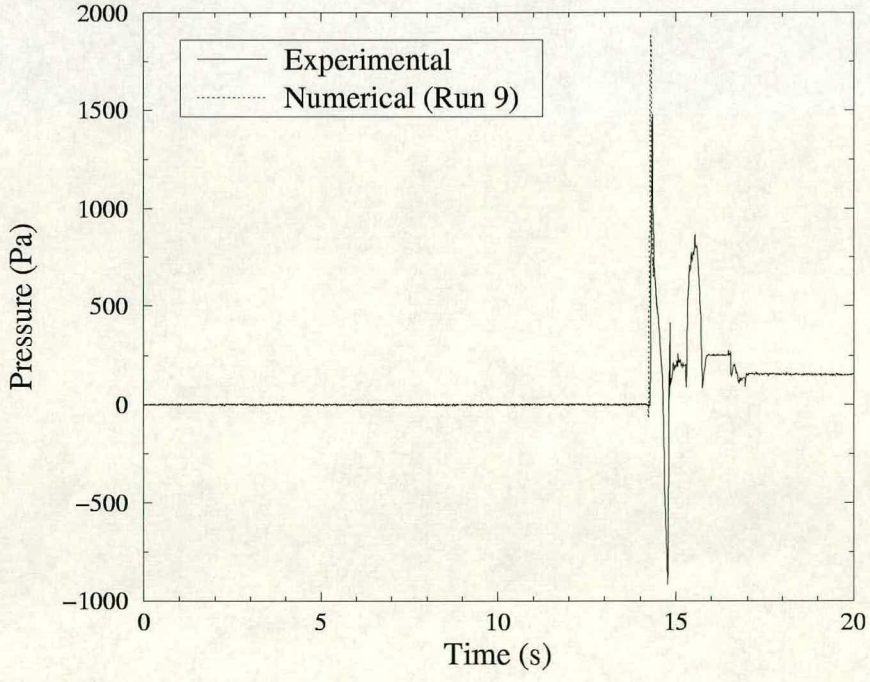

Figure 6.33: Top pressure transducer records for "air 2" wave. The top pressure transducer is located 0.781m up the vertical wall.

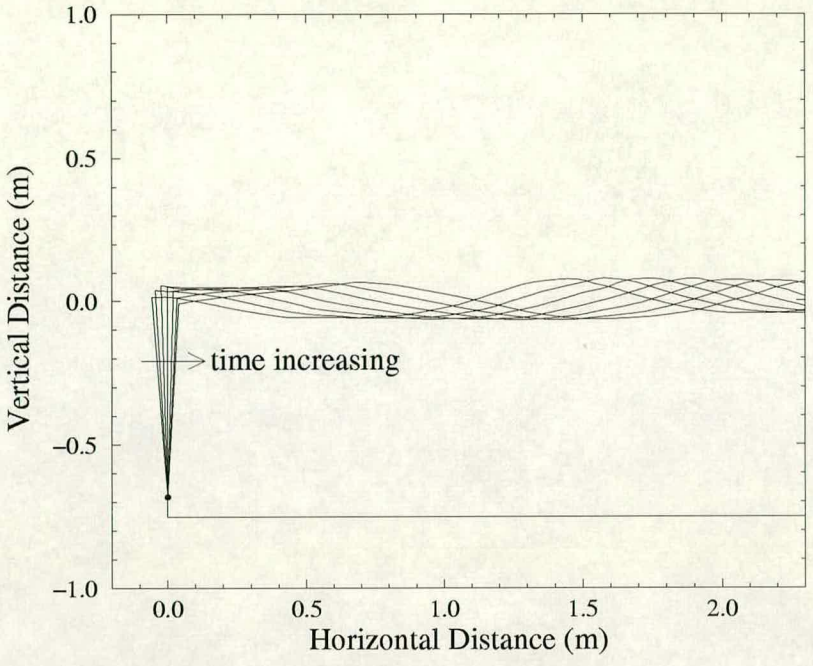

Figure 6.34: Waves being generated by the paddle wavemaker for the experiment "air 2" wave. The numerical free-surface profiles correspond to the times $t = 9.3, 9.4, 9.5, \ldots, 9.9$ seconds.

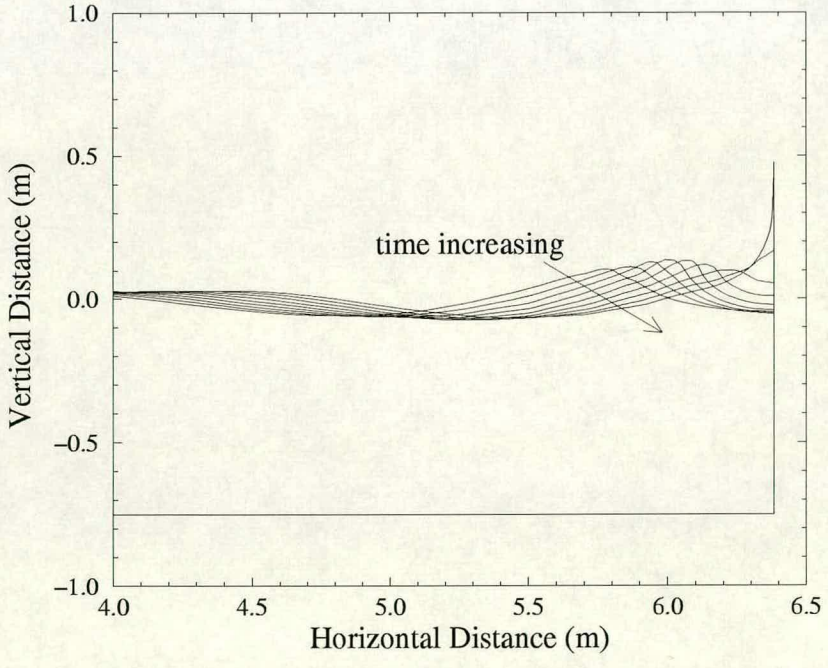

Figure 6.35: "Air 2" wave impacting against the wall. The numerical free-surface profiles correspond to the times $t = 13.95, 14.00, 14.05, \ldots, 14.35$ seconds.

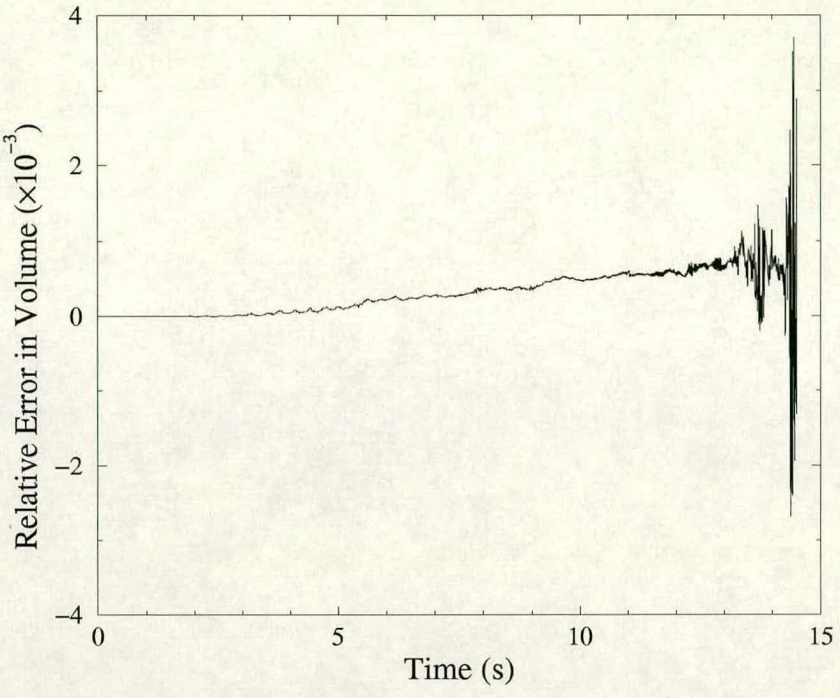

Figure 6.36: The relative error in the volume against time for the simulation of "air 2" wave.

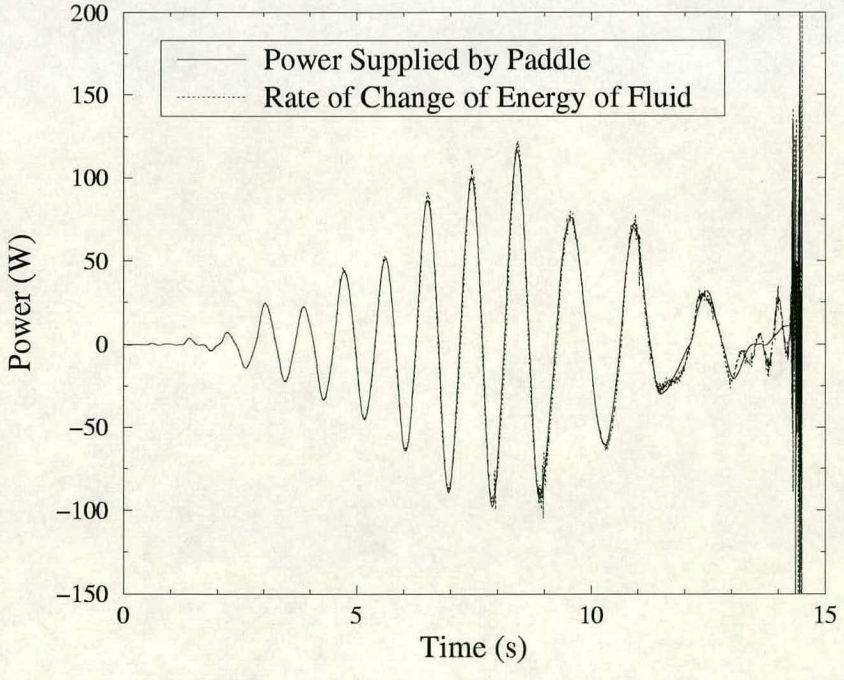

Figure 6.37: The power supplied by the paddle and the rate of change of the energy of the fluid against time for the simulation of "air 2" wave.

Chapter 7

Conclusions & Further Work

7.1 Conclusions

In this section the main conclusions are dealt with; more detailed conclusions can be found in the "Summary" sections of chapters 3, 4 & 6.

This thesis was concerned with the numerical prediction of free-surface flows and especially free-surface flows in the vicinity of surface-piercing bodies.

In chapter 2 it was shown that the simplified theoretical framework of potential theory could adequately capture the essential physics involved in the above flows. Also, in chapter 2, one of the most successful numerical methods for modelling nonlinear free-surface potential flows, namely the Boundary-Integral Method (BIM), was introduced and reviewed. This is the method that was chosen for use in the present study.

It is well known that BIMs can have problems at corners in the boundary of the fluid domain and especially at corners between the free-surface and surface-piercing bodies. It is also well known that most of these problems are caused by the fact that the potential flow solution can be singular at such points.

Chapter 3 described in detail the development of the present stable, accurate & efficient two-dimensional Boundary-Integral Method. Consequently, chapter 3 fulfills aim 1 of this thesis (see page 4).

The present BIM is based on the very successful BIM of Vinje & Brevig [55] & [56]. However, the present BIM goes beyond Vinje & Brevig's method by assuming that the complex potential $\beta(z)$ varies cubically between nodes, instead of just linearly. The way this cubic approximation is calculated depends on whether the interval of interest is adjacent to a corner or not. This extension of Vinje & Brevig's method was performed rigorously and it was found that:

1. Great care is required when choosing the right branch cut for complex logarithms. This point also applies to the case when $\beta(z)$ varies linearly between nodes but it was not mentioned by any of the researchers who used that method.

2. There is no need to calculate internal angles at the boundary nodes. That is, there is no need to calculate $\theta(z_k)$ for $k = 1, \ldots, N$ (see equation (3.10)).

A method to smooth out possible weak singularities in $\beta(z)$ or $\beta_t(z)$ at free-surface/body intersection point was also developed. This method works by forcing the Cauchy-Riemann equations for $\beta(z)$ and $\beta_t(z)$ to hold at such points. This method was named the "corner-correction" method and it is similar to the "BC-correction" method of Otta *et al.* [40].

The last major procedure developed for the present BIM was the smoothing & regridding procedure. This procedure tries to suppress free-surface instabilities and it is based on the smoothing & regridding procedure of Tsai & Yue [53]. The smoothing procedure uses cubic smoothing splines to smooth the free-surface and the regridding procedure uses an inverse interpolation method to place more nodes in regions of high curvature and less nodes in regions of low curvature subject to a minimum and maximum node spacing. These two procedures were developed rigorously. Also, features of the present problem were exploited in order to make the present smoothing procedure as efficient as possible.

The present BIM was then compared against the three main investigative techniques used in science. That is, the results of the present BIM were then compared against an analytical solution, the results of another numerical method and the results of an experiment.

In chapter 4 the results of the present BIM were compared against a small-time analytical solution for the flow caused by a vertical plate uniformly accelerating from rest into an initially undisturbed semi-infinite strip of inviscid, incompressible fluid of finite depth h. This small-time analytical solution was obtained by King & Needham [35]. The author believes that this chapter represents the first time that the results of a BIM have been compared against an exact analytical solution for an extreme potential flow at the intersection between a free-surface and a body. This chapter also fulfills aim 2 of this thesis (see page 4).

In addition to the above comparison a previously unnoticed feature of the analytical solution was identified and presented in this chapter. This feature is the "kink" near the plate in the inner analytical solution. Since this feature is so close to the main point of interest, namely the free-surface/plate intersection point, it is very important.

After this "kink" in the inner analytical solution had been examined the present BIM was then applied to the above accelerating plate problem.

Initially, the "corner-correction" procedure of subsection 3.5.2 was not used and it was found that the numerical scheme broke down almost immediately. The reason for this breakdown was shown to be the $z\log z$ type singularity in $\beta_t(z)$ at the free-surface/plate intersection point at $t = 0$. Following this it was decided that the "corner-correction" procedure should be used for the rest of this study.

Although the "corner-correction" procedure smoothes out singularities in $\beta(z)$ and $\beta_t(z)$ at free-surface/body intersection points, and in so doing slightly alters

the mathematical problem being solved, it was found that there was very good agreement between the numerical results and the small-time analytical solution for the accelerating plate problem. The BIM managed to predict very well the outer solution, the inner solution, the height of the free-surface at the plate and the velocity potential (& its partial time derivative) at the free-surface/plate intersection point. In addition, if the node spacing was small enough, the BIM managed to qualitatively predict the "kink" in the inner analytical solution. However, the BIM was not able to fully resolve the "kink"[1] because a very small node spacing would require a very, very small time-step in order not to violate a local Courant type stability condition.

Next, the results of the present BIM for the accelerating plate problem and for times after the time when the small-time analytical solution ceases to be valid were examined. These results appear to be very good: both volume and energy are conserved very well. However, the numerical scheme eventually broke down due to free-surface instabilities.

Finally, in chapter 4, the present BIM, with the smoothing & regridding procedure of subsection 3.5.3, was applied to the accelerating plate problem. It was found that careful use of the smoothing & regridding procedure successfully suppressed free-surface instabilities, enabling very long-term runs to be performed. A very long-term run was carried out for the case of the plate accelerating at $2g$ and it was found that the free-surface began to overturn.

In chapter 6 the results of the present BIM were compared against the results of an experiment. In the experiment, deep-water waves were generated in a wave flume by a paddle wavemaker and then impacted against a vertical wall. Unlike

[1]The "kink" (which is actually a complicated oscillation) is really a very small feature, even on the scale of the inner region it is small, and so resolving the "kink" with the BIM is very difficult.

in most other comparison between the results of a BIM and the results of an experiment, in this comparison the geometry of the physical wave flume and the motion of the physical wavemaker were duplicated exactly in the numerical wave flume. This chapter fulfilled aims 3 & 4 of this thesis (see page 5) and it was also useful for aim 2 of this thesis (see page 4).

In all, six different types of deep-water waves were impacted against the vertical wall; from steep unbroken waves, which simply sloshed violently against the wall, to waves which broke against the wall entrapping air pockets.

For these waves, full-length[2] numerically predicted wavegauge records were compared against full-length measured wavegauge records for two wavegauges, one located approximately half way down the flume and the other located on the vertical wall. Also, full-length numerically predicted pressure transducer records were compared against full-length measured pressure transducer records for three pressure transducers on the wall. For this study the main interest was in the wall wavegauge records. In the experimental comparison by Zhang *et al.* [61], where the geometry of the wave flume and the motion of the wavemaker were also duplicated in the BIM, there were no full-length numerically predicted and measured free-surface elevation records at the wall.

In general the numerical results agreed very well with the results from the experiments. However, for some of the runs agreement was not so good during the last few seconds before impact. This problem might have been caused by the fact that the minimum node spacing on a regridded free-surface $h_{\min}$ was too large to properly resolve the steepening and overturning of the free-surface. Attempts were made to reduce $h_{\min}$ but it was found that the present BIM had slight stability problems over such long runs, especially for small $h_{\min}$. It was

[2]That is, for the whole length of the run.

proposed that the most likely cause of these stability problems was the *modified* higher order discretisation of the boundary at corners and the *modified* high-order numerical differentiation scheme at corners.

Incidentally, the author believes that chapter 6 represents the first time that the motion of an *absorbing* wavemaker has been duplicated in a numerical wave flume. Consequently, because of the generally good agreement between the numerical results and the results from the experiments, it can be concluded that the wavemaker in the numerical wave flume is as good an absorbing wavemaker as the wavemaker in the physical wave flume.

7.2 Further Work

As mentioned by King & Needham, in the title of their paper [35], the small-time analytical solution to the uniformly accelerating plate problem is only part 1 of their study. Part 2 of their study, on which they are currently working, is the small-time analytical solution to the impulsively started (vertical) plate problem of Appendix A. For the latter case the resultant flow is more extreme with a stronger singularity at the free-surface/plate intersection point at $t = 0$. This time, instead of a $z\log z$ type singularity in $\beta_t(z)$ at $t = 0$ and $z = 0$, there is a $z\log z$ type singularity in $\beta(z)$ at $t = 0$ and $z = 0$. Consequently, for the latter case there is an unbounded upwards *velocity* of the intersection point at $t = 0$ instead of just an unbounded upwards *acceleration* of the intersection point at $t = 0$ (see pages 100 & 184). If King & Needham manage[3] to obtain this small-time analytical solution to the impulsively started plate problem then it would be very interesting to apply the present BIM to the same problem and compare

[3]Much more sophisticated asymptotic theory is required to find the small-time analytical solution to the impulsively started plate problem than was required to find the small-time analytical solution to the uniformly accelerating plate problem.

numerical and analytical results.

Another interesting piece of further work would be to calculate the closed-form solution to the oscillations which make up the "kink" in the inner solution of the small-time analytical solution to the uniformly accelerating plate problem (see figure 4.3). This would involve trying to calculate the $o(x_{\text{inner}})$ term in equation (4.6) to as many orders of x_{inner} as possible.

A third possible piece of further work relates to the present comparison with experiments (Chapter 6). As mentioned in subsection 6.3.7 the value of the minimum node spacing on a regridded free-surface h_{min} was too large to resolve the steepening and overturning of the free-surface for some of the later "waves" in the comparison. It was also stated in subsection 6.3.7 that when h_{min} was reduced it was difficult to find values of the other five run-controlling parameters in order to give a stable run. Consequently, it would be interesting to do a systematic search of the parameter space in an attempt to find such a stable run.

Finally, the present numerical wave flume was developed to be very flexible and user-friendly. As a result of this the code can be easily applied to a wide range of practical problems. For example, the code could be used to study waves impacting against sloping walls, waves breaking on beaches or waves propagating over bars.

Appendix A

The Impulsively Started Plate Problem

Consider the impulsively started plate problem at $t = 0$.

A plate is impulsively started from rest at $t = 0$ and moved with constant velocity U into an initially undisturbed, semi-infinite strip of fluid of finite depth h with a free-surface and a gravitational restoring force.

Non-Dimensionalisation The problem is non-dimensionalised using the same non-dimensionalisation as that described in section 3.3 and it is found that there is only one governing parameter, namely the Froude number $\mathrm{Fr} = U/\sqrt{gh}$.

A.1 The Vertical Plate Case

Firstly, consider the case when the plate is vertical, with a view to finding the form of the complex potential $\beta(z)$ near the plate/free-surface intersection point at $t = 0$ (intersection angle $\frac{\pi}{2}$). Figure A.1 shows the boundary conditions. The form of the stream function ψ on the plate is given by equation (3.3).

Now $\beta(z)$ is analytic away from corners and therefore along the free-surface the following Cauchy-Riemann equation holds

$$\phi_x = \psi_y.$$

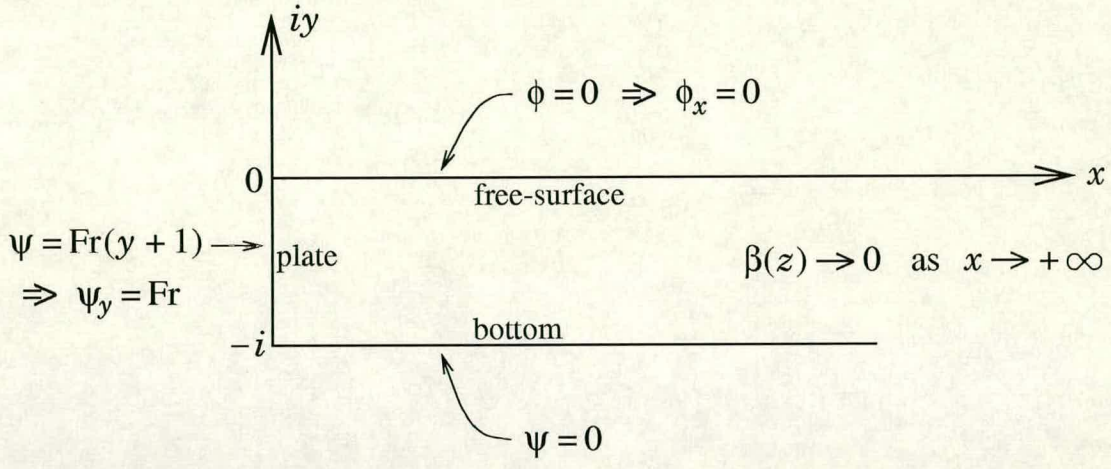

Figure A.1: Boundary conditions for an impulsively started vertical plate at $t = 0$.

Thus the boundary conditions for the function ψ_y on the plate and the free-surface are given in figure A.2. A function which satisfies these boundary conditions for ψ_y is

$$f(x, y) = -\frac{2\mathrm{Fr}}{\pi}\theta$$

and this is the real part of the function

$$F(z) = \frac{2\mathrm{Fr}}{\pi} i \log z,$$

which is analytic over the whole fluid domain except $z = 0$. Subtracting $F(z)$ from $d\beta/dz = \psi_y + i\psi_x$ leaves a function which is certainly analytic in the entire fluid domain except $z = 0$. This function also does not violate the Cauchy-Riemann equations at $z = 0$ and so it is analytic everywhere in the whole fluid domain, including $z = 0$. Thus

$$\frac{d\beta}{dz} = \frac{2\mathrm{Fr}}{\pi} i \log z + \text{analytic part.} \tag{A.1}$$

From equation (A.1), and using the fact that $d\beta/dz = u - iv$, the vertical

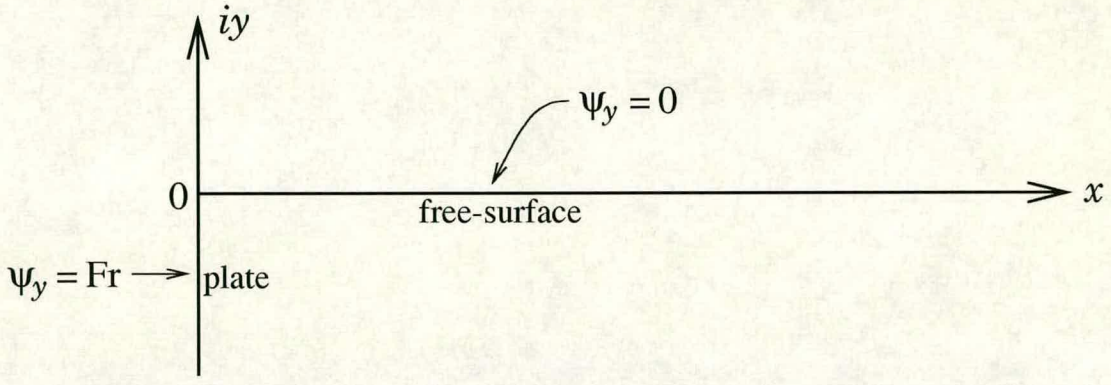

Figure A.2: ψ_y on the plate and on the free-surface.

velocity v in the fluid domain at $t = 0$ is

$$v = -\frac{2\mathrm{Fr}}{\pi}\log r - \mathrm{Im}(\text{analytic part}), \tag{A.2}$$

where $r = |z|$. By definition the analytic part is necessarily bounded and so therefore its imaginary part is also bounded. As a result v is dominated by the $\log r$ term as $r \to 0$, and the upward velocity of the fluid particle at $z = 0$ and $t = 0$ is unbounded.

Finally, to obtain the form of $\beta(z)$ at $t = 0$ equation (A.1) is integrated to give

$$\beta(z) = \frac{2\mathrm{Fr}}{\pi} i\Big(z\log z - z + \frac{\pi}{2}\Big) + \text{analytic part}, \tag{A.3}$$

where the whole of the first term satisfies the boundary conditions for ϕ & ψ given on the free-surface and the plate, as shown in figure A.1. Thus, for the impulsively started vertical plate problem there is a $z\log z$ type singularity in $\beta(z)$ at the plate/free-surface intersection point at $t = 0$.

A.2 The Sloping Plate Case

Now consider the case when the plate is sloping, with a view to finding the form of the complex potential $\beta(z)$ near the plate/free-surface intersection point at $t = 0$

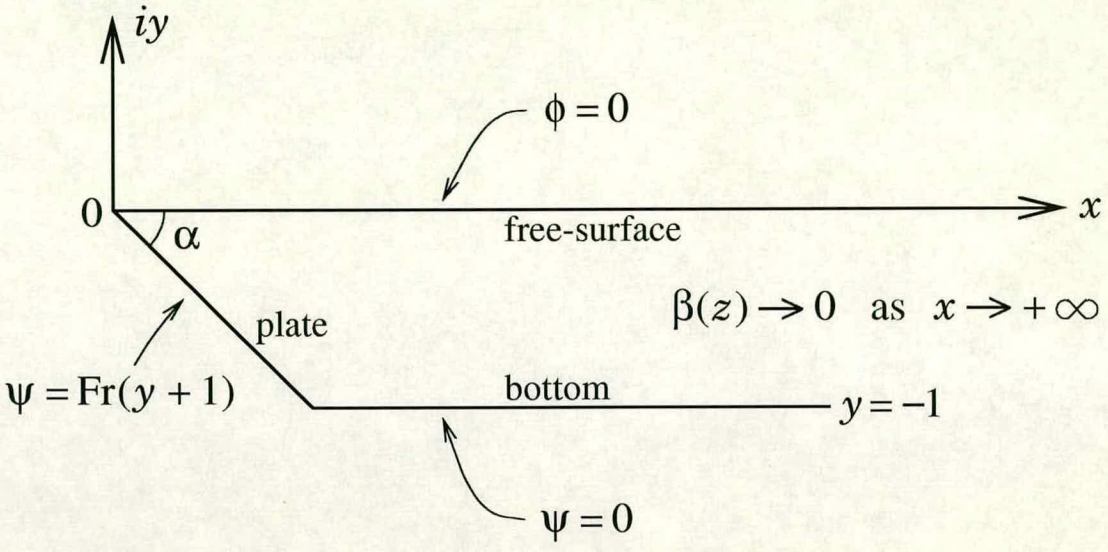

Figure A.3: Boundary conditions for an impulsively started sloping plate at $t = 0$.

(intersection angle α). Figure A.3 shows the boundary conditions. The sloping plate can either slope forwards, as in figure A.3, or it can slope backwards. That is α must satisfy $0 < \alpha < \frac{\pi}{2}$ or $\frac{\pi}{2} < \alpha < \pi$.

A complex potential which satisfies the boundary conditions on the free-surface and the plate but does not satisfy the boundary condition on the bottom or the far-field boundary condition is

$$\beta(z) = i\mathrm{Fr}(1 - (\tan\alpha)z). \tag{A.4}$$

In fact this equation gives the leading order behaviour, at $z = 0$, of the complex potential which satisfies all the boundary conditions in figure A.3. Therefore, for the impulsively started sloping plate problem the complex potential is analytic at the plate/free-surface intersection point at $t = 0$.

Appendix B

Calculation of the Influence Functions $\Gamma_{k,j}$

Consider a corner in the boundary of the fluid domain, as shown in figure B.1. Suppose that the variation of β between two adjacent nodes is approximated by a cubic. The way this cubic is calculated is described in section 3.5. Then for $j = \ldots, i-3, i-2, i+1, i+2, \ldots$

$$\begin{aligned}
&\int_{C_{j,j+1}} \frac{\beta(z)}{z - z_k} dz \\
&\approx \frac{\beta_{j-1}}{(z_{j-1} - z_j)(z_{j-1} - z_{j+1})(z_{j-1} - z_{j+2})} \int_{C_{j,j+1}} \frac{(z - z_j)(z - z_{j+1})(z - z_{j+2})}{z - z_k} dz \\
&+ \frac{\beta_j}{(z_j - z_{j-1})(z_j - z_{j+1})(z_j - z_{j+2})} \int_{C_{j,j+1}} \frac{(z - z_{j-1})(z - z_{j+1})(z - z_{j+2})}{z - z_k} dz \\
&+ \frac{\beta_{j+1}}{(z_{j+1} - z_{j-1})(z_{j+1} - z_j)(z_{j+1} - z_{j+2})} \int_{C_{j,j+1}} \frac{(z - z_{j-1})(z - z_j)(z - z_{j+2})}{z - z_k} dz \\
&+ \frac{\beta_{j+2}}{(z_{j+2} - z_{j-1})(z_{j+2} - z_j)(z_{j+2} - z_{j+1})} \int_{C_{j,j+1}} \frac{(z - z_{j-1})(z - z_j)(z - z_{j+1})}{z - z_k} dz.
\end{aligned} \tag{B.1}$$

For $j = i-1$ the contour of integration in the integrals on the right hand side of equation (B.1) remains $C_{j,j+1}$ (that is $C_{i-1,i}$) but all the other indices on the right hand side of equation (B.1) that contain j have 1 subtracted from them.

For $j = i$ the contour of integration in the integrals on the right hand side of equation (B.1) remains $C_{j,j+1}$ (that is $C_{i,i+1}$) but all the other indices on the

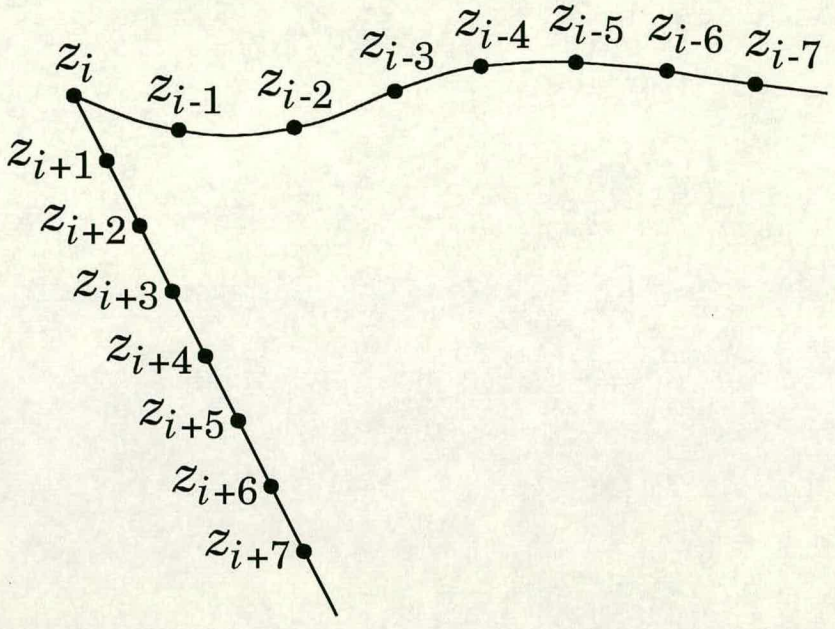

Figure B.1: A typical distribution of nodes near a corner.

right hand side of equation (B.1) that contain j have 1 added to them.

Now let

$$I_1(i,j,k,l,m,n) \stackrel{\text{def}}{=} \int_{C_{i,j}} \frac{(z-z_k)(z-z_l)(z-z_m)}{z-z_n} dz. \tag{B.2}$$

If $i \leq n \leq j$ (i & j are distinct integers and $i < j$) then the integrand of this integral is normally singular. However, if in addition $n = k$ or $n = l$ or $n = m$ (k, l & m are distinct integers), then the integrand is not singular.

If $n = k$ or $n = l$ or $n = m$ then

$$\begin{aligned} I_1(i,j,k,l,m,n) &= \int_{C_{i,j}} (z-z_p)(z-z_q)dz \\ &= \int_{C_{i,j}} z^2 - (z_p+z_q)z + z_p z_q \, dz \\ &= \frac{1}{3}(z_j^3 - z_i^3) - \frac{1}{2}(z_p+z_q)(z_j^2 - z_i^2) + z_p z_q (z_j - z_i), \end{aligned} \tag{B.3}$$

where p & q are the two integers out of k, l & m not equal to n.

If $n < i$ and $n > j$ and n does not equal any of k, l & m then

$$\begin{aligned} I_1(i,j,k,l,m,n) = & \\ & \int_{C_{i,j}} \frac{z^3 + az^2 + bz + c}{z - z_n} dz \\ = & \int_{C_{i,j}} z^2 + (a + z_n)z + b + z_n(a + z_n) + \frac{c + z_n(b + z_n(a + z_n))}{z - z_n} dz \\ = & \frac{1}{3}(z_j^3 - z_i^3) + \frac{1}{2}(a + z_n)(z_j^2 - z_i^2) + (b + z_n(a + z_n))(z_j - z_i) \\ & + (c + z_n(b + z_n(a + z_n))) \ln \frac{z_j - z_n}{z_i - z_n}, \end{aligned} \tag{B.4}$$

where $a = -(z_k + z_l + z_m)$, $b = z_k z_l + z_k z_m + z_l z_m$ and $c = -z_k z_l z_m$. Also, note that

$$c + z_n(b + z_n(a + z_n)) = (z_n - z_k)(z_n - z_l)(z_n - z_m). \tag{B.5}$$

Great care must be taken to ensure that the logarithm on the right hand side of equation (B.4) is the correct logarithm to take.

For $z \in \mathbb{C} \setminus \{0\}$ and $\alpha \in \mathbb{R}$ the associated logarithm of z is given by

$$\ln_\alpha z \stackrel{\text{def}}{=} \ln |z| + i \arg_\alpha z, \tag{B.6}$$

where $\arg_\alpha z$ is the argument of z such that

$$\alpha - \pi < \arg_\alpha z \leq \alpha + \pi.$$

The logarithm in equation (B.4) is the *principal* logarithm and corresponds to $\alpha = 0$.

Basically, the choice of logarithm in equation (B.4) depends on how much the subcontour $C_{i,j}$ winds round z_n. Here it can be shown that, in all practical situations, the angle δ that $C_{i,j}$ winds round z_n satisfies $-\pi < \delta \leq \pi$, and this means that the principal logarithm is the correct logarithm to take.

B.1 Influence Functions for $k \neq j$

Now there is sufficient information to calculate the influence functions $\Gamma_{k,j}$ for $k \neq j$. This is done by firstly using equation (3.10) together with equation (B.1) and the two paragraphs that follow it. Then the coefficients of β_j are collected together.

For the case $k = j$ integrals with singular integrands have to be evaluated, and so treatment of this case is considered later.

Therefore, for $k \neq j$ & $j = \ldots, i-5, i-4, i+4, i+5, \ldots$

$$\begin{aligned}
\Gamma_{k,j} &= \frac{1}{(z_j - z_{j-3})(z_j - z_{j-2})(z_j - z_{j-1})} I_1(j-2, j-1, j-3, j-2, j-1, k) \\
&+ \frac{1}{(z_j - z_{j-2})(z_j - z_{j-1})(z_j - z_{j+1})} I_1(j-1, j, j-2, j-1, j+1, k) \\
&+ \frac{1}{(z_j - z_{j-1})(z_j - z_{j+1})(z_j - z_{j+2})} I_1(j, j+1, j-1, j+1, j+2, k) \\
&+ \frac{1}{(z_j - z_{j+1})(z_j - z_{j+2})(z_j - z_{j+3})} I_1(j+1, j+2, j+1, j+2, j+3, k).
\end{aligned} \tag{B.7}$$

For $k \neq j$ & $j = i - 3$

$$\begin{aligned}
\Gamma_{k,j} &= \frac{1}{(z_j - z_{j-3})(z_j - z_{j-2})(z_j - z_{j-1})} I_1(j-2, j-1, j-3, j-2, j-1, k) \\
&+ \frac{1}{(z_j - z_{j-2})(z_j - z_{j-1})(z_j - z_{j+1})} I_1(j-1, j, j-2, j-1, j+1, k) \\
&+ \frac{1}{(z_j - z_{j-1})(z_j - z_{j+1})(z_j - z_{j+2})} I_1(j, j+1, j-1, j+1, j+2, k) \\
&+ \frac{1}{(z_j - z_{j+1})(z_j - z_{j+2})(z_j - z_{j+3})} I_1(j+1, \underline{j+3}, j+1, j+2, j+3, k).
\end{aligned} \tag{B.8}$$

The underline shows the difference between this case and (B.7).

For $k \neq j$ & $j = i + 3$

$$\begin{aligned}
\Gamma_{k,j} &= \frac{1}{(z_j - z_{j-3})(z_j - z_{j-2})(z_j - z_{j-1})} I_1(\underline{j-3}, j-1, j-3, j-2, j-1, k) \\
&+ \frac{1}{(z_j - z_{j-2})(z_j - z_{j-1})(z_j - z_{j+1})} I_1(j-1, j, j-2, j-1, j+1, k) \\
&+ \frac{1}{(z_j - z_{j-1})(z_j - z_{j+1})(z_j - z_{j+2})} I_1(j, j+1, j-1, j+1, j+2, k) \\
&+ \frac{1}{(z_j - z_{j+1})(z_j - z_{j+2})(z_j - z_{j+3})} I_1(j+1, j+2, j+1, j+2, j+3, k).
\end{aligned} \tag{B.9}$$

Again the underline shows the difference between this case and (B.7).

For $k \neq j$ & $j = i - 2$

$$\begin{aligned}
\Gamma_{k,j} &= \frac{1}{(z_j - z_{j-3})(z_j - z_{j-2})(z_j - z_{j-1})} I_1(j-2, j-1, j-3, j-2, j-1, k) \\
&+ \frac{1}{(z_j - z_{j-2})(z_j - z_{j-1})(z_j - z_{j+1})} I_1(j-1, j, j-2, j-1, j+1, k) \\
&+ \frac{1}{(z_j - z_{j-1})(z_j - z_{j+1})(z_j - z_{j+2})} I_1(j, j+2, j-1, j+1, j+2, k).
\end{aligned} \tag{B.10}$$

For $k \neq j$ & $j = i + 2$

$$\begin{aligned}
\Gamma_{k,j} &= \frac{1}{(z_j - z_{j-2})(z_j - z_{j-1})(z_j - z_{j+1})} I_1(j-2, j, j-2, j-1, j+1, k) \\
&+ \frac{1}{(z_j - z_{j-1})(z_j - z_{j+1})(z_j - z_{j+2})} I_1(j, j+1, j-1, j+1, j+2, k) \\
&+ \frac{1}{(z_j - z_{j+1})(z_j - z_{j+2})(z_j - z_{j+3})} I_1(j+1, j+2, j+1, j+2, j+3, k).
\end{aligned} \tag{B.11}$$

For $k \neq j$ & $j = i - 1$

$$\begin{aligned}
\Gamma_{k,j} &= \frac{1}{(z_j - z_{j-3})(z_j - z_{j-2})(z_j - z_{j-1})} I_1(j-2, j-1, j-3, j-2, j-1, k) \\
&+ \frac{1}{(z_j - z_{j-2})(z_j - z_{j-1})(z_j - z_{j+1})} I_1(j-1, j+1, j-2, j-1, j+1, k).
\end{aligned} \tag{B.12}$$

For $k \neq j$ & $j = i+1$

$$\begin{aligned}\Gamma_{k,j} &= \frac{1}{(z_j - z_{j-1})(z_j - z_{j+1})(z_j - z_{j+2})} I_1(j-1, j+1, j-1, j+1, j+2, k) \\ &+ \frac{1}{(z_j - z_{j+1})(z_j - z_{j+2})(z_j - z_{j+3})} I_1(j+1, j+2, j+1, j+2, j+3, k).\end{aligned} \tag{B.13}$$

For $k \neq j$ & $j = i$

$$\begin{aligned}\Gamma_{k,j} &= \frac{1}{(z_j - z_{j-3})(z_j - z_{j-2})(z_j - z_{j-1})} I_1(j-2, j, j-3, j-2, j-1, k) \\ &+ \frac{1}{(z_j - z_{j+1})(z_j - z_{j+2})(z_j - z_{j+3})} I_1(j, j+2, j+1, j+2, j+3, k).\end{aligned} \tag{B.14}$$

B.2 Influence Functions for $k = j$

Now consider calculating the influence functions $\Gamma_{k,j}$ for $k = j$. Unfortunately, in this case, each one of equations (B.7) to (B.14) has integrals with singular integrands. Consequently, much more care is required to calculate the influence functions when $k = j$.

Firstly, define

$$\begin{aligned}&I_2(i, j, k, l, m, n) = \\ &\quad \int_{C_{i,j}} z^2 + (a + z_n)z + b + z_n(a + z_n)\, dz \\ &= \frac{1}{3}(z_j^3 - z_i^3) + \frac{1}{2}(a + z_n)(z_j^2 - z_i^2) + (b + z_n(a + z_n))(z_j - z_i),\end{aligned} \tag{B.15}$$

where, as before, $a = -(z_k + z_l + z_m)$, $b = z_k z_l + z_k z_m + z_l z_m$ and $c = -z_k z_l z_m$. The above equation is equation (B.4) with the logarithmic term removed. It is this logarithmic term which causes the problems when $k = j$.

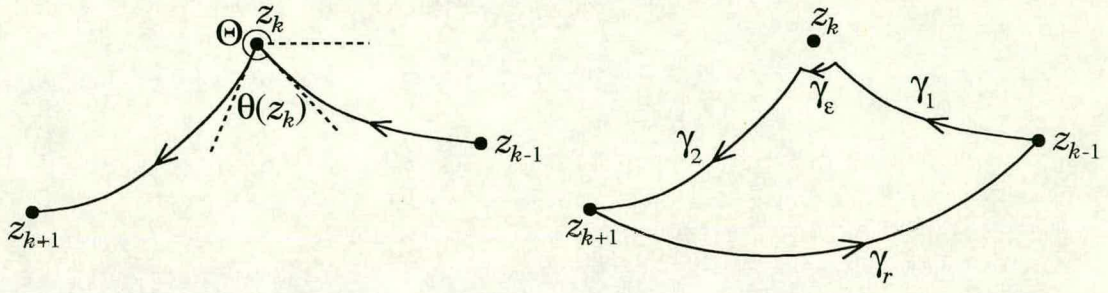

Figure B.2: The subcontour $C_{k-1,k+1}$ and a construction of contours used to find I.

Then for $k = j = \ldots, i-5, i-4, i+4, i+5, \ldots$

$$\begin{aligned}
\Gamma_{k,j} &= \frac{1}{(z_j - z_{j-3})(z_j - z_{j-2})(z_j - z_{j-1})} I_1(j-2, j-1, j-3, j-2, j-1, k) \\
&+ \frac{1}{(z_j - z_{j-2})(z_j - z_{j-1})(z_j - z_{j+1})} I_2(j-1, j, j-2, j-1, j+1, k) \\
&+ \frac{1}{(z_j - z_{j-1})(z_j - z_{j+1})(z_j - z_{j+2})} I_2(j, j+1, j-1, j+1, j+2, k) \\
&+ \frac{1}{(z_j - z_{j+1})(z_j - z_{j+2})(z_j - z_{j+3})} I_1(j+1, j+2, j+1, j+2, j+3, k) \\
&+ \mathrm{PV} \int_{C_{k-1,k+1}} \frac{dz}{z - z_k}. \qquad \text{(B.16)}
\end{aligned}$$

The above equation was obtained by using equations (B.7), (B.4), (B.15) & (B.5). The first four lines on the right hand side of equation (B.16) are easily calculated using equations (B.4) & (B.15). However, the integral on the last line on the right hand side of equation (B.16) has a singular integrand.

Let

$$I = \mathrm{PV} \int_{C_{k-1,k+1}} \frac{dz}{z - z_k}. \qquad \text{(B.17)}$$

Figure B.2 is a schematic showing the subcontour $C_{k-1,k+1}$ as well as a construction of contours used to evaluate I. The arc shaped contour $-\gamma_\varepsilon$ in the figure is given by

$$z = z_k + \varepsilon e^{i\alpha} \quad \text{for} \quad \Theta \leq \alpha \leq \Theta + \theta(z_k) \qquad \text{(B.18)}$$

and the contour γ_r is a return contour.

From figure B.2 it can be seen that

$$I = \lim_{\varepsilon \to 0} \left(\int_{\gamma_1} + \int_{\gamma_2} \frac{dz}{z - z_k} \right). \tag{B.19}$$

However, by Cauchy's integral theorem

$$\int_{\gamma_1} + \int_{\gamma_\varepsilon} + \int_{\gamma_2} + \int_{\gamma_r} \frac{dz}{z - z_k} = 0 \tag{B.20}$$

and therefore

$$\int_{\gamma_1} + \int_{\gamma_2} \frac{dz}{z - z_k} = \int_{-\gamma_\varepsilon} \frac{dz}{z - z_k} + \int_{-\gamma_r} \frac{dz}{z - z_k}. \tag{B.21}$$

Consider the first integral on the right hand side of the above equation. By a similar analysis to that on page 15

$$\lim_{\varepsilon \to 0} \int_{-\gamma_\varepsilon} \frac{dz}{z - z_k} = i\theta(z_k). \tag{B.22}$$

In addition, the second integral on the right hand side of equation (B.21) can be shown to be

$$\int_{-\gamma_r} \frac{dz}{z - z_k} = \ln_{-\pi} \frac{z_{k+1} - z_k}{z_{k-1} - z_k}. \tag{B.23}$$

The reason why the logarithm on the right hand side of the above equation is $\ln_{-\pi}$ is because the contour $-\gamma_r$ will, in all cases, sweep out an angle of between 0 and -2π around the node z_k.

Finally, using equations (B.19) to (B.23) gives

$$I = i\theta(z_k) + \ln_{-\pi} \frac{z_{k+1} - z_k}{z_{k-1} - z_k}. \tag{B.24}$$

Substitution of this equation into equation (B.17) and then into equation (B.16) suggests a redefinition of $\Gamma_{k,k}$ in equation (3.11) due to the fact that the term

$i\theta(z_k)\beta_k$ will now appear on both sides of equation (3.11). This redefinition of the influence functions is

$$\Gamma'_{k,j} = \begin{cases} \Gamma_{k,j} & \text{for } k \neq j, \\ \Gamma_{k,j} - i\theta(z_k) & \text{for } k = j. \end{cases} \tag{B.25}$$

With this redefinition of $\Gamma_{k,j}$ the left hand side of equation (3.11) can be cancelled and equation (3.11) becomes

$$\sum_{j=1}^{N} \Gamma'_{k,j}\beta_j = 0 \quad \text{for } k = 1, \ldots, N. \tag{B.26}$$

As a consequence of this redefinition the internal angles ($\theta(z_k)$ for $k = 1, \ldots, N$) need never be calculated.

Therefore, taking all of the above into account, the new influence functions for $k = j$ are as follows (from now on drop the $'$ from the redefined $\Gamma_{k,j}$).

For $k = j = \ldots, i-5, i-4, i+4, i+5, \ldots$

$$\begin{aligned} \Gamma_{k,j} &= \frac{1}{(z_j - z_{j-3})(z_j - z_{j-2})(z_j - z_{j-1})} I_1(j-2, j-1, j-3, j-2, j-1, k) \\ &+ \frac{1}{(z_j - z_{j-2})(z_j - z_{j-1})(z_j - z_{j+1})} I_2(j-1, j, j-2, j-1, j+1, k) \\ &+ \frac{1}{(z_j - z_{j-1})(z_j - z_{j+1})(z_j - z_{j+2})} I_2(j, j+1, j-1, j+1, j+2, k) \\ &+ \frac{1}{(z_j - z_{j+1})(z_j - z_{j+2})(z_j - z_{j+3})} I_1(j+1, j+2, j+1, j+2, j+3, k) \\ &+ \ln_{-\pi} \frac{z_{k+1} - z_k}{z_{k-1} - z_k}. \end{aligned} \tag{B.27}$$

For $k = j = i - 3$

$$\begin{aligned} \Gamma_{k,j} &= \frac{1}{(z_j - z_{j-3})(z_j - z_{j-2})(z_j - z_{j-1})} I_1(j-2, j-1, j-3, j-2, j-1, k) \\ &+ \frac{1}{(z_j - z_{j-2})(z_j - z_{j-1})(z_j - z_{j+1})} I_2(j-1, j, j-2, j-1, j+1, k) \\ &+ \frac{1}{(z_j - z_{j-1})(z_j - z_{j+1})(z_j - z_{j+2})} I_2(j, j+1, j-1, j+1, j+2, k) \\ &+ \frac{1}{(z_j - z_{j+1})(z_j - z_{j+2})(z_j - z_{j+3})} I_1(j+1, j+3, j+1, j+2, j+3, k). \\ &+ \ln_{-\pi} \frac{z_{k+1} - z_k}{z_{k-1} - z_k}. \end{aligned} \tag{B.28}$$

For $k = j = i + 3$

$$\begin{aligned}
\Gamma_{k,j} &= \frac{1}{(z_j - z_{j-3})(z_j - z_{j-2})(z_j - z_{j-1})} I_1(j-3, j-1, j-3, j-2, j-1, k) \\
&+ \frac{1}{(z_j - z_{j-2})(z_j - z_{j-1})(z_j - z_{j+1})} I_2(j-1, j, j-2, j-1, j+1, k) \\
&+ \frac{1}{(z_j - z_{j-1})(z_j - z_{j+1})(z_j - z_{j+2})} I_2(j, j+1, j-1, j+1, j+2, k) \\
&+ \frac{1}{(z_j - z_{j+1})(z_j - z_{j+2})(z_j - z_{j+3})} I_1(j+1, j+2, j+1, j+2, j+3, k). \\
&+ \ln_{-\pi} \frac{z_{k+1} - z_k}{z_{k-1} - z_k}. \qquad \text{(B.29)}
\end{aligned}$$

For $k = j = i - 2$

$$\begin{aligned}
\Gamma_{k,j} &= \frac{1}{(z_j - z_{j-3})(z_j - z_{j-2})(z_j - z_{j-1})} I_1(j-2, j-1, j-3, j-2, j-1, k) \\
&+ \frac{1}{(z_j - z_{j-2})(z_j - z_{j-1})(z_j - z_{j+1})} I_2(j-1, j, j-2, j-1, j+1, k) \\
&+ \frac{1}{(z_j - z_{j-1})(z_j - z_{j+1})(z_j - z_{j+2})} I_2(j, j+2, j-1, j+1, j+2, k). \\
&+ \ln_{-\pi} \frac{z_{k+2} - z_k}{z_{k-1} - z_k}. \qquad \text{(B.30)}
\end{aligned}$$

For $k = j = i + 2$

$$\begin{aligned}
\Gamma_{k,j} &= \frac{1}{(z_j - z_{j-2})(z_j - z_{j-1})(z_j - z_{j+1})} I_2(j-2, j, j-2, j-1, j+1, k) \\
&+ \frac{1}{(z_j - z_{j-1})(z_j - z_{j+1})(z_j - z_{j+2})} I_2(j, j+1, j-1, j+1, j+2, k) \\
&+ \frac{1}{(z_j - z_{j+1})(z_j - z_{j+2})(z_j - z_{j+3})} I_1(j+1, j+2, j+1, j+2, j+3, k). \\
&+ \ln_{-\pi} \frac{z_{k+1} - z_k}{z_{k-2} - z_k}. \qquad \text{(B.31)}
\end{aligned}$$

For $k = j = i - 1$

$$\begin{aligned}
\Gamma_{k,j} &= \frac{1}{(z_j - z_{j-3})(z_j - z_{j-2})(z_j - z_{j-1})} I_1(j-2, j-1, j-3, j-2, j-1, k) \\
&+ \frac{1}{(z_j - z_{j-2})(z_j - z_{j-1})(z_j - z_{j+1})} I_2(j-1, j+1, j-2, j-1, j+1, k). \\
&+ \ln_{-\pi} \frac{z_{k+1} - z_k}{z_{k-1} - z_k}. \qquad \text{(B.32)}
\end{aligned}$$

For $k = j = i + 1$

$$\begin{aligned}\Gamma_{k,j} &= \frac{1}{(z_j - z_{j-1})(z_j - z_{j+1})(z_j - z_{j+2})} I_2(j-1, j+1, j-1, j+1, j+2, k) \\ &+ \frac{1}{(z_j - z_{j+1})(z_j - z_{j+2})(z_j - z_{j+3})} I_1(j+1, j+2, j+1, j+2, j+3, k). \\ &+ \ln_{-\pi} \frac{z_{k+1} - z_k}{z_{k-1} - z_k}. \end{aligned} \tag{B.33}$$

For $k = j = i$

$$\begin{aligned}\Gamma_{k,j} &= \frac{1}{(z_j - z_{j-3})(z_j - z_{j-2})(z_j - z_{j-1})} I_2(j-2, j, j-3, j-2, j-1, k) \\ &+ \frac{1}{(z_j - z_{j+1})(z_j - z_{j+2})(z_j - z_{j+3})} I_2(j, j+2, j+1, j+2, j+3, k). \\ &+ \ln_{-\pi} \frac{z_{k+2} - z_k}{z_{k-2} - z_k}. \end{aligned} \tag{B.34}$$

In summary, equations (B.7) to (B.14) and (B.27) to (B.34) give the influence functions $\Gamma_{k,j}$ for the equation

$$\sum_{j=1}^{N} \Gamma_{k,j} \beta_j = 0 \quad \text{for } k = 1, \ldots, N. \tag{B.35}$$

Finally, a consequence of this method for finding the influence functions $\Gamma_{k,j}$ is that there must be at least 6 nodes between corners (not counting the corner nodes themselves). Otherwise some nodes between these two corners would "feel" both corners and the calculation of these influence functions would be even more complicated than it already is.

Appendix C

Construction of the Matrix Equation $A\boldsymbol{x} = \boldsymbol{b}$

Consider the discretised numerical wavetank in figure 3.1, and consider the construction of the matrix equation $A\boldsymbol{x} = \boldsymbol{b}$ for the unknown part of β at each z_k. This matrix equation is constructed from equation (3.12).

The discretised version of equation (3.5) that is equivalent to equation (3.12) is

$$\mathrm{Re}\Big\{\sum_{j=1}^{N}\Gamma_{k,j}\beta_j\Big\} = 0, \tag{C.1}$$

for z_k on C_ϕ. Similarly, the equivalent discretised version of equation (3.6) is

$$\mathrm{Re}\Big\{i\sum_{j=1}^{N}\Gamma_{k,j}\beta_j\Big\} = 0 \quad \Leftrightarrow \quad \mathrm{Im}\Big\{\sum_{j=1}^{N}\Gamma_{k,j}\beta_j\Big\} = 0, \tag{C.2}$$

for z_k on C_ψ.

Since the method of Lin *et al.* [37] is used to treat the corners at z_1 and z_{N_1} both ϕ and ψ are prescribed here and the total number of unknowns is $N-2$. Hence, A is an $(N-2)\times(N-2)$ matrix and $\boldsymbol{x}$ & $\boldsymbol{b}$ are column vectors with $N-2$ elements. The $N-2$ unknowns are

$$x_1 = \psi_2, \ldots, x_{N_1-2} = \psi_{N_1-1}, x_{N_1-1} = \phi_{N_1+1}, \ldots, x_{N-2} = \phi_N. \tag{C.3}$$

Also, because ψ is only unique up to a constant it is possible to set $\psi \equiv 0$ along the stationary boundary which includes the bottom, the beach and the model breakwater. Therefore

$$\psi_1 = \psi_{N_2} = \psi_{N_2+1} = \cdots = \psi_N = 0. \tag{C.4}$$

Using the above information the matrix equation is constructed as follows.

For z_k on C_ϕ, *i.e.* $2 \le k \le N_1 - 1$

$$\mathrm{Re}\Big\{\sum_{j=1}^{N} \Gamma_{k,j}\beta_j\Big\} = 0,$$

$$\Leftrightarrow\ \mathrm{Re}\Big\{\Gamma_{k,1}\phi_1 + \sum_{j=2}^{N_1-1} \Gamma_{k,j}(\phi_j + ix_{j-1}) + \Gamma_{k,N_1}(\phi_{N_1} + i\psi_{N_1}) + \sum_{j=N_1+1}^{N_2-1} \Gamma_{k,j}(x_{j-2} + i\psi_j) + \sum_{j=N_2}^{N} \Gamma_{k,j}x_{j-2}\Big\} = 0,$$

$$\Leftrightarrow\ \sum_{j=1}^{N_1} \mathrm{Re}(\Gamma_{k,j})\phi_j - \sum_{j=2}^{N_1-1} \mathrm{Im}(\Gamma_{k,j})x_{j-1} - \sum_{j=N_1}^{N_2-1} \mathrm{Im}(\Gamma_{k,j})\psi_j + \sum_{j=N_1+1}^{N} \mathrm{Re}(\Gamma_{k,j})x_{j-2} = 0,$$

$$\Leftrightarrow\ -\sum_{j=2}^{N_1-1} \mathrm{Im}(\Gamma_{k,j})x_{j-1} + \sum_{j=N_1+1}^{N} \mathrm{Re}(\Gamma_{k,j})x_{j-2} = -\sum_{j=1}^{N_1} \mathrm{Re}(\Gamma_{k,j})\phi_j + \sum_{j=N_1}^{N_2-1} \mathrm{Im}(\Gamma_{k,j})\psi_j. \tag{C.5}$$

Hence, if $A_{k,j}$ is the element of A in row k and column j then

$$A_{k,j} = -\mathrm{Im}(\Gamma_{k+1,j+1}) \quad \text{for } 1 \le k \le N_1 - 2 \ \&\ 1 \le j \le N_1 - 2, \tag{C.6}$$

$$A_{k,j} = \mathrm{Re}(\Gamma_{k+1,j+2}) \quad \text{for } 1 \le k \le N_1 - 2 \ \&\ N_1 - 1 \le j \le N - 2, \tag{C.7}$$

and if b_k is the kth element of $\boldsymbol{b}$ then

$$b_k = -\sum_{j=1}^{N_1} \mathrm{Re}(\Gamma_{k+1,j})\phi_j + \sum_{j=N_1}^{N_2-1} \mathrm{Im}(\Gamma_{k+1,j})\psi_j \quad \text{for } 1 \le k \le N_1 - 2. \tag{C.8}$$

For z_k on C_ψ, *i.e.* $N_1 + 1 \le k \le N$

$$\mathrm{Im}\Big\{\sum_{j=1}^{N} \Gamma_{k,j}\beta_j\Big\} = 0,$$

$$\Leftrightarrow \mathrm{Im}\Big\{\Gamma_{k,1}\phi_1 + \sum_{j=2}^{N_1-1} \Gamma_{k,j}(\phi_j + ix_{j-1}) + \Gamma_{k,N_1}(\phi_{N_1} + i\psi_{N_1}) + \sum_{j=N_1+1}^{N_2-1} \Gamma_{k,j}(x_{j-2} + i\psi_j) + \sum_{j=N_2}^{N} \Gamma_{k,j}x_{j-2}\Big\} = 0,$$

$$\Leftrightarrow \sum_{j=1}^{N_1} \mathrm{Im}(\Gamma_{k,j})\phi_j + \sum_{j=2}^{N_1-1} \mathrm{Re}(\Gamma_{k,j})x_{j-1} + \sum_{j=N_1}^{N_2-1} \mathrm{Re}(\Gamma_{k,j})\psi_j + \sum_{j=N_1+1}^{N} \mathrm{Im}(\Gamma_{k,j})x_{j-2} = 0,$$

$$\Leftrightarrow \sum_{j=2}^{N_1-1} \mathrm{Re}(\Gamma_{k,j})x_{j-1} + \sum_{j=N_1+1}^{N} \mathrm{Im}(\Gamma_{k,j})x_{j-2} = -\sum_{j=1}^{N_1} \mathrm{Im}(\Gamma_{k,j})\phi_j - \sum_{j=N_1}^{N_2-1} \mathrm{Re}(\Gamma_{k,j})\psi_j. \tag{C.9}$$

Hence, the remaining elements of A are

$$A_{k,j} = \mathrm{Re}(\Gamma_{k+2,j+1}) \quad \text{for } N_1 - 1 \le k \le N - 2 \;\&\; 1 \le j \le N_1 - 2, \tag{C.10}$$

$$A_{k,j} = \mathrm{Im}(\Gamma_{k+2,j+2}) \quad \text{for } N_1 - 1 \le k \le N - 2 \;\&\; N_1 - 1 \le j \le N - 2, \tag{C.11}$$

and the remaining elements of $\boldsymbol{b}$ are

$$b_k = -\sum_{j=1}^{N_1} \mathrm{Im}(\Gamma_{k+2,j})\phi_j - \sum_{j=N_1}^{N_2-1} \mathrm{Re}(\Gamma_{k+2,j})\psi_j \quad \text{for } N_1 - 1 \le k \le N - 2. \tag{C.12}$$

Appendix D

The Five-Point Numerical Differentiation Scheme

Consider numerically differentiating $\beta(z)$ on the free-surface (or on any side between corners). In this study this is done by using a five-point numerical differentiation scheme.

Let node z_i be the node at which the derivative is required and let β_i' be the approximation to $\frac{d\beta}{dz}(z_i)$. β_i is the approximation to $\beta(z_i)$ that was found by solving the matrix equation (3.13).

There are five possible forms of this five-point scheme depending on where node z_i is in relation to the end points (corners) of the side of interest. Figure D.1 shows these five different cases. Consider each case in turn.

Case 1

In this case z_i is not a corner and it is not immediately adjacent to a corner. Thus the the five-point scheme used is

$$\beta_i' = c_1\beta_{i-2} + c_2\beta_{i-1} + c_3\beta_i + c_4\beta_{i+1} + c_5\beta_{i+2}, \tag{D.1}$$

where the coefficients $c_1, \ldots, c_5$ are dependent only on $z_{i-2}, \ldots, z_{i+2}$. These coefficients are found as follows.

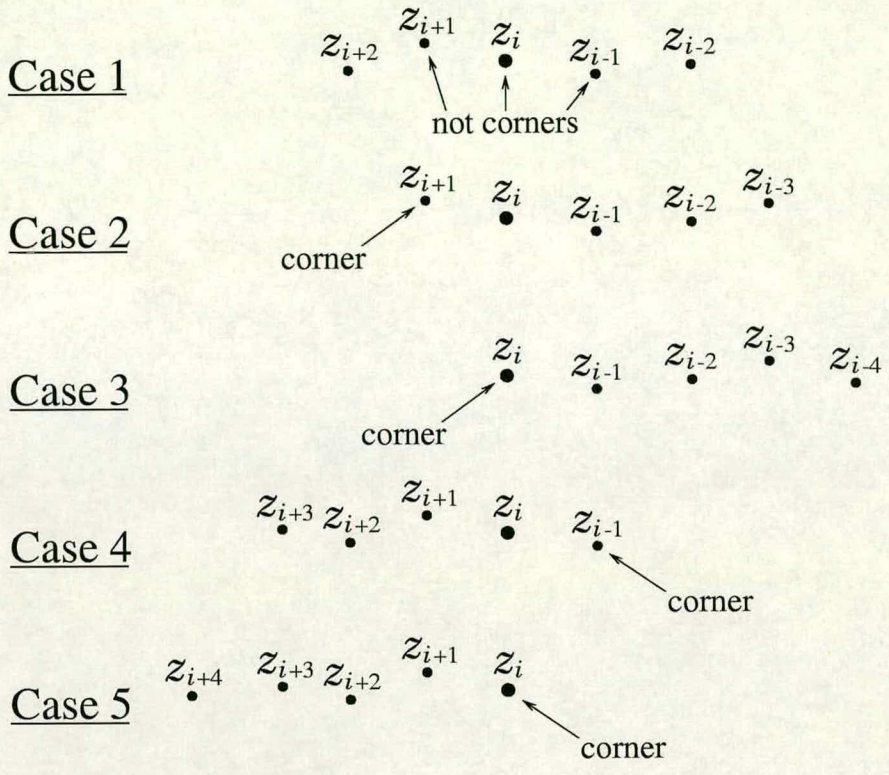

Figure D.1: The five different cases for the five-point numerical differentiation scheme.

Firstly, $\beta_{i-2}, \ldots, \beta_{i+2}$ are Taylor expanded about z_i to give

$$\beta_{i-2} = \beta_i + \Delta_1\beta_i' + \frac{(\Delta_1)^2}{2}\beta_i'' + \frac{(\Delta_1)^3}{6}\beta_i''' + \frac{(\Delta_1)^4}{24}\beta_i^{IV} + \cdots, \tag{D.2}$$

$$\beta_{i-1} = \beta_i + \Delta_2\beta_i' + \frac{(\Delta_2)^2}{2}\beta_i'' + \frac{(\Delta_2)^3}{6}\beta_i''' + \frac{(\Delta_2)^4}{24}\beta_i^{IV} + \cdots, \tag{D.3}$$

$$\beta_i \quad = \beta_i, \tag{D.4}$$

$$\beta_{i+1} = \beta_i + \Delta_3\beta_i' + \frac{(\Delta_3)^2}{2}\beta_i'' + \frac{(\Delta_3)^3}{6}\beta_i''' + \frac{(\Delta_3)^4}{24}\beta_i^{IV} + \cdots, \tag{D.5}$$

$$\beta_{i+2} = \beta_i + \Delta_4\beta_i' + \frac{(\Delta_4)^2}{2}\beta_i'' + \frac{(\Delta_4)^3}{6}\beta_i''' + \frac{(\Delta_4)^4}{24}\beta_i^{IV} + \cdots, \tag{D.6}$$

where

$$\Delta_1 = z_{i-2} - z_i, \quad \Delta_2 = z_{i-1} - z_i, \quad \Delta_3 = z_{i+1} - z_i \quad \& \quad \Delta_4 = z_{i+2} - z_i. \tag{D.7}$$

Then equations (D.2) to (D.6) are substituted into equation (D.1) and the

coefficients of $\beta_i, \ldots, \beta_i^{IV}$ are equated to yield the following matrix equation

$$\begin{bmatrix} 1 & 1 & 1 & 1 & 1 \\ \Delta_1 & \Delta_2 & 0 & \Delta_3 & \Delta_4 \\ (\Delta_1)^2 & (\Delta_2)^2 & 0 & (\Delta_3)^2 & (\Delta_4)^2 \\ (\Delta_1)^3 & (\Delta_2)^3 & 0 & (\Delta_3)^3 & (\Delta_4)^3 \\ (\Delta_1)^4 & (\Delta_2)^4 & 0 & (\Delta_3)^4 & (\Delta_4)^4 \end{bmatrix} \begin{bmatrix} c_1 \\ c_2 \\ c_3 \\ c_4 \\ c_5 \end{bmatrix} = \begin{bmatrix} 0 \\ 1 \\ 0 \\ 0 \\ 0 \end{bmatrix}. \tag{D.8}$$

The solution of this matrix equation is

$$c_1 = \frac{-\Delta_2\Delta_3\Delta_4}{\Delta_1(\Delta_1-\Delta_2)(\Delta_1-\Delta_3)(\Delta_1-\Delta_4)}, \tag{D.9}$$

$$c_2 = \frac{-\Delta_1\Delta_3\Delta_4}{\Delta_2(\Delta_2-\Delta_1)(\Delta_2-\Delta_3)(\Delta_2-\Delta_4)}, \tag{D.10}$$

$$c_3 = -\left(\frac{1}{\Delta_1}+\frac{1}{\Delta_2}+\frac{1}{\Delta_1}+\frac{1}{\Delta_4}\right), \tag{D.11}$$

$$c_4 = \frac{-\Delta_1\Delta_2\Delta_4}{\Delta_3(\Delta_3-\Delta_1)(\Delta_3-\Delta_2)(\Delta_3-\Delta_4)}, \tag{D.12}$$

$$c_5 = \frac{-\Delta_1\Delta_2\Delta_3}{\Delta_4(\Delta_4-\Delta_1)(\Delta_4-\Delta_2)(\Delta_4-\Delta_3)}. \tag{D.13}$$

Case 2

In this case z_{i+1} is a corner and thus the five-point scheme used is

$$\beta_i' = c_1\beta_{i-3} + c_2\beta_{i-2} + c_3\beta_{i-1} + c_4\beta_i + c_5\beta_{i+1}, \tag{D.14}$$

where the coefficients $c_1, \ldots, c_5$ are dependent only on $z_{i-3}, \ldots, z_{i+1}$. These coefficients are found as follows.

Firstly, $\beta_{i-3}, \ldots, \beta_{i+1}$ are Taylor expanded about z_i to give

$$\beta_{i-3} = \beta_i + \Delta_1\beta_i' + \frac{(\Delta_1)^2}{2}\beta_i'' + \frac{(\Delta_1)^3}{6}\beta_i''' + \frac{(\Delta_1)^4}{24}\beta_i^{IV} + \cdots, \tag{D.15}$$

$$\beta_{i-2} = \beta_i + \Delta_2\beta_i' + \frac{(\Delta_2)^2}{2}\beta_i'' + \frac{(\Delta_2)^3}{6}\beta_i''' + \frac{(\Delta_2)^4}{24}\beta_i^{IV} + \cdots, \tag{D.16}$$

$$\beta_{i-1} = \beta_i + \Delta_3\beta_i' + \frac{(\Delta_3)^2}{2}\beta_i'' + \frac{(\Delta_3)^3}{6}\beta_i''' + \frac{(\Delta_3)^4}{24}\beta_i^{IV} + \cdots, \tag{D.17}$$

$$\beta_i = \beta_i, \tag{D.18}$$

$$\beta_{i+1} = \beta_i + \Delta_4\beta_i' + \frac{(\Delta_4)^2}{2}\beta_i'' + \frac{(\Delta_4)^3}{6}\beta_i''' + \frac{(\Delta_4)^4}{24}\beta_i^{IV} + \cdots, \tag{D.19}$$

where

$$\Delta_1 = z_{i-3} - z_i, \quad \Delta_2 = z_{i-2} - z_i, \quad \Delta_3 = z_{i-1} - z_i \quad \& \quad \Delta_4 = z_{i+1} - z_i. \tag{D.20}$$

Then equations (D.15) to (D.19) are substituted into equation (D.14) and the coefficients of $\beta_i, \ldots, \beta_i^{IV}$ are equated to yield the following matrix equation

$$\begin{bmatrix} 1 & 1 & 1 & 1 & 1 \\ \Delta_1 & \Delta_2 & \Delta_3 & 0 & \Delta_4 \\ (\Delta_1)^2 & (\Delta_2)^2 & (\Delta_3)^2 & 0 & (\Delta_4)^2 \\ (\Delta_1)^3 & (\Delta_2)^3 & (\Delta_3)^3 & 0 & (\Delta_4)^3 \\ (\Delta_1)^4 & (\Delta_2)^4 & (\Delta_3)^4 & 0 & (\Delta_4)^4 \end{bmatrix} \begin{bmatrix} c_1 \\ c_2 \\ c_3 \\ c_4 \\ c_5 \end{bmatrix} = \begin{bmatrix} 0 \\ 1 \\ 0 \\ 0 \\ 0 \end{bmatrix} \tag{D.21}$$

$$\Leftrightarrow \begin{bmatrix} 1 & 1 & 1 & 1 & 1 \\ \Delta_1 & \Delta_2 & 0 & \Delta_3 & \Delta_4 \\ (\Delta_1)^2 & (\Delta_2)^2 & 0 & (\Delta_3)^2 & (\Delta_4)^2 \\ (\Delta_1)^3 & (\Delta_2)^3 & 0 & (\Delta_3)^3 & (\Delta_4)^3 \\ (\Delta_1)^4 & (\Delta_2)^4 & 0 & (\Delta_3)^4 & (\Delta_4)^4 \end{bmatrix} \begin{bmatrix} c_1 \\ c_2 \\ c_4 \\ c_3 \\ c_5 \end{bmatrix} = \begin{bmatrix} 0 \\ 1 \\ 0 \\ 0 \\ 0 \end{bmatrix}. \tag{D.22}$$

The matrix equation (D.22) is basically the same as equation (D.8). Therefore, the solution of (D.21) can simply be obtained from equations (D.9) to (D.13), giving

$$c_1 = \frac{-\Delta_2\Delta_3\Delta_4}{\Delta_1(\Delta_1 - \Delta_2)(\Delta_1 - \Delta_3)(\Delta_1 - \Delta_4)}, \tag{D.23}$$

$$c_2 = \frac{-\Delta_1\Delta_3\Delta_4}{\Delta_2(\Delta_2 - \Delta_1)(\Delta_2 - \Delta_3)(\Delta_2 - \Delta_4)}, \tag{D.24}$$

$$c_3 = \frac{-\Delta_1\Delta_2\Delta_4}{\Delta_3(\Delta_3 - \Delta_1)(\Delta_3 - \Delta_2)(\Delta_3 - \Delta_4)}, \tag{D.25}$$

$$c_4 = -\left(\frac{1}{\Delta_1} + \frac{1}{\Delta_2} + \frac{1}{\Delta_1} + \frac{1}{\Delta_4}\right), \tag{D.26}$$

$$c_5 = \frac{-\Delta_1\Delta_2\Delta_3}{\Delta_4(\Delta_4 - \Delta_1)(\Delta_4 - \Delta_2)(\Delta_4 - \Delta_3)}. \tag{D.27}$$

The five-point schemes for cases 3,4 & 5 can be obtained in a similar manner.

Appendix E

Proof of the Acceleration Equation

To prove that

$$\frac{Dw}{Dt} = \frac{\partial w}{\partial t} + \overline{w}\frac{dw}{dz}. \tag{E.1}$$

Consider first the LHS. Then

$$\frac{Dw}{Dt} = \frac{D}{Dt}(u - iv) = \frac{Du}{Dt} - i\frac{Dv}{Dt} = a_x - ia_y,$$

where a_x & a_y are respectively the horizontal & vertical components of acceleration (in this case the subscripts x & y do not mean partial differentiation w.r.t. x & y respectively). Now

$$\begin{aligned} a_x &= \frac{Du}{Dt} \\ &= \frac{\partial u}{\partial t} + \boldsymbol{u}.\nabla u \\ &= \frac{\partial u}{\partial t} + u\frac{\partial u}{\partial x} + v\frac{\partial u}{\partial y}, \end{aligned}$$

where $\boldsymbol{u} = (u, v)$. However, since the flow is irrotational $\frac{\partial u}{\partial y} = \frac{\partial v}{\partial x}$ and the above equation becomes

$$a_x = \frac{\partial u}{\partial t} + u\frac{\partial u}{\partial x} + v\frac{\partial v}{\partial x}. \tag{E.2}$$

Similarly

$$\begin{aligned} a_y &= \frac{Dv}{Dt} \\ &= \frac{\partial v}{\partial t} + \boldsymbol{u}.\nabla v \\ &= \frac{\partial v}{\partial t} + u\frac{\partial v}{\partial x} + v\frac{\partial v}{\partial y}, \end{aligned}$$

but since the flow is incompressible $\frac{\partial v}{\partial y} = -\frac{\partial u}{\partial x}$ and the above equation becomes

$$a_y = \frac{\partial v}{\partial t} + u\frac{\partial v}{\partial x} - v\frac{\partial u}{\partial x}. \tag{E.3}$$

Taking equations (E.2) & (E.3) together gives

$$\text{LHS} = \frac{\partial u}{\partial t} + u\frac{\partial u}{\partial x} + v\frac{\partial v}{\partial x} + i\left(v\frac{\partial u}{\partial x} - u\frac{\partial v}{\partial x} - \frac{\partial v}{\partial t}\right). \tag{E.4}$$

Now consider the RHS

$$\frac{dw}{dz} = \frac{\partial u}{\partial x} - i\frac{\partial v}{\partial x},$$

$$\begin{aligned} \therefore \quad \text{RHS} &= \frac{\partial u}{\partial t} - i\frac{\partial v}{\partial t} + (u+iv)\left(\frac{\partial u}{\partial x} - i\frac{\partial v}{\partial x}\right) \\ &= \frac{\partial u}{\partial t} - i\frac{\partial v}{\partial t} + u\frac{\partial u}{\partial x} + v\frac{\partial v}{\partial x} + i\left(v\frac{\partial u}{\partial x} - u\frac{\partial v}{\partial x}\right) \\ &= \frac{\partial u}{\partial t} + u\frac{\partial u}{\partial x} + v\frac{\partial v}{\partial x} + i\left(v\frac{\partial u}{\partial x} - u\frac{\partial v}{\partial x} - \frac{\partial v}{\partial t}\right). \end{aligned} \tag{E.5}$$

Therefore

$$\text{LHS} = \text{RHS}.$$

Hence Proved

Appendix F

Calculating the Cubic Smoothing Splines

This appendix is concerned with calculating the cubic smoothing spline $S(\tau)$ which minimises the functional (3.36). Initially the notation and the format will be roughly similar to that of de Boor [12].

To restate what was said on page 71, $S(\tau)$ is a cubic spline with simple knots at $\tau_2, \ldots, \tau_{N_1-1}$ and satisfying the "natural" end conditions

$$S''(\tau_1) = S''(\tau_{N_1}) = 0.$$

Therefore, $S(\tau)$ can be completely described on $[\tau_i, \tau_{i+1}]$ once S and S'' at τ_i and τ_{i+1} are known (see Press *et al.* [43]). Set

$$a_i := S(\tau_i) \quad \& \quad c_i := S''(\tau_i)/2 \quad \text{for} \quad i = 1, \ldots, N_1. \tag{F.1}$$

Then the "natural" boundary conditions and the requirement that $S(\tau)$ has a continuous first derivative combine to give the linear system

$$\begin{aligned} c_1 &= 0, \\ c_{i-1}\Delta\tau_{i-1} + c_i 2(\Delta\tau_{i-1} + \Delta\tau_i) + c_{i+1}\Delta\tau_i &= 3\left(\frac{\Delta a_i}{\Delta\tau_i} - \frac{\Delta a_{i-1}}{\Delta\tau_{i-1}}\right), \\ &\qquad \text{for} \quad i = 2, \ldots, N_1 - 1, \\ c_{N_1} &= 0, \end{aligned} \tag{F.2}$$

for the c_i's in terms of the a_i's. In the above equation $\Delta\tau_i = \tau_{i+1} - \tau_i$ and $\Delta a_i = a_{i+1} - a_i$. For the moment the fact that $\Delta\tau_i = 1$ for $i = 1, \ldots, N_1 - 1$ (see equation (3.35)) will not be used. This is in order to show the generality of some of the following results.

Now let $\boldsymbol{c} := (c_i)_2^{N_1-1}$ and $\boldsymbol{a} := (a_i)_1^{N_1}$, and notice that $\boldsymbol{c}$ is a vector of length $N_1 - 2$, while $\boldsymbol{a}$ is a vector of length N_1. Then equation (F.2) can be written in matrix form as

$$R\boldsymbol{c} = 3Q^T\boldsymbol{a}, \tag{F.3}$$

where R is the symmetric, tridiagonal matrix of order $N_1 - 2$ having the general row

$$\Delta\tau_{i-1}, \qquad 2(\Delta\tau_{i-1} + \Delta\tau_i), \qquad \Delta\tau_i$$

and Q^T is the tridiagonal matrix of order $(N_1 - 2) \times N_1$ with general row

$$\frac{1}{\Delta\tau_{i-1}}, \qquad -\frac{1}{\Delta\tau_{i-1}} - \frac{1}{\Delta\tau_i}, \qquad \frac{1}{\Delta\tau_i}.$$

Next, the RHS of equation (3.36) is expressed in terms of $\boldsymbol{a}$ and $\boldsymbol{c}$. For any straight line l,

$$\int_0^h \big(l(x)\big)^2 dx = \frac{h}{3}\left(\big(l(0)\big)^2 + l(0)l(h) + \big(l(h)\big)^2\right).$$

Therefore, for S a cubic spline, the RHS of equation (3.36) has the value

$$\lambda \sum_{i=1}^{N_1} (f_i - a_i)^2 + \frac{4}{3}(1-\lambda) \sum_{i=1}^{N_1-1} \Delta\tau_i (c_i^2 + c_i c_{i+1} + c_{i+1}^2). \tag{F.4}$$

In matrix form, this reads

$$\lambda(\boldsymbol{f} - \boldsymbol{a})^T(\boldsymbol{f} - \boldsymbol{a}) + \frac{2}{3}(1-\lambda)\boldsymbol{c}^T R\boldsymbol{c}, \tag{F.5}$$

where $\boldsymbol{f} := (f_i)_1^{N_1}$. By using equation (F.3), $\boldsymbol{c} = 3R^{-1}Q^T\boldsymbol{a}$, (F.5) can be written entirely in terms of $\boldsymbol{a}$ as

$$\begin{aligned}&\lambda(\boldsymbol{f}-\boldsymbol{a})^T(\boldsymbol{f}-\boldsymbol{a}) + 6(1-\lambda)(R^{-1}Q^T\boldsymbol{a})^T R(R^{-1}Q^T\boldsymbol{a})\\ &\quad = \lambda(\boldsymbol{f}-\boldsymbol{a})^T(\boldsymbol{f}-\boldsymbol{a}) + 6(1-\lambda)\boldsymbol{a}^T Q R^{-1}Q^T\boldsymbol{a}, \qquad \text{(F.6)}\end{aligned}$$

where the facts that $(R^{-1})^T = (R^T)^{-1}$ and R is symmetric have been used.

Expression (F.6) can be thought of as a second-degree polynomial function $P(\boldsymbol{a})$, where $P : \mathbb{R}^{N_1} \to \mathbb{R}$. In order to show that this function has a minimum it is necessary to show that its Hessian is positive definite. The Hessian of (F.6) is

$$2\big(\lambda I + 6(1-\lambda)QR^{-1}Q^T\big). \qquad \text{(F.7)}$$

Now, the matrix I is symmetric and positive definite, and the the matrix $QR^{-1}Q^T$ is symmetric and positive semidefinite. Therefore, for $\lambda \in (0,1)$, (F.7) is the sum of a positive multiple of a positive definite matrix with a positive multiple of a positive semidefinite matrix, and so (F.7) is positive definite. Notice that de Boor claims that $(R^{-1}Q^T)^T R(R^{-1}Q^T) = QR^{-1}Q^T$ is positive definite, which is incorrect.

To show that $QR^{-1}Q^T$ is positive semidefinite takes several stages.

Firstly, it is necessary to show that R is positive definite. From the two equations (F.4) & (F.5) it can be seen that

$$\boldsymbol{c}^T R\boldsymbol{c} = 2\sum_{i=1}^{N_1-1} \Delta\tau_i(c_i^2 + c_i c_{i+1} + c_{i+1}^2)$$

but

$$c_i^2 + c_i c_{i+1} + c_{i+1}^2 = \left(c_i + \frac{c_{i+1}}{2}\right)^2 + \frac{3c_{i+1}^2}{4} \geq 0,$$

with equality iff $c_i = c_{i+1} = 0$. Hence, since $\Delta\tau_i > 0 \ \ \forall i$, the following is true

$$\boldsymbol{c}^T R\boldsymbol{c} \geq 0 \quad \text{with equality iff} \quad \boldsymbol{c} = 0.$$

Therefore R is positive definite.

Next, from Lemma 7 and Theorem 10c of [33] the matrix R^{-1} is also positive definite.

Finally, to show that $QR^{-1}Q^T$ is positive semidefinite the following "Observation" from page 399 of [30] is used.

Observation F.1 *Let A be an $n \times n$ positive definite matrix. If C is an $n \times m$ matrix, then C^TAC is positive semidefinite. Furthermore,* $\text{rank}(C^TAC) = \text{rank}(C)$, *so that C^TAC is positive definite iff C has* rank m.

By replacing A by R^{-1}, C by Q^T, n by $N_1 - 2$ and m by N_1 the above observation can be applied to the present situation. Therefore, $QR^{-1}Q^T$ is at least positive semidefinite. However, it is not positive definite because, by the first "rank inequality" on page 13 of [30], $\text{rank}(Q^T) \leq \min\{N_1, N_1 - 2\} = N_1 - 2$, and so $\text{rank}(Q^T) \neq N_1$.

Hence $QR^{-1}Q^T$ is positive semidefinite

Returning to the task in hand, because (F.7) is positive definite (F.6) is minimised when $\boldsymbol{a}$ satisfies

$$-2\lambda(\boldsymbol{f} - \boldsymbol{a}) + 12(1 - \lambda)QR^{-1}Q^T\boldsymbol{a} = \boldsymbol{0}$$

or, using (F.3) and simplifying,

$$\lambda(\boldsymbol{f} - \boldsymbol{a}) = 2(1 - \lambda)Q\boldsymbol{c}. \tag{F.8}$$

In order to obtain a linear system for $\boldsymbol{c}$, both sides of (F.8) are multiplied by $3Q^T$ and then (F.3) is used again to get

$$\lambda(3Q^T\boldsymbol{f} - R\boldsymbol{c}) = 6(1 - \lambda)Q^TQ\boldsymbol{c}$$

or

$$\big(6(1-\lambda)Q^TQ + \lambda R\big)\boldsymbol{c} = 3\lambda Q^T\boldsymbol{f}.$$

Let now $\boldsymbol{u}$ be such that

$$\boldsymbol{c} = 3\lambda\boldsymbol{u}. \tag{F.9}$$

Then, in summary,

$$\big(6(1-\lambda)Q^TQ + \lambda R\big)\boldsymbol{u} = Q^T\boldsymbol{f} \tag{F.10}$$

and, by (F.8),

$$\boldsymbol{a} = \boldsymbol{f} - 6(1-\lambda)Q\boldsymbol{u}. \tag{F.11}$$

Equation (F.10) is the matrix equation which needs to be solved in order to obtain the cubic smoothing spline $S(\tau)$. Once it has been solved $\boldsymbol{c}$ & $\boldsymbol{a}$ are easily found via equations (F.9) & (F.11) respectively, with the result that $S(\tau)$ is fully determined (see the comment on page 206). That is, the derivatives of S at a knot τ_i are

$$\begin{aligned} S(\tau_i) &= a_i \\ S'(\tau_i) &= \frac{\Delta a_i}{\Delta\tau_i} - \frac{S''(\tau_i)}{2}\Delta\tau_i - \frac{S'''(\tau_i^+)}{6}(\Delta\tau_i)^2 \\ S''(\tau_i) &= 6\lambda u_i \\ S'''(\tau_i^+) &= \frac{S''(\tau_{i+1}) - S''(\tau_i)}{\Delta\tau_i} \end{aligned} \tag{F.12}$$

and the jth derivative of S at a general point τ, in terms of the above derivatives, is

$$D^jS(\tau) = \sum_{m=j}^{3} D^mS(\tau_i^+)\frac{(\tau-\tau_i)^{m-j}}{(m-j)!}, \tag{F.13}$$

where i is the integer such that

$$\tau_i \le \tau < \tau_{i+1}$$

Up until this point this appendix has followed fairly closely the work of de Boor [12]. However, from now on original material will be presented concerning the efficient solution of matrix equation (F.10) for the present situation.

For the present situation equation (3.35) holds, and so

$$\Delta\tau_i = 1 \quad \text{for} \quad i = 1, \ldots, N_1 - 1.$$

As a result equation (F.10) becomes

$$6(1-\lambda)T\boldsymbol{u} = Q^T\boldsymbol{f}, \tag{F.14}$$

where T is the following $(N_1 - 2)\times(N_1 - 2)$ matrix

$$T = \begin{bmatrix}
\frac{36-32\lambda}{6(1-\lambda)} & \frac{25\lambda-24}{6(1-\lambda)} & 1 & & & & & \\
\frac{25\lambda-24}{6(1-\lambda)} & \frac{36-32\lambda}{6(1-\lambda)} & \frac{25\lambda-24}{6(1-\lambda)} & 1 & & & & \\
1 & \frac{25\lambda-24}{6(1-\lambda)} & \frac{36-32\lambda}{6(1-\lambda)} & \frac{25\lambda-24}{6(1-\lambda)} & 1 & & & \\
 & \ddots & \ddots & \ddots & \ddots & \ddots & & \\
 & & 1 & \frac{25\lambda-24}{6(1-\lambda)} & \frac{36-32\lambda}{6(1-\lambda)} & \frac{25\lambda-24}{6(1-\lambda)} & 1 & \\
 & & & 1 & \frac{25\lambda-24}{6(1-\lambda)} & \frac{36-32\lambda}{6(1-\lambda)} & \frac{25\lambda-24}{6(1-\lambda)} & \\
 & & & & 1 & \frac{25\lambda-24}{6(1-\lambda)} & \frac{36-32\lambda}{6(1-\lambda)} &
\end{bmatrix}. \tag{F.15}$$

This matrix is a symmetric, pentadiagonal, Toeplitz (equal elements along diagonals parallel to the principal diagonal) matrix, which can therefore be factorised as described in the following algorithm (see exercise 13.19 on page 381 of [3]).

Algorithm F.2 *Given an $n \times n$ symmetric, pentadiagonal, Toeplitz matrix T, whose first row is $[\alpha, \beta, 1, 0, \ldots, 0]$, it can be factorised as $T = PAP^T$, where $P = [p_{ij}]$ is a bidiagonal and $A = [a_{ij}]$ is symmetric and tridiagonal. The elements*

of A are defined by

$$a_{i,i+1} = b_i \quad \text{for} \quad i = 1, 2, \ldots, n-1,$$

$$a_{11} = \alpha, \qquad a_{22} = (\beta - b_2)b_1,$$

$$a_{ii} = \left(\beta - b_i - \frac{1}{b_{i-2}}\right) b_{i-1} \quad \text{for} \quad i = 3, 4, \ldots, n,$$

where

$$b_1 = \beta, \qquad b_2 = \beta - \frac{\alpha}{\beta}, \qquad b_3 = \beta - \frac{\alpha}{b_2} + \frac{\beta}{b_2 b_1},$$

$$b_{i+1} = \beta - \frac{\alpha}{b_i} + \frac{\beta}{b_i b_{i-1}} - \frac{1}{b_i b_{i-1} b_{i-2}} \quad \text{for} \quad i = 3, 4, \ldots, n-1.$$

The factorisation exists provided no b_i is zero, and P has 1's along the principal diagonal and subdiagonal elements $p_{21} = 0$, $p_{i+1,i} = 1/b_{i-1}$ for $i = 2, \ldots, n-1$. Hence inversion of T reduces to the inversion of a bidiagonal and a tridiagonal matrix.

As can be seen from equation (F.15) for a given N_1 the matrix T is a submatrix of T for a larger N_1. An advantage of the above factorisation is that this also applies to the factors P & A. For a given N_1 the matrices P & A are submatrices of P & A for a larger N_1. Unfortunately, because N_1 (the number of nodes on the free-surface) can change after each regridding (see page 77) it is not possible to do this factorisation once at the start of a simulation. Instead, in a simulation the largest N_1 to date and the corresponding factors P & A are stored, if the current N_1 exceeds this largest N_1 the extra factor elements needed are calculated. This makes this smoothing algorithm very efficient in terms of computer time.

The next stage of this analysis relies on the fact that the matrix A is not only symmetric and tridiagonal but also positive definite. In order to prove this takes several stages.

Firstly, it is necessary to show that T is positive definite. From the two equations (F.10) & (F.14) it can be seen that

$$T = Q^T Q + \frac{\lambda}{6(1-\lambda)} R.$$

Now the matrix $Q^T Q$ is at least positive semidefinite, if not positive definite, because

$$\boldsymbol{x}^T Q^T Q \boldsymbol{x} = \|Q\boldsymbol{x}\|_2^2 \geq 0,$$

where $\|\cdot\|_2$ is the standard Euclidean norm. Also, as has already been shown on page 208, R is positive definite. Therefore, since T is the sum of a matrix which is at least positive semidefinite with a positive multiple ($\lambda \in (0,1)$) of a positive definite matrix, then T is positive definite.

The second step in proving that A is positive definite is to consider the factorisation of T in algorithm F.2. That is,

$$T = PAP^T,$$

where P is a lower-triangular, bidiagonal matrix with 1's along the principal diagonal, and so $\det(P) = 1$. Therefore, P is non-singular and

$$A = P^{-1}T(P^T)^{-1} = P^{-1}T(P^{-1})^T.$$

Consequently, by replacing A by T, C by $(P^{-1})^T$ and n & m by $N_1 - 2$ in observation F.1 it can be applied to the above equation to show that A is at least positive semidefinite. Moreover, observation F.1 shows that A is in fact positive definite because $(P^{-1})^T = (P^T)^{-1}$ is non-singular and so $\operatorname{rank}\big((P^{-1})^T\big) = N_1 - 2$.

Having shown that the symmetric, tridiagonal matrix A is also positive definite it is then possible to factorise it, as T was. In this case the factorisation is

$$A = LDL^T,$$

where L, like P, is a lower-triangular, bidiagonal matrix with 1's along the principal diagonal and D is a diagonal matrix.

Again, for a given N_1 these factors L & D are submatrices of the corresponding factors for a larger N_1. As a result a similar method to that used for the factors of T can be used here to make the smoothing algorithm run even faster.

The following algorithm (see Algorithm 5.3-7. on page 97 of [21]) uses this factorisation in order to solve a symmetric, tridiagonal, positive definite matrix equation. Note that the first "For k" loop in this algorithm corresponds to the calculation of the factors L & D. By the end of this loop $e_1, \ldots, e_{n-1}$ contain the subdiagonal elements of L while $d_1, \ldots, d_n$ contain the diagonal elements of D.

Algorithm F.3 *Given an $n \times n$ symmetric, tridiagonal, positive definite matrix A and $\boldsymbol{b} \in \mathbb{R}^n$, the following algorithm overwrites $\boldsymbol{b}$ with the solution to $A\boldsymbol{x} = \boldsymbol{b}$. It is assumed that the diagonal of A is stored in $(d_1, \ldots, d_n)$ and the superdiagonal in $(e_1, \ldots, e_{n-1})$.*

For $k = 2, \ldots, n$

$t := e_{k-1}$

$e_{k-1} := t/d_{k-1}$

$d_k := d_k - te_{k-1}$

For $k = 2, \ldots, n$

$b_k := b_k - e_{k-1}b_{k-1}$

For $k = 1, \ldots, n$

$b_k := b_k/d_k$

For $k = n-1, \ldots, 1$

$b_k := b_k - e_k b_{k+1}$

This algorithm requires $5n$ flops.

To sum up, the main difficulty in calculating the cubic smoothing spline $S(\tau)$ is in obtaining the vector $\boldsymbol{u}$. Once $\boldsymbol{u}$ has been found the vectors $\boldsymbol{c}$ & $\boldsymbol{a}$ are easily obtained via equations (F.9) & (F.11) respectively, and $S(\tau)$ is fully determined. In order to obtain $\boldsymbol{u}$ the following matrix equation must be solved (see equation (F.14))

$$T\boldsymbol{u} = \frac{1}{6(1-\lambda)} Q^T \boldsymbol{f}, \tag{F.16}$$

where the RHS is known from the given data and T is a symmetric, pentadiagonal, positive definite, Toeplitz matrix, which is also known. Conveniently, this matrix factorises as

$$T = PAP^T,$$

where P is a lower-triangular, bidiagonal matrix with 1's along the principal diagonal and A is a symmetric, tridiagonal, positive definite matrix. Consequently, the solution of (F.16) can be obtained by solving the following three simple matrix equations in turn.

Firstly, the equation

$$P\boldsymbol{u}_1 = \frac{1}{6(1-\lambda)} Q^T \boldsymbol{f},$$

is solved for $\boldsymbol{u}_1$ using a unit lower-triangular matrix equation solver (see Algorithm 5.3-2. on page 93 of [21]).

Then the equation

$$A\boldsymbol{u}_2 = \boldsymbol{u}_1,$$

is solved for $\boldsymbol{u}_2$ using the symmetric, tridiagonal, positive definite matrix equation solver described in Algorithm F.3.

Finally, the equation

$$P^T\boldsymbol{u} = \boldsymbol{u}_2,$$

is solved for $\boldsymbol{u}$ using a unit upper-triangular matrix equation solver (see Algorithm 5.3-3. on page 94 of [21]).

In this solution process the factors of T and A only vary in size but not in structure from one smoothing & regridding to the next. As a result these factors do not have to be completely recalculated each time the smoothing algorithm is called. This makes the present smoothing algorithm very efficient.

Appendix G

Adaptive Regridding Subject to Node Spacing Constraints

This appendix describes the regridding algorithm which was adapted from the regridding algorithm given in subsection 3.5.3 to include constraints on the node spacing. These constraints are

$$h_{\min} \leq |\tilde{z}_k - \tilde{z}_{k-1}| \leq h_{\max}, \tag{G.1}$$

for all adjacent nodes $\tilde{z}_k$ & $\tilde{z}_{k-1}$ on the regridded free-surface.

The details of this adapted algorithm are as follows.

Firstly, set $\tilde{z}_1 = z_1$ (the first point in the regridded (rezoned) mesh is where the smoothed free-surface meets the far end wall).

Next, suppose that $\tilde{s}_{k-1}$, $I(\tilde{s}_{k-1})$, $\tilde{\tau}_{k-1}$ & $\tilde{z}_{k-1}$ have been found for some $k \geq 2$. That is, step $k-1$ is complete.

Step *k*

Add I_{step} onto $I(\tilde{s}_{k-1})$ and find the candidate for $\tilde{s}_k$ such that

$$I(\tilde{s}_k) = I(\tilde{s}_{k-1}) + I_{\text{step}}, \tag{G.2}$$

or

$$\tilde{s}_k = I^{-1}\big(I(\tilde{s}_{k-1}) + I_{\text{step}}\big). \tag{G.3}$$

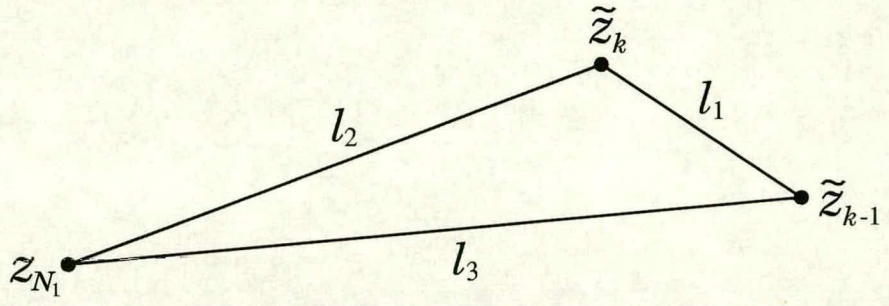

Figure G.1: The nodes $\tilde{z}_{k-1}$, $\tilde{z}_k$ & z_{N_1} and the distances between them l_1, l_2 & l_3, for case **(A)**.

From $\tilde{s}_k$ find $\tilde{r}_k$ and $\tilde{z}_k$, then calculate $l_1 \stackrel{\text{def}}{=} |\tilde{z}_k - \tilde{z}_{k-1}|$, as shown in figure G.1. If $h_{\min} \leq l_1 \leq h_{\max}$ go to **(A)** else go to **(B)**.

(A) $\tilde{z}_k$ is a possible candidate for a point in the rezoned mesh.

Calculate $l_2 \stackrel{\text{def}}{=} |z_{N_1} - \tilde{z}_k|$, also shown in figure G.1.

(A1) If $l_2 \geq 2h_{\min}$ accept $\tilde{z}_k$ and

(A1a) if $I(\tilde{s}_k) < I_{\text{step}} \times (N_{1_{\text{desired}}} - 2)$ or $l_2 > h_{\max}$ (that is, enough curvature to fit another point or $\tilde{z}_k$ cannot be the penultimate point in the rezoned mesh) repeat procedure for step $k+1$, storing l_2 in l_3.

(A1b) if $I(\tilde{s}_k) \geq I_{\text{step}} \times (N_{1_{\text{desired}}} - 2)$ and $l_2 \leq h_{\max}$ (that is, not enough curvature to fit another point and $\tilde{z}_k$ satisfies the criteria for being the penultimate point in the rezoned mesh) terminate the procedure, setting $\widetilde{N}_1 = k + 1$ and $\tilde{z}_{\widetilde{N}_1} = z_{N_1}$.

(A2) If $2h_{\min} > l_2 \geq h_{\min}$ then accept $\tilde{z}_k$ and terminate procedure, setting $\widetilde{N}_1 = k + 1$ and $\tilde{z}_{\widetilde{N}_1} = z_{N_1}$.

(A3) If $l_2 < h_{\min}$ then choose another $\tilde{z}_k$. From step $k-1$ it is known that $l_3 \geq 2h_{\min}{}^{\dagger}$ and $\left(I(\tilde{s}_{k-1}) < I_{\text{step}} \times (N_{1_{\text{desired}}} - 2) \text{ or } l_3 > h_{\max}\right)$. This is

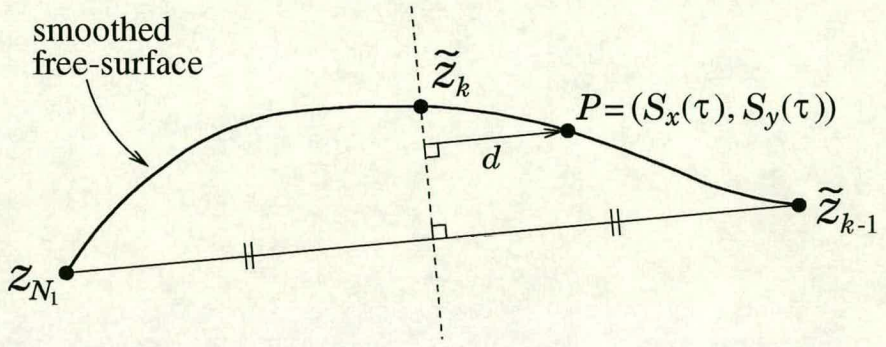

Figure G.2: Finding $\tilde{z}_k$ for case **(A3)**.

because (A1a) is the only way the algorithm can proceed. The idea is to choose $\tilde{z}_k$ such that it lies on the smoothed free-surface equidistant from $\tilde{z}_{k-1}$ and z_{N_1}. By † and the triangle inequality this distance will be $\geq h_{\min}$.

Method for Calculating $\tilde{z}_k$

Consider figure G.2. Newton-Raphson iteration is applied to the equation $d(\tau) = 0$ in order to obtain the root $\tau = \tilde{\tau}_k$ and hence find $\tilde{z}_k$.

Once $\tilde{z}_k$ has been found terminate procedure, setting $\widetilde{N}_1 = k + 1$ and $\tilde{z}_{\widetilde{N}_1} = z_{N_1}$.

(B) $\tilde{z}_k$ is not a possible candidate for a point in the rezoned mesh.

Must choose another $\tilde{z}_k$. At the moment $l_1 < h_{\min}$ or $l_1 > h_{\max}$. Consequently, the following algorithm was devised to produce another $\tilde{z}_k$ for which $h_{\min} \leq l_1 \leq h_{\max}$.

$n := 0$

$m := 0$

repeat

if $(l_1 < h_{\min})$ then

$\tilde{s}_k = \tilde{s}_{k-1} + (1 + nr)h_{\min}$

$n := n + 1$

else if $(l_1 > h_{\max})$ then

$\tilde{s}_k = \tilde{s}_{k-1} + h_{\max}/(1 + mr)$

$m := m + 1$

end if

recompute l_1

until $(h_{\min} \leq l_1 \leq h_{\max})$

(In the present study r was set at 0.1)

Once a $\tilde{z}_k$ which satisfies $h_{\min} \leq l_1 \leq h_{\max}$ has been found go to **(A)**.

Cases	$\frac{D\cdot}{Dt}$	$\frac{D^2\cdot}{Dt^2}$	
(1)	<0	<0	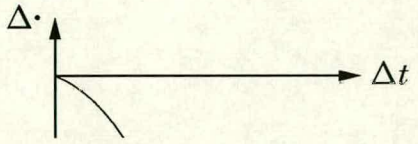
(2)	<0	≈0	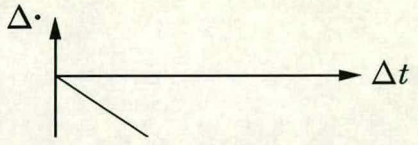
(3)	<0	>0	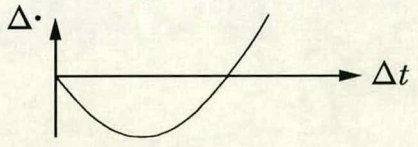
(4)	≈0	<0	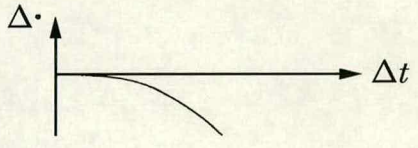
(5)	≈0	≈0	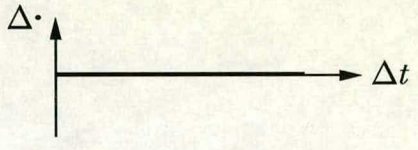
(6)	≈0	>0	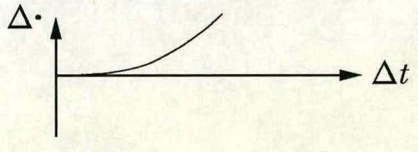
(7)	>0	<0	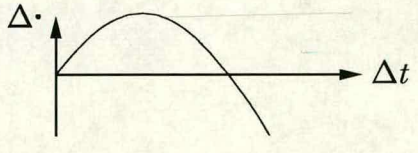
(8)	>0	≈0	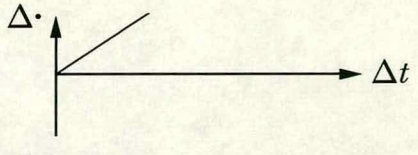
(9)	>0	>0	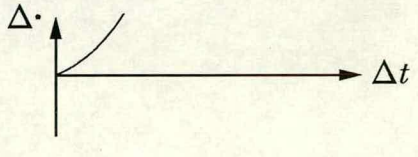

Figure H.1: The 9 different cases for finding Δt.

and consider each of the 9 cases in turn

Case (1) $v < 0$ & $a < 0$

$$-L = v\Delta t + \frac{1}{2}a(\Delta t)^2$$

$$\therefore \quad \frac{1}{2}a(\Delta t)^2 + v\Delta t + L = 0$$

$$\therefore \quad \Delta t = \frac{-v \overset{\text{note sign}}{\overset{\downarrow}{-}} \sqrt{v^2 - 2aL}}{a}. \tag{H.3}$$

The highlighted negative sign in equation (H.3) comes from careful consideration of the first graph in figure H.1, together with the sign of v and the sign of a.

Case (2) $v < 0$ & $a \approx 0$ (*i.e.* $|a| \leq \text{tol}_1$, for some small +ve tolerance tol_1 supplied by the user.)

$$\therefore \quad \Delta t = \frac{-L}{v}. \tag{H.4}$$

Case (3) $v < 0$ & $a > 0$

Can $\Delta\cdot = -L$? (Refer to the third graph in figure H.1).

$$-L = v\Delta t + \frac{1}{2}a(\Delta t)^2$$

$$\therefore \quad \frac{1}{2}a(\Delta t)^2 + v\Delta t + L = 0$$

$$\therefore \quad \Delta t = \frac{-v \pm \sqrt{v^2 - 2aL}}{a}.$$

So require $v^2 - 2aL \geq 0$ for $\Delta\cdot = -L$ for some Δt.

Strategy

If $|v^2 - 2aL| \leq \text{tol}_2$ (for some small +ve tol_2 supplied by the user) then

$$\Delta t = -\frac{v}{a}. \tag{H.5}$$

Else if $v^2 - 2aL > \text{tol}_2$ then

$$\Delta t = \frac{-v \overset{\text{note sign}}{\underset{\downarrow}{-}} \sqrt{v^2 - 2aL}}{a}. \tag{H.6}$$

Else (*i.e.* if $v^2 - 2aL < -\text{tol}_2$ (cannot find a Δt such that $\Delta\bullet = -L$))

$$L = v\Delta t + \frac{1}{2}a(\Delta t)^2$$

$$\therefore \quad \frac{1}{2}a(\Delta t)^2 + v\Delta t - L = 0$$

$$\therefore \quad \Delta t = \frac{-v \overset{\text{note sign}}{\underset{\downarrow}{+}} \sqrt{v^2 + 2aL}}{a}. \tag{H.7}$$

Case (4) $v \approx 0$ & $a < 0$ (*i.e.* $|v| \leq \text{tol}_1$)

$$-L = \frac{1}{2}a(\Delta t)^2$$

$$\therefore \quad \Delta t = \sqrt{\frac{-2L}{a}}. \tag{H.8}$$

Case (5) $v \approx 0$ & $a \approx 0$ (*i.e.* $|v| \leq \text{tol}_1$ & $|a| \leq \text{tol}_1$)

$$\Delta t = (\Delta t)_{\max}, \tag{H.9}$$

where $(\Delta t)_{\max}$ is the maximum time-step (see page 77).

Case (6) $v \approx 0$ & $a > 0$ (*i.e.* $|v| \leq \text{tol}_1$)

$$\begin{aligned} L &= \frac{1}{2}a(\Delta t)^2 \\ \therefore \quad \Delta t &= \sqrt{\frac{2L}{a}}. \end{aligned} \tag{H.10}$$

Case (7) $v > 0$ & $a < 0$

Can $\Delta\cdot = L$? (Refer to the seventh graph in figure H.1).

$$\begin{aligned} L &= v\Delta t + \frac{1}{2}a(\Delta t)^2 \\ \therefore \quad \frac{1}{2}a(\Delta t)^2 &+ v\Delta t - L = 0 \\ \therefore \quad \Delta t &= \frac{-v \pm \sqrt{v^2 + 2aL}}{a}. \end{aligned}$$

So require $v^2 + 2aL \geq 0$ for $\Delta\cdot = L$ for some Δt.

Strategy

If $|v^2 + 2aL| \leq \text{tol}_2$ then

$$\Delta t = -\frac{v}{a}. \tag{H.11}$$

Else if $v^2 + 2aL > \text{tol}_2$ then

$$\Delta t = \frac{-v \overset{\text{note sign}}{\underset{\downarrow}{+}} \sqrt{v^2 + 2aL}}{a}. \tag{H.12}$$

Else (*i.e.* if $v^2 + 2aL < -\text{tol}_2$ (cannot find a Δt such that $\Delta\bullet = L$))

$$-L = v\Delta t + \frac{1}{2}a(\Delta t)^2$$

$$\therefore \quad \frac{1}{2}a(\Delta t)^2 + v\Delta t + L = 0$$

$$\therefore \quad \Delta t = \frac{-v \overset{\text{note sign}}{\underset{\downarrow}{-}} \sqrt{v^2 - 2aL}}{a}. \tag{H.13}$$

Case (8) $v > 0$ & $a \approx 0$ (*i.e.* $|a| \leq \text{tol}_1$)

$$\therefore \quad \Delta t = \frac{L}{v}. \tag{H.14}$$

Case (9) $v > 0$ & $a > 0$

$$L = v\Delta t + \frac{1}{2}a(\Delta t)^2$$

$$\therefore \quad \frac{1}{2}a(\Delta t)^2 + v\Delta t - L = 0$$

$$\therefore \quad \Delta t = \frac{-v \overset{\text{note sign}}{\underset{\downarrow}{+}} \sqrt{v^2 + 2aL}}{a}. \tag{H.15}$$

In conclusion, once this above procedure has been applied to both coordinate directions for every free-surface node there will be a set of $2N_1$ time-steps

(where N_1 is the number of nodes on the free-surface). The time-step $(\Delta t)_{\text{dynamic}}$ can then be calculated by finding the minimum of this set.

Appendix I

Calculating a Bound on the Error in Approximating η^* by a Truncated Integral

The purpose of this appendix is to calculate a bound on the absolute value of the error in approximating η^* by a truncated version of the integral on the RHS of equation (4.5).

In order to find this bound several properties of the gamma function need to be used. These properties are (see Arfken [1])

$$\Gamma(\tfrac{1}{2}) = \sqrt{\pi}, \tag{I.1}$$

$$\Gamma(z+1) = z\Gamma(z) \tag{I.2}$$

and

$$\Gamma(z+1) = z!\,. \tag{I.3}$$

The function $z!$ in the last equation is called the *factorial function*, and for large $|z|$

$$z! \approx \sqrt{2\pi} z^{z+\frac{1}{2}} e^{-z}. \tag{I.4}$$

The above equation is "Stirling's formula".

Having stated these properties of the gamma function, now consider the main task of finding the bound. For a given value of the parameter σ and a given x_{inner}, the value of η^* is determined by the following equation (see equation (4.5))

$$\begin{aligned}\eta^* &= \frac{\sigma\Gamma\left(\frac{3}{2}\right)}{2\pi i}\int_{c-i\infty}^{c+i\infty}\frac{(2\sigma/\pi x_{\text{inner}})^p\,dp}{p(1+p)\sin\left(\frac{1}{2}\pi p\right)\Gamma\left(p+\frac{3}{2}\right)} \quad (0<c<2)\\ &= \frac{\sigma}{4\sqrt{\pi}\,i}\int_{c-i\infty}^{c+i\infty}\frac{(2\sigma/\pi x_{\text{inner}})^p\,dp}{p(1+p)\sin\left(\frac{1}{2}\pi p\right)\Gamma\left(p+\frac{3}{2}\right)} \quad (0<c<2), \qquad \text{(I.5)}\end{aligned}$$

where equations (I.2) & (I.1) have been used to obtain the second line.

Now, equation (I.5) can be simplified by letting

$$F(p) = \frac{\sigma}{4\sqrt{\pi}\,i}\frac{(2\sigma/\pi x_{\text{inner}})^p}{p(1+p)\sin\left(\frac{1}{2}\pi p\right)\Gamma\left(p+\frac{3}{2}\right)}, \qquad \text{(I.6)}$$

so that

$$\eta^* = \int_{c-i\infty}^{c+i\infty} F(p)\,dp. \qquad \text{(I.7)}$$

The above integral cannot be numerically integrated because the interval of integration is infinite. However, η^* can be accurately approximated by truncating the interval of integration and then numerically integrating. This is because

$$\eta^* \approx \int_{c-iY}^{c+iY} F(p)\,dp, \qquad \text{(I.8)}$$

for some sufficiently large $Y > 0$.

Consider the error in approximating η^* by the RHS of equation (I.8). This error is

$$\int_{c-i\infty}^{c-iY} + \int_{c+iY}^{c+i\infty} F(p)\,dp \qquad \text{(I.9)}$$

and by the triangle inequality its absolute value satisfies

$$\left|\int_{c-i\infty}^{c-iY} + \int_{c+iY}^{c+i\infty} F(p)\,dp\right| \le \left|\int_{c-i\infty}^{c-iY} F(p)\,dp\right| + \left|\int_{c+iY}^{c+i\infty} F(p)\,dp\right|. \qquad \text{(I.10)}$$

To proceed further, on the two contours of integration in (I.10) let

$$p = c + iy \;\Rightarrow\; dp = i\,dy.$$

Therefore

$$\begin{aligned}\left|\int_{c-i\infty}^{c-iY} F(p)\,dp\right| + \left|\int_{c+iY}^{c+i\infty} F(p)\,dp\right| &= \left|\int_{-\infty}^{-Y} F(c+iy)i\,dy\right| + \left|\int_{Y}^{\infty} F(c+iy)i\,dy\right| \\ &\leq \int_{-\infty}^{-Y} |F(c+iy)|\,dy + \int_{Y}^{\infty} |F(c+iy)|\,dy.\end{aligned} \tag{I.11}$$

Now consider $|F(c+iy)|$ for large $|y|$. From equation (I.6)

$$|F(p)| = \frac{\sigma}{4\sqrt{\pi}} \frac{|(2\sigma/\pi x_{\text{inner}})^p|}{|p(1+p)|\,\left|\sin\left(\frac{1}{2}\pi p\right)\right|\,\left|\Gamma\left(p+\frac{3}{2}\right)\right|}. \tag{I.12}$$

To investigate the magnitude of $F(p)$ for large $|y|$ it is necessary to consider the magnitude of each of the terms in (I.12) for large $|y|$. The term $(2\sigma/\pi x_{\text{inner}})^p$ is equal to $e^{p\ln(2\sigma/\pi x_{\text{inner}})}$, so that

$$|(2\sigma/\pi x_{\text{inner}})^p| = e^{c\ln(2\sigma/\pi x_{\text{inner}})} = (2\sigma/\pi x_{\text{inner}})^c. \tag{I.13}$$

Also, for large $|y|$

$$|p(1+p)| \approx |y|^2 \tag{I.14}$$

and

$$\left|\sin\left(\tfrac{1}{2}\pi p\right)\right| \approx \sinh\left(\tfrac{1}{2}\pi|y|\right) \approx \frac{e^{\frac{1}{2}\pi|y|}}{2}, \tag{I.15}$$

where the fact that if $z = x + iy$ then $|\sin z|^2 = \sin^2 x + \sinh^2 y$ has been used in (I.15).

Finally, from Stirling's formula (equation (I.4)), for large $|y|$

$$\begin{aligned}\Gamma\left(p+\tfrac{3}{2}\right) &\approx \sqrt{2\pi}\left(p+\tfrac{1}{2}\right)^{p+1} e^{-p-\frac{1}{2}} \\ &= \sqrt{2\pi}\, e^{(p+1)\ln(p+\frac{1}{2})-p-\frac{1}{2}} \\ &\approx \sqrt{2\pi}\, e^{(c+1+iy)(\ln|y|\pm i\frac{\pi}{2})-c-\frac{1}{2}-iy},\end{aligned} \tag{I.16}$$

where the $\pm$ is for $y \gtrless 0$ respectively. Consequently

$$\left|\Gamma\left(p+\tfrac{3}{2}\right)\right| \approx \sqrt{2\pi}\, e^{(c+1)\ln|y| - \frac{\pi}{2}|y| - c - \frac{1}{2}}$$

$$\therefore \quad \left|\Gamma\left(p+\tfrac{3}{2}\right)\right| \approx \sqrt{2\pi}\, |y|^{c+1} e^{-\frac{\pi}{2}|y| - c - \frac{1}{2}}. \tag{I.17}$$

With this last result there is now sufficient information to approximate the magnitude of $F(p)$ for large $|y|$. That is, by using (I.13), (I.14), (I.15) & (I.17) together with equation (I.12) the following approximation is obtained for large $|y|$

$$|F(c+iy)| \approx \frac{\sigma}{2\sqrt{2}\pi} \frac{(2\sigma/\pi x_{\text{inner}})^c e^{c+\frac{1}{2}}}{|y|^{c+3}}. \tag{I.18}$$

Thus

$$\int_{-\infty}^{-Y} |F(c+iy)|\, dy + \int_{Y}^{\infty} |F(c+iy)|\, dy$$

$$\approx \frac{\sigma}{\sqrt{2}\pi} (2\sigma/\pi x_{\text{inner}})^c e^{c+\frac{1}{2}} \int_{Y}^{\infty} \frac{dy}{y^{c+3}}$$

$$\boxed{= \frac{\sigma}{\sqrt{2}\pi} \frac{(2\sigma/\pi x_{\text{inner}})^c e^{c+\frac{1}{2}}}{(c+2)Y^{c+2}}}. \tag{I.19}$$

In conclusion, by examining inequality (I.10) and inequality (I.11) it can be seen that (I.19) is indeed a bound on the absolute value of the error when η^* is approximated by the truncated integral on the RHS of equation (I.8).

Bibliography

[1] G. Arfken. *Mathematical Methods for Physicits.* Academic Press, third edition, 1985.

[2] G. R. Baker, D. I. Meiron, and S. A. Orszag. Generalized vortex methods for free-surface flow problems. *J. Fluid Mech.*, 123:477–501, 1982.

[3] S. Barnett. *Matrices: Methods and Applications.* Oxford Applied Mathematics and Computing Science Series. Clarendon Press, Oxford, 1990.

[4] G. K. Batchelor. *An Introduction to Fluid Dynamics.* Cambridge University Press, 1967.

[5] E. S. Chan and W. K. Melville. Deep-water plunging wave pressures on a vertical plane wall. *Proc. R. Soc. Lond. A*, 417:95–131, 1988.

[6] A. Chopra. *The Volume Of Fluid Technique for the Numerical Simulation of Water Waves.* PhD thesis, The University of Edinburgh, 1997.

[7] A. Chopra and C. A. Greated. Development and validation of the volume of fluid technique for water wave dynamics. In *Proc. 6th Intl. Symp. Comput. Fluid Dyn.*, volume 1, pages 212–217, Lake Tahoe, Nevada, USA, September 1995.

[8] R. Cointe. Numerical simulation of a wave channel. *Engineering Analysis with Boundary Elements*, 7(4):167–177, 1990.

[9] M. J. Cooker. A boundary-integral method for water wave motion over irregular beds. *Engineering Analysis with Boundary Elements*, 7(4):205–213, 1990.

[10] M. J. Cooker and D. H. Peregrine. Computations of violent motion due to waves breaking against a wall. In *Proc. 22nd Intl. Conf. Coastal Eng.*, volume 1, pages 164–176, Delft, 1990. A.S.C.E.

[11] M. J. Cooker and D. H. Peregrine. Wave breaking and wave imapct pressures. In D. H. Peregrine and J. Loveless, editors, *Developments in Coastal Engineering*, pages 47–64. University of Bristol, 1991.

[12] C. de Boor. *A Practical Guide to Splines*, volume 27 of *Applied Mathematical Sciences*. Springer-Verlag, 1978.

[13] R. DeBar. Fundamentals of the KRAKEN code. Technical Report UCIR-760, Lawerence Livermore National Lab., 1974.

[14] J. W. Dold. An efficient surface-integral algorithm applied to unsteady gravity waves. *J. Comput. Phys.*, 103:90–115, 1992.

[15] J. W. Dold and D. H. Peregrine. An efficient boundary-integral method for steep unsteady water waves. In K. W. Morton and M. J. Baines, editors, *Numerical Methods for Fluid Dynamics II*, pages 671–679. Oxford University Press, 1986.

[16] D. G. Dommermuth and D. K. P. Yue. A high-order spectral method for the study of nonlinear gravity waves. *J. Fluid Mech.*, 184:267–288, 1987.

[17] D. G. Dommermuth and D. K. P. Yue. Numerical simulations of nonlinear axisymmetric flows with a free surface. *J. Fluid Mech.*, 178:195–219, 1987.

[18] D. G. Dommermuth, D. K. P. Yue, W. M. Lin, R. J. Rapp, E. S. Chan, and W. K. Melvile. Deep-water plunging breakers: a comparison between potential theory and experiments. *J. Fluid Mech.*, 189:423–442, 1988.

[19] P. T. Fink and W. K. Soh. A new approach to roll-up calculations of vortex sheets. *Proc. R. Soc. Lond. A*, 362:195–209, 1978.

[20] D. I. M. Forehand, J. G. B. Byatt-Smith, and C. A. Greated. Numerical prediction of extreme free-surface flows caused by body/fluid interaction. In *Proc. 6th Intl. Symp. Comput. Fluid Dyn.*, volume 1, pages 312–317, Lake Tahoe, Nevada, USA, September 1995.

[21] G. H. Golub and C. F. Van Loan. *Matrix Computations.* North Oxford Academic, Oxford, 1983.

[22] M. Greenhow. Wedge entry into initially calm water. *Applied Ocean Research*, 9(4):214–223, 1987.

[23] M. Greenhow. A complex variable method for the floating-body boundary-value problem. *J. Comput. Appl. Math.*, 46:115–128, 1993.

[24] M. Greenhow, T. Vinje, P. Brevig, and J. Taylor. A theoretical and experimental study of the capsize of Salter's duck in extreme waves. *J. Fluid Mech.*, 118:221–239, 1982.

[25] S. Grilli, J. Skourup, and I. A. Svendsen. An efficient boundary element method for nonlinear water waves. *Engineering Analysis with Boundary Elements*, 6(2):97–107, 1989.

[26] S. T. Grilli and R. Subramanya. Quasi-singular integrals in the modeling of nonlinear water waves in shallow water. *Engineering Analysis with Boundary Elements*, 13:181–191, 1994.

[27] S. T. Grilli and I. A. Svendsen. Corner problems and global accuracy in the boundary element solution of nonlinear wave flows. *Engineering Analysis with Boundary Elements*, 7(4):178–195, 1990.

[28] F. H. Harlow and J. E. Welch. Numerical calculation of time-dependent viscous incompressible flow of fluid with free surface. *Phys. Fluids*, 8:2182–2189, 1965.

[29] C. W. Hirt and B. D. Nichols. Volume of fluid method for the dynamics of free boundaries. *J. Comput. Phys.*, 39:201–225, 1981.

[30] R. A. Horn and C. R. Johnson. *Matrix Analysis.* Cambridge University Press, 1985.

[31] J. M. Hyman and M. J. Naughton. Static rezone methods for tensor-product grids. *Lectures in Applied Mathematics*, 22:321–343, 1985. AMS, Providence.

[32] M. de St Q. Isaacson. Nonlinear-wave effects on fixed and floating bodies. *J. Fluid Mech.*, 120:267–281, 1982.

[33] C. R. Johnson. Positive definite matrices. *Amer. Math. Monthly*, 77:259–264, 1970.

[34] O. D. Kellogg. *Foundations of Potential Theory.* Springer-Verlag, 1929. (reprinted 1967).

[35] A. C. King and D. J. Needham. The initial development of a jet caused by fluid, body and free-surface interaction. Part 1. A uniformly accelerating plate. *J. Fluid Mech.*, 268:89–101, 1994.

[36] D. B. Kothe and W. J. Rider. Comments on modeling interfacial flows with

volume-of-fluid methods. Technical Report LA-UR-94-3384, Los Alamos National Lab., 1995.

[37] W. M. Lin, J. N. Newman, and D. K. P. Yue. Nonlinear forced motions of floating bodies. In *Proc. 15th Symp. on Naval Hydro.*, pages 33–49, Hamburg, 1984. Washington: National Academy Press.

[38] Y. Liu, D. G. Dommermuth, and D. K. P. Yue. A high-order spectral method for nonlinear wave-body interactions. *J. Fluid Mech.*, 245:115–136, 1992.

[39] M. S. Longuet-Higgins and E. D. Cokelet. The deformation of steep surface waves on water. *Proc. R. Soc. Lond. A*, 350:1–26, 1976.

[40] A. K. Otta, I. A. Svendsen, and S. T. Grilli. Unsteady free surface waves in a region of arbitary shape. Research Report CACR-92-10, Center for Applied Coastal Research, Department of Civil Engineering, University of Delaware, Newark, Delaware 19716, 1992.

[41] D. H. Peregrine. Flow due to a vertical plate moving in a channel. Unpublished Note, 1972.

[42] C. Pozrikidis. *Boundary Integral and Singularity Methods for Linearized Viscous Flow.* Cambridge Univ. Press, Cambridge, 1992.

[43] W. H. Press, S. A. Teukolsky, W. T. Vetterling, and B. P. Flannery. *Numerical Recipes in Fortran: The Art of Scientific Computing.* Cambridge University Press, second edition, 1992.

[44] H. A. Priestley. *Intoduction to Complex Analysis.* Clarendon Press, Oxford, revised edition, 1990.

[45] A. Nestegård. Comparative study of fully non-linear wave simulation programs. Technical Report 94-2041, Det Norske Veritas Research As, Høvik, Norway, 1994.

[46] K. She, C. A. Greated, and W. J. Easson. Development of a two-dimensional numerical wave tank. In *Proceedings of the Second International Offshore and Polar Engineering Conference*, volume III, pages 102–109, San Francisco, 1992.

[47] D. J. Skyner. *The Mechanics of Extreme Water Waves.* PhD thesis, The University of Edinburgh, 1992.

[48] D. J. Skyner. A comparison of numerical predictions and experimental measurements of the internal kinematics of a deep-water plunging wave. *J. Fluid Mech.*, 315:51–64, 1996.

[49] W. J. Sternberg and T. L. Smith. *The Theory of Potential and Spherical Harmonics.* Number 3 in Mathematical Expositions. University of Toronto Press, Toronto, 1944.

[50] I. A. Svendsen. Mixed boundary value problem for Laplace's equation in domain of arbitrary shape. Progress Report 23, 33–38, Coastal Engineering Laboratory, Technical University of Denmark, 1971.

[51] I. A. Svendsen and I. G. Jonsson. *Hydrodynamics of Coastal Regions.* Den Private Ingeniørfond, Technical University of Denmark, Lyngby, Denmark, 1976.

[52] M. Tanaka, J. W. Dold, M. Lewy, and D. H. Peregrine. Instability and breaking of a solitary wave. *J. Fluid Mech.*, 185:235–248, 1987.

[53] W.-T. Tsai and D. K. P. Yue. Interactions between a free surface and a vortex sheet shed in the wake of a surface-piercing plate. *J. Fluid Mech.*, 257:691–721, 1993.

[54] W.-T. Tsai and D. K. P. Yue. Computation of nonlinear free-surface flows. *Annu. Rev. Fluid Mech.*, 28:249–278, 1996.

[55] T. Vinje and P. Brevig. Breaking waves on finite water depths. Report R-111.81, The University of Trondheim and The Ship Research Institute of Norway, Trondheim, Norway, 1981.

[56] T. Vinje and P. Brevig. Nonlinear, two-dimensional ship motions. Report R-112.81, The University of Trondheim and The Ship Research Institute of Norway, Trondheim, Norway, 1981.

[57] T. Vinje and P. Brevig. Numerical simulation of breaking waves. *Adv. Water Resources*, 4:77–82, 1981.

[58] B. J. West, K. A. Brueckner, R. S. Janda, D. M. Midler, and R. L. Milton. A new numerical method for surface hydrodynamics. *J. Geophys Res.*, 92(C11):803–824, 1987.

[59] S. A. Yang and A. T. Chwang. An experimental study of nonlinear waves produced by an accelerating plate. *Physics of Fluids A*, 4(11):2456–2465, 1992.

[60] D. L. Youngs. Time-dependent multi-material flow with large fluid distortion. In K. W. Morton and M. J. Baines, editors, *Numerical Methods for Fluid Dynamics*, pages 273–285. Academic Press, 1982.

[61] S. Zhang, D. K. P. Yue, and K. Tanizawa. Simulation of plunging wave impact on a vertical wall. *J. Fluid Mech.*, 327:221–254, 1996.